

INVESTIGATION OF SOME SELF-OPTIMIZING CONTROL
PROBLEMS FOR NET-ZERO ENERGY BUILDINGS

by

Xiao Li

A Dissertation Submitted in
Partial Fulfillment of the
Requirements for the Degree of

Doctor of Philosophy
in Engineering

at

The University of Wisconsin-Milwaukee

May 2013

ABSTRACT
INVESTIGATION OF SOME SELF-OPTIMIZING CONTROL
PROBLEMS FOR NET-ZERO ENERGY BUILDINGS

by

Xiao Li

University of Wisconsin-Milwaukee, 2013
Under the Supervision of Professor Yaoyu Li and Dr. John E. Seem

Green buildings are sustainable buildings designed to be environmentally responsible and resource efficient. The Net-Zero Energy Building (NZEB) concept is anchored on two pillars: reducing the energy consumption and enhancing the local energy generation. In other words, efficient operation of the existing building equipment and efficient power generation of building integrated renewable energy sources are two important factors of NZEB development. The heating, ventilation and air conditioning (HVAC) system is an important class of building equipment that is responsible for large portion of building energy usage, while the building integrated photovoltaic (BIPV) system is well received as the key technology for local generation of clean power. Building system operation is a low-investment practice that aims low operation and maintenance (O&M) cost. However, building HVAC and BIPV are systems subject to complicated intrinsic processes and highly variable environmental conditions and occupant behavior. Control, optimization

and monitoring of such systems desire simple and effective approaches that require the least amount of model information and the use of smallest number but most robust sensor measurements. Self-optimizing control strategies promise a competitive platform for control, optimization and control integrated monitoring for building systems, and especially for the development of cost-effective NZEB. This dissertation study endorses this statement with three aspects of work relevant to building HVAC and BIPV, which could contribute several small steps towards the ramification of the self-optimizing control paradigm.

This dissertation study applies self-optimizing control techniques to improve the energy efficiency of NZEB from two aspects. First, regarding the building HVAC efficiency, the dither based extremum seeking control (DESC) scheme is proposed for energy efficient operation of the chilled-water system typically used in the commercial building ventilation and air conditioning (VAC) systems. To evaluate the effectiveness of the proposed control strategy, Modelica based dynamic simulation model of chilled water chiller-tower plant is developed, which consists of a screw chiller and a mechanical-draft counter-flow wet cooling tower. The steady-state performance of the cooling tower model is validated with the experimental data in a classic paper and good agreement is observed. The DESC scheme takes the total power consumption of the chiller compressor and the tower fan as feedback, and uses the fan speed setting as the control input. The inner loop controllers for the chiller operation include two proportional-integral (PI) control loops for regulating the evaporator superheat and the chilled water temperature. Simulation was conducted on the whole dynamic simulation model with different environment conditions. The simulation results demonstrated the effectiveness of the

proposed ESC strategy under abrupt changes of ambient conditions and load changes. The potential for energy savings of these cases are also evaluated. The back-calculation based anti-windup ESC is also simulated for handling the integral windup problem due to actuator saturation.

Second, both maximum power point tracking (MPPT) and control integrated diagnostics are investigated for BIPV with two different extremum seeking control strategies, which both would contribute to the reduction of the cost of energy (COE). In particular, the Adaptive Extremum Seeking Control (AESC) is applied for PV MPPT, which is based on a PV model with known model structure but unknown nonlinear characteristics for the current-voltage relation. The nonlinear uncertainty is approximated by a radial basis function neural network (RBFNN). A Lyapunov based inverse optimal design technique is applied to achieve parameter estimation and gradient based extremum seeking. Simulation study is performed for scenarios of temperature change, irradiance change and combined change of temperature and irradiance. Successful results are observed for all cases. Furthermore, the AESC simulation is compared to the DESC simulation, and AESC demonstrates much faster transient responses under various scenarios of ambient changes.

Many of the PV degradation mechanisms are reflected as the change of the internal resistance. A scheme of detecting the change of PV internal shunt resistance is proposed using the available signals in the DESC based MPPT with square-wave dither. The impact of the internal resistance on the transient characteristics of step responses is justified by using the small-signal transfer function analysis. Simulation study is performed for both the single-string and multi-string PV examples, and both cases have

demonstrated successful results. Monotonic relationship between integral error indices and the shunt internal resistance is clearly observed. In particular, for the multi-string, the inter-channel coupling is weak, which indicates consistent monitoring for multi-string operation. The proposed scheme provides the online monitoring ability of the internal resistance condition without any additional sensor, which benefits further development of PV degradation detection techniques.

© Copyright by Xiao Li, 2013
All Rights Reserved

To My Parents & My Wife

TABLE OF CONTENTS

LIST OF FIGURES	xii
LIST OF TABLES	xvii
NOMENCLATURE	xviii
ACKNOWLEDGEMENTS	xxviii
Chapter 1 Introduction	1
1.1. Control Related Issues of Interest for Net-Zero Energy Buildings	3
1.1.1. Chilled Water System in Commercial Buildings.....	3
1.1.2. Building Integrated Photovoltaic System	5
1.1.3. Major Objective of Dissertation.....	7
1.2. Research Problems and Approaches	8
1.2.1. Self-Optimizing Control for Efficient Operation of Chilled-Water Plant	8
1.2.2. Dynamic Simulation Modeling of Chiller-Tower Plant	12
1.2.3. ESC Based MPPT Control on Photovoltaic System	14
1.2.4. DESC MPPT and Integrated PV System Diagnostics	17
1.3. Problem Statements for Dissertation Research	20
1.4. Organization of the Dissertation	20
Chapter 2 Literature Review	22
2.1. Review of Extremum Seeking Control (ESC) Techniques.....	22
2.1.1. Review of Dither Based Extremum Seeking Control.....	23
2.1.2. Chilled Water System in Commercial Buildings.....	25
2.2. Previous Work on Modeling of Chilled-Water Plant	29
2.2.1. Literature Review on Cooling Tower Modeling.....	29

2.2.2.	Literature Review on Screw Chiller Modeling	33
2.3.	Control and Optimization Techniques on Chilled Water System	36
2.4.	MPPT Techniques on Photovoltaic System	40
2.5.	PV System Degradation and Detection Techniques	45
Chapter 3 Modeling of Chilled Water Plant		48
3.1.	Dynamic Modeling of Counter Flow Wet Cooling Tower	48
3.1.1.	Cooling Tower Modeling.....	52
3.1.2.	Determination of NTU and Le_f	57
3.1.3.	Model of Related Components Used in Simulation	59
3.1.3.A.	Cooling Tower Fan	59
3.1.3.B.	Condenser Water Pump.....	60
3.1.3.C.	Collection Basin	61
3.2.	Simulation Study for Cooling Tower Modeling	62
3.2.1.	Steady-State Simulation and Comparison	62
3.2.2.	Transient Simulation	65
3.3.	Modeling of Screw Chiller.....	72
3.3.1.	Screw Compressor	72
3.3.2.	Condenser, Evaporator and Expansion Valve	73
Chapter 4 ESC Based Optimization Control of Chilled Water System.....		75
4.1.	Proposed Controls in Chilled Water System	76
4.2.	Overview of Design Guildelines for Dither ESC	77
4.3.	Simulation Study.....	79
4.3.1.	Dither ESC Design.....	79
4.3.2.	Case Study	81
Chapter 5 Maximum Power Point Tracking for Photovoltaic System Using Adaptive Extremum Seeking Control.....		94

5.1.	Photovoltaic System Model	95
5.2.	AESC Based MPPT Design for PV Systems.....	98
5.2.1.	Analytical Modeling of PV Dynamics.....	98
5.2.2.	Design of AESC Based PV MPPT	99
5.3.	Simulation Study.....	108
Chapter 6 Detection of Internal Resistance Change for Photovoltaic Arrays Using Extremum Seeking Control MPPT Integrated Signals		121
6.1.	Simulation Model of Photovoltaic System	122
6.2.	Extremum Seeking Control Based PV MPPT	123
6.2.1.	Single-Input ESC MPPT for Single-String PV System.....	123
6.2.2.	Multi-Input ESC MPPT for Multi-String PV System	126
6.3.	ESC Integrated Detection of Change of Internal Shunt Resistance.....	132
6.4.	Summary	141
Chapter 7 Conclusion and Future Work		143
7.1.	Summary of Research Work and Contribution	143
7.2.	Recommended Future Work	147
References.....		149
Appendices.....		173
A.	Calculation of the Merkel's Number	173
B.	Parameters for Steady-State Evaluation of Cooling Tower Model	176
C.	Chiller Cycle Component Modeling.....	178
C.1.	Condenser and Evaporator	178
C.1.1.	Finite Volume Method Based Modeling.....	178
C.1.2.	Variable Refrigerant Level (VRL) Based Modeling.....	190
C.2.	Expansion Device.....	192
C.2.1.	Orifice Plate.....	193

	C.2.2. Thermal Expansion Valve	195
D.	Component Parameters Used in Chiller-Tower Cycle Simulation.....	198
E.	Controller Parameters Used in DESC Based Chilled Water System Optimization Simulation	202
F.	PV MPPT Using Adaptive ESC Simulink	207
G.	Multi-String PV MPPT and Internal Resistance Change Detection Using Square-Wave Dithered ESC Simulink.....	211

LIST OF FIGURES

Figure 1.1: Chart of global energy consumption and U.S. energy consumption [1]	1
Figure 1.2: Chart of U.S. electricity consumption, 2001~2010 [1]	2
Figure 1.3: Block diagram of typical chilled water system (reproduction of Fig. 2A in [2])	4
Figure 1.4: Tradeoff between energy consumption of chiller and cooling tower (reproduction of Fig. 2 in [3])	9
Figure 1.5: Basic system diagram of ESC working on chiller-tower cycle (reproduction of Fig. 2C in [2])	12
Figure 1.6: I - V and P - V curves at temperature 25°C under different irradiance rates where (a) is the I - V curves and (b) is the P - V curves	14
Figure 1.7: I - V and P - V curves at irradiance rate 1000W/m ² , under different temperatures where (a) is the I - V curves and (b) is the P - V curves.....	15
Figure 1.8: P - V Characteristics with different internal shunt resistances	18
Figure 1.9: I - V Characteristics with different internal shunt resistances	18
Figure 2.1: Block diagram of dither ESC	25
Figure 2.2: System structure for AESC.	27
Figure 3.1: Schematic diagram for mechanical draft counter flow wet cooling tower.....	49
Figure 3.2: Illustration of control volumes for cooling tower modeling	53
Figure 3.3: Energy balance between neighboured water and air control volumes	53
Figure 3.4: Mass balance between neighbored water and air control volumes	54
Figure 3.5: Dymola layout for evaporative cooling process of cooling tower	63
Figure 3.6: Comparison for outlet water temperature between model prediction and measured data.....	64
Figure 3.7: Transient profile of water outlet temperature in simulation test 1 with stand- alone cooling tower model.....	66
Figure 3.8: Transient profile of water cell temperatures in simulation test 1 with stand- alone cooling tower model.....	67

Figure 3.9: Transient profile of water outlet temperature in simulation test 2 with stand-alone cooling tower model.....	68
Figure 3.10: Transient profile of water cell temperatures in simulation test 2 with stand-alone cooling tower model.....	69
Figure 3.11: Dymola layout for the whole system of cooling tower model	70
Figure 3.12: Transient profile of water outlet temperature for comparison between tower body and collection basin output water	71
Figure 3.13: Simulation results of Lewis relation in the transient test	71
Figure 4.1: Schematic for the ESC control system for chiller-tower plant.....	77
Figure 4.2: Block diagram of modified anti-windup ESC.....	79
Figure 4.3: Comparison of full simulation model and the 2 nd -order estimate	80
Figure 4.4: Static map from cooling tower fan speed to total power consumption.....	82
Figure 4.5: ESC on chiller tower system with fixed operation condition, fan speed and power consumption.....	83
Figure 4.6: Superheat control results for ESC with fixed operation condition.....	83
Figure 4.7: Chilled water temperature control for ESC with fixed operation condition ..	84
Figure 4.8: Static maps for T_{EW} decreased from 12°C to 10°C	85
Figure 4.9: ESC simulation results for T_{EW} decreased from 12°C to 10°C	85
Figure 4.10: Superheat profile for ESC tower fan control when T_{EW} drops from 12°C to 10°C.....	86
Figure 4.11: Chilled water temperature profile for ESC tower fan control when T_{EW} drops from 12°C to 10°C.....	86
Figure 4.12: Change of ambient-air condition: the air temperature decreases from 37°C to 35°C , and the relative humidity increases from 20% to 80%	87
Figure 4.13: Static power map for two ambient air conditions: temperature and relative humidity of 37°C and 20% versus 35 °C and 80%	88
Figure 4.14: ESC simulation results when the ambient air condition changed from 37°C and 20% RH to 35°C and 80% RH	89

Figure 4.15: Superheat profile under ESC tower fan control when the ambient air condition changed from 37°C and 20% RH to 35°C and 80% RH.....	89
Figure 4.16: Chiller leaving water temperature profile under ESC tower fan control when the ambient air condition changed from 37°C and 20% RH to 35°C and 80% RH.....	90
Figure 4.17: Fast ramp changes in evaporator inlet water temperature for simulation case to demonstrate integral windup and anti-windup ESC test.....	91
Figure 4.18: ESC integral windup for simulation case 4 with actuator saturation	92
Figure 4.19: Simulation results of case 4 with anti-windup ESC	92
Figure 5.1: PV cell equivalent circuit	96
Figure 5.2: PV array with front-end buck converter.....	97
Figure 5.3: Comparison of PV MPPT results with AESC and dither ESC	110
Figure 5.4: AESC MPPT with a step change of temperature from 25°C to 17°C.	111
Figure 5.5: Dither ESC MPPT with a step change of temperature 25°C to 17°C.....	112
Figure 5.6: AESC MPPT with a step change of irradiance rate from 1000 to 500W/m ²	113
Figure 5.7: Dither ESC MPPT with a step change of irradiance rate from 1000 to 500W/m ²	114
Figure 5.8: AESC MPPT with a simultaneous step change of both temperature (25°C to 17°C) and irradiance rate (1000 to 800W/m ²)	115
Figure 5.9: Dither ESC MPPT with a simultaneous step change of both temperature (25°C to 17°C) and irradiance rate (1000 to 800W/m ²).....	116
Figure 5.10: AESC MPPT with a step change of irradiance rate from 1000 to 300W/m ²	117
Figure 5.11: AESC MPPT with a ramp change of temperature from 25°C to 17°C.....	118
Figure 5.12: AESC MPPT under a combined change of irradiance rate and temperature	119
Figure 6.1: PV device with voltage control using a buck converter.....	123
Figure 6.2: Block diagram of dither ESC based PV MPPT.....	123
Figure 6.3: Step responses of PV full simulation model and the 2 nd –order estimate	124

Figure 6.4: P - V characteristic of single PV module under nominal conditions.....	125
Figure 6.5: ESC simulation results for single-string PV under nominal conditions.....	126
Figure 6.6: Schematic illustration for series connected multi-string structure	127
Figure 6.7: Multi-input ESC scheme for multi-string PV system	128
Figure 6.8: P - V curves for two-string PV array: String 1 with 25°C and 1000 W/m ² , String 2 with 25°C and 500 W/m ²	129
Figure 6.9: 3-D power map for the two-string PV system in Fig. 6.8	130
Figure 6.10: Voltage profiles for two-input ESC MPPT with sinusoidal dither: String 1 with 25°C and 1000 W/m ² , String 2 with 25°C and 500 W/m ²	131
Figure 6.11: Power profiles for two-input ESC MPPT with sinusoidal dither: String 1 with 25°C and 1000 W/m ² , String 2 with 25°C and 500 W/m ²	132
Figure 6.12: PV array linear circuit model current source ($v_{PV} < V_{mp}$).....	133
Figure 6.13: ESC simulation results for single PV module under nominal conditions with duty ratio as control input: upper subplot: power; middle subplot: voltage; lower subplot: duty ratio	135
Figure 6.14: Comparison of ESC searched voltage with different shunt resistances	136
Figure 6.15: ESC simulation for two-string PV array of different internal resistance ...	140
Figure C.1: Modelica model layout of the condenser model (reproduced and modified with permission from TIL's <i>TubeAndTube</i> heat exchanger model)	179
Figure C.2: Illustrative diagram for the dp/dt assumption	183
Figure C.3: Illustration of water and refrigerant sides' heat transfer in basic cell models	184
Figure C.4: Illustrative diagram of heat transfer regions in the evaporator	188
Figure C.5: Illustrative diagram of heat transfer regions in the condenser	189
Figure C.6: Modelica model of a VRL-based condenser in TIL	192
Figure C.7: Control volume of an orifice plate	193
Figure C.8: Illustrative diagram of forces acting on a TXV	195
Figure D.1: Dymola layout of chiller-tower cycle	198

Figure E.1: Dymola layout for the simulation of dither ESC based optimization control of chilled-water system	202
Figure E.2: Dymola layout of dither ESC controller	203
Figure E.3: Dymola layout for the simulation of anti-windup ESC based optimization control of chilled water system	204
Figure E.4: Dymola layout of anti-windup ESC controller	205
Figure F.1: Simulink layout of adaptive ESC based PV MPPT, control law and PV system plant	207
Figure F.2: Simulink layout of adaptive ESC based PV MPPT, state and tracking error estimates	208
Figure F.3: Simulink layout of adaptive ESC based PV MPPT, design parameters	209
Figure F.4: Simulink layout of adaptive ESC based PV MPPT, parameter learning and dither signal	209
Figure F.5: Simulink layout of PV array plant	210
Figure G.1: Simulink layout of square-wave dither ESC on multi-string structure	211
Figure G.2: Simulink layout of multi-string PV plant	212

LIST OF TABLES

Table 3.1: Comparison of cooling tower simulation model and experimental data	63
Table 3.2: Definitions of Scenarios 1 and 2 involved in simulation test 1	65
Table 3.3: Definitions of Scenarios 1 and 2 involved in simulation test 2	68
Table 6.1: Estimated maximum achievable power and integral performance indices of square-wave dither output under different shunt resistance R_p	137
Table 6.2: Integral performance indices of square-wave dither output under different R_p with multi-string framework.....	140
Table B.1: Geometric parameters used in steady-state evaluation of cooling tower model	176
Table B.2: Initial conditions for water and moist air	177
Table D.1: Geometric parameters of the condenser and evaporator.....	199
Table D.2: Parameters of the dp / dt components.....	199
Table D.3: Parameters of the orifice valve	199
Table D.4: Parameters of the screw compressor.....	199
Table D.5: Parameters of the cooling tower	200
Table D.6: Parameters of the cooling tower fan	200
Table E.1: Parameters of the controllers used in the ESC based chilled water system optimization	205

NOMENCLATURE

Abbreviations

1D	One-dimensional
AESC	Adaptive extremum seeking control
AH	Absolute humidity
AHU	Air-handling units
ANN	Artificial neural network
BIPV	Building integrated photovoltaics
CFD	Computational fluid dynamics
COE	Cost of energy
COP	Coefficient of performance
CSB-SQP	Complete simulation-based sequential quadratic programming
DAE	Differential algebraic equation
DESC	Dither based extremum seeking control
DOE	Department of energy
ESC	Extremum seeking control
FFD	Fault detection diagnostics
FMI	Functional mock-up interface
FV	Finite volume
GA	Generic algorithm
HC	Hill climbing
HVAC	Heating, ventilation, and air conditioning
IAE	Integrated absolute error
Ift	Institut für Thermodynamik

IncCond	Incremental conductance
ISE	Integral squared error
ITAE	Integral time-weighted absolute error
ITSE	Integral time-weighted squared error
Le _f	Lewis relation
LTI	Linear time invariant
LUT	Look-up table
MPP	Maximum power point
MPPT	Maximum power point tracking
NREL	National renewable energy laboratory
NTU	Number of units
NZEB	Net-zero energy building
ODE	Ordinary differential equation
O&M	Operation and maintenance
PI, PD	Proportional-integral, proportional-derivative
PLR	Part load ratio
P&O	Perturbation and observation
PRBS	Pseudo random binary sequence
PV	Photovoltaic
PWM	Pulse-width modulator
RBNN	Radial basis function neural network
RH	Relative humidity
SCOP	System coefficient of performance
SEIA	Solar energy industries association
SISO	Single input single output

SPARK	Simulation problem analysis and research kernel
TIL	TLK-IfT-Library
VSD	Variable speed drive

Latin Symbols

a, a_i	Dither amplitudes
a_c, b_c	Positive constants in AESC design
a_{if}	Ideality factor
A_T	Cross-sectional area of the cooling tower
A_{TXV}	Thermal expansion valve's effective flow area
A_v	Surface area of water droplets per unit volume
$b_i(s)$	Basis function kernels
c, c_i	AESC design parameter to be assigned in the control design process
$c_{p,w,i} (c_{pm,i})$	Local specific heat of water (moist air)
$c_{pa,i} (c_{pv,i})$	Local specific heat of dry air (water vapor)
$c_{pw,cb}$	Specific heat of water in the collection basin
c_{CT}, n_{CT}	Empirical constants specific to a particular tower design
C, L, R	Capacitance, inductance and resistance
d	AESC dither signal
d_1	Demodulating signal
d_2	Dither signal
d_r	Ratio of the molecular weight of water to the molecular weight of air

d_D, D	Duty ratio
$e_{pump,loss}$	A constant exponent for power loss calculation
e_x, e_s	State estimated error
E_g	Bandgap energy of the semiconductor
$F_{HP}(s), F_{LP}(s)$	High-pass filter and low-pass filter
$F_I(s), F_O(s)$	Input dynamics and output dynamics
G, G_n	Actual and nominal irradiance rate on the device surface
$h_{c,in}, h_{c,out}$	Specific enthalpies for the inlet and outlet refrigerant of compressor
$h_{C,i}(h_{D,i})$	Local heat (mass) transfer coefficient
$h_{cb,in}, h_{cb,out}$	Specific enthalpies for the inlet and outlet water of collection basin
$h_{f,g,i}$	Latent heat of vaporization depending on the local water temperature
h_i	Amplitude of the square-wave dithered voltage signal
$h_{pump}(h_{cb})$	Specific enthalpy of the water in the pump (collection basin)
$h_{pump,in}, h_{pump,out}$	Specific enthalpies for the inlet and outlet water of pump
$h_{w,i}$	Specific enthalpy of the i^{th} water cell
$h_{w,in,i}, h_{w,out,i}$	Specific enthalpies of the inlet and outlet water flow of the i^{th} water cell
$\dot{H}_{a,in,i}, \dot{H}_{a,out,i}$	Inlet and outlet air enthalpies of the i^{th} moist air cell
$\Delta H_{w,i}$	Enthalpy change of the i^{th} water cell
$\dot{H}_{w,in,i}, \dot{H}_{w,out,i}$	Inlet and outlet water enthalpies of the i^{th} water cell
$i(V)$	Nonlinear mapping between the output current and the terminal voltage of the PV array
i_L	Inductor current

I_0	Reverse saturation (or leakage) current of the diode
$I_{0,n}$	Nominal saturation current
I_{PV}	Light generated current that is proportional to the irradiance
$I_{PV,n}$	Light generated current at the nominal condition (25°C and 1000W/m ²)
k	Boltzmann constant, $1.3806503 \times 10^{-23}$ J/K
k_1, k_2	Scaled factors
k_3, k_4	Positive constants in AESC design
k_x, k_s	AESC design parameters
k_{x0}, k_{s0}, k_{z0}	Positive constants in AESC design
$K(s)$	ESC compensator
K_A	Anti-windup gain
K_I	Short-circuit temperature coefficient
Le, Le_f	Lewis number and Lewis relation, respectively
$\dot{m}_{a,in} (\dot{m}_{w,in})$	Tower inlet air (water) mass flow rate
$\dot{m}_{c,in}, \dot{m}_{c,out}$	Refrigerant mass flow rate at the compressor inlet and outlet
$\dot{m}_{cb,in}, \dot{m}_{cb,out}$	Inlet and outlet mass flow rates of the collection basin
$\dot{m}_{cb,makeup}$	Water mass flow rate from some source of make-up water
$\dot{m}_{evp,i}$	Vapor mass transfer flow rate from the i^{th} water cell to the neighbored moist air cell
$\dot{m}_{pump,in}, \dot{m}_{pump,out}$	Inlet and outlet mass flow rates of the water pump
$m_{w,i}$	Mass of water stored in the i^{th} water cell
$\dot{m}_{w,in,i}, \dot{m}_{w,out,i}$	Inlet and outlet water mass flow rates of the i^{th} water cell

Me_M	Merkel's number
n	Noise signal
n_c	Compressor speed
$n_{fan}(n_{pump})$	Rotational speed of the fan (pump)
$n_{fan,0}(n_{pump,0})$	Nominal speed of the fan (pump)
N_k	Number of kernels used in the RBFNN
$N_s(N_p)$	Number of PV cells connected in series (parallel)
$\Delta p_{fan}(\Delta p_{pump})$	Actual pressure increase for the fan (pump)
$\Delta p_{fan,0}(\Delta p_{pump,0})$	Pressure increase for zero volume flow rate for the fan (pump)
$\Delta p_{fan,affinity,0}$	Pressure increase for zero volume flow rate of the fan follow the fan affinity law
$\Delta p_{pump,affinity,0}$	Pressure increase for zero volume flow rate of the pump follow the affinity law
$P_{c,in}, P_{c,out}$	Compressor inlet and outlet pressures
P_{max}	Maximum power output
q	Electron charge with the value of $1.60217646 \times 10^{-19}$ C
\dot{q}_i	Heat flow transferred from the i^{th} water cell to the neighbored moist air cell
$\dot{q}_{lat,i}$	Latent heat flow transferred from the i^{th} water cell to the neighbored moist air cell
$\dot{q}_{sen,i}$	Sensible heat flow transferred from the i^{th} water cell to the neighbored moist air cell
$Q_{fan}(Q_{pump})$	Actual volume flow rate for the fan (pump)
$Q_{fan,0}(Q_{pump,0})$	Volume flow rate for zero pressure increase of the fan (pump)

$Q_{fan,affinity,0}$	Volume flow rate for zero pressure increase of the fan following the fan affinity law
$Q_{pump,affinity,0}$	Volume flow rate for zero pressure increase of the pump following the affinity law
R_{eq}	Thévenin equivalent resistance
R_o	Resistive load
R_p	PV internal shunt (parallel) resistance
R_s	PV internal series resistance
s, x	System states
\hat{s}, \hat{x}	Predictions of the system states
s_{comp}	Slide-valve control of the compressor
S	Basis function vector
t	Current simulation time
t_1, t_2	Selected time period
T, T_n	Actual and nominal temperatures
$T_{a,i}$	Local air temperature
$T_{db,in}, T_{db,out}$	Tower inlet and outlet dry bulb temperatures
T_{EW}	Evaporator inlet water temperature
$T_{pump,w}(T_{cb,w})$	Local water temperature in the pump (collection basin)
$T_{w,i}$	Local water temperature
$T_{w,in}$	Tower inlet water temperature
$T_{w,out,cal}$	Model predicted water outlet temperature
$T_{wb,in}$	Tower inlet wet bulb temperature

u	Control input
u_{opt}	Optimal control input
v_w	Velocity of water droplets under free fall
V, I	Output voltage and current
V_{cell}	Cell volume
$V_{c,max}$	Theoretical compressor volume with full load condition
$V_{effective}$	Water droplet volume in the i^{th} water cell
V_{eq}	Thévenin equivalent voltage
V_i	Voltage signals
V_{is}	Mean value of the steady-state voltage signals
$V_M (I_M)$	Maximum voltage (current) of the PV system
V_o	Terminal voltage
V_{oc}	Open circuit voltage
$V_{pump} (V_{cb})$	Volume of the water in the pump (collection basin)
V_t	Thermal voltage of the array with N_s cells connected in series
V_T	Total tower volume
w_m	Upper bound of weight norm
W	RBF NN parameters
W_{fan}	Fan power
$W_{pump,loss}$	Actual power loss of the pump at the rotational speed n_{pump}
$W_{pump,loss,0}$	Power loss of the pump at nominal speed
$W_{pump,shaft}$	Pump shaft power

\hat{W}	Estimate of the true weights W^*
\tilde{W}	Parameter estimation error for RBF NN
y	Objective function
z_s	Optimization oriented tracking error

Greek Symbols

α, α_i	ESC dither phase angles
$\beta_{pump}(\beta_{cb})$	Local isobaric coefficient of expansion in the water pump (collection basin)
$\beta_{w,i}$	Isobaric coefficient of expansion in the i^{th} water cell
γ_c	Ratio of specific heats in the compressor
γ_w	Positive gains for parameter update law in AESC design
δ_c	Positive constant in AESC design
ε	Positive constant in AESC design
ζ	Damping ratio
$\eta_{c,a}, \eta_{c,mo}, \eta_{c,me}$	Adiabatic efficiency, motor efficiency and mechanical efficiency of the compressor
$\eta_{c,v}$	Volumetric efficiency of the compressor
ϕ_i	Center of the Gaussian function
σ_i	Width of the Gaussian function
η_{fan}	Fan efficiency
$\eta_{fan,m}$	Fan motor efficiency
$\mu(x)(\mu(s))$	Unknown static nonlinearity of state $x(s)$

$\mu_l(t)$	Approximation error
$\rho_{c,in}, \rho_{c,out}$	Refrigerant densities at the compressor inlet and outlet
$\rho_{pump,w}(\rho_{cb,w})$	Local water density in the pump (collection basin)
$\rho_{w,i}$	Water density of the i^{th} water cell
$\omega_{a,i}$	Local humidity ratio of the moist air
ω_c	Cut-off frequency of the system input dynamics
ω_d, ω_i	ESC dither frequencies
ω_n	Undamped natural frequency
$\omega_{s,w,i}$	Saturated air humidity ratio at the local water temperature

ACKNOWLEDGEMENTS

This dissertation would not have been possible without the help of many people in assorted ways. I would like to take this opportunity to express my gratitude to them all in my sincerely acknowledgement. In the first place I would like to express my gratefully and sincerely thanks to my advisors Prof. Yaoyu Li and Dr. John E. Seem for their supervision, advice, and guidance from every stage of my research. Their comments and valuable suggestions are the persistent reminder for me to pursue the high quality in my work. Their dedication and serious attitude always inspire and enrich my growth as a student and a researcher.

I would like to thank Prof. Ronald A. Perez, Prof. Tien-Chien Jen and Prof. Guangwu Xu served as the rest of my committee members for their precious time and support.

Support and help from members at UWM Mechatronics lab are gratefully acknowledged, especially thanks for the previous work of Pengfei Li and Peng Lei, which provide a solid basis of my work.

I also want to thank Dr. Willi Tegethoff, Dr. Andre Thüring and Dr. Sven Fosterling for TLK-Thermo's collaboration help on TIL Library.

I am also greatly indebted to the continuous funding support from Johnson Controls, Inc. during my Ph.D. research, from which I have the opportunity to focus on my research without the fear of the trouble in the rear.

Above all and the most needed, I would like to record my thanks to my family for their unflinching encouragement and support in various ways.

Chapter 1. Introduction

Buildings consume large portion of energy in the industrialized nations. For instance, about 40% of the primary energy consumption in the U.S. comes from the building sector [1], in which 18% for commercial and 22% for residential buildings. As shown in Fig. 1.1, the building sector bears the largest energy usage compared to the transportation sector (28%) and the industrial sector (32%), and accounts for about 2/3 of the U.S. electricity consumption in 2010 (Fig. 1.2) [1]. As consequence, the CO₂ emission from the buildings is also significant. About 39% of the U.S. total carbon emissions are coming from the building sector with 18% from the commercial buildings and 21% from the residential buildings [4].

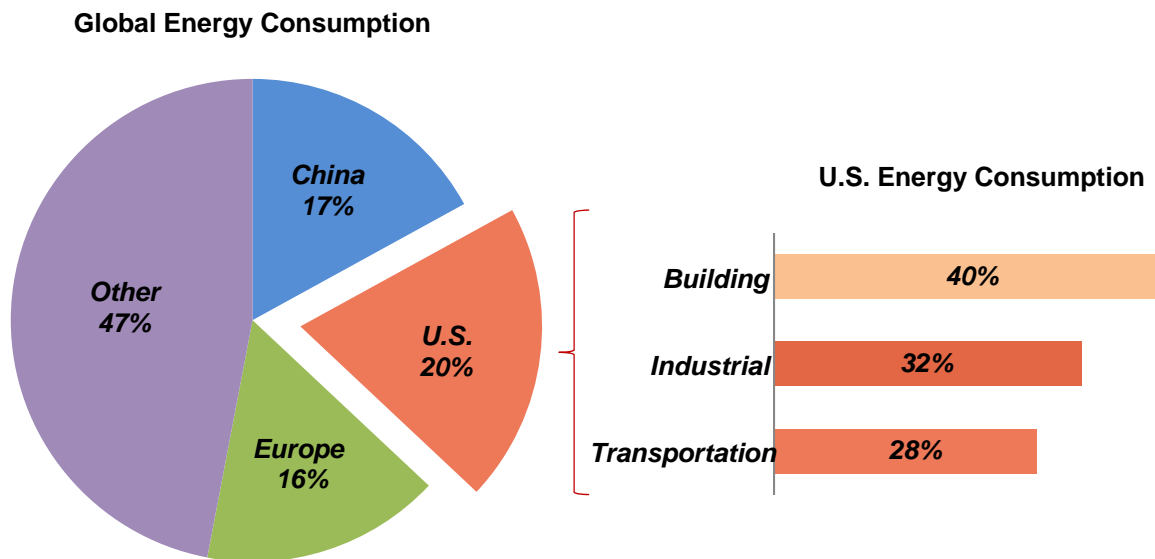


Figure 1.1: Chart of global energy consumption and U.S. energy consumption [1]

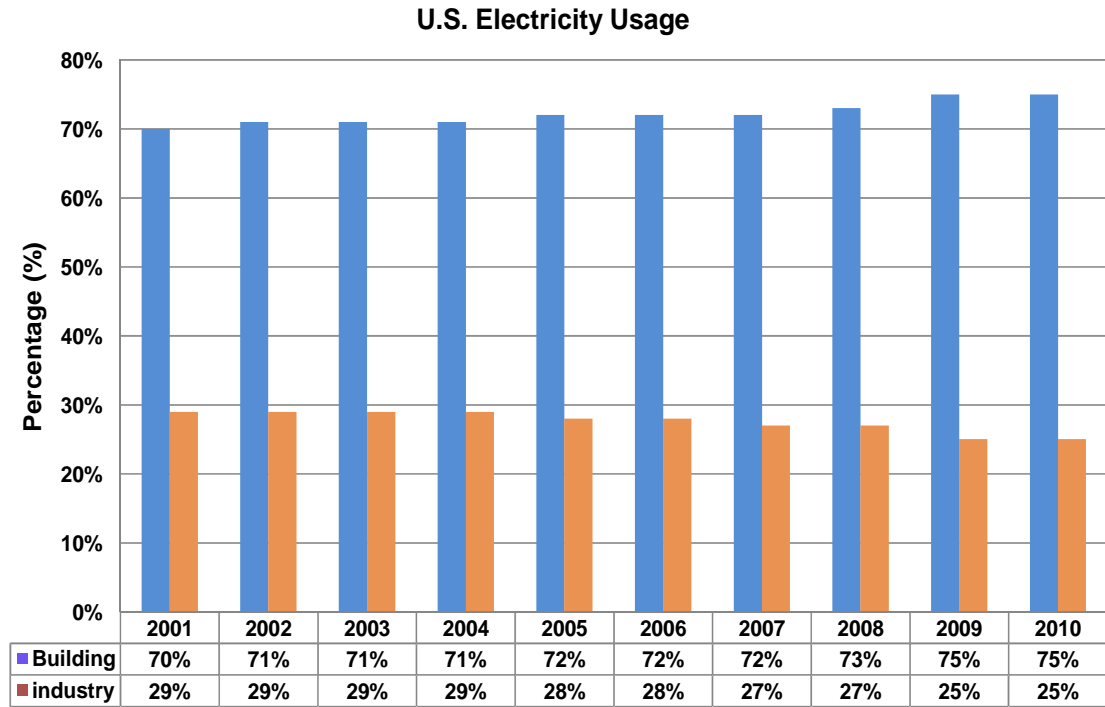


Figure 1.2: Chart of U.S. electricity consumption, 2001~2010 [1]

Energy efficiency and use of renewable/clean energy have become key factors for contemporary building development. Recently, the Green Building concept has drawn much attention worldwide, which aims to achieve sustainable, environmentally responsible and resource efficient buildings [5]. The so-called Net-Zero Energy Building (NZEB) has been well received as the goal to be implemented for the decades to come [6]. Development of NZEB requires both the enhancement of energy efficiency for the existing building HVAC equipment, and also the efficient power generation of building integrated renewable energy resources such as wind and solar. This dissertation study investigates self-optimizing control problems of both aspects, i.e. the efficient operation of chilled-water chiller-tower plant and the maximum power point tracking (MPPT) for photovoltaic systems.

1.1. Control Related Issues of Interest for Net-Zero Energy Buildings

The Green Building is also referred as Sustainable Building or High Performance Building [6]. The earliest investigations and practices of green buildings date back to the 1970s, around the first oil crisis [5]. The green building design aims to reduce the overall impact from the building construction, equipment operation and maintenance, energy and resources consumption, and pollutions of the buildings on both of the indoor and outdoor environments [6]. The idea of sustainable construction and maintenance has become much more attractive lately, very popular in the building research field and the architectural design practice. The NZEB concept reflects the accompanied view for energy usage in green buildings [7]. The U.S. DOE and its National Renewable Energy Laboratory (NREL) have defined the NZEB as follows: “A net-zero energy building (NZEB) is a residential or commercial building with greatly reduced energy needs through efficiency gains such that the balance of energy needs can be supplied with renewable technologies” [8]. The U.S. DOE has also established goals for “creating the technology and knowledge base for cost effective net-zero energy commercial buildings by 2025” [8]. The NZEB requires measures taken for both the energy efficiency and the renewable energy source.

1.1.1. Chilled Water System in Commercial Buildings

For commercial buildings, HVAC systems are critical for providing comfort and health indoor environment, and meanwhile, they also take a high percentage of the overall energy consumption [1, 9]. For 2010, the U.S. Department of Energy (DOE) estimated that about 54% of site energy consumption and 43% of primary energy consumption of the residential building sector come from the HVAC operation, in which 9% for space

cooling and 45% for space heating in site energy consumption and 15.1% and 27.8% in primary energy consumption respectively [1]. For the commercial building sector, HVAC accounts for 42.8% of site energy consumption (26.6% for space heating, 10.1% for space cooling and 6.1% for ventilation) and 39.6% of primary energy consumption (16.0% for space heating, 14.5% for space cooling and 9.1% for ventilation) [1].

In particular, the chilled-water system is widely adopted by high-capacity ventilation and air-conditioning (VAC) systems to balance the cooling of the indoor environment with chilled water. Figure 1.3 shows the schematic of a typical configuration of chilled-water VAC system for commercial buildings, which consists of three main components: air handling unit, electric chiller and cooling tower.

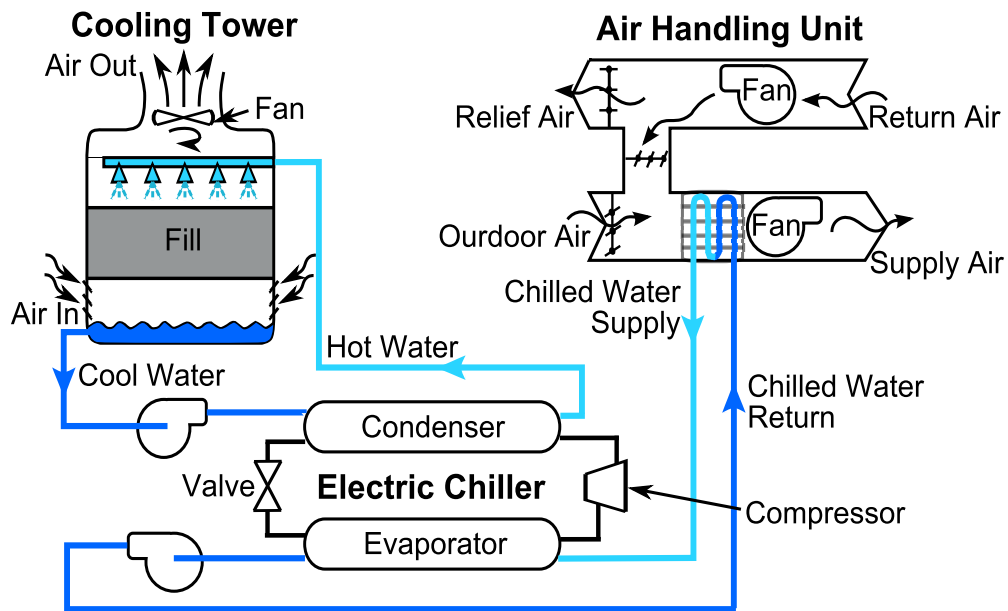


Figure 1.3: Block diagram of typical chilled water system (reproduction of Fig. 2A in [2])

The chilled water is pumped to the air-handling units (AHU) to provide indoor space cooling and then circulated back to the chiller with higher temperature. Via the vapor compression refrigeration cycle in the chiller, the heat is transferred from the refrigerant to the condensing water. Then the evaporative cooling of the cooling tower helps to reject

heat to the ambient via the heat and mass transfers occurring at the direct contact between the hot water droplets and the inlet moist air [9].

For the chilled-water VAC system, the main power consumption is due to the chiller compressor and the cooling tower fan. Efficient operation of the chilled-water VAC system is thus critical for the energy efficiency for the operation of commercial buildings [10]. Due to the significant variations in ambient, load and equipment conditions, the system behavior can vary dramatically. For real-time optimization of the energy efficiency, nearly model-free adaptive control strategy, or the so-called self-optimizing control strategy, is ideal for such system. Optimization and control techniques have been studied for chilled water system in the past [3, 7, 8, 11]. However, most of the existing methods are based empirical models, which are difficult to apply in practice due to the environmental changes and equipment degradation. A key interest in this dissertation study is to investigate on a class of self-optimizing strategy, the dither-demodulation based extremum seeking control (ESC), for the real-time set-point optimization for the chilled-water VAC system without detailed system knowledge.

1.1.2. Building Integrated Photovoltaic System

Development of NZEB inevitably requires building integrated (or local) renewable power generation, such as wind and solar. Solar energy is an attractive renewable energy source due to its zero-emission nature and abundant availability, displacing the daytime demand for the electric power from fossil fuels and facilitating peak-load shaving. Solar power generation has experienced dramatic growth in the past decade, 40 GW in 2010 comparing to 0.7 GW in 1996 [12]. The Solar Energy Industries Association (SEIA) predicts that “the global capacity of solar power will reach 980 GW by 2020” [13].

The PV power generation is considered highly amenable for building integration, which can well take advantage of the surface areas available on the façade or roof [14]. The PV systems appeared in the U.S. buildings in the 1970s, with stand-alone PV modules mounted on remote areas of buildings. Later in the 1980s, the rooftop PV panels started to gain attention [15]. The Building Integrated Photovoltaics (BIPV) concept was introduced in the 1990s, which is a directly integration of photovoltaic system onto the building surfaces. Compared to the conventional installation of rack-mounted PV, BIPV is reported to have about 10% potential decrease in the resultant system prices due to the hardware and labor saving [16]. But the no-spacing design structure of BIPV may also lead to a reduced performance by possibly higher average operating temperature [16].

The high cost of energy (COE) has been a major problem for the PV system, which has been dealt with two kinds of measures. One is to improve material and manufacturing. There have been great efforts in reducing the material cost and developing materials structured with better conversion efficiency. The other is to improve the operation and maintenance (O&M). From the operational standpoint, it is desired to maintain the PV system at its maximum power efficiency in real time [17]. However, the PV system characteristics are always changing with changes in the environmental condition. The so-called *Maximum Power Point Tracking* (MPPT) operation is needed to seek and track the maximum power point (MPP) in real time against the internal and/or external uncertainties. There have been various strategies developed for PV MPPT, in model based or model free. This dissertation aims to investigate two kinds of self-optimizing control strategy: in addition to the aforementioned dither-demodulation extremum seeking control, of particular interest is the adaptive extremum seeking

(AESC) which is based on the knowledge of the structure of nonlinear dynamics of the PV system.

Another important issue, from the condition based maintenance standpoint, is the need for online monitoring. Degradation in PV devices leads to inferior power generation and even malfunctioning operation. It is thus critical to identify degraded PV modules during online operation, which helps scheduling timely maintenance to prevent low-efficiency operation or even catastrophic failures. Many forms of PV device degradation are related to the change of the internal resistance [18]. Therefore, online detection of changes in internal resistance is critical for detecting faulty or degraded modules. Moreover, from the cost effectiveness standpoint, using the inherent signals available in the PV control system (typical MPPT control) is definitely more preferable than using additional sensors or performing offline measurements. Therefore, this dissertation investigates, in addition to PV MPPT.

1.1.3. Major Objective of Dissertation

In summary, this dissertation study aims to study the efficient operation for energy *usage* and energy *generation* local to the green buildings, with the following two objectives:

- 1) Develop self-optimizing control strategy for real-time efficient operation of chilled-water VAC system using extremum seeking control.
- 2) Develop extremum seeking control based PV MPPT strategies, and in parallel, develop the online scheme for detecting the changes in internal resistance using MPPT control inherent signals, both with potential for reducing the COE.

These research objectives bear the common benefit for the cost effectiveness for of the future net-zero energy buildings.

1.2. Research Problems and Approaches

As indicated in the previous section, this dissertation study mainly focuses on two major objectives: energy saving by achieving efficient operation of chilled water system and enhances renewable energy generation by maximizing the power output of PV system as well as the MPPT integrated PV degradation detection. In this section, the technical challenges for these two aspects of work will be described in more detail, and based on which the respective research approaches will be presented.

1.2.1. Self-Optimizing Control for Efficient Operation of Chilled-Water Plant

Energy efficient operation of the chilled-water system is important for the energy saving purpose of commercial buildings.

For operation of chilled-water plant, a major issue is to minimize the total power consumption in real time. Chiller can operate more efficiently when receiving colder condenser water from cooling tower. According to [19], an empirical rule is “for every one degree drop in condenser water temperature, chiller efficiency will increase 2%”. Meanwhile, for a given ambient condition, lowering the condenser inlet water temperature implies higher air-flow rate for the cooling tower operation, i.e. demanding for higher power consumption of tower fan. Braun and Diderrich [3] studied the relation between relative tower airflow and total power consumption of chiller compressor and cooling tower fan, as shown in Fig. 1.4. The power of tower fan increases monotonically with the air flow rate, while the chiller power decreases monotonically. As a result, the relation between the total power consumption (tower fan power + chiller compressor) and the relative tower airflow demonstrates a convex profile, which yields a global minimum

as shown in Fig 1.4. This fact implies the feasibility for applying various gradient-search based optimization methods.

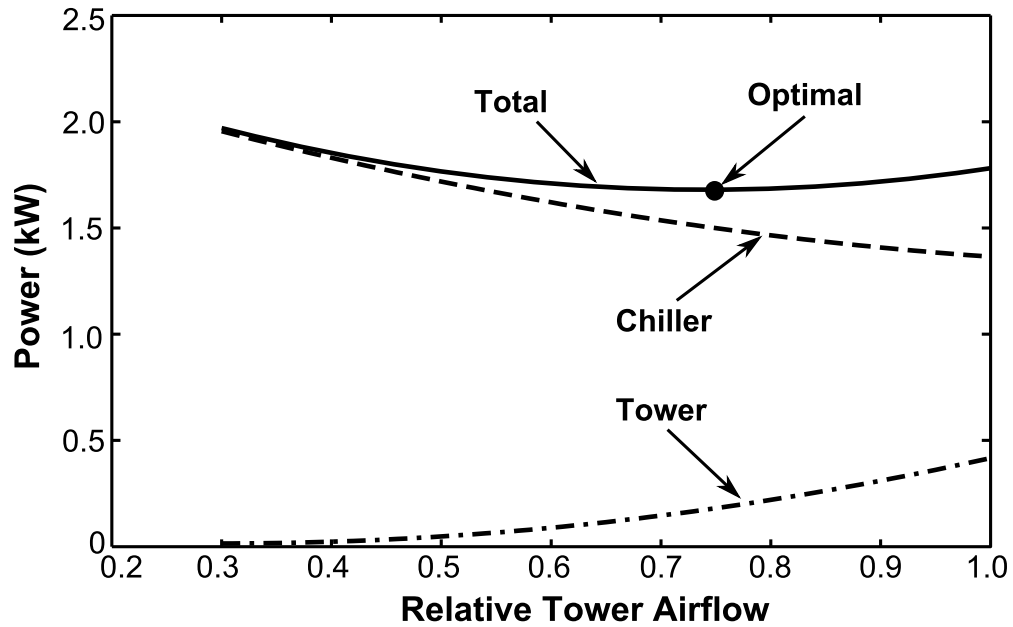


Figure 1.4: Tradeoff between energy consumption of chiller and cooling tower
(reproduction of Fig. 2 in [3])

In the past, model based optimization and control techniques have been investigated. These methods bear the benefits in terms of accuracy and stability [3, 10, 20, 21]. However, such methods are difficult to use in practice for several reasons. First, the control/optimization oriented first-principle models are difficult to obtain because the dynamics of chilled water system and the interactions among system components are rather complicated. Second, the chilled-water plant behavior is highly affected by the ambient conditions, i.e. depending on the accurate and reliable measurements of temperature and humidity of the ambient air. Third, regarding the methods built upon the data-driven models, frequent model calibration is required, and even so, can be far from complete because a full coverage of all possible load and ambient conditions is virtually impossible before the system degrades to a different condition. Therefore, self-

optimizing strategies with least dependency on model knowledge are very attractive for the real-time optimization of chilled-water plant operation. In this dissertation study, the ESC method is considered as a self-optimizing control solution for the efficient operation of chilled-water plant.

The ESC application for the chilled-water system has recently been investigated by United Technology Research Center and their collaborators [22, 23]. In particular, Sane *et al.* [23] investigated a dither ESC scheme by regulating the condenser supply temperature with some simulation results. In spite of the success demonstrated, there are two major deficiencies in this work. First, using the condenser supply temperature as the ESC input requires implementation of an inner-loop control, which demands for additional controller design and reliable water temperature measurement. Second, there is no information provided by the authors about the simulation platform used, whether the simulation was performed on simple empirical models or detailed physical models. Since the dither ESC is a dynamic scheme of gradient search, the input and output dynamics are critical for the choice of the ESC parameters. It is more desirable to evaluate the ESC design with high-fidelity dynamic simulation models of chilled-water system.

Based on these two considerations, the ESC based chilled-water control is conducted from the following two aspects. First, instead of using the condenser supply water temperature, the tower fan speed set point is used. With the wide adoption of variable speed drive (VSD) for cooling tower fan, such choice of ESC input is easy and simple for practical implementation. It saves the development of an inner loop controller for the condenser supply water temperature, the installation and maintenance of the associated temperature sensors. Therefore, such scheme is simpler and more robust than the scheme

by Sane *et al.* [21], and meanwhile achieving the exactly same control/optimization objective without any compromise. Second, a dynamic simulation model is developed for a chilled-water plant using Modelica based platform. In particular, the plant mainly consists of a screw chiller and a mechanical draft counter flow wet tower. With the equation-based multi-physical modeling capability of Modelica based platform, high-fidelity dynamic simulation models can be developed to model the processes of evaporation cooling, mixing and the vapor compression refrigeration cooling cycle involved. Furthermore, the ESC design can be evaluated on a more trustworthy platform.

The proposed dither-ESC (DESC) tower fan control scheme is implemented with a hierarchical control structure as shown in Fig. 1.5. The total power is used as the feedback to the DESC controller and the cooling tower fan speed is chosen as the DESC input. For the chiller operation, in addition to efficiency, there are two basic control requirements: the evaporator superheat and the chiller leaving-water temperature [9, 24]. Regulation of the evaporator superheat can avoid the liquid refrigerant to enter the compressor, which would otherwise damage the compressor. Maintaining the chiller leaving-water temperature is an important requirement for the terminal control of the air handling units (AHU) [25]. To satisfy these two requirements, two inner-loop proportional-integral (PI) controls are implemented with relatively consistent performance, which secures the higher level ESC operation. The effective flow area of the thermal expansion valve is controlled to regulate the evaporator superheat, while compressor capacity is controlled to regulate the chilled water leaving temperature, as shown in Fig. 1.5.

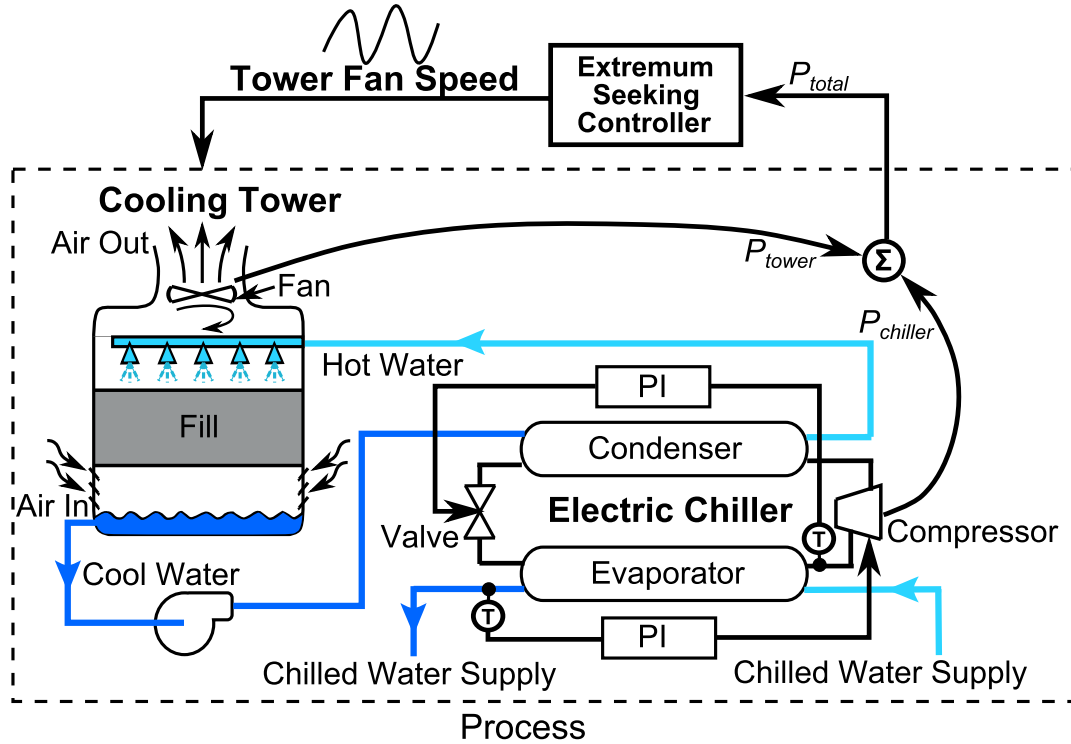


Figure 1.5: Basic system diagram of ESC working on chiller-tower cycle (reproduction of Fig. 2C in [2])

1.2.2. Dynamic Simulation Modeling of Chiller-Tower Plant

As discussed in the previous subsection, a high-fidelity dynamic simulation model for the chilled water plant is critical for designing and evaluating the ESC controller. This dissertation study develops Modelica based dynamic simulation model for the chilled-water system, as well as the controllers involved in the ESC scheme in Fig. 1.5.

Modelica[®] is an object-oriented, equation based, acausal modeling language that is particular powerful for dynamic simulation modeling for multi-physical systems [26]. In Modelica, a model can be developed as an object with associate attributed defined in the component, which is very convenient for reuse ability. Various software development platforms have been developed for Modelica based modeling. Dymola is so far deemed

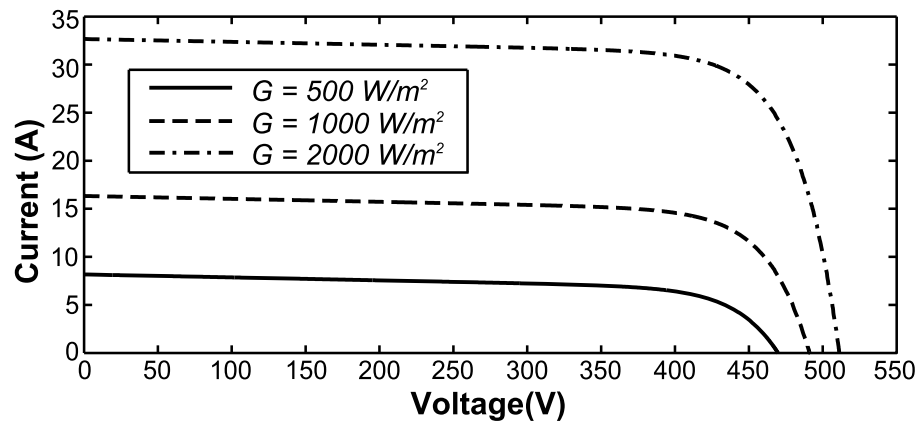
the most popular platform by industry and academia [27]. Initiated by Hilding Elmqvist, Dymola can translate the Modelica equations into hybrid differential algebraic equations (DAE) equation with a symbolic translator. With the state-of-the-arts index reduction algorithms, Dymola can handle large DAE systems which are typical for complex thermofluid applications. In contrast to Simulink[®] [28], Dymola bears the acausal ability of Modelica language, which allows bidirectional data flow. System simulation does not require any pre-determination of computational flow. Dymola can handle both continuous, discrete-event or mixed signal systems. Via functional mock-up interfaces (FMI), Dymola can be interfaced to other simulation platforms such as Simulink. This dissertation study uses Dymola Versions 6.1 and 2012 FD1 [27] with Modelica[®] Version 2.2.1 [26].

In addition to the Dymola platform, the chilled-water plant modeling in this study has also adopted the TIL/IfT Suite library developed by TLK-Thermo [29]. Compared to many other existing Modelica libraries for thermal system modeling, the inheritance structure of TIL is considered much more advantageous for model development and extension.

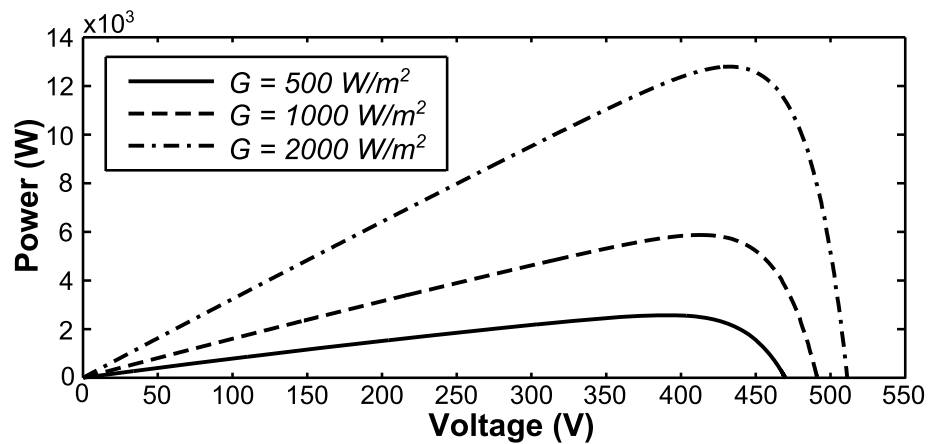
In this study, the chiller-tower plant simulated includes a screw chiller and a counter-flow mechanical-draft wet cooling tower. For the screw chiller, a twin-screw compressor model is developed in this study following the work by [30], while other components such as condenser, evaporator and expansion valve have been adopted from the existing work [29, 31]. More effort in this study has been made to the modeling of the cooling tower, which includes the finite-volume-method based modeling for the evaporation cooling process, mixing tank, pump and water pipes.

1.2.3. ESC Based MPPT Control on Photovoltaic System

As described in Section 1.1, in order to reduce the cost of energy (COE), it is ideal to maintain the PV operation at its maximum achievable efficiency in real time. For actual PV systems, the current-voltage (I - V) and power-voltage (P - V) characteristics are nonlinear and affected by the intrinsic (e.g. aging of the device) and external (e.g. irradiance intensity and temperature) conditions that are both uncertain through operation. Figures 1.6 and 1.7 show the I - V and P - V curves of a PV system under different irradiation rates and different temperatures, respectively.

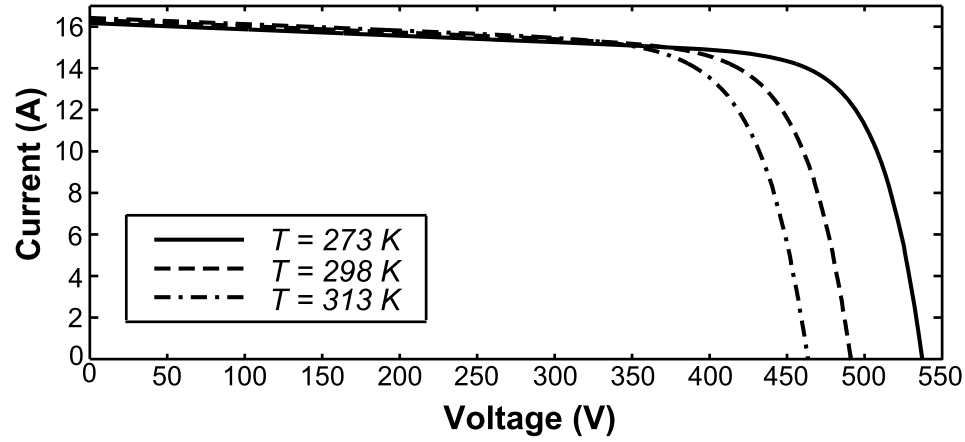
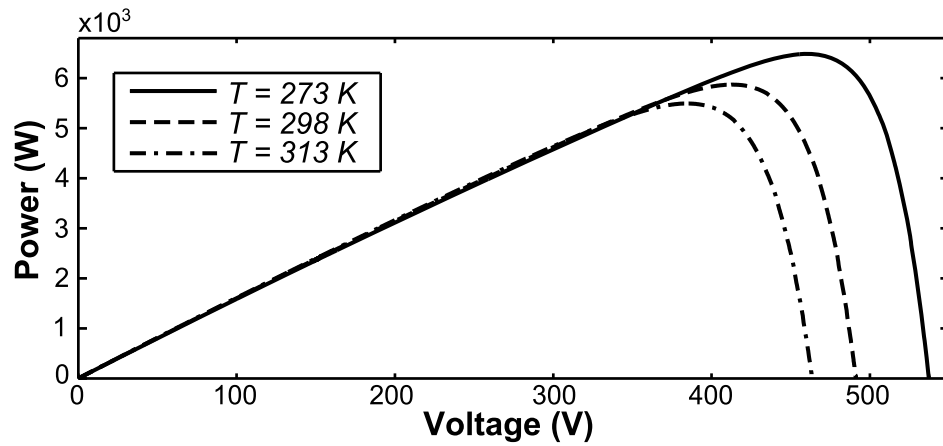


(a) I - V curves



(b) P - V curves

Figure 1.6: I - V and P - V curves at temperature 25 °C under different irradiance rates

(a) I - V curves(b) P - V curvesFigure 1.7: I - V and P - V curves at irradiance rate 1000W/m^2 , under different temperatures

PV MPPT aims to search for the MPP in real time regardless of the changes of PV intrinsic characteristics and environmental uncertainties [17]. Conventional MPPT techniques are based on static optimization algorithm, such as the perturbation and observation (P&O) method [32], the incremental conductance (IncCond) method [33] and the hill climbing (HC) method [34] and many more [35-37]. Recently, the Extremum Seeking Control (ESC) has drawn great attention with its nearly model-free self-optimizing ability [38-42].

The dither based extremum seeking control scheme is investigated and deployed on both single- and multi-string PV structure in this dissertation study, as shown in Chapter 6. For dither ESC MPPT design, the power output is the only need feedback signal. The dither ESC realizes the gradient search process by extracting the gradient information through a dither-demodulation scheme. The dither ESC design does not need any system model structure, and stabilizing loop gain is mainly determined by the second-order derivative (or Hessian). For PV MPPT, the power-voltage curves in Figures 1.6 and 1.7 have significantly different slopes at the two sides of the MPP, which implies that the loop gain has to be chosen small enough to handle the situation when the search starts from the steeper side.

For PV power conversion system, the overall characteristics are determined by both PV device physics and the conversion circuitry. The models of the power conversion circuits are quite tractable and relatively simpler, while in comparison, the current-voltage relation can be considered as a nonlinear static map of relatively consistent shape. Therefore, such partial knowledge of system model structure can be best utilized to design a self-optimizing controller with better convergence properties. In this dissertation study, the adaptive extremum seeking control (AESC) scheme is also investigated for MPPT of single-string PV system. In particular, the radial basis function (RBF) neural network is used to approximate the complex nonlinearity for the $I(V)$ characteristics. The asymmetry in characteristics is naturally included in the structure of the nonlinear state equations. A projection algorithm based parameter learning law is applied to guarantee the convergence of the RBF parameters [43]. The convergence to the optimum and the stability of the controlled system is secured by a Lyapunov based inverse optimal design

technique. The adaptive ESC scheme is evaluated by simulation study. The PV module/array model and the control system are built with Matlab® R2009a Simulink® 7.3 SimPowerSystems. Adaptive ESC achieves a fast searching speed and excellent searching performance with different environment changes.

1.2.4. DESC MPPT and Integrated PV System Diagnostics

Due to the high initial cost and low conversion efficiency of the PV system, the PV modules are normally required to provide stable and high performance over 20 years [44-46]. However, the PV device may degrade or even fail over time or by accident. There are many types of degradation mechanisms for PV devices, such as deterioration of packaging material, loss of adhesion, bad interconnects between cells and modules, degradation due to moisture intrusion, degradation of the semiconductor device, cracked cells, hot spot formation and many other problems related to water ingress or temperature stress [47, 48]. Most degradation mechanisms lead to higher serial resistance and/or low shunt resistance, which may result in overall power output reduction and even excessive surface heating [18]. Figures 1.8 and 1.9 show the P - V and I - V characteristics with different shunt resistances, respectively.

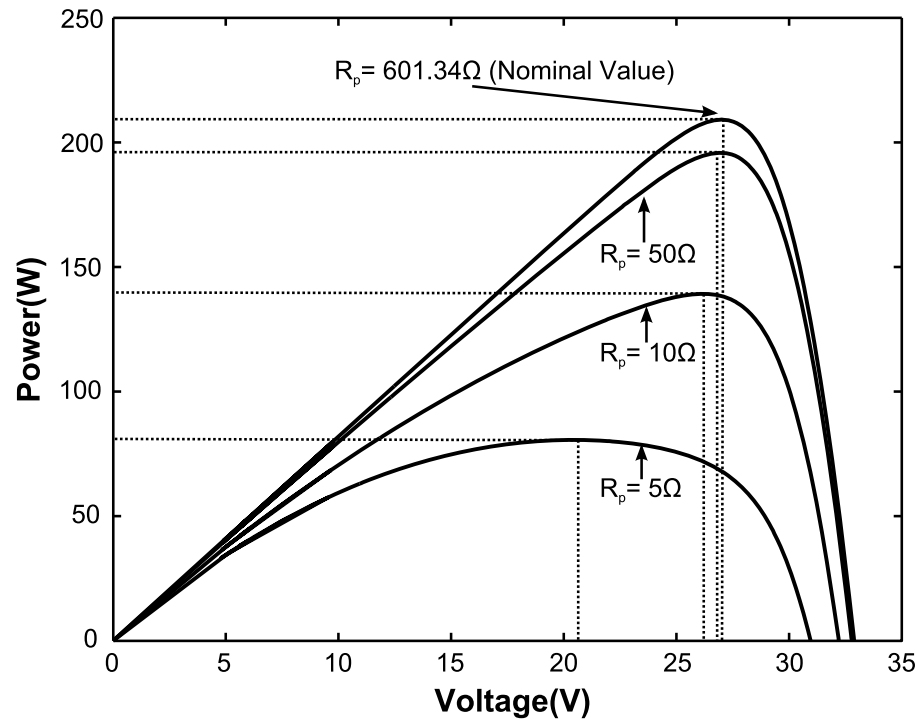


Figure 1.8: P - V Characteristics with different internal shunt resistances

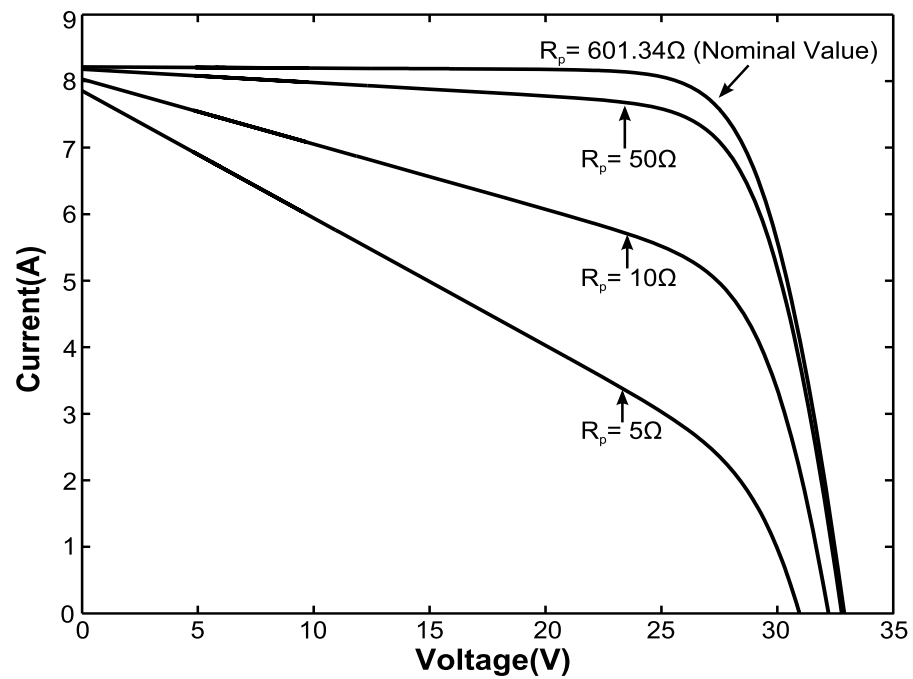


Figure 1.9: I - V Characteristics with different internal shunt resistances

The PV system performance can be significantly affected by device degradation [49]. It is therefore beneficial for PV system operation to be able to detect the degraded or faulty modules in real time so that they can be replaced in time so as to reduce the possible loss of power generation. As many degradation mechanisms are linked to the change of internal resistances, it is desirable to monitor the change of internal resistance in real time.

To the author's best knowledge, the existing techniques for monitoring the PV internal resistance are offline [50-53], which reduces the COE due to the interruption of power generation process and the need for additional maintenance cost. It is thus desirable to develop techniques for monitoring the internal resistance online using the measurement(s) already available in PV operation, e.g. the MPPT input and/or output signals.

This dissertation study investigates a scheme for online detection of change in internal resistance for PV modules, based on the signals available in the dither ESC. For dither ESC with square-wave dither signals, the steady-state output is effectively a train of small-amplitude step responses. The transient performance indices of such step responses are heavily affected by the internal resistance. Therefore, extracting the relevant transient characteristics of the steady-state signals of dither ESC MPPT is expected to help detect the change of internal resistance in real time in a control-integrated fashion. In particular, the shunt resistance is selected as the target parameter. For multi-string operation, the degradation/fault related change of internal resistance for individual module can be isolated with the dither frequency used for each string.

1.3. Problem Statements for Dissertation Research

As a summary of the description in Section 1.2, the dissertation research aims to address the following four research tasks:

- 1) Develop an extremum seeking control based tower fan controller for efficiency operation of chilled-water plant in real time, using the total power as feedback and the tower fan speed setpoint as input.
- 2) Develop a Modelica based dynamic simulation model for a chilled-water system that consists of a screw chiller and a mechanical-draft counter-flow cooling tower.
- 3) For dither ESC based MPPT scheme with square-wave dither input, develop a detection scheme for monitoring the internal resistance using the steady-state variables available for the dither ESC MPPT.
- 4) Develop an adaptive extremum seeking control based PV MPPT scheme.

1.4. Organization of the Dissertation

The reminder of this dissertation is organized as follows.

Chapter 2 provides a review of literatures on the topics relevant to the aforementioned research problems. The achievements and limitations of the existing research are discussed, which aims to justify the motivations for the proposed research approaches.

Chapter 3 represents the dynamic modeling of a mechanical-draft counter-flow wet cooling tower. The chapter starts with the cooling tower modeling along with the determination of the overall number of units (NTU) and the Lewis relation (Le_f). Some related component models adopt the TIL library are also shown. The simulation results for steady state scenarios provided by a classic literature are provided, and compared with

an existing work. Then, a transient simulation of the dynamic cooling tower model follows. Finally, the modeling of the screw chiller is presented.

The ESC tower fan control of the chilled water system is presented in Chapter 4. The inner-loop controllers for the chiller operations are described. An overview of the dither based extremum seeking control design is presented, followed by the particular design for the problem of interest. The simulation and case studies are provided for different scenarios.

Chapter 5 designs the maximum power point tracking for photovoltaic system using adaptive extremum seeking control technique. A simplified PV system model is obtained by an averaging scheme. Then, the AESC design procedure is presented, based on Lyapunov stability theorem and the use of the RBF neural network. The simulation results are shown with comparison to those by the dither ESC scheme.

Chapter 6 investigates the ESC MPPT integrated detection scheme for the change of internal shunt resistance for PV systems. Dither ESC based MPPT is implemented for both single- and multi-string PV systems with square wave dither input. A small-amplitude transfer function analysis justifies the effect of the internal resistance on the step-response transient of the steady-state signals of the square-wave ESC. Simulation study is performed for both single- and multi-string scenarios.

The contributions of this dissertation research are summarized in Chapter 7, along with the future work.

Chapter 2. Literature Review

This chapter provides a review of literature related to the topics investigated in this dissertation research. First, the two extremum seeking control schemes, i.e. the dither based extremum seeking control (DESC) and the adaptive extremum seeking control (AESC), are reviewed. Then, two main aspects of research relevant to the ESC control of the chiller-tower system are reviewed, i.e. modeling of the chilled-water plant and optimization and control techniques for the chilled-water systems, followed by the discussion on the existing work of ESC control for the chiller-tower system. For the photovoltaic system, the previous MPPT techniques are first reviewed, followed by the typical multi-string configurations. Then, the PV device degradation issues are reviewed, as well as the existing detection techniques. The major achievements and the drawbacks in the foregoing modeling and control problems are discussed, which motivates the reiteration of the major objectives and methodologies considered by this dissertation research.

2.1. Review of Extremum Seeking Control (ESC) Techniques

In a broad sense, extremum seeking control refers to a large class of control strategies that can search for the unknown and often time-varying optimal input set point for nonlinear systems with respect to certain performance index. There are several categories of ESC techniques, with different schemes to achieve the optimality in the spirit of gradient search, such as switching ESC, dither ESC, sliding-mode ESC, numerical optimization (e.g. simultaneous perturbation stochastic algorithms) based ESC, among

others [54]. In this dissertation study, two types of ESC techniques have been investigated for the chilled-water system and PV MPPT applications, i.e. the Dither ESC and the Adaptive ESC. These two techniques are reviewed in this section.

2.1.1. Review of Dither Based Extremum Seeking Control

The idea of extremum seeking was first discovered in the work by Leblanc [55] in 1922, with application to electric railways. Significant research efforts had been made to the further development of ESC techniques and various applications between 1940s and 1970s [56-61]. Blackman presented a review of extremum seeking in 1962 [62]. In 1968, Meerkov investigated the averaging based stability analysis in extremum seeking system [63]. Sternby [64] gave a survey on extremum seeking control and also investigated different model-based control problems with questioning the effectiveness of extremum seeking [65]. Åström and Wittenmark, in the last chapter of their class text on adaptive control [66], give an overview extremum seeking control, and consider ESC as one of the most promising techniques in the adaptive control area. In particular, they pointed out the need for clear guidelines of ESC design and the stability proof.

The first stability proof of single parameter ESC on general single-input-single-output (SISO) dynamic nonlinear plant was provided by Krstić and Wang [67] using both the averaging and the singular-perturbation methods. Later, a discrete-time ESC scheme was investigated by Choi *et al.* [68]. Their analysis was confined to “a class of plants with a series combination of linear input dynamics, static nonlinearity performance map and also linear output dynamics”. A mild sufficient condition of exponentially convergence to a neighborhood of the extremum value is guaranteed by an averaging analysis. Krstić and co-workers [67, 69, 70] further discussed the dither based extremum seeking scheme and

investigated the local stability and performance improvement of DESC. Tan *et al.* [71-73] extended the ESC stability discussion to the global stage with a simplified extremum seeking scheme, the tradeoff between the attraction domain size and the ES convergence speed is also shown. Nešić [74] summarized the investigations of the dynamic properties for typical extremum seeking controllers, and showed that adaptively change the dither amplitude can achieve global ES when local extrema exist.

Later, multiple-parameter ESC was also investigated. Rotea [75] provided an averaging analysis on a multi-parameter extremum seeking algorithm with the measurement noise included, followed by giving a set of design guidelines. In parallel, Walsh [76] investigated a new control law with a discrete-time setting. The exponential stability was proved with the averaging analysis as well. Ariyur and Krstić [77, 78] presented a multi-parameter ESC framework with formal treatment of time-varying optimum inputs. Standard LTI control techniques were used to derive a set of design guidelines. The design difficulty is quantitatively evaluated with the considerations of the number of parameters and the shape of the unknown performance index map.

A simple description of dither based ESC is presented as follows. The ESC is to find the optimal input $u_{opt}(t)$ in real time for a generally unknown and/or time-varying objective function $l(t, u)$ with the online measurement of the objective value to be minimized [67, 75], i.e.

$$u_{opt} = \arg \min_{u \in R^m} l(t, u) \quad (2.1)$$

where $u(t)$ is the input vector. A typical dither ESC block diagram is shown in Fig. 2.1. $F_I(s)$ and $F_O(s)$ denote the input and output dynamics, respectively. The output of the

objective function y , which may be corrupted by noise n , is assumed to be directly measurable for feedback. The dither and demodulation signals are required to be periodic, e.g. sinusoidal or square-wave. For the sinusoidal case, the dither and demodulation signals can be defined as

$$d_1^T(t) = [\sin(\omega_1 t) \quad \cdots \quad \sin(\omega_m t)] \quad (2.2)$$

$$d_2^T(t) = [a_1 \sin(\omega_1 t + \alpha_1) \quad \cdots \quad a_m \sin(\omega_m t + \alpha_m)] \quad (2.3)$$

where ω_i , α_i are the frequency and phase angle respectively. $d_1(t)$ and $d_2(t)$ are used in combination to extract the gradient of the objective function. The perturbed output of $F_O(s)$ passes the high-pass filter $F_{HP}(s)$, multiplied by the demodulating signal $d_1(t)$, and then passes the low-pass filter $F_{LP}(s)$. The resultant signal is proportional to the gradient $\partial l / \partial u(\hat{u})$. By closing the loop with an integrator, the gradient will approach to zero provided that the closed-loop stability holds. The compensator $K(s)$ can be added to enhance the transient performance.

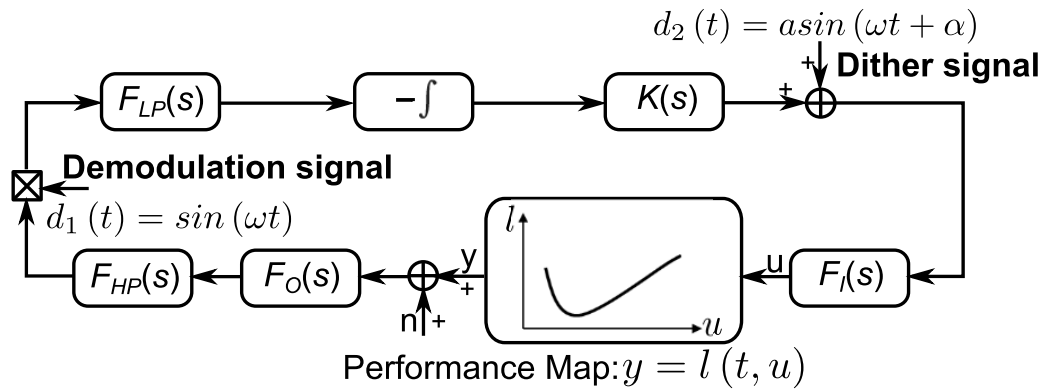


Figure 2.1: Block diagram of dither ESC

2.1.2. Adaptive Extremum Seeking Control

The Adaptive Extremum Seeking Control (AESC) scheme was proposed by Guay and his co-workers [43, 79-82]. The AESC aims to optimize a selected objective function for

nonlinear systems with parametric uncertainties. The system model structure is required to be available for the AESC design. Different from the dither based ESC, the output of the objective function is assumed not measured or measurable, and cannot be fed back to the controller either. Under such assumption, state feedback is needed to maintain access to system behavior. There are two distinctive but related goals for the AESC design: parameter estimation and the extremum seeking. The corresponding design tasks are to drive both the parameter estimation error and derivative of the objective function to zero. The convergence of the relevant dynamics is secured by applying the inverse optimal design technique. Dither signals are introduced to provide the persistent excitation required.

Later, Guay *et al.* [43] extended their work to handle the system with uncertain output equation by utilizing the radial basis function neural network (RBFNN) and the projection-algorithm based parameter learning law. The weight parameters in the RBFNN involved are estimated in the foregoing fashion. DeHaan and Guay [79] further added the ability of handling the state constrained nonlinear system to AESC based on [81]. The logarithmic barrier function is used to handle the state constraints. The parameter convergence in AESC control design was also discussed later by Adetola and Guay [83] for a class of nonlinear systems. Several applications of AESC for different research areas have been presented recently [84-87]. Steen investigated the AESC scheme for a Haldane kinetics bioreactor with specific interest on the persistent excitation condition. [84]. Hudon *et al.* optimized the productivity of a tubular reactor with limited actuation information, i.e. only temperature information, to estimate the unmeasured concentration at the exit of the reactor [85]. Cougnon *et al.* investigated the AESC

application on fed-batch bioreactors with Haldane kinetics. In this work, the substrate concentration is assumed as the only available on-line measurement [86]. Li *et al.* applied the AESC scheme on PV MPPT problem [87].

The AESC framework adopted in this dissertation research follows [43], which is briefly reviewed as follows. As illustrated in Figure 2.2, the AESC is concerned with the generalized system dynamics [43]:

$$\dot{x} = f[x, \mu(x), u] \quad (2.4)$$

with the objective function

$$y = h[x, \mu(x)] \quad (2.5)$$

where output y is assumed not directly measureable.

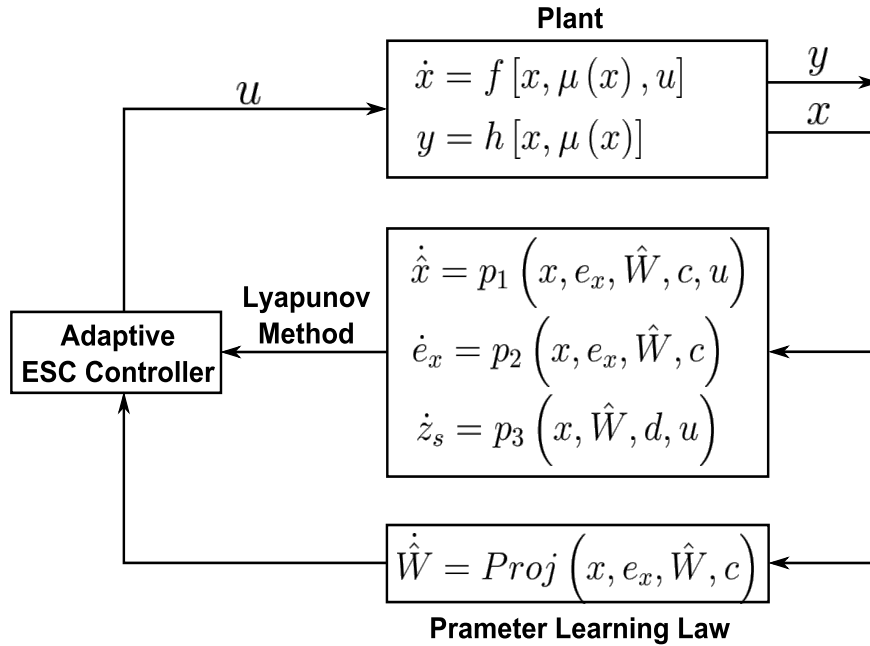


Figure 2.2: System structure for AESC

The structure information for $f[x, \mu(x), u]$ and $h[x, \mu(x)]$ are required for the AESC design with the observable system states $x \in R^n$, $\mu(x)$ is unknown static nonlinearity, and

u is the control input to be designed. The estimated state dynamics $\dot{\hat{x}}$, the estimated state error dynamics \dot{e}_x and the optimization oriented tracking error dynamics \dot{z}_s are then represented as follows:

$$\dot{\hat{x}} = p_1(x, e_x, \hat{W}, c, u) \quad (2.6)$$

$$\dot{e}_x = p_2(x, e_x, \hat{W}, c) \quad (2.7)$$

$$\dot{z}_s = p_3(x, \hat{W}, d, u) \quad (2.8)$$

where c represents the design parameters to be assigned in the control design process, \hat{W} is the estimated RBFNN parameters to be described next, and d is the dither signal to be designed to provide persistent excitation.

In [43, 88], the RBFNN was proposed to approximate the nonlinearity $\mu(x)$, i.e.

$$\mu[x(t)] = W^{*T} S[x(t)] + \mu_l(t) \quad (2.9)$$

where $\mu_l(t)$ is the approximation error, and the ideal weight W^* is obtained by

$$W^* := \arg \min_{W \in \Omega_w} \left\{ \sup |W^T S(x) - \mu(x)| \right\} \quad (2.10)$$

where $\Omega_w = \{W \mid \|W\| \leq w_m\}$. w_m is the upper bound of the weight norm, which is chosen at the design stage. An adaptive learning technique using projection algorithm is used to online estimate the unknown parameters.

$$\dot{\hat{W}} = \text{Proj}(x, e_x, \hat{W}, c) \quad (2.11)$$

A Lyapunov-based controller is designed to ensure the convergence of the state trajectory into an adjustable neighborhood of the optimum depending on the approximation error $\mu_l(t)$.

2.2. Previous Work on Modeling of Chilled-Water Plant

As stated in Chapter 1, high-fidelity dynamic simulation models of the chiller-tower system is highly desired as virtual plant for evaluating the control and optimization schemes. In this dissertation research, a counter-flow mechanical-draft cooling tower is adopted, along with a screw chiller. In this section, previous work on the modeling of cooling tower will be reviewed first, followed by the review on the modeling of the screw compressor. These reviews set forth a good foundation for the modeling efforts to be presented in Chapter 3. The other relevant components in the chilled water plant adopt Li's work [31] and the TIL Library [29].

2.2.1. Literature Review on Cooling Tower Modeling

Based on the evaporation cooling mechanism, the cooling towers are commonly used to reject the heat to the atmosphere in large thermal systems, such as power generation units, water-cooled refrigeration and air conditioning for commercial buildings [9]. The cooling towers can be categorized in different manners [9]:

- Heat transfer: dry cooling towers, wet cooling towers, and fluid coolers.
- Air flow generation: natural-draft cooling towers, mechanical-draft cooling towers, and fan assisted natural-draft cooling towers.
- Relative orientation between the air and the water flow paths: cross flow cooling towers, counter flow cooling towers.

In this dissertation research, the mechanical-draft counter flow wet cooling tower is considered as it is used more for the chilled-water plants of commercial buildings.

A lot of work has been done for modeling cooling towers in the past century. Walker *et al.* [89] proposed a basic theory of cooling tower operation in 1923. Merkel [90] developed the first practical theory including the differential equations of heat and mass transfer, which has been well received as the basis for most work on cooling tower modeling and analysis [9, 91-96]. In Merkel's model, both sensible and latent heat transfer processes are considered based on the driving potential from the enthalpy difference. In order to simplify the analysis, the water loss from evaporation and drift are neglected in Merkel's treatment, and the Lewis relation is assumed as unity. Although these assumptions make the cooling tower model relatively simple and easy to implement, the effective tower volume is also underestimated by 5-15% [97]. Nottage [98] and Yadigaroglu and Pastor [99] tried to make some advanced changes on Merkel's cooling tower model to achieve better accuracy in practice. The mathematical analysis and effect of the approximations used in Merkel's work were studied by Baker and Shryock [100], and they attempted to minimize the steady-state error by a different approach. They claimed that each improvement on model accuracy may enhance the difficulty of analysis.

Lowe and Christie [101] studied the heat transfer processes and the pressure drop performance for cooling towers with different slash packings, and they proposed a method to obtaining the volume transfer coefficient from the estimated tower performance data with the parameters of tower coefficient and tower exponent. Threlkeld [102] included the water loss due to evaporation and the actual Lewis number into the cooling tower analysis. Jaber and Webb [103] introduced the effectiveness-NTU (number of transfer units) design method for counter-flow cooling towers using Merkel's

simplified theory. Sutherland [97] carried out a more rigorous analysis of cooling tower including water loss by evaporation at 1983.

Braun and his co-workers [104, 105] gave a detailed analysis on cooling tower modeling, and developed effectiveness models by assuming a linearized air saturation enthalpy and a modified definition of effectiveness models using the constant saturation specific heat c_s . A modeling framework was developed for estimating the water loss and then validated over a wide range of operating conditions. Bernier [106, 107] presented a one-dimensional (1D) analysis of an idealized spray-type tower, which showed how the cooling tower performance is affected by the fill height, the water retention time, the air and water mass flow rates. Stoecker [108] proposed an empirical model of cooling tower with constant air and water flow rates based on polynomial approximation. Söylemez [109] proposed a way to estimate the size of the forced draft cooling tower, and utilize an iterative technique to predict the tower performance.

Kloppers and Kröger [110] investigated the loss coefficient correlation for wet-cooling tower fills, and proposed a new formulation of empirical equation which correlates the fill-loss-coefficient data more effectively. They also compared the aforementioned methods by Merkel and Poppe [111], and the e-NTU methods [112]. They claimed that all these approaches predicted practically identical water outlet temperatures for both mechanical and natural draft towers. Poppe's approach gave lower water outlet temperature than the other two for natural draft towers. Jameel *et al.* [94, 113] considered a counter flow wet cooling tower for its performance characteristics investigation. The heat and mass transfer effort is studied with an additional consideration on the direct contact of water and air. A theoretical model is proposed with

experimental evaluation. A mathematical model for a mechanical-draft cooling tower is studied by Fisenko *et al.* [114]. The model solves a boundary-value problem for the ODE system (ODE). The performance changes of water droplets and moist air are investigated. Qureshi and Zubair [92] proposed a more comprehensive model of wet cooling towers in 2006. Their analysis included the consideration of the spray and rain zones, for a better estimation of the tower performance. More recently, Wetter [115] proposed a static cooling tower model using Modelica with static mapping to the performance curve of a York cooling tower.

Most existing models for cooling towers [91, 93, 116-120] are steady state or effectiveness models. As stated in Chapter 1, the dynamic modeling of cooling tower is desired for control design and fault detection and diagnostics (FDD), and to the author's best knowledge, no work has been reported on the dynamic model prior to this dissertation research [121, 122].

In this dissertation research, a dynamic model for a mechanical draft counter-flow wet cooling tower is presented based on 1D heat and mass balance dynamic equations. The assumptions from Braun's work [105] were followed to simplify the analysis. Heat and mass transfer is only considered in the direction normal to the medium flows, while the heat and mass transfer through tower walls to the environment is neglected. The mass fraction of water vapor in the moist air is approximated equal to the humidity ratio. Several distinctive treatments are performed in this study. First, the mutative water and air specific heats are used to relax the constraints, by use of the property calculation capability available in the TIL Media Library [29]. Second, instead of considering the Lewis relation as unity, the formulation in [123] is followed. Thirdly, the finite volume

(FV) method is applied in order to achieve more robust performance for start-up and all load-change transients [124]. The control volumes of water and moist air were defined separately, with opposite flow directions. Dynamic mass and energy balances were evaluated for each control volume, and the heat and mass transfer are considered between each pair of water and moist-air control volumes. The proposed model includes both sensible and latent heat transfer effects on the tower performance. The balance between the water loss and the humidity increase in the moist air is reinforced through all the control volumes. The water loss is determined by the mass transfer coefficient based on the geometry and performance map of specific cooling tower.

2.2.2. Literature Review on Screw Chiller Modeling

Screw chiller is one of the most common types of vapor compression system with the advantage of high efficiency, high reliability and wide operating range [9]. Screw compressor is the key component in the screw chillers, which is based on the positive-displacement rotary mechanism. Two types of screw compressors are utilized for refrigeration and air conditioning applications: single screw and twin screw, both can be used with fluid injection and economizers [25]. In this dissertation study, a non-economized twin-screw compressor without fluid injection is considered.

Many thermodynamic and CFD (computational fluid dynamics) models have been developed for screw compressor in the literature [125-130]. Jonsson [131] presented the performance simulation of twin-screw compressors with economizer. The mathematical description of the geometrical design is involved to describe the thermodynamic process. Wu *et al.* [132] gave experimental investigations on the performance of the twin-screw type refrigeration compressor with the effects from both the economizer type and the

superfeed pressure by using indicator diagram. Stosic *et al.* [133] presented the mathematical modeling and performance calculation for screw compressors. Different envelope methods are used to model different rotor profiles of the screw compressors. Detailed mathematical models are also provided with performance calculation and design configuration. Lee *et al.* [134] presented theoretical models of both oil-less and oil-injected twin-screw air compressors, in which the performance of the compressors are evaluated through simulation with different design parameters such as the rotor profile, the geometric clearance, and the oil injection conditions.

Seshaiah [135] investigated the performance of the oil injected twin-screw air compressor with specific consideration of compressing different light and heavy gasses. A mathematical model [136] with standard thermodynamic relations and the ideal gas law is implemented with more detailed investigation on volumetric efficiency and adiabatic efficiency of the screw compressor. Experimental evaluations yield that the overall uncertainties of the volumetric and adiabatic efficiencies are $\pm 18.08\%$ and $\pm 10.54\%$, respectively. A dynamic model of a twin-helical-screw compressor with oil-flooded configuration was presented by Krichel and Sawodny [137]. Separate mathematical models are set up for the four components of the screw compressor, i.e. the intake valve, the twin screws, the motor and the oil/air separator. A compressor-storage system is simulated with Simulink, and the dynamic behavior is evaluated with experimental data. Liu *et al.* [138] proposed a screw compressor model for performance prediction and simulation of the associated refrigeration system. Several regression models are given for different components of the screw compressor under different design parameters and operating conditions. However, most of the screw compressor

models in the literatures are detailed to the component level. In this dissertation research, the focus is mainly on the energy consumption of the chiller system, while the dynamics of screw compressor is much faster than other components in the screw chiller [130, 133]. Most of the aforementioned models tend to be too complicate for such purpose. Therefore, a simple and yet effective screw compressor model should be considered.

Fu *et al.* [139] presented a steady-state simulation model of liquid screw chiller. Both non-economized and economized screw compressor models are investigated with polytropic assumptions for the inlet and outlet *temperature-pressure* relation. The performance prediction errors are with in $\pm 10\%$ in large cooling capacity tests for seven different chiller systems. They extended the work to involve the dynamics from the thermal effect in the evaporator. The screw compressor model still remain as static model due to the very small thermal inertia [140]. Zhang *et al.* [30, 141] further extended Fu *et al.*'s work [139] to transient modeling of an air cooled screw chiller without significant changes on the static model of screw compressor. The model and control performances are validated with experimental data with reasonably prediction of the transient behavior.

The screw compressor model used in this dissertation research adopts Zhang's work [30]. A polytropic static compression model from [30] is adopted with adjustable slide valve opening for further compressor control purpose. The volumetric efficiency is obtained by the pressure-volume relation applied in [139]. The electrical power consumption of the screw compressor is calculated by the actual work done to the refrigerant flow divide by the assumed adiabatic, motor and mechanical efficiencies [139].

2.3. Control and Optimization Techniques on Chilled Water System

Proper control and optimization strategy is critical for efficient operation of chilled-water system due to potential variations in ambient, load and equipment conditions. Modeling, control and optimization techniques have been extensively investigated for the chilled-water system in the past [3, 7, 8, 10, 11, 14, 15, 21-23, 142-151]. Kaya and Sommer [11] presented a supervisory control strategy for chillers by finding the optimal difference between the chilled water supply temperature and the return temperature due to the trade-off between the energy costs for pumping and refrigeration. A 2nd-order polynomial empirical models are used to estimate the COP (coefficient of performance). Chow *et al.* [7] investigated a global optimization strategy for absorption chiller system by involving artificial neural network (ANN) and genetic algorithm (GA). Sowell and Haves [144] compared the performances of several building simulation platforms including Simulation Problem Analysis and Research Kernel (SPARK) and HVACSIM+. Yao *et al.* [21] presented an optimal operation of chilled-water system by performing a constrained optimization based on the empirical models of the system components, and an index of *system coefficient of performance* (SCOP) was proposed to evaluate the energy saving benefit. Lu *et al.* [142] investigated the condenser water loop of the centralized HVAC system, and provided an optimization strategy based on empirical models in terms of the COP and the PLR (part load ratio). Sun and Reddy [143] presented a model based optimal control strategy for building HVAC systems using the CSB-SQP (complete simulation-based sequential quadratic programming) technique.

Fong *et al.* [8] presented the component based chilled water system simulation with mathematical descriptions of chiller and cooling coil, and discussed the dynamic control

and optimization algorithm based on the developed simulation platform. Ma *et al.* [10] proposed a supervisory control strategy for online control and optimization of building cooling water systems based on GA (genetic algorithm) and empirical models. Yu and Chan [14] discussed the economic benefits from the chiller system energy optimization, and presented an optimal cooling water temperature control based on empirical PLR models. Liu and Chuah [15] proposed an hourly regulated optimal control scheme by controlling the difference between the ambient wet bulb temperature and the condenser water temperature instead of directly finding the optimal condenser water temperature. A regression function is used to predict the optimal approach temperature.

In particular, Braun and Diderrich [3] studied the coupling between the power consumption of chiller compressor and cooling tower fan. As shown in Fig. 1.4, they demonstrated that the tower fan power increases with the relative tower airflow, while the chiller power decreases. As net effect, the total power consumption shows a global minimum. The total power curve also demonstrates a strong convex characteristic, which would facilitate the use of any gradient search type of optimization methods. Then, the authors proposed an open-loop control scheme to search for the near optimal fractional tower airflow based on the parameter estimation of the design characteristics of the chiller and cooling tower. Furthermore, Fig. 1.4 suggests convex (nearly quadratic) characteristics for the total power map, which guarantees the possibility of locating the global minimum with online search for the optimal air flow for the cooling tower.

Similar to Braun and Diderrich's study, most existing methods to the control and optimization of the chilled-water systems have been based on nominal/empirical models. In practice, due to the significant variation in ambient conditions and the hard-to-estimate

system degradation, such models may often be inaccurate. In this study, in order to overcome the change in the total power map due to unknown environment changes and the hard estimated system degradation, the extremum seeking control (ESC), as a major class of self-optimizing control strategies, is adopted.

As described in Section 2.1, the objective of ESC is to search for the optimal input in real time in a nearly model-free fashion. Recently, the ESC scheme has drawn quite attention for HVAC applications [152]. Li *et al.* [153] presented an ESC scheme for efficient operation of the air-side economizer. Burns and Laughman [154] investigated a multiple inputs extremum seeking scheme to optimize the energy consumption of the vapor compression cycle. For the chilled-water systems, application of ESC has been recently investigated by United Technology Research Center and their collaborators [22, 23]. Tyagi *et al.* [22] presented a work with golden-section search as their extremum seeking solution for determining the optimal condenser supply water temperature based on an oracle function. Such scheme may lead to long searching time in practice since every step of search needs to wait for the system transient to settle. Also, such method is more vulnerable to external disturbance and variation of plant behavior. For the same problem, Sane *et al.* [23] described a dither ESC solution, where the condenser supply temperature is again used as the control input. Simulation results were shown without mentioning the details about the simulation platform. As the dither ESC is a dynamic scheme of gradient search, the key aspects of its design are the choice of dither frequency with respect to the input dynamics and the compensation for the phase change due to the input and output dynamics and the high-pass filter. An ESC design of such may not be sufficient without simulation on a dynamic model of the cooling tower and chiller. Also,

the control input adopted in [23] and [22], i.e. the condenser supply water temperature, is not a variable that can be directly manipulated in practice. Some inner loop control of the cooling tower must be implemented. Also, additional cost is induced for installation and maintenance for the associated temperature sensor.

With these concerns considered, this dissertation research handles the ESC based chilled-water system control problem with two different perspectives. First, a Modelica [26] based dynamic simulation model platform is developed for the cooling tower in Dymola [27]. Second, the cooling tower fan speed, instead of the condenser supply water temperature, is used as the input for the ESC control design [2]. With the typical variable-speed drive (VSD) equipped for the cooling towers nowadays, setting the VSD frequency or the fan motor speed is direct and simple [155]. In comparison, the scheme of using the condenser inlet water temperature relies on the associated temperature measurement and some inner loop controller for such temperature regulation. The proposed scheme eliminates such dependency, which would be more cost effective and reliable. With constant condenser water flow rate assumed, the total power consumption of the chiller compressor and the cooling tower fan is used as the performance index for feedback. In particular, a screw chiller is chosen for the simulation plant model, which would not affect the generality of the results for plants with other types of chillers. The proposed ESC framework is illustrated in the schematic in Fig. 1.5.

In practical chiller operation, the tower fan has both maximum and minimum speed limits. The control input (cooling tower fan speed) may be saturated to its upper bound during certain operating conditions. Due to the presence of the integrator in the ESC loop, integral windup is inevitable for ESC system operations and may slow down or disable

the optimal searching ability of ESC. Li and Seem [156] proposed a back-calculation based anti-windup ESC scheme, which was later applied by [153] for the ESC operation of the air-side economizer. In this dissertation research, this scheme is applied to the ESC operation of the chilled water system under fan speed saturation.

The details of screw chiller modeling and chilled water system optimization control design will be presented in Chapter 4.

2.4. MPPT Techniques on Photovoltaic System

As described in Chapter 1, MPPT control of the PV system aims to locate and maintain the MPP for online operation regardless the change of the PV intrinsic and environment uncertainties. Many MPPT techniques have been proposed in the literature [17, 33, 35-37, 39-42, 157-160], most of which are based on static optimization algorithm, such as the perturbation-and-observation (P&O) method [32], the incremental conductance (IncCond) method [33] and the hill climbing (HC) method [34, 161]. The P&O method is well known and has been widely used for its simplicity. It operates by changing the PV array voltage periodically. The array power is observed to seek the desired direction towards higher power output. The IncCond method tunes the operating point with the idea of gradient search (dP_{PV}/dV_{PV}). The HC method directly considers the relationship of the duty ratio and power output, the local MPP can be searched if the difference between dP_{PV}/dD and zero can be eliminated by feedback control. Some other techniques like look-up table (LUT) [35], voltage/current based PV generator [36] and fuzzy logic [37] are also developed. However, the static optimization based searching methods often have slower convergence and may be limited when the system undergoes quick change of

environment conditions.

Dynamic MPPT control methods [162-167] have recently been studied more, aiming to improve the transient performance. Hiyama *et al.* [162] proposed a simple neural network (NN) structure to provide identification of the optimal operating point of the PV system, and then achieved the real time continuous estimation of the MPP with the information from the NN. Simoes *et al.* [163] investigated a fuzzy algorithm based MPPT technique to continuously on-line track the maximum power, the scheme was successfully implemented in experimental test with RISC microcontroller. Wilamowski and Li [164] also presented a fuzzy based PV MPPT scheme, the output circuit voltage and short circuit current are observed to represent the temperature and illumination information in the fuzzy controller, respectively. Noguchi *et al.* [165] proposed a novel PV MPPT method based on a short-current pulse of the PV system. The short-current pulse amplitude is used to represent the optimum operating current with a proportional parameter k . Fast power-versus-current curve scanning is utilized to adaptively estimate the value of k and overcome the disturbances from environment. Yoshida *et al.* [166] extended the P&O method by selecting the switching ripples from DC/DC converter as the perturbing signal, MPPT with high speed performance has been achieved by monitoring the photovoltaic array power with the knowledge of dynamic characteristics of the arrays. Chu and Chen [167] investigated a sliding mode control scheme for MPPT of PV system, a switched system model was discussed for the controller design purpose. $\partial P_{PV} / \partial I_{PV}$ is selected as the sliding function to guarantee the estimation of the MPP.

The Extremum Seeking Control (ESC), as a class of nearly model-free self-optimizing control strategies that can search for the unknown and/or time varying optimal

input parameter regarding a given performance index of a nonlinear plant process, has drawn great attention [67, 69-74, 168, 169]. The ESC based MPPT methods have been investigated most recently [38-42, 170-175]. Levy *et al.* [38] adopted a classic switching ESC scheme well studied in 1950's for PV MPPT, while providing a Lyapunov type of stability proof. Brunton *et al.* [39] developed a novel extremum seeking scheme with inverter ripple to treat the PV MPPT problem under rapidly varying weather conditions. The experimental results of the proposed ES method were compared to P&O method with a much faster transient performance. Lei *et al.* [41] investigated the dither ESC based MPPT with a specified treatment of partial shading, an initial discussion about ESC integrated detection of internal resistance change is also presented. Then a further discussion is extended to the global MPPT control on PV system with variable shading, a sequential ESC based scheme is proposed and validated with simulation studies [40]. Moura and Chang [42] presented a ESC MPPT scheme with Lyapunov based switching. The sinusoidal perturbation signal can be exponentially decayed when the system converged to a neighborhood of the MPP, which may lead to a higher power efficiency with smaller bias to the optimal point. Leyva *et al.* [170] further extended their previous study [38] and implemented and verified the proposed sinusoid based ESC scheme with an experimental solar generator. Zazo *et al.* [171] presented a Newton-like ESC scheme to deal with the PV MPPT problem. Both the gradient and the estimation of the PV characteristic Hessian are utilized to track the MPP with the help of sinusoidal dither signals. Zhang *et al.* [172] investigated a practical extension of dither ESC with variable step-size for the PV MPPT problem. Faster response speed and improved accuracy are claimed for the proposed scheme. Malek *et al.* [173] discussed the MPPT problem on a

PV based electrical power system for a satellite. Two different algorithms, i.e. Integer Order ESC and Fractional Order ESC are proposed and compared. The proposed techniques are implemented and tested with both simulations and experiments and received higher conversion efficiency than traditional MPPT methods used in satellite power supply systems. Ghaffari *et al.* [175] presented a multivariable gradient based ESC schemes on the power optimization problem for PV system with micro-converters. A further investigation of using Newton's update law can improve the slow convergence of ESC controller in the multivariable systems [174].

As described in Section 2.1, such ESC scheme extracts gradient information using the pair of dither and demodulation signals, high-pass and low-pass filters. By closing the control loop with integrator, the gradient-proportional signal is driven to zero in steady state for achieving the optimality. As the gradient information is locked to the selected dither frequency, this scheme is robust to process noise and variation of the performance map [38-42].

In spite of the success demonstrated in these work, the dither ESC based MPPT schemes have shown certain limitations. As an inherent limitation of the dither ESC framework, its validity is often limited to the neighborhood of the optimum (equilibrium), and the ESC design addresses the stability and performance issues based on assumption of specific functional form for performance map, e.g. quadratic function. Structural nonlinearity in the performance map cannot be taken into account explicitly, which may limit the performance. For example, the P - V characteristic bears very different slopes at the two sides of the MPP. As a safe choice, the ESC loop gain has to be limited by the steeper side, which may lead to slow convergence if searching from the gradual (low-

voltage) side.

With the foregoing consideration, this dissertation research approaches the PV MPPT problem with AESC reviewed in Section 2.1. The AESC controller is designed based on the knowledge of the system model structure and certain objective function that is defined based on measurable state variables [81]. Continuous kernel functions can be used to approximate the unknown nonlinear output mapping, for which the parameters are estimated by some parameter learning law derived with the Lyapunov based inverse optimal design technique. The AESC scheme searches for both the optimal parameters and the optimal input simultaneously. As the asymmetry of the nonlinear map of P - V characteristics is dealt with by the parameter learning process, the AESC is expected to achieve better transient performance in the PV MPPT. In particular, the PV output power is simply the product of the terminal voltage and current, thus the objective function is hinged on the nonlinear characteristics of $I(V)$. The I - V characteristics can be dramatically varied with intrinsic and environmental conditions such as temperature and irradiance.

For PV power conversion system, the power converter related circuitry is easier to obtain tractable models, while no simple closed-form model is available for the I - V characteristics [176-178]. Therefore, the RBFNN is adopted as the assumed functional for the AESC design [43]. Similar to [43], the Gaussian RBF kernel [88] is adopted to approximate the unknown $I(V)$ characteristics. A Lyapunov-based adaptive learning control technique is applied to guarantee the convergence of the overall system output to an adjustable, approximation error dependent neighborhood of the optimum.

2.5. PV System Degradation and Detection Techniques

As described in Chapter 1, degradation monitoring is critical for the practice of condition based maintenance which can also reduce the COE of PV power generation [52, 179]. Although the commercial PV module's warrantee is typically up to 20 years, earlier degradation or failure still happens due to multiple reasons such as dirty PV device surface, ultraviolet, high temperature, high humidity and intrinsic degradation of the p-n junctions [180, 181].

Front-surface soiling is a degradation mode that comes from the dirt on the PV device surface. It may cause relatively lower power losses (less than 10%) and it could be detected visually [182]. Degradation caused by light induction or high temperature also occurs over time. Light induced degradation (Staebler-Wronski effect) [183], is due to the broken Si-Si bonds in the depletion region of the cell and will lead to meta-stable defects. This kind of PV degradation can be detected by observing the I - V characteristics periodically [184]. The high temperature may also cause degradation by decreasing the open circuit voltage V_{oc} and leading to an overall reduction to the PV device power generation [185]. The temperature induced module degradation can also be detected by measuring the I - V characteristics. Optical degradation is another mode of module degradation caused by the effects from ultraviolet, temperature and humidity, which may cause the discoloration of the encapsulating material [186]. The optical degradation can be visually detected using 375 nm ultraviolet lamp illumination [50]. The degradation from the reflectivity increase of the anti-reflective coating can also reduce the power generation efficiency by reducing the absorption of the income incident photons. The I - V curve monitoring can also help in this case [51].

Intrinsic degradation of PV module is mainly reflected by the change of the internal resistances of the PV cell. The PV cell performance can be reduced by decreasing the shunt resistance or increase of the series resistance [187-189]. The series resistance R_s in the PV cell is mainly related to two parts: the resistances from the metal contacts and the current movement through the emitter and the base of the cell [182], respectively. It increases gradually due to the thermal and environmental effects. Increase of R_s leads to the decrease of the PV cell output voltage and the power loss of the PV device [182]. Dark I - V characteristics measurement can be used to evaluate the condition changes of the series resistance [53]. The shunt resistance R_p is another major factor in the PV cell to cause significant power loss. The impurities and crystal damage in the PV cell may introduce alternate current paths for the light-generated current. It will cause the increase of the shunt current, and lead to the PV performance reduction. The condition change of the shunt resistance can also be monitored by dark I - V characteristics measurement [51]. In this dissertation research, the change of the shunt resistance is investigated.

For the condition monitoring purpose, variables like PV array voltage and current can be selected, while the I - V characteristic measurement is also a major technique to detect the PV module degradation. With the open-circuit I - V curve obtained, it has been proposed [49] that the internal series resistance may be obtained based on its proportionality with the slope of I - V curve, or as intercept of the slope of I - V curve [18]. With the complete evaluation of the PV modules before installation, the degradation could be warned with offline evaluation of the system characteristic [184]. Signal processing [190], thermal infrared imaging [191] and other methods [192] have also been investigated for PV device fault detection and diagnostics. However, all these methods

are either offline with require large number of measurements under different irradiation levels or need to rely on the reliability of multiple sensors [193].

In this dissertation research, another advantage of the dither ESC has been considered, especially when square-wave dither input is applied. Under square-wave dither, the steady-state ESC output consists of a number of small-amplitude step responses, and the transient characteristics of such step responses are affected by certain system parameters. For PV operation, the internal shunt resistance has significant impact on the transient characteristics of the dithered output, and thus it is expected to use such correlation to detect the possible PV degradation and faults. This approach provides a control integrated diagnostic probe for PV degradation detection, which is a cost-effective scheme for PV condition monitoring.

Chapter 3. Modeling of Chilled Water Plant

For the ESC control, the chilled-water plant being simulated consists of a water-cooled screw chiller and a mechanical-draft counter-flow wet cooling tower. The cooling tower model follows the work by Braun *et al.* in [105]. The screw compressor modeling follows the work by Zhang *et al.* in [30], while the condenser, evaporator and expansion device models are based on the work by Li, *et al.* in [194]. For other components, such as fan, pump, collection basin, we have adopted the counterparts in the TIL Library 2.0.1 [29]. In this chapter, the dynamic model of the cooling tower is presented in Section 3.1.1, with discussion about the determinations of number of transfer units (NTU) and Lewis relation (Le_f) in Section 3.1.2. Section 3.1.3 presents the component-level models for fan, pump and collection basin. The developed cooling tower model is evaluated with the experimental data from Simpson and Sherwood [195] in Section 3.2, in terms of the steady-state value of the outlet water temperature. The dynamic behavior is also simulated under the change of inlet conditions, although no validation can be provided at this stage. The screw chiller model is discussed in Section 3.2. The screw compressor model is presented in Section 3.2.1. Other components in the chiller cycle are briefly described in Section 3.2.2, including condenser, evaporator and expansion valve. These component models are adopted from [31], and their detailed description are given in the Appendix C.

3.1. Dynamic Modeling of Counter Flow Wet Cooling Tower

This section presents a dynamic simulation model for a typical mechanical draft counter-flow wet cooling tower.

For cooling tower operation, heat rejection is accomplished via the heat and mass transfer occurring at the direct contact between hot water droplets and ambient air. Figure 3.1 shows the schematic of a mechanical draft counter flow wet cooling tower that is typically used for chilled water system in commercial buildings.

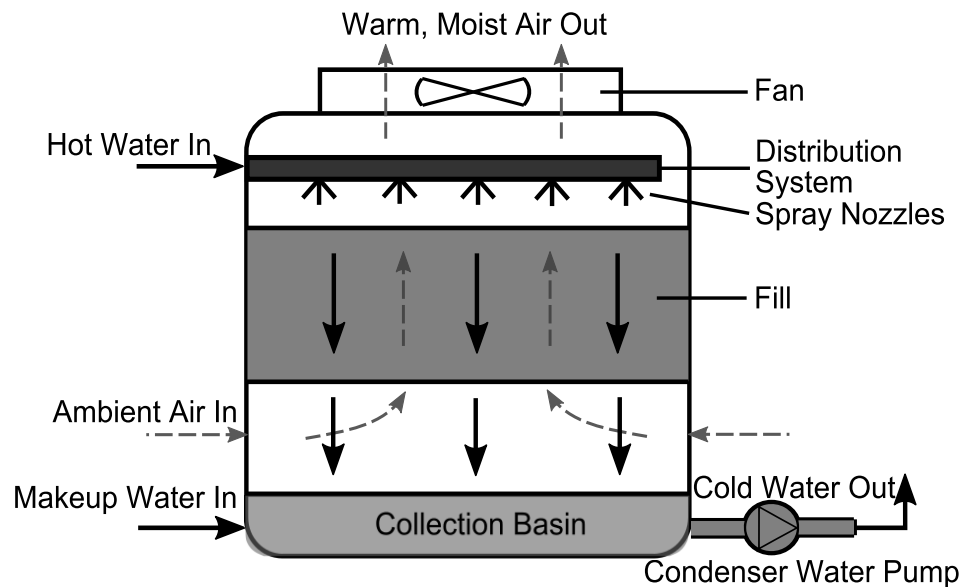


Figure 3.1: Schematic diagram for mechanical draft counter flow wet cooling tower

The cooling tower includes fan, distribution system, spray nozzles, fill (packing), collection basin and condenser pump. The warm water from chiller is sprayed downward through the pressurized nozzles and then flows through the fill, and the evaporative cooling occurs as the air flow is pulled upward by the tower fan through the fill. The fill is used to increase both the surface area and contact time between the air and water flows. For relatively dry air, the warm water can be cooled to a temperature below the ambient dry-bulb temperature. During the process, some water is evaporated into the air while some water is lost by misting effect (drift). Therefore, an external source of water, called makeup water, is needed to compensate for the water loss due to evaporation and drift. The condenser pump drives the water back to the chiller.

In this dissertation research, the dynamic modeling of cooling tower system components adopt both the free packages from Modelica Standard Library and the commercial packages from the TLK/IfT Library (TIL) [196]. Furthermore, the extended developments of the models are established as follows:

- 1) Water and moist air side models are re-developed to describe the evaporative cooling process of the cooling tower instead of the common heat exchangers. The transient behavior of the thermal process is considered due to further optimization control purpose.
- 2) The one-dimensional heat and mass transfer between the water and air streams is established by utilizing the overall number of transfer units (NTU) and Lewis relation (Le_f).
- 3) The collection basin model of the cooling tower is developed, which provides important additional dynamics for the cooling tower system.

Dynamic modeling of cooling tower is beneficial for control design and fault detection and diagnostics of the chilled-water systems [9]. The proposed dynamic model of the cooling tower is based on the one-dimensional dynamic heat and mass balance equations. The assumptions from Braun's work [105] were followed to simplify the analysis:

- 1) Heat and mass transfer is only considered in one dimensional, the perpendicular direction of the flows.
- 2) The cooling tower is assumed well sealed, no heat and mass transfer through the walls to the environment.

- 3) The humidity ratio is used to approximate the mass fraction of the water vapor in the moist air.
- 4) The cross-sectional area of the tower is assumed uniform.
- 5) The water and moist air temperatures are assumed uniform at any cross section.

Several distinctive treatments are carried out in this study:

- 1) Mutative water and air specific heats are used to relax the constraints, with the help of the property calculation capability available in the TIL Media Library [196].
- 2) The formulation in Bosnjakovic's work [123] is followed instead of considering the Lewis relation as unity.
- 3) The finite volume method is applied in order to achieve more robust performance for start-up and all load change transients [124].
- 4) NTU and Le_f are used to characterize the heat and mass transfer coefficients for specific tower design due to the difficulty in getting a general correlation for heat and mass transfer in cooling tower [106].

The control volumes of water and moist air are defined separately, with opposite flow directions. Dynamic mass and energy balances are evaluated for each of the control volumes, the heat and mass transfer are considered between each pair of the water and moist-air control volumes. The proposed model includes both sensible and latent heat transfer effects on the tower performance. The balance between the water loss and the humidity increase in the moist air is reinforced through all the control volumes. The

water loss is determined by the mass transfer coefficient based on the geometry and performance map of specific cooling tower. The associated evaporation cooling process and its related components are model developed by utilizing Modelica (Version 2.2.1) [26] with Dymola (Versions 6.1 and 2012 FD1) [27], TIL Library 2.0.1 and TIL Media Library 2.0.4 [29].

3.1.1. Cooling Tower Modeling

The evaporative cooling process of the mechanical-draft counter-flow wet cooling tower is modeled with the finite volume method, as shown in Fig. 3.2. The control volumes for water and moist air are constructed, respectively. The water and moist air flows are in opposite directions. Dynamic mass and energy balances are established for both water- and air-sides, with control volumes shown in Fig. 3.3 and Fig. 3.4, respectively. The heat and mass transfer are considered between each pair of the water and moist air control volumes. The transient mass and energy storage is treated at the water side but neglected at the air side.

For the i^{th} water-side control volume, the energy balance is established as

$$\Delta H_{w,i} = \dot{H}_{w,in,i} - \dot{H}_{w,out,i} - \dot{q}_i \quad (3.1)$$

where $\Delta H_{w,i}$ is the enthalpy change for the cell, $\dot{H}_{w,in,i}$ is the inlet water enthalpy, $\dot{H}_{w,out,i}$ is the outlet water enthalpy, respectively. \dot{q}_i is the heat flow transferred to the neighboured (also the i^{th}) moist-air cell, which includes both sensible heat flow and the latent heat flow due to evaporation. Equation (3.1) can be expanded into

$$m_{w,i} \cdot c_{p,w,i} \cdot \frac{dT_{w,i}}{dt} = \dot{m}_{w,in,i} (h_{w,in,i} - h_{w,i}) - \dot{m}_{w,out,i} (h_{w,out,i} - h_{w,i}) - \dot{q}_i \quad (3.2)$$

where $m_{w,i}$ is the mass of water stored in the cell, $c_{p,w,i}$ is the specific heat of water (which can be determined by the local water temperature $T_{w,i}$) in the cell, $\dot{m}_{w,in,i}$ and $\dot{m}_{w,out,i}$ are the mass flow rates for the inlet and outlet water flow, respectively. $h_{w,in,i}$ and $h_{w,out,i}$ are the specific enthalpy of the inlet and outlet water flow, respectively, and $h_{w,i}$ is the specific enthalpy of water in the cell.

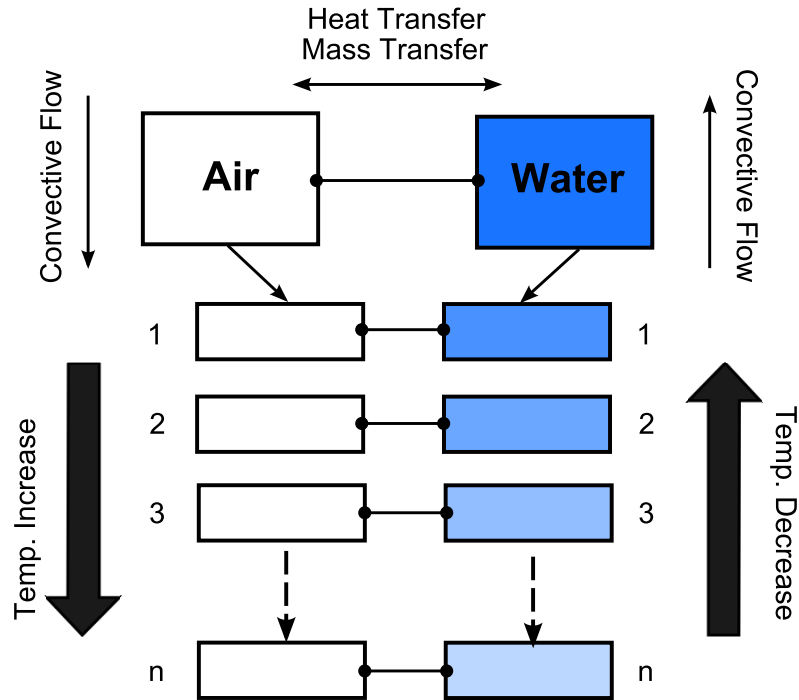


Figure 3.2: Illustration of control volumes for cooling tower modeling

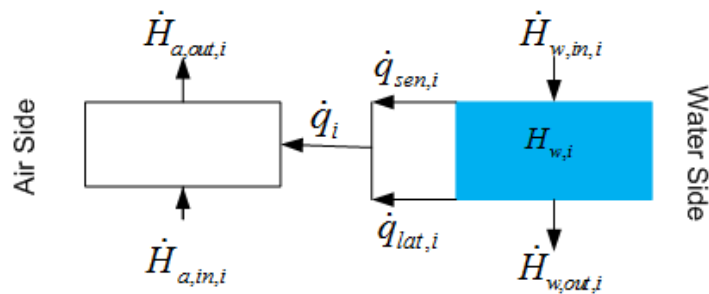


Figure 3.3: Energy balance between neighbored water and air control volumes

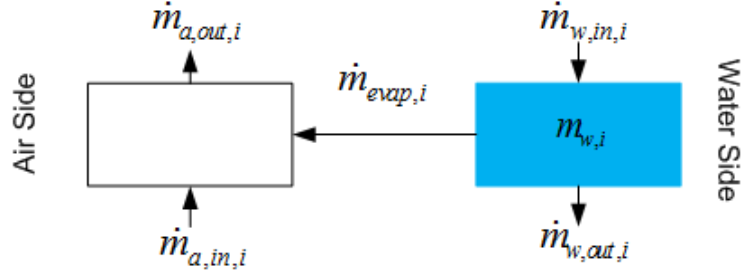


Figure 3.4: Mass balance between neighbored water and air control volumes

For the mass balance of the same water-side control volume, cell volume V_{cell} is assumed as constant, while water density $\rho_{w,i}$ may change with evaporation and temperature change in the cell. The dynamic mass balance follows

$$\frac{dm_{w,i}}{dt} = \dot{m}_{w,in,i} - \dot{m}_{w,out,i} - \dot{m}_{evap,i} \quad (3.3)$$

$$m_{w,i} = V_{effective} \cdot \rho_{w,i} \quad (3.4)$$

where $\dot{m}_{evap,i}$ is the vapour mass transfer flow rate into the moist air side. $V_{effective}$ is the water droplet volume in the cell. The ratio of water droplet per unit volume of the tower is around the level of 0.001 [106]. Substituting Eq. (3.4) into Eq. (3.3) yields

$$\frac{d(V_{effective}\rho_{w,i})}{dt} = \frac{dV_{effective}}{dt}\rho_{w,i} + V_{effective}\frac{d\rho_{w,i}}{dt} = \dot{m}_{w,in,i} - \dot{m}_{w,out,i} - \dot{m}_{evap,i} \quad (3.5)$$

$V_{effective,i}$ can be obtained by [107]:

$$V_{effective} = \frac{V_{cell}}{\rho_{w,i}A_T v_w} \dot{m}_{w,in} \quad (3.6)$$

where v_w is the velocity of water droplets under free fall (no packing), is assumed as constant. A_T is the cross-sectional area of the tower. Taking the time derivative of Eq. (3.6) yields

$$\frac{dV_{effective}}{dt} \rho_{w,i} = \frac{V_{cell}}{A_T v_w} \frac{d\dot{m}_{w,in}}{dt} \quad (3.7)$$

Equation (3.7) reveals that if $\dot{m}_{w,in}$ does not vary much, $V_{effective}$ can be assumed as constant; otherwise, the gradient of $\dot{m}_{w,in}$ is needed to account for the change of $V_{effective}$.

The time derivative of density ρ can be expressed as function of pressure P and specific enthalpy h [196]:

$$\frac{d\rho}{dt} = \left(\frac{\partial \rho}{\partial P} \right)_h \frac{dP}{dt} + \left(\frac{\partial \rho}{\partial h} \right)_P \frac{dh}{dt} \quad (3.8)$$

As the cell pressure is approximately constant for the cooling tower operation, Eq. (3.8) can be simplified as

$$\frac{d\rho}{dt} = -\frac{\beta \rho}{c_{pw}} \cdot \frac{dh}{dt} = -\beta \rho \frac{dT}{dt} \quad (3.9)$$

where $\beta = -\frac{1}{\rho} \left(\frac{\partial \rho}{\partial T} \right)_P$ is the isobaric coefficient of expansion and c_{pw} is the specific heat capacity at constant pressure. Substituting Eq. (3.9) into Eq. (3.5) leads to the mass balance of the i^{th} water cell:

$$\dot{m}_{w,in,i} - \dot{m}_{w,out,i} - \dot{m}_{evap,i} = -V_{effective} \beta_{w,i} \rho_{w,i} \frac{dT_{w,i}}{dt} + \frac{V_{cell}}{A_T v_w} \cdot \frac{d\dot{m}_{w,in}}{dt} \quad (3.10)$$

where $\beta_{w,i}$ and $\rho_{w,i}$ can be determined by the local water temperature.

At the air side, the steady-state relations were derived following the detailed analysis model [105], i.e.

$$\dot{H}_{a,in,i} - \dot{H}_{a,out,i} + \dot{q}_i = 0 \quad (3.11)$$

$$\dot{q}_i = \dot{q}_{sen,i} + \dot{q}_{lat,i} \quad (3.12)$$

The sensible and latent heat flow rates can be determined by

$$\dot{q}_{sen,i} = h_{C,i} A_V V_{cell} (T_{w,i} - T_{a,i}) \quad (3.13)$$

$$\dot{q}_{lat,i} = h_{f,g,i} \cdot \dot{m}_{evap,i} = h_{f,g,i} \cdot h_{D,i} A_V V_{cell} (\omega_{s,w,i} - \omega_{a,i}) \quad (3.14)$$

where $h_{C,i}$ is the local heat transfer coefficient, A_V is the surface area of water droplets per unit volume, $T_{a,i}$ is the local air temperature, $h_{f,g,i}$ is the latent heat of vaporization depending on the local water temperature. $h_{D,i}$ is the local mass transfer coefficient, $\omega_{s,w,i}$ is the saturated air humidity ratio at the local water temperature, and $\omega_{a,i}$ is the local humidity ratio of the moist air.

The fill is used in most cooling towers, however, it is usually hard to predict its heat rejection performance analytically because of the difficulty in evaluating the contact time and the surface area between the moist air and the water streams through the fill [106]. The fouling in the packing materials may result in a reduction in the overall effectiveness of the tower and make it even harder to evaluate the fill geometry accurately. Due to the difficulty in getting a general correlations for heat and mass transfer in cooling tower in terms of the physical tower characteristics, the NTU and the Lewis relation Le_f have been used to characterize the heat and mass transfer coefficients for specific tower designs [105].

The mass transfer coefficient can be derived by using the overall NTU for mass transfer, i.e.

$$NTU = \frac{h_{D,i} A_V V_T}{\dot{m}_{a,in}} \quad (3.15)$$

where V_T is the total tower volume and $\dot{m}_{a,in}$ is the inlet air flow rate. The mass transfer coefficient can thus be determined with

$$h_{D,i}A_V = \frac{NTU \cdot \dot{m}_{a,in}}{V_T} \quad (3.16)$$

which varies with the tower geometry, NTU and tower inlet air flow rate. The heat transfer coefficient is determined by

$$h_{C,i}A_V = \frac{Le_f \cdot NTU \cdot c_{pm,i} \cdot \dot{m}_{a,in}}{V_T} \quad (3.17)$$

where Le_f is defined as

$$Le_f = \frac{h_{C,i}}{h_{D,i}c_{pm,i}} \quad (3.18)$$

and the local specific heat of moist air $c_{pm,i}$ is determined by

$$c_{pm,i} = c_{pa,i} + \omega_{a,i}c_{pv,i} \quad (3.19)$$

where $c_{pa,i}$ is the local specific heat of dry air and $c_{pv,i}$ is the local specific heat of water vapor [104]. $h_{C,i}$ may change with the local value of Le_f and $c_{pm,i}$.

3.1.2. Determination of NTU and Le_f

The Merkel's number Me_M can be related to the mass transfer coefficient by [197]:

$$Me_M = \frac{h_D A_V V_T}{\dot{m}_{w,in}} = c_{CT} \left(\frac{\dot{m}_{w,in}}{\dot{m}_{a,in}} \right)^{n_{CT}} \quad (3.20)$$

where $\dot{m}_{w,in}$ is the inlet water flow rate of cooling tower, c_{CT} and n_{CT} are empirical constants specific to a particular tower design. Kröger [198] presented a methodology to obtaining the Merkel's number from experimental data with empirical equations of thermal properties (see Appendix A). Multiplying both sides of Eq. (3.20) by $\dot{m}_{w,in} / \dot{m}_{a,in}$ leads to

$$NTU = c \left(\frac{\dot{m}_{w,in}}{\dot{m}_{a,in}} \right)^{n+1} \quad (3.21)$$

where coefficients c_{CT} and n_{CT} can be fitted from the performance measurements for a specific tower on a log-log plot [105].

The Lewis relation has been discussed in literature. Poppe and Rogener [111] cited the definition of Lewis relation according to [123], i.e.

$$Le_f = Le^{2/3} \left[\left(\frac{\omega_{s,w} + d_r}{\omega_a + d_r} - 1 \right) / \ln \left(\frac{\omega_{s,w} + d_r}{\omega_a + d_r} \right) \right] \quad (3.22)$$

where Le is the Lewis number, assumed as a constant as 0.865. d_r is the ratio of the molecular weight of water to the molecular weight of air, which is a constant of 0.622. Grange [199] and Bourillot [200] claimed that for a wet cooling tower, Eq. (3.22) is approximately 0.92. Kloppers and Kröger [201] stated that, if the ambient air is very humid, variation of the Lewis relation has little influence on the water outlet temperature, and neither on the heat rejected from the cooling tower; while for dry conditions, variation of the Lewis relation can lead to significantly different results. It was also suggested that the equation by [123] should be used, and a numerical value of 0.92 be preferred when the fill performance test data is insufficient to accurately predict the Lewis relation of a particular fill.

The simulation evaluation of the steady-state value of the cooling tower model will be shown in Section 3.1.4.A. In particular, the Lewis relation value will also be shown, the simulation results shows a very close value around 0.92.

3.1.3. Model of Related Components Used in Simulation

3.1.3.A. Cooling Tower Fan

The tower fan modeling follows the *TIL.MoistAirComponents.Fans.Fan2ndOrder* component in the TIL Library [29]. From the fan affinity law, the volume flow rate, pressure increase and rotational speed are related by

$$Q_{fan,affinity,0} = Q_{fan,0} \cdot \frac{n_{fan}}{n_{fan,0}} \quad (3.23)$$

$$\Delta p_{fan,affinity,0} = \Delta p_{fan,0} \cdot \left(\frac{n_{fan}}{n_{fan,0}} \right)^2 \quad (3.24)$$

where $n_{fan,0}$ is the nominal speed, n_{fan} is the rotational speed, $Q_{fan,0}$ is the volume flow rate for zero pressure increase, and $Q_{fan,affinity,0}$ is the volume flow rate for zero pressure increase following the fan affinity law. For zero volume flow rate, $\Delta p_{fan,0}$ denotes the pressure increase and $\Delta p_{fan,affinity,0}$ denotes the pressure increase following the fan affinity law [196]. The actual pressure increase can be determined with

$$\Delta p_{fan} = \Delta p_{fan,affinity,0} \cdot \left(1 - \frac{Q_{fan}}{Q_{fan,affinity,0}} \right)^2 \quad (3.25)$$

Then the fan power can be given by

$$W_{fan} = \frac{\Delta p_{fan} \cdot Q_{fan}}{\eta_{fan} \eta_{fan,m}} \quad (3.26)$$

where η_{fan} is the fan efficiency and $\eta_{fan,m}$ is the motor efficiency. η_{fan} can be determined by a polynomial regression of the manufacture's data [202].

3.1.3.B. Condenser Water Pump

The condenser water pump model is intended to predict the power consumption by the pump. A constant pressure change could be set up in later simulations due to the assumption of constant condenser water flow rate. The TIL pump model *TIL.LiquidComponents.Pumps.Pump2ndOrder* has been adopted [29], with the pump affinity law defined similarly to that for the fan modeling, which are given as:

$$Q_{pump,affinity,0} = Q_{pump,0} \cdot \frac{n_{pump}}{n_{pump,0}} \quad (3.27)$$

$$\Delta p_{pump,affinity,0} = \Delta p_{pump,0} \cdot \left(\frac{n_{pump}}{n_{pump,0}} \right)^2 \quad (3.28)$$

where n_{pump} is the rotational speed, $n_{pump,0}$ is the nominal speed, $Q_{pump,0}$ is the volume flow rate for zero pressure increase, and $Q_{pump,affinity,0}$ is the volume flow rate for zero pressure increase following the pump affinity law. For zero volume flow rate, $\Delta p_{pump,0}$ denotes the pressure increase and $\Delta p_{pump,affinity,0}$ the pressure increase following the pump affinity law. The actual pressure increase can be determined with

$$\Delta p_{pump} = \Delta p_{pump,affinity,0} \cdot \left(1 - \frac{Q_{pump}}{Q_{pump,affinity,0}} \right)^2 \quad (3.29)$$

The power loss and the shaft power of the pump can then be determined by

$$W_{pump,loss,0} = \left(\frac{1}{\eta_{pump,0}} - 1 \right) \cdot \Delta p_{pump,0} \cdot Q_{pump,0} \cdot \frac{2}{3^{1.5}} \quad (3.30)$$

$$W_{pump,loss} = W_{pump,loss,0} \cdot \left(\frac{n_{pump}}{n_{pump,0}} \right)^{e_{pump,loss}} \quad (3.31)$$

$$W_{pump,shaft} = W_{pump,loss} + \Delta p_{pump} \cdot Q_{pump} \quad (3.32)$$

where $W_{pump,loss,0}$ is the power loss at nominal speed, $\eta_{pump,0}$ is the nominal efficiency, $W_{pump,loss}$ is the actual power loss at rotational speed η_{pump} , and $e_{pump,loss}$ is a constant exponent for power loss calculation.

The mass and energy balances for the pump are

$$\dot{m}_{pump,in} - \dot{m}_{pump,out} = -\beta_{pump} \rho_{pump,w} V_{pump} \frac{dT_{pump,w}}{dt} \quad (3.33)$$

$$c_{pw,pump} \frac{dT_{pump,w}}{dt} = \frac{\dot{m}_{pump,in} (h_{pump,in} - h_{pump}) - \dot{m}_{pump,out} (h_{pump,out} - h_{pump}) + W_{pump,shaft}}{\rho_{pump,w} V_{pump}} \quad (3.34)$$

where $\dot{m}_{pump,in}$ and $\dot{m}_{pump,out}$ are the inlet and outlet flow rates of the water pump, respectively. β_{pump} is the local isobaric coefficient of expansion in the pump. $\rho_{pump,w}$ is the local water density in the pump. $T_{pump,w}$ is the local water temperature in the pump. V_{pump} is the volume of water in the pump, which is generally treated as a constant. $h_{pump,in}$ and $h_{pump,out}$ are the specific enthalpies for the inlet and outlet water, respectively. h_{pump} is the specific enthalpy of water in the pump, and $W_{pump,shaft}$ is the pump shaft power.

3.1.3.C. Collection Basin

The mass and energy balance equations of the collection basin can be established as [196]:

$$\dot{m}_{cb,in} - \dot{m}_{cb,out} + \dot{m}_{cb,makeup} = -\beta_{cb} \rho_{cb,w} V_{cb} \frac{dT_{cb,w}}{dt} \quad (3.35)$$

$$c_{pw,cb} \frac{dT_{cb,w}}{dt} = \frac{\dot{m}_{cb,in} (h_{cb,in} - h_{cb}) - \dot{m}_{cb,out} (h_{cb,out} - h_{cb}) + \dot{m}_{cb,makeup} (h_{cb,makeup} - h_{cb})}{\rho_{cb,w} V_{cb}} \quad (3.36)$$

where $\dot{m}_{cb,makeup}$ is the water flow rate from some source of make-up water. h_{cb} is the specific enthalpy of water in the collection basin. The volume of water V_{cb} in the collection basin is assumed to be constant for now. So the flow of water make-up is equal to the total water loss from evaporation. $\dot{m}_{cb,in}$ and $\dot{m}_{cb,out}$ are the inlet and outlet water flow rates of collection basin, respectively. β_{cb} is the local isobaric coefficient of expansion in the basin, and $\rho_{cb,w}$ is the local water density. $T_{cb,w}$ is the local water temperature in the basin. $h_{cb,in}$ and $h_{cb,out}$ are the specific enthalpies for the inlet and outlet water, respectively.

3.2. Simulation Study for Cooling Tower Modeling

Simulation study is conducted to study the behavior and the performance of the dynamic model of cooling tower. Both steady-state and transient performance of the cooling tower evaporative cooling process will be shown below. The steady-state value of the cooling tower outlet water temperature is evaluated with the experimental data from [195]. The parameters used in the simulation are listed in Appendix B. The solver is selected as Dassel and the tolerance setting in this simulation is selected as 0.0001.

3.2.1. Steady-State Simulation and Comparison

Figure 3.5 shows the Dymola layout of the model of evaporation cooling process for the cooling tower, developed with TIL library. There are five inputs in the cooling tower model, i.e. the inlet moist-air flow rate, inlet moist-air temperature, inlet moist-air humidity ratio, the inlet water flow rate and the inlet water temperature.

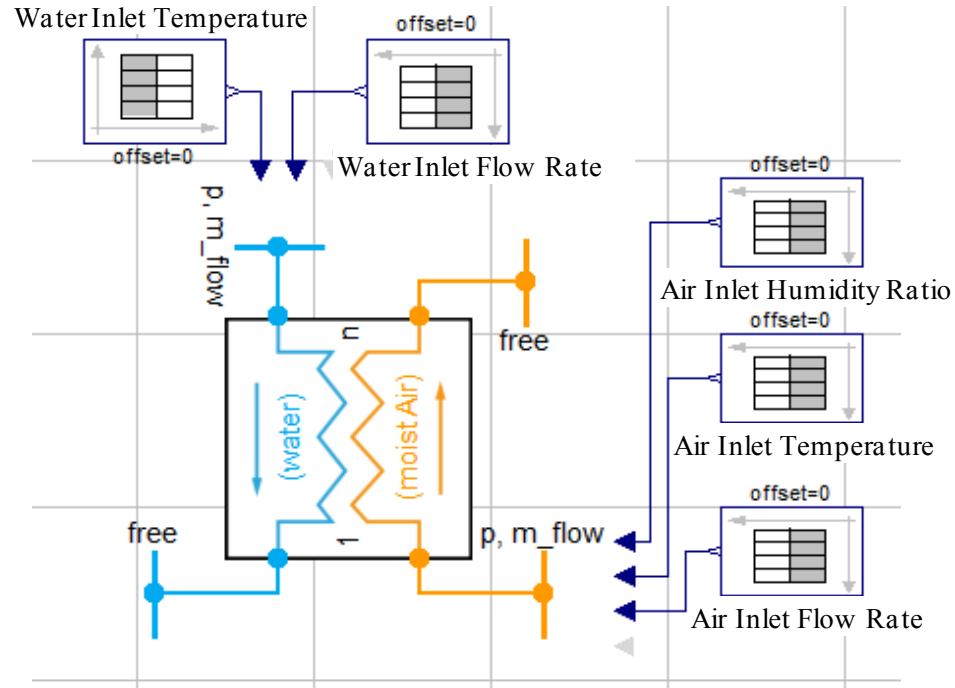


Figure 3.5: Dymola layout for evaporative cooling process of cooling tower

The steady-state performance of the proposed model is evaluated with the experimental data from [195], with five cases compared in Table 3.1. $T_{w,out,cal}$ is the model predicted water outlet temperature. Figure 3.6 plots all the experimental data of the outlet water temperature and those predicted with the proposed model. The prediction error has the mean of 0.344K and the standard derivation of the 0.428K, which is comparable to the results in [105].

TABLE 3.1
COMPARISON OF COOLING TOWER SIMULATION MODEL AND EXPERIMENTAL DATA

Cases	1	2	3	4	5
$T_{w,in} (^{\circ}\text{C})$	33.22	34.39	43.61	38.78	43.06
$T_{w,out} (^{\circ}\text{C})$	25.50	29.00	27.89	29.33	29.72

$T_{db,in} (^{\circ}\text{C})$	28.83	31.78	35.00	35.00	35.72
$T_{wb,in} (^{\circ}\text{C})$	21.11	26.67	23.89	26.67	26.67
$T_{db,out} (^{\circ}\text{C})$	28.44	31.22	32.78	33.28	33.89
$\dot{m}_{a,in} (\text{kg/s})$	1.187	1.165	1.158	1.265	1.157
$\dot{m}_{w,in} (\text{kg/s})$	1.009	1.009	0.755	1.009	0.755
$T_{w,out,cal} (^{\circ}\text{C})$	25.46	28.78	28.12	29.87	29.94

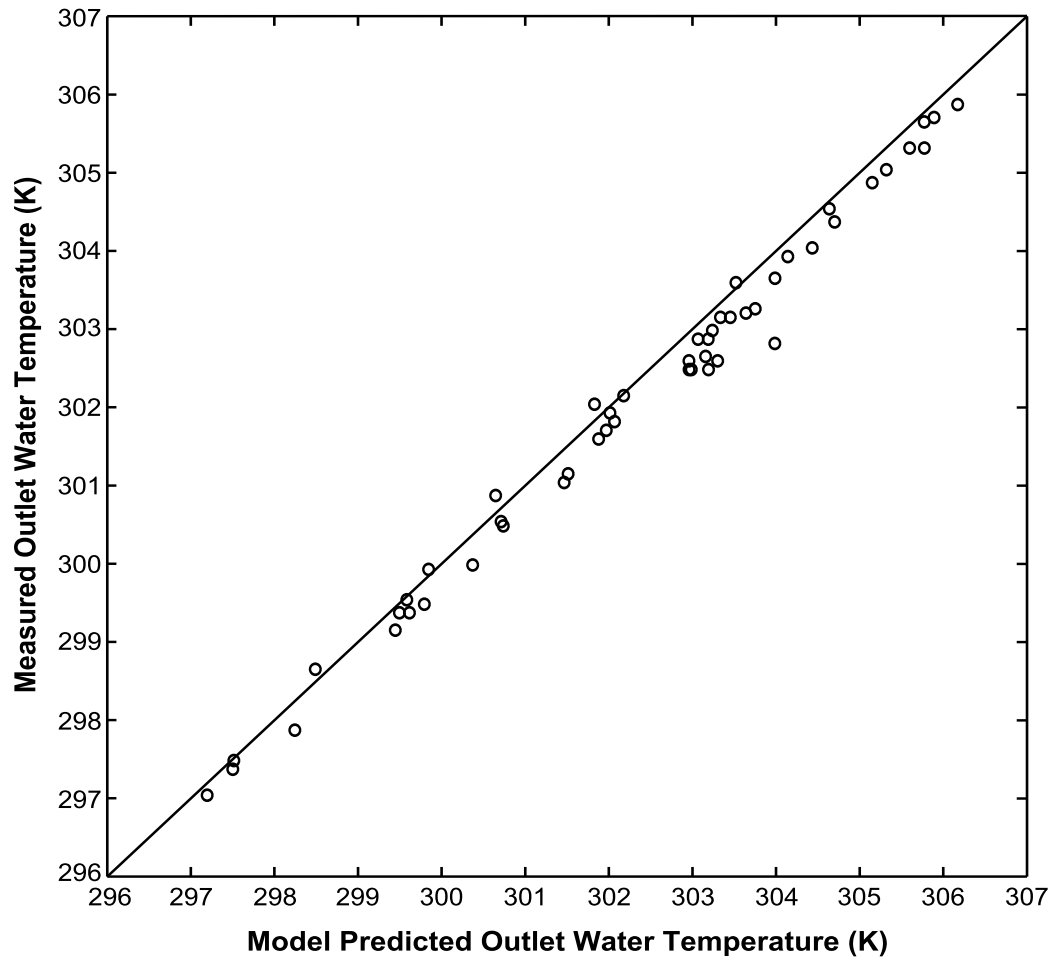


Figure 3.6: Comparison for outlet water temperature between model prediction and measured data

3.2.2. Transient Simulation

Since no field test data is available by the time period of this study, an investigation into the media condition change through the tower cells is provided to evaluate the validity of the transient description. All the condition changes in the case studies use a very fast ramp change with ramp duration as 0.01 sec.

For simulation Test 1, the transient profile for the change from Scenario 1 to Scenario 2 as defined in Table 3.2. is observed under the changes of the inlet water temperature, the inlet air temperature and the inlet air humidity ratio. Figure 3.7 shows the profile of outlet water temperature. The water inlet temperature and the air inlet dry bulb temperature increase, which may cause an increase of the water outlet temperature. Meanwhile, the decrease of the relative humidity of the inlet air may cause a decrease of the water outlet temperature. For static model simulation, only the increase between the two states could be observed with the missing transient performance. The dynamic model in this dissertation study demonstrates a significant undershoot.

TABLE 3.2
DEFINITIONS OF SCENARIOS 1 AND 2 INVOLVED IN SIMULATION TEST 1

Scenario	1	2
$T_{w,in} (^{\circ}\text{C})$	38.78	48.06
RH (%)	65.3	51.4
AH (kg/m^3)	0.0192	0.0162
$T_{db,in} (^{\circ}\text{C})$	31.86	33.11
$\dot{m}_{a,in} (\text{kg}/\text{s})$	1.1584	1.1584

$\dot{m}_{w,in}$ (kg/s)	0.7548	0.7548
$T_{w,out,cal}$ (°C)	29.08	29.53

The water temperature performances in different cells are shown in Fig. 3.8. Because water is treated as in an inverse direction in the model, as shown in Fig. 3.2, so the water flow direction is: given inlet water temperature, cell 7, cell 5, cell 3 and outlet water temperature (water cells of even number is omitted). Please refer to Fig. 3.2 for the cell numbering.

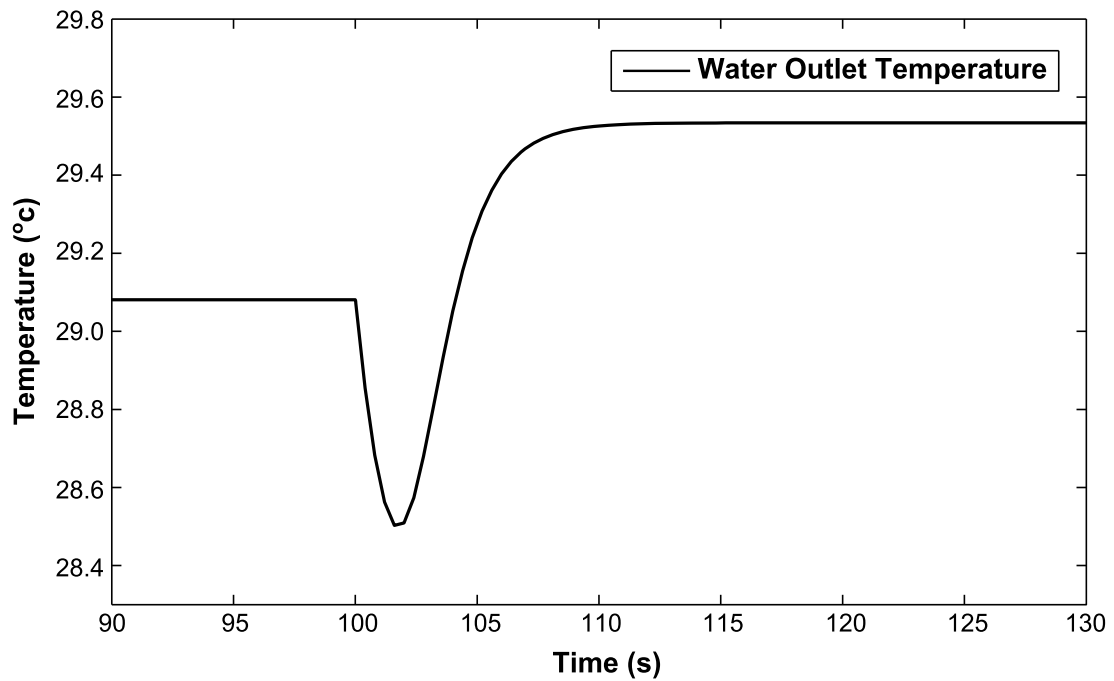


Figure 3.7: Transient profile of water outlet temperature in simulation test 1 with stand-alone cooling tower model

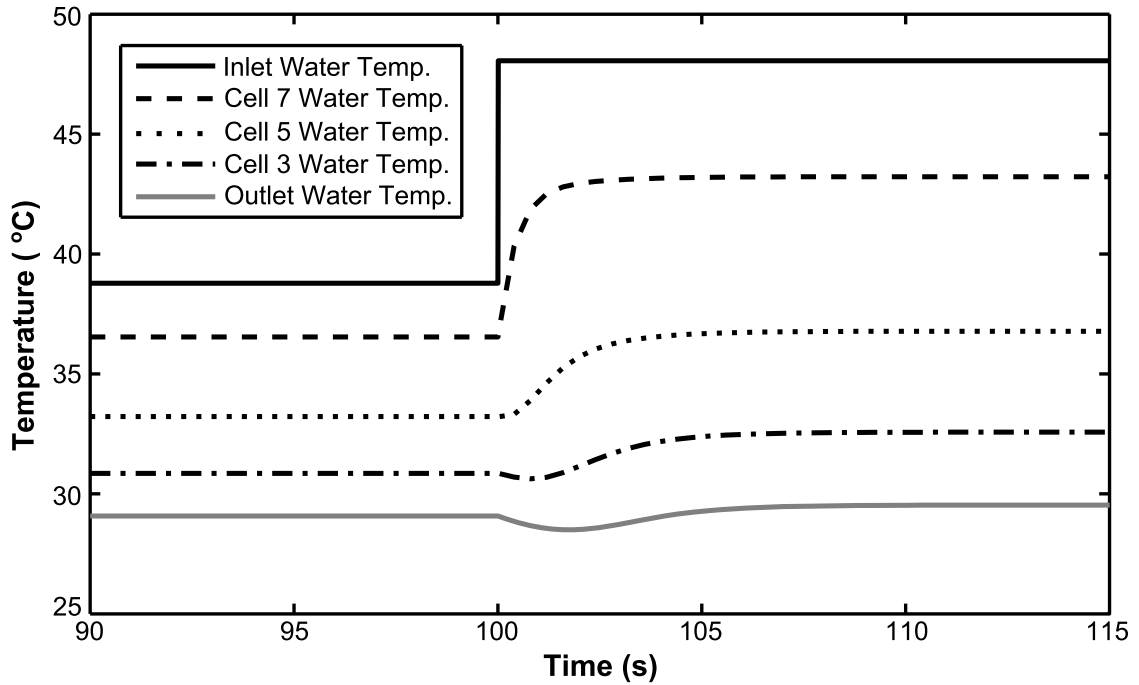


Figure 3.8: Transient profile of water cell temperatures in simulation test 1 with stand-alone cooling tower model

The tower inlet water becomes warmer during the condition change specified, but the effect cannot affect the outlet water temperature instantly, the warm water need to flow a long distance before it get to the tower outlet. Meanwhile, the decrease of the relative humidity of the inlet moist air will directly affect the outlet water temperature due to the counter flow structure of the cooling tower, so the tower outlet water temperature will decrease at the beginning of the condition change. Finally, when the warm water sprays downwards and arrives the tower outlet, the outlet water temperature will increase, and reach the same steady state result may shown in the static models. So there is an undershoot occurs instead of a smooth transient.

An opposite test is shown in Fig. 3.9, which demonstrates the transient performance from scenario 1 to scenario 2 in Table 3.3.

TABLE 3.3
DEFINITIONS OF SCENARIOS 1 AND 2 INVOLVED IN SIMULATION TEST 2

Scenarios	1	2
$T_{w,in} (^{\circ}\text{C})$	48.78	38.06
RH (%)	65.3	82.6
AH (kg/m^3)	0.0192	0.0262
$T_{db,in} (^{\circ}\text{C})$	31.86	33.11
$\dot{m}_{a,in} (\text{kg}/\text{s})$	1.1584	1.1584
$\dot{m}_{w,in} (\text{kg}/\text{s})$	0.7548	0.7548
$T_{w,out,cal} (^{\circ}\text{C})$	30.58	31.85

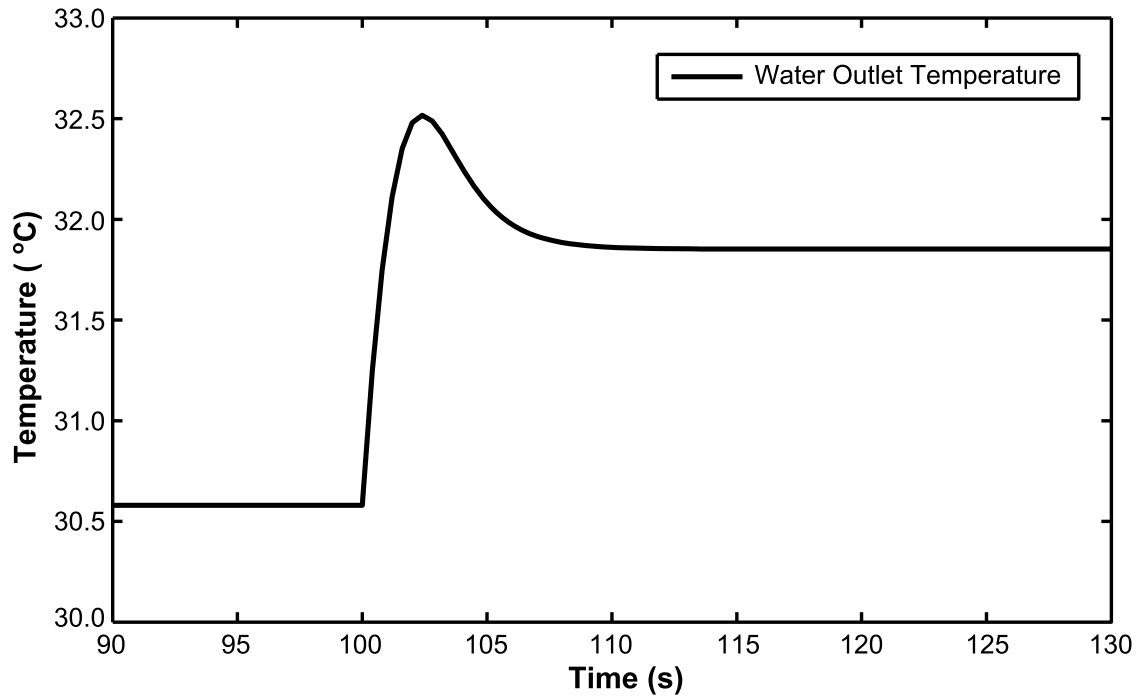


Figure 3.9: Transient profile of water outlet temperature in simulation test 2 with stand-alone cooling tower model

In test 2, the inlet water temperature decrease from 49°C to 38°C will may lead to a decrease of the outlet water temperature. Meanwhile the relative humidity of the inlet moist air increases from 65.3% to 82.6%, which may lead to an increase of the outlet water temperature. The steady state result shows a final increase on the temperature of the outlet water. However, the simulated transient performance shows an overshoot instead of a smooth transient. The water temperature performance change in different cells is shown in Fig. 3.10, with a similar explanation as test 1.

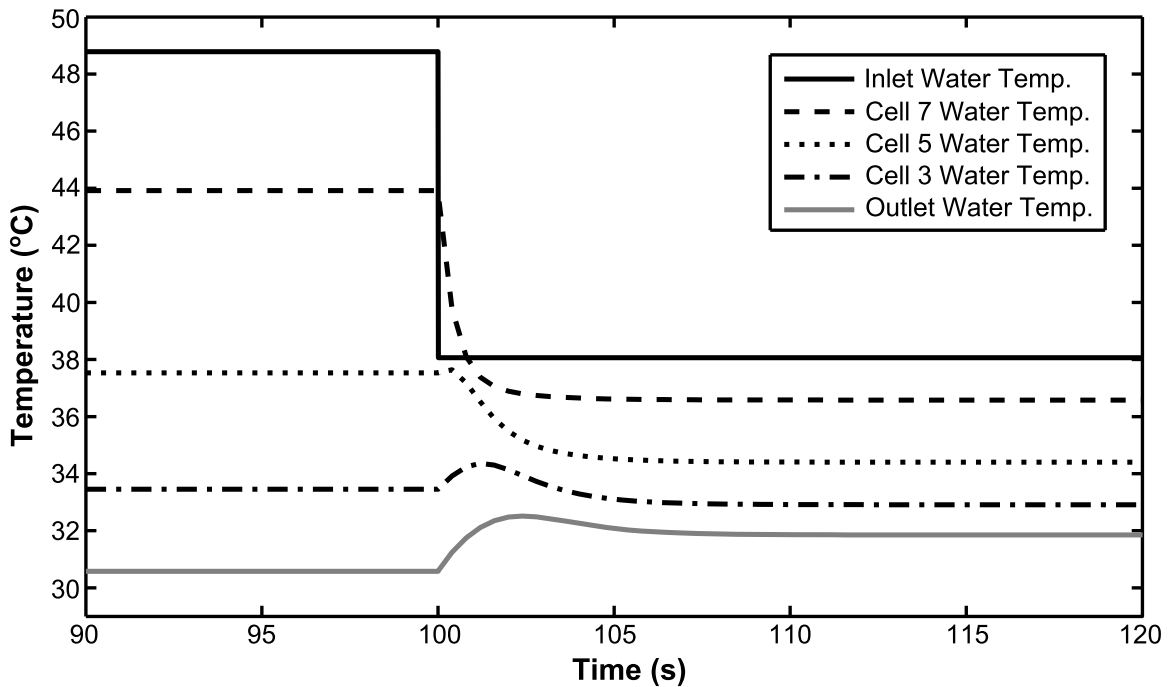


Figure 3.10: Transient profile of water cell temperatures simulation test 2 with stand-alone cooling tower model

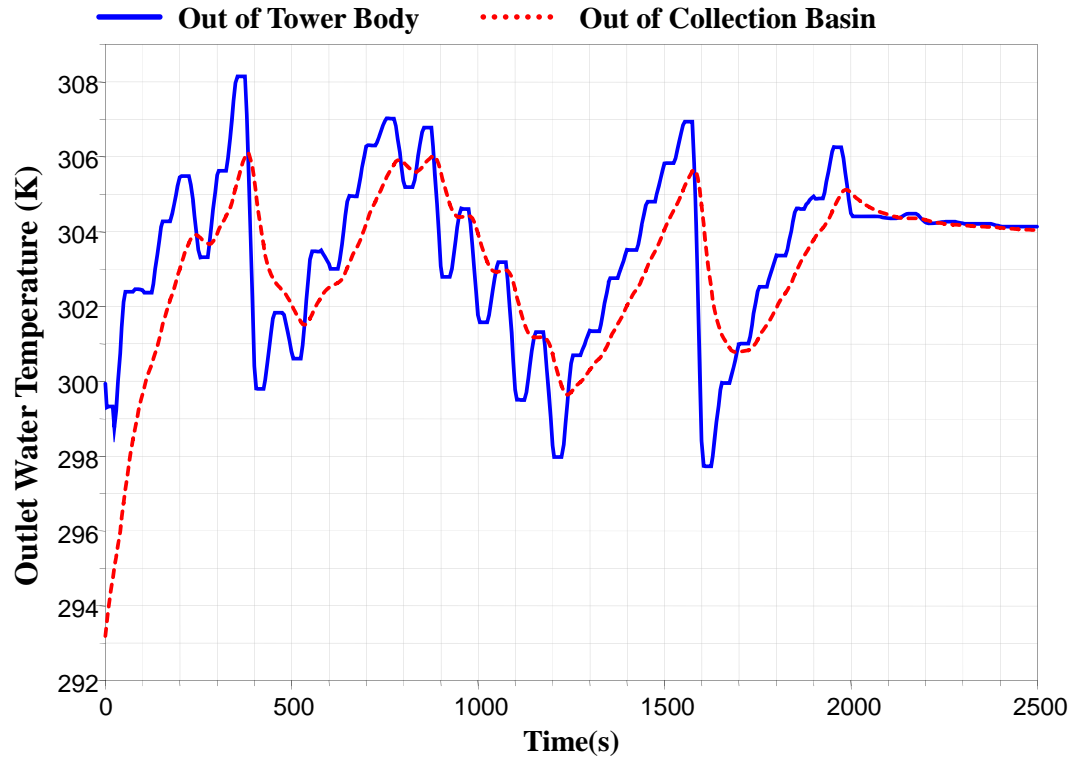


Figure 3.12: Transient profile of water outlet temperature for comparison between tower body and collection basin output water

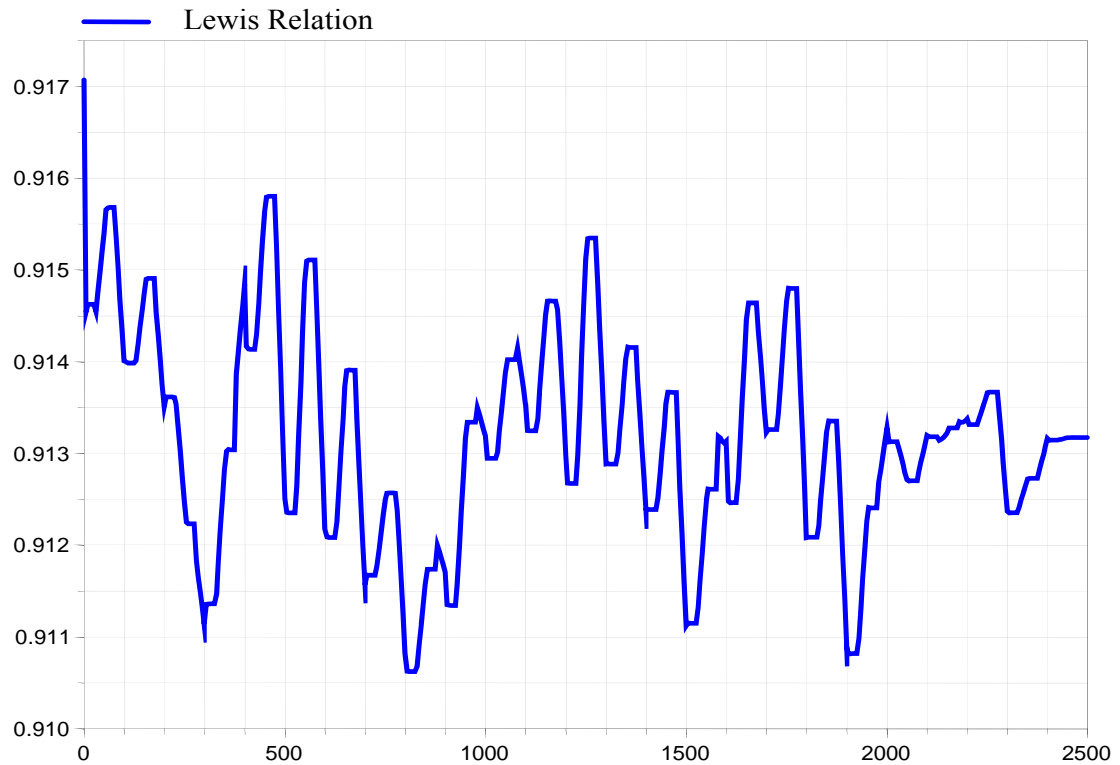


Figure 3.13: Simulation results of Lewis relation in the transient test

3.3. Modeling of Screw Chiller

3.3.1. Screw Compressor

The dynamics of screw compressor is much faster than that of the entire chiller cycle. For this dissertation study, a detailed transient model of screw compressor is not necessary for the energy efficiency investigation. Instead, a polytropic static compression model developed by [30] is adopted:

$$\dot{m}_{c,in} = s_{comp} \rho_{c,in} n_c V_{c,max} \eta_{c,v} \quad (3.37)$$

$$P_{c,out} = P_{c,in} \left(\frac{\rho_{c,out}}{\rho_{c,in}} \right)^{\gamma_c} \quad (3.38)$$

where $\dot{m}_{c,in}$ is the refrigerant mass flow rate at the compressor inlet, and $s_{comp} \in [0, 1]$ is the slide-valve control, which determines the compressor load. s_{comp} is used to regulate the chilled water temperature. $\rho_{c,in}$ and $\rho_{c,out}$ are the refrigerant densities at the compressor inlet and outlet, respectively. n_c is the compressor speed. $V_{c,max}$ is the theoretical compressor volume with full load condition. $P_{c,in}$ and $P_{c,out}$ are the compressor inlet and outlet pressures, respectively. γ_c is the ratio of specific heats in the compressor, and $\eta_{c,v}$ is the volumetric efficiency. The volumetric efficiency could be obtained from the pressure volume curve [130]. ASHARE [9] suggests the pressure-volume curve characteristic for the pressure ratio ranging from 2 to 9, for both the twin-screw and the single screw compressors.

The volumetric efficiency is determined as

$$\eta_{c,v} = 0.95 - 0.0125 \cdot \left(\frac{P_{c,out}}{P_{c,in}} \right) \quad (3.39)$$

following [139]. The electrical power consumed by the compressor is

$$W_{c,elec} = \frac{\dot{m}_{c,out} \cdot (h_{c,out} - h_{c,in})}{\eta_{c,a} \eta_{c,mo} \eta_{c,me}} \quad (3.40)$$

where $\dot{m}_{c,out}$ is the refrigerant mass flow rate at the compressor outlet. $h_{c,in}$ and $h_{c,out}$ are the inlet and outlet specific enthalpies, respectively. $\eta_{c,a}$, $\eta_{c,mo}$ and $\eta_{c,me}$ are the adiabatic efficiency, motor efficiency and mechanical efficiency, chosen as 0.8, 0.85 and 0.95, respectively [139].

3.3.2. Condenser, Evaporator and Expansion Valve

The shell-and-tube heat exchanger models of condenser and evaporator in the screw chiller follow the work by [31, 194] with same geometry and parameter configuration, the detailed description will be listed in Appendix C and D. Both exchangers are of the counter-flow type with in-tube water flow. Based upon the adoption of concentric heat exchanger, the shell-side heat transfer area is calculated based on the water tubes outer surface area and the surface enhancement factor. The finite volume method is applied for both the water and the refrigerant sides. The heat transfer is considered between each pair of the cells. The mass and energy balances are set for each cell (in both refrigerant and water side).

The expansion valve model in [196] is adopted, which assumes a quadratic relation between the mass flow rate and the pressure difference across the valve. The effective flow area is set as an external input, which can be used to regulate the evaporator superheat for the chiller. No transient mass storage is assumed for the expansion valve

model, and an isenthalpic throttling process is considered. The geometry and parameter settings are adjusted to fit the entire combination with the cooling tower cycle; the detailed description will be shown in the Appendix C.

Chapter 4. ESC Based Optimization Control of Chilled Water System

Energy efficient operation of chilled-water systems is important for the energy saving of commercial buildings. This chapter presents an ESC scheme for energy efficient operation of the chilled-water system. The Modelica based dynamic simulation model developed in Chapter 3 is used for demonstrating the effectiveness of the proposed control strategy. The ESC scheme takes the total power consumption of chiller compressor and tower fan as feedback, and uses the fan speed setting as control input. The inner-loop controllers for the chiller operation include two PI control loops for regulating the evaporator superheat and the chilled water temperature. All the controllers and chiller-tower plant model are integrated into simulation platform. Simulation was conducted for three scenarios: fixed condition, change in evaporator inlet water temperature, and change in ambient air condition. The simulation results demonstrated the effectiveness of the proposed ESC strategy, and the potential for energy saving is also evaluated. Also investigated is the ESC windup issue caused by the limitation of the fan's maximum operation speed. A back-calculation anti-windup ESC scheme is applied and its effectiveness is validated by simulation results.

The proposed control framework for chilled water system is presented in Section 4.1. In Section 4.2, the ESC design guideline is reviewed and the ESC controller is designed based on the estimated system input dynamics, the modified anti-windup ESC scheme is also discussed. The simulation case studies are shown in Section 4.3, and the summary will be provided in Section 4.4.

4.1. Proposed Controls in Chilled Water System

As mentioned earlier in Chapter 1, in addition to the power consumption, two critical variables must be well controlled: the evaporator superheat and the chiller leaving water temperature. First, the superheat control is important for chiller operation. In the evaporator, liquid refrigerant has a much higher heat transfer coefficient than the vaporized refrigerant. The two-phase flow is desirable for enhancing the cooling capacity of the system. Meanwhile, if not all the liquid refrigerant gets vaporized before entering the compressor, the remained liquid will damage the compressor. So the *evaporator superheat* must be maintained to ensure both safety and efficiency [9, 24]. Notice that varying the evaporator superheat can lead to different cooling efficiency, while this study does not pursue the optimal superheat setpoint. Also, as required by the AHU operation, the chilled water temperature is expected to be maintained around a setpoint [9].

To satisfy these two needs, two inner-loop PI controllers are implemented to regulate the evaporator superheat and the chiller leaving water temperature by tuning the expansion valve's effective flow area (A_{TXV}) and the screw compressor slide-valve opening (s_{comp}), respectively. The schematic of the chiller-tower system with both the ESC controller and the inner-loop PI controllers is shown in Fig. 4.1. The setpoints for the evaporator superheat and the chilled water temperature are 5°C and 7°C, respectively [25].

For simplicity, the cooling tower inlet water mass flow rate is assumed unchanged, so the variable part of the entire system power consumption consists of the power consumption of the screw compressor and that of the cooling tower fan. The dither based ESC framework is applied to the chiller-tower cycle to minimize the total power

consumption of the screw chiller and cooling tower fan by tuning the tower fan speed, as shown in Fig. 4.1.

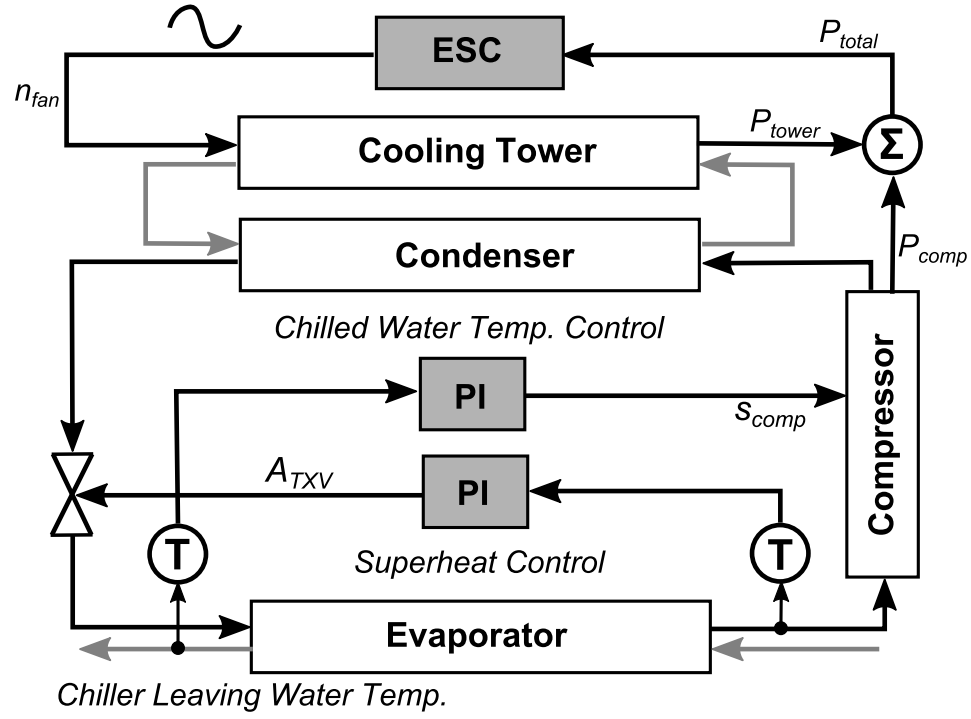


Figure 4.1: Schematic for the ESC control system for chiller-tower plant

4.2. Overview of Design Guidelines for Dither ESC

As shown in Section 2.1.1, a typical design of a dither based extremum seeking control strategy needs to determine several framework components [75]:

- Dither signal $d_1(t) = a \sin(\omega_d t)$ and demodulation signal $d_2(t) = \sin(\omega_d t + \alpha)$, including dither frequency, dither amplitude and the phase difference between the dither and demodulation signals.
- High-pass and the low-pass filters
- Compensator

The dither frequency should be chosen well within the bandwidth of the input dynamics. The input dynamics can be estimated by applying certain appropriate inputs depending on the system order, e.g. step, ramp or pseudo random binary sequence (PRBS) inputs. After the transfer function $F_I(s)$ is estimated, a proper dither frequency ω_d can be selected. Empirically, ω_d could be selected in the range of $1/3$ and $1/10$ of the cut-off frequency ω_c of the system input dynamics.

The dither amplitude a needs to be selected with two considerations. A small dither amplitude can reduce the output oscillation at steady state, while it cannot be too small, otherwise the dithered output would be buried in the measurement noise at the dither frequency. For the purpose for extracting the gradient information, the high pass filter and low pass filter need to be designed so that ω_d resides in the pass-band of $F_{HP}(s)$ and the stop-band of $F_{LP}(s)$. The phase angle α is selected to compensate for the phase shift due to the plant dynamics and the high pass filter $F_{HP}(s)$. If the output dynamics is negligible, the following relation should be satisfied:

$$\theta = \angle F_I(j\omega) + \angle F_{HP}(j\omega) + \alpha \in \left(-\frac{\pi}{2}, \frac{\pi}{2}\right) \quad (4.1)$$

A value close to 0 is recommended for θ .

For the simplest ESC design, the compensator $K(s)$ can be chosen as a constant. Krstić showed that the transient performance can be improved by selecting proportional-derivative (PD) compensator for $K(s)$ [69].

The ESC method achieves the convergence to the system optimality based on an integral action on the gradient proportional signal extracted by the pair of dither-

demodulation signals, high-pass and low-pass filters. For practical systems, all actuators have physical limitations, which saturate the control actions at certain point. For example, in this study, the tower fan speed setting has both upper and lower bounds. Therefore integral windup could be a problem for ESC system operations. To avoid the integral windup, a number of anti-windup techniques have been proposed in the past for PI or PID controllers [203-207]. Li and Seem [156] proposed a back calculation based anti-windup strategy for ESC systems, as shown in Fig. 4.2, which is compatible with the simple nature of extremum seeking control. Recently, Li *et al.* [153] applied this scheme to the ESC control of the air-side economizer for dealing with the damper saturation situations. In this study, this scheme is again applied to deal with the possible integral windup due to the fan speed saturation.

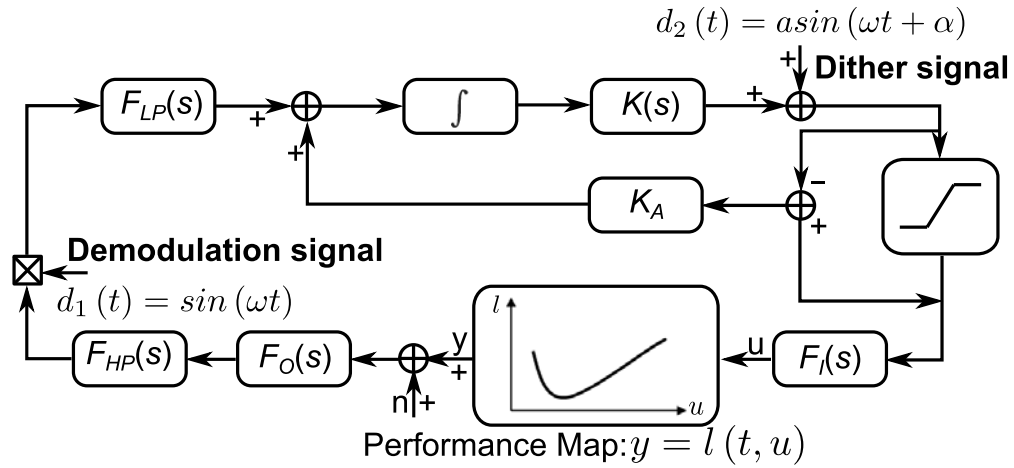


Figure 4.2: Block diagram of modified anti-windup ESC

4.3. Simulation Study

4.3.1. Dither ESC Design

The ESC tower fan control strategy is designed based on the idea described in previous sections for the plant modeled in Chapter 2. First, the input dynamics from the tower fan

speed to the total power consumption is estimated based on the system responses of several step changes at both sides of the optimum. Scenarios for both increasing and decreasing the fan speed are tested for each fan speed selected. Figure 4.3 compares the several scaled step responses of the simulation model and the fitted second order approximation.

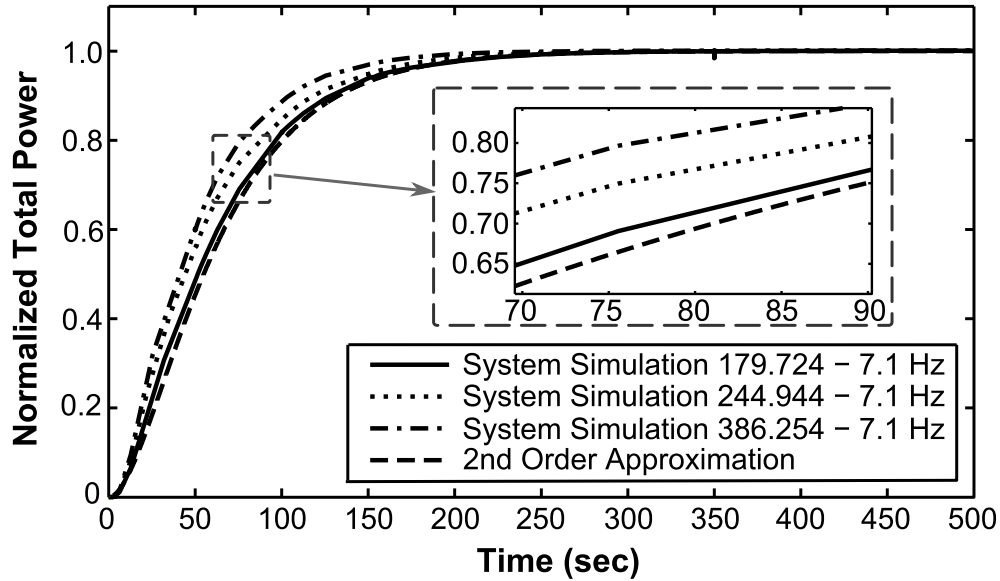


Fig. 4.3: Comparison of full simulation model and the 2nd-order estimate

The input dynamics is estimated based on the slowest step response to achieve better robustness in further designed controller:

$$\hat{F}_l(s) = \frac{0.0316^2}{s^2 + 2 \cdot 1.06 \cdot 0.0316s + 0.0316^2} \quad (4.2)$$

where the undamped natural frequency $\omega_n = 0.0316$ rad/sec is obtained by estimating the 10% to 90% rise time from the tested step responses. The damping ratio ζ is estimated by manually tuning around the average value obtained from the regression analysis. The result shows good fitting even with some very different inputs. The cutoff frequency of

the input dynamics ω_c is about 0.0187 rad/sec. The dither frequency ω_d is thus selected at 0.0043 rad/sec. Then, $F_{HP}(s)$ and $F_{LP}(s)$ are chosen as

$$F_{HP}(s) = \frac{s^2}{s^2 + 2 \cdot 0.65 \cdot 0.0025 + 0.0025^2} \quad (4.3)$$

$$F_{LP}(s) = \frac{0.003^2}{s^2 + 2 \cdot 0.65 \cdot 0.003 + 0.003^2} \quad (4.4)$$

The dither amplitude is selected as 7.1 Hz for the VSD input. The dither phase angle is selected as -0.604 radian to ensure $\theta \approx 0$ under the estimated input dynamics of Eq. (4.2).

4.3.2. Case Study

The designed ESC is then simulated on the dynamic simulation model of the chiller-tower system that was described in Chapter 3. The ESC performance is first tested with a fixed operating condition. The relative humidity and temperature for the cooling-tower inlet air flow are set as 20% and 310K, respectively. The temperature and mass flow rate of the evaporator inlet water are set as 285.15K and 13.2kg/s, respectively. In the following cases, all the ESC controller gains were selected as 0.031. For the anti-windup ESC case, the back calculation gain was selected as 0.12.

Case 1: Fixed Operation Condition:

Figure 4.4 shows the static map from cooling tower fan speed to the power consumptions of the chiller compressor and the tower fan, with the optimal fan speed and power consumption estimated as 250.351 Hz and 231174 W, respectively.

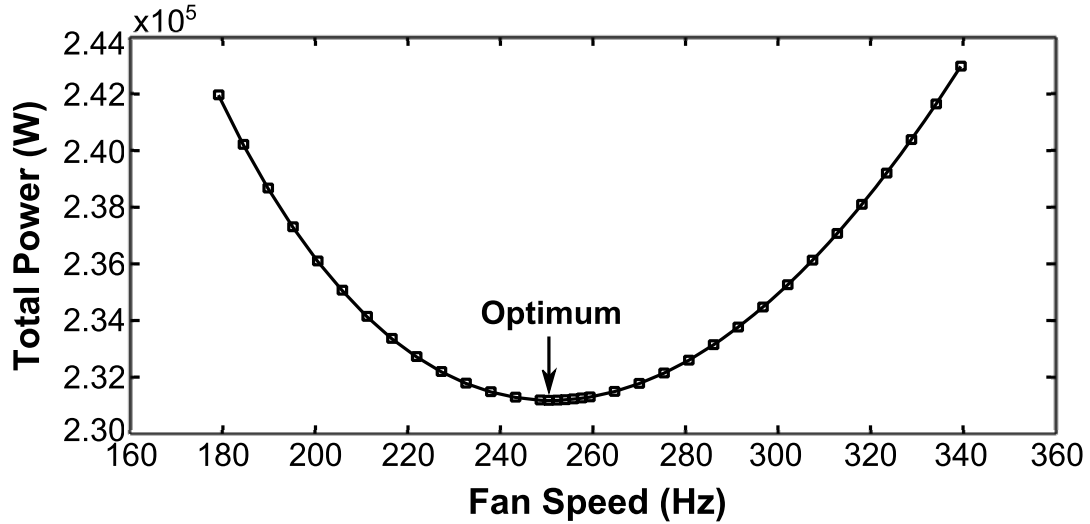


Figure 4.4: Static map from cooling tower fan speed to total power consumption

The simulation first starts at a fixed fan speed of 200 Hz, and the ESC controller is turned on at $t = 5000$ sec. As shown in Fig. 4.5, the ESC settled with the average steady-state fan speed of 256.302Hz and the total power of 232018 W, respectively, with the 1% settling time of about 11720 sec. Compared to the estimated optimum in the static map, the steady-state error is about 2.37% and 0.37% for the fan speed and the total power, respectively. Notice that Fig. 4.5 shows that the estimated optimal fan speed falls within the range of the input dither. The evaporator superheat and the corresponding valve effective flow area are shown in Fig. 4.6, and Figure 4.7 shows the profiles of the chilled-water temperature and the compressor slide-valve opening. It reveals that both evaporator superheat and chilled-water temperature follow the given references well and the corresponding valve effective flow area and compressor slide-valve opening adjust smoothly to fit the requirements.

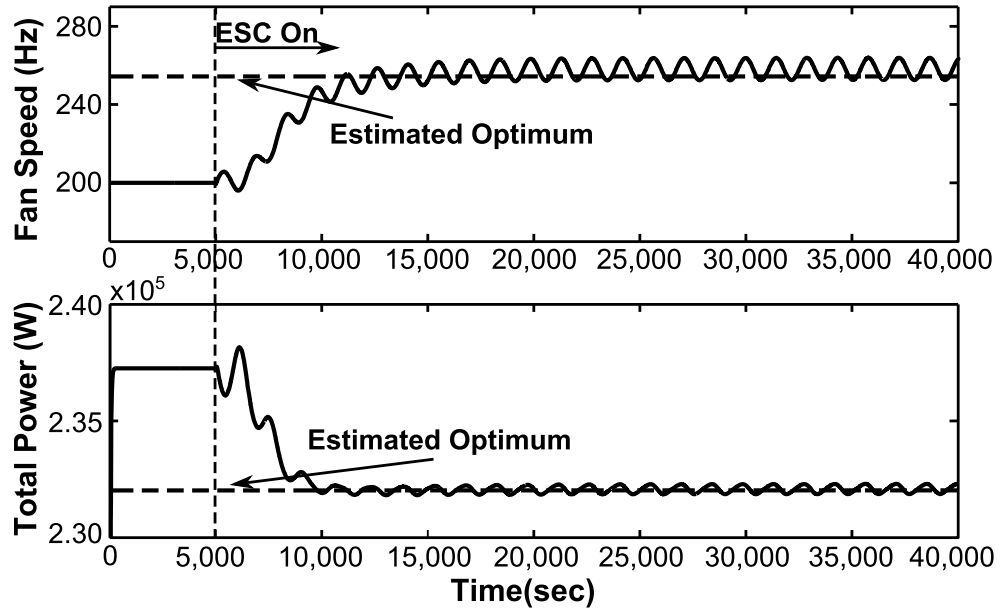


Figure 4.5: ESC on chiller tower system with fixed operation condition, fan speed and power consumption

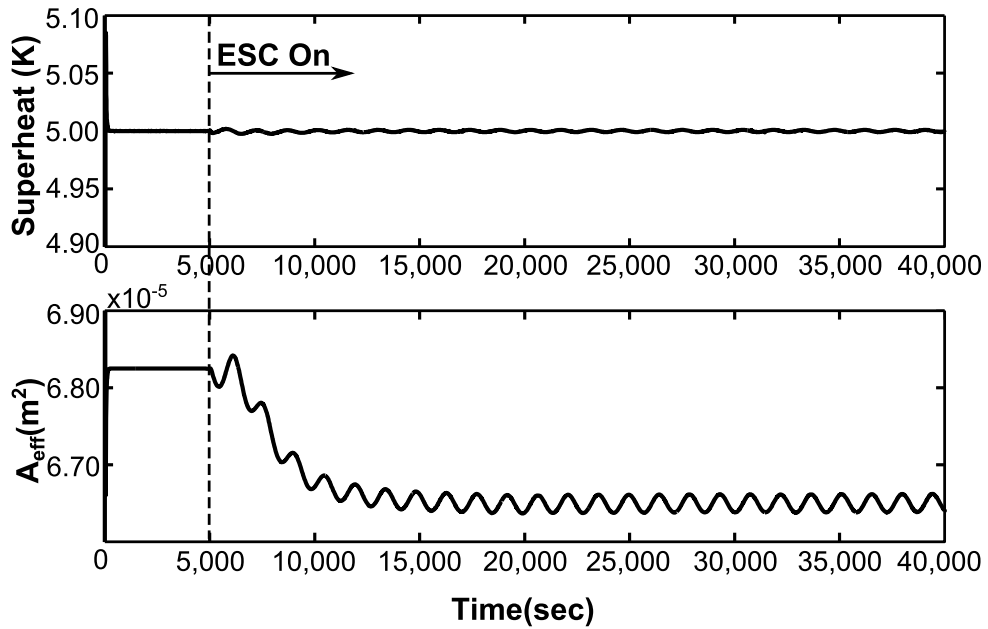


Figure 4.6: Superheat control results for ESC with fixed operation condition

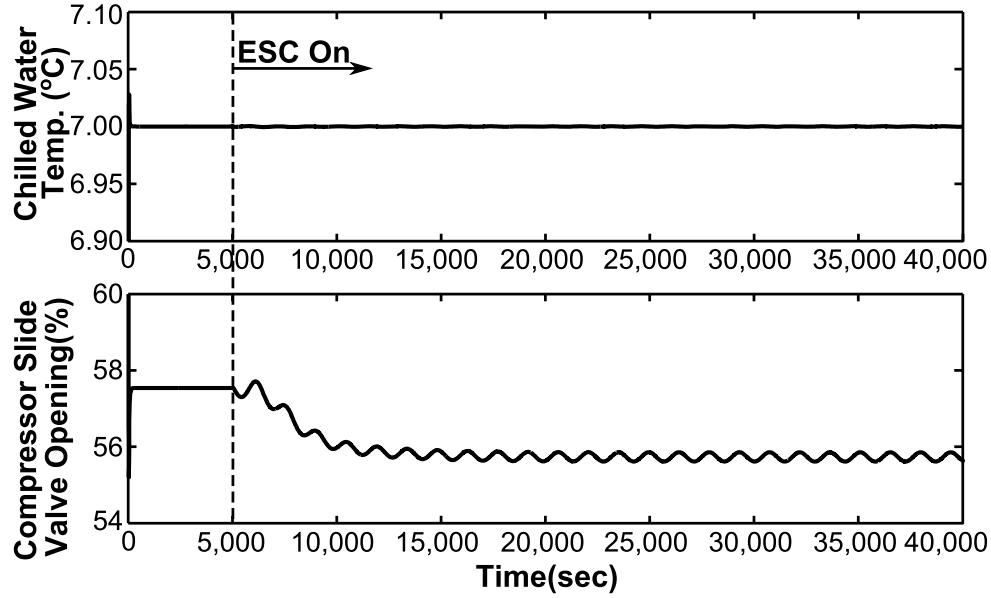


Figure 4.7: Chilled water temperature control for ESC with fixed operation condition

Case 2: Decrease of Evaporator Inlet Water Temperature

The ESC controller is then tested with a ramp change in the evaporator inlet water temperature T_{EW} (e.g. due to a load reduction) from 12°C to 10°C in 3000 second starting from $t = 60000$ second. The static maps of the two conditions are shown in Fig. 4.8, with the optimal point being (250.351 Hz, 231174 W) for the first condition, and (179.345 Hz, 86527.3 W) for the second condition, respectively. The first condition is the same as the previous case of fixed condition.

As shown in Fig. 4.9, when the ESC settled to steady state, the average fan speed and power consumption are about 182.714 Hz and 86538.4 W, respectively, differing from the estimated optimum by only 1.88% and 0.013%, respectively. The 1% settling time of power output is about 13735 second. Also, as marked in Fig. 4.8, if the fan speed remained unchanged during the ramp change, the system would operate at point *A*, which consumes 91759.1 W. Therefore, ESC adapts the system operation with power saving of 5231.8W (5.7%). The evaporator superheat and the corresponding valve effective flow

area are shown in Fig. 4.10. Figure 4.11 shows the profiles of the chilled-water temperature and the compressor slide-valve opening.

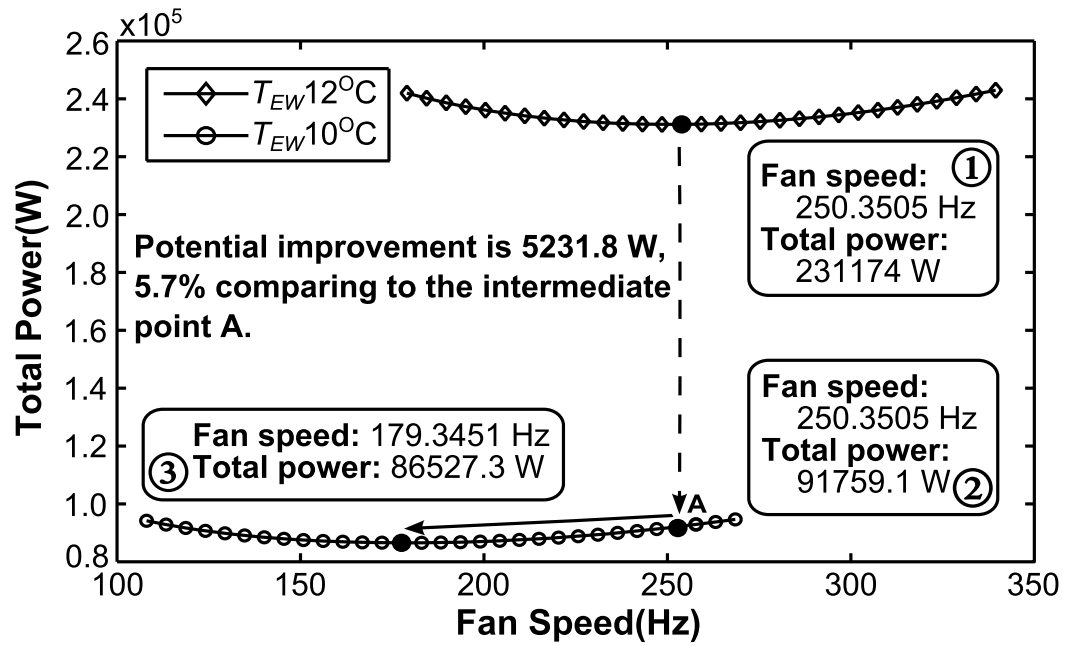


Figure 4.8: Static maps for T_{EW} decreased from 12°C to 10°C

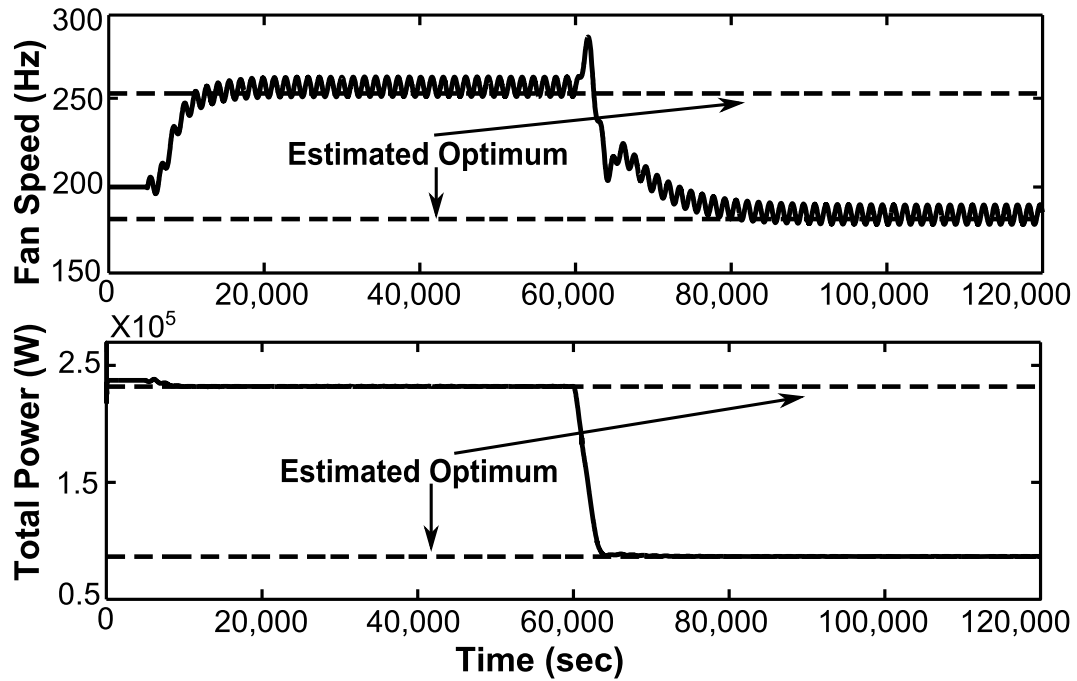


Figure 4.9: ESC simulation results for T_{EW} decreased from 12°C to 10°C

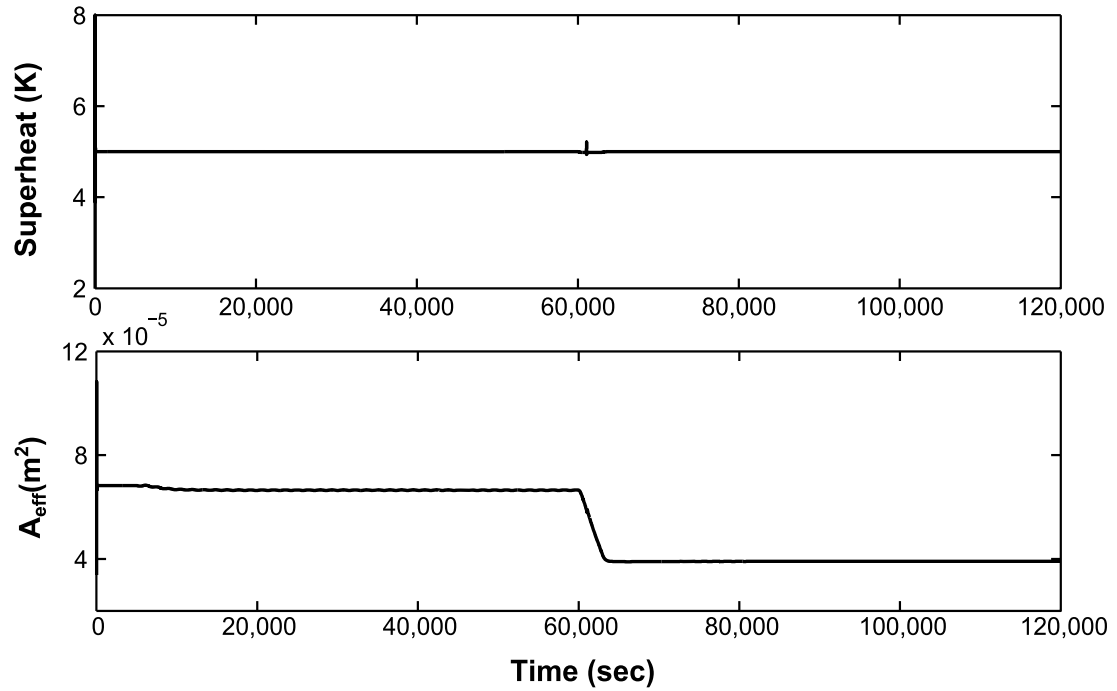


Figure 4.10: Superheat profile for ESC tower fan control when T_{EW} drops from 12°C to 10°C

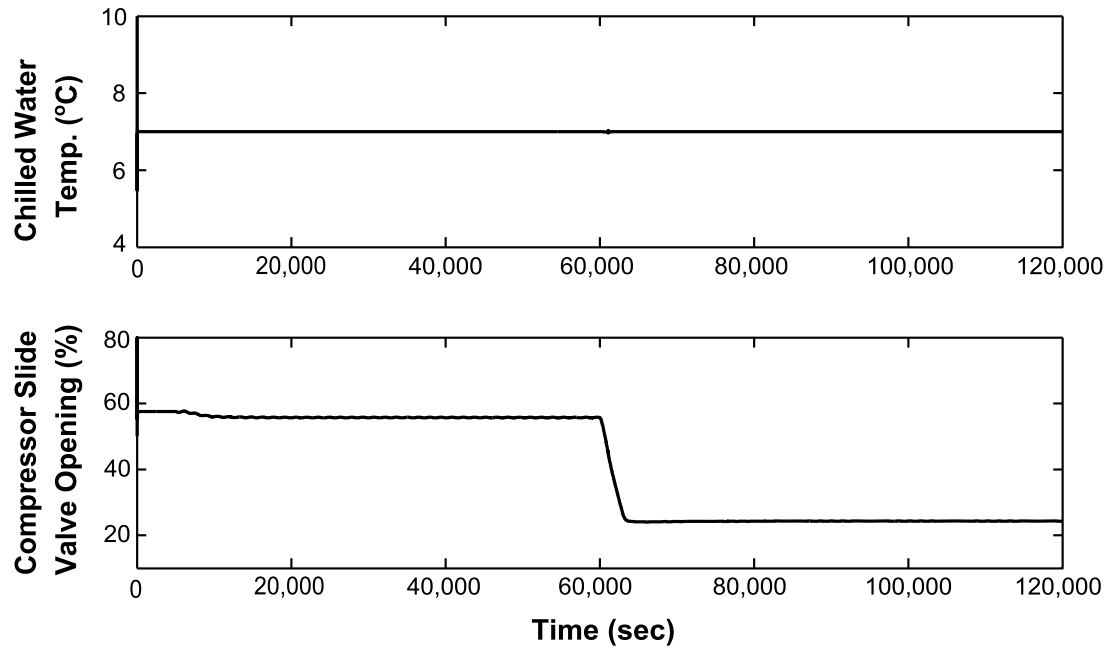


Figure 4.11: Chilled water temperature profile for ESC tower fan control when T_{EW} drops from 12°C to 10°C

Case 3: Change of Ambient-Air Temperature and Relative Humidity:

Then the ESC controller is tested with the change of ambient condition. As shown in Fig. 4.12, the cooling tower inlet air temperature drops from 37°C to 35°C, and the relative humidity increases from 20% to 80%. The ramp starts at $t = 60000$ second, and lasts for 3000 seconds. The static maps of the two conditions are shown in Fig. 4.13. The optimal point of the second condition is at 275.089 Hz and 357564 W.

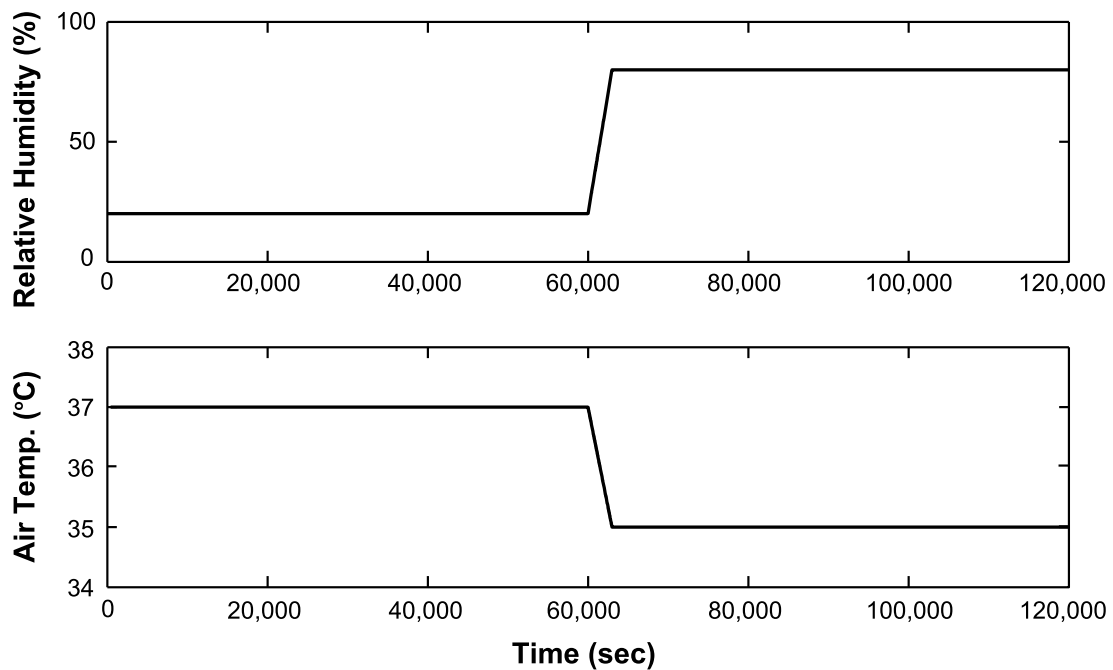


Figure 4.12: Change of ambient-air condition: the air temperature decreases from 37°C to 35°C, and the relative humidity increases from 20% to 80%

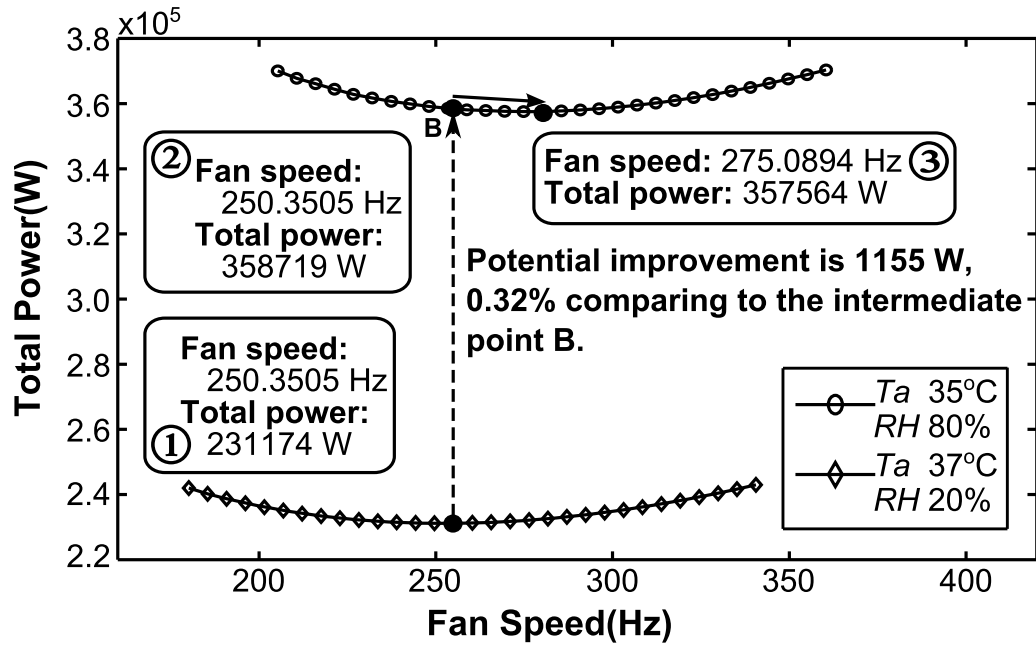


Figure 4.13: Static power map for two ambient air conditions: temperature and relative humidity of 37°C and 20% versus 35°C and 80%

Figure 4.14 shows that the ESC searched average steady-state fan speed and total power consumption of the second condition are about 279.915 Hz and 357721 W, respectively. The differences are only 1.75% and 0.044%, respectively, compared to the modeled optimal values. Again, the estimated optimal fan speed from the static map falls within the range of input dither. The power output settles within $\pm 1\%$ of the steady state values at about 4823 sec. If the fan speed remained unchanged during the ramp change, the operation would be at point B in Fig. 4.13, which indicates that the adaptation of ESC achieves an 0.32% (1155W) power saving. The evaporator superheat and the corresponding valve effective flow area are shown in Fig. 4.15. The controlled chilled water temperature and corresponding compressor slide-valve opening are shown in Fig. 4.16. These results indicate satisfactory inner-loop control performance and reasonable control input profiles.

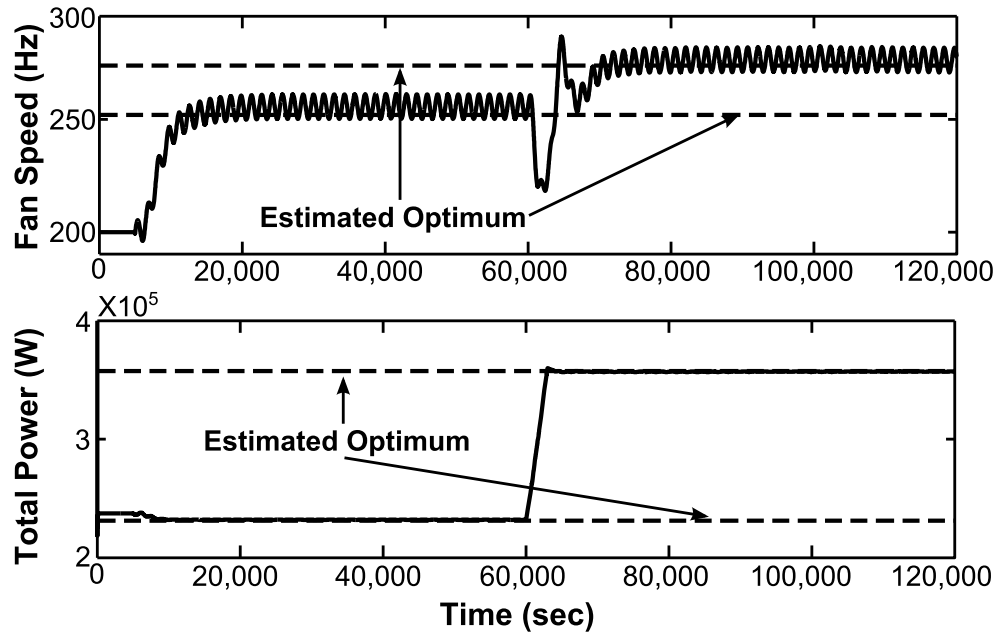


Figure 4.14: ESC simulation results when the ambient air condition changed from 37°C and 20% RH to 35°C and 80% RH

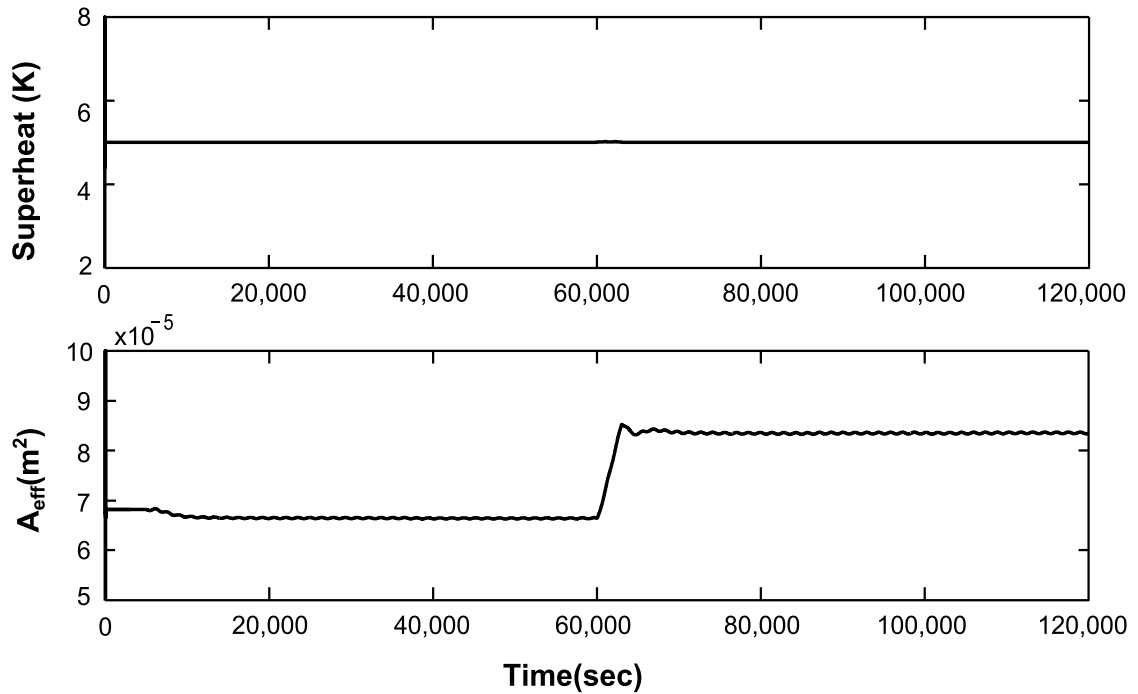


Figure 4.15: Superheat profile under ESC tower fan control when the ambient air condition changed from 37°C and 20% RH to 35°C and 80% RH

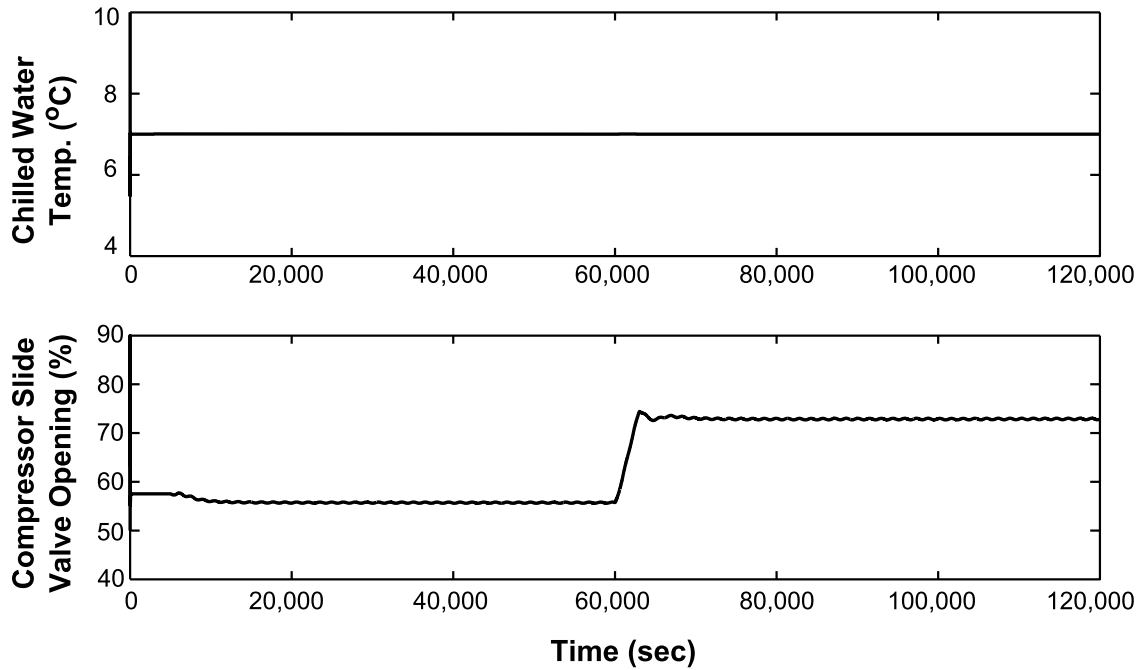


Figure 4.16: Chiller leaving water temperature profile under ESC tower fan control when the ambient air condition changed from 37°C and 20% RH to 35°C and 80% RH

Case 4: ESC Integral Windup and Anti-windup ESC

Finally, the effectiveness of the back-calculation anti-windup ESC is verified by simulation. The allowed maximum fan speed is assumed as 290 Hz. The plant is assumed to experience a change in the evaporator inlet water temperature change (load change). No ambient environment change is applied, and all other settings are same as the case of fixed operation condition. As shown in Fig. 4.17, the evaporator inlet water temperature is initially set at 12 °C. At 60000 sec, a ramp change is introduced to T_{EW} , bringing an increase to 13 °C in 5000 seconds. Then at 125000 sec, another 5000 sec ramp change brings T_{EW} back to 12 °C.

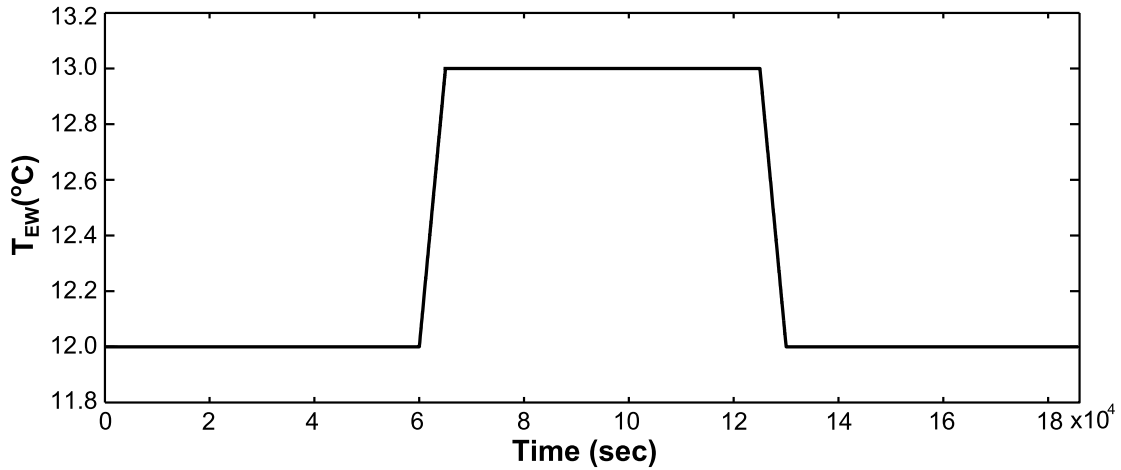


Figure 4.17: Fast ramp changes in evaporator inlet water temperature for simulation case to demonstrate integral windup and anti-windup ESC test

Figure 4.18 shows that the integral windup problem of the standard ESC with actuation saturation. In the upper subplot, the optimum is successfully achieved by the ESC search before the first ramp change. From 60000 sec on, under the change of system condition, the fan speed is saturated at 290 Hz. When the second ramp change is applied, the ESC fails to search for the new optimum due to the integral windup. The fan speed is stuck at the saturation limit (i.e. 290 Hz). The lower subplot of Fig. 4.18 shows the difference between the total power consumptions for ESC search and the actual optimum based on the static map.

Then the back-calculation based anti-windup ESC scheme is applied to the same case above. As shown in Fig. 4.19, the antiwindup ESC responds to the system condition change when the second ramp change of T_{EW} starts and converges to the new optimum successfully. The simulation results show that the modified antiwindup ESC scheme could effectively solve the potential integral windup problem caused by system actuator saturation.

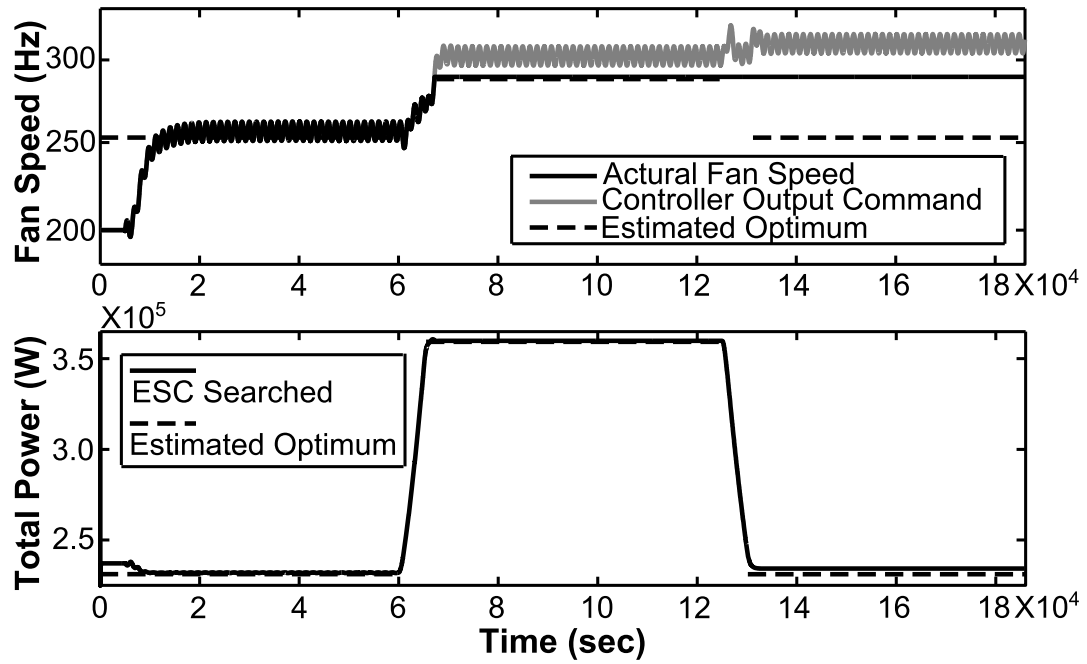


Figure 4.18: ESC integral windup for simulation case 4 with actuator saturation

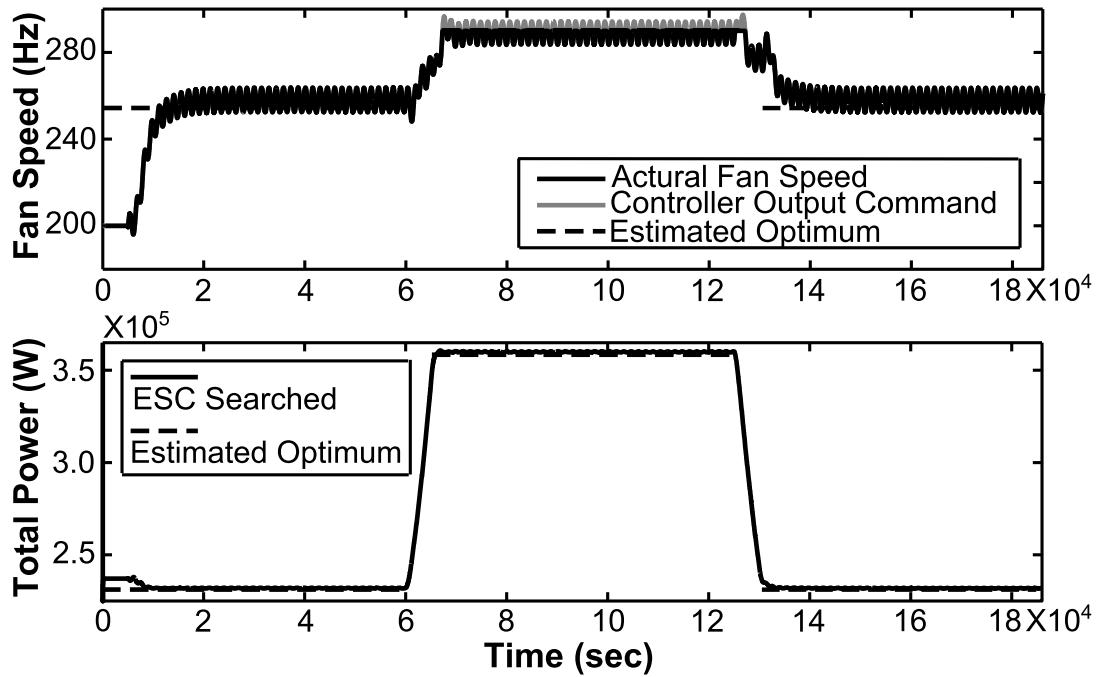


Figure 4.19: Simulation results of case 4 with anti-windup ESC

In summary, the proposed ESC scheme is validated with simulations on the detailed simulation model of the chiller-tower plant. It is noteworthy that the extremum seeking

capability demonstrated does not rely on the knowledge of the plant models. Compared to the model based methods in the aforementioned literatures, this scheme does not rely on unreliable sensors or accurate process model, which makes the method much more robust to sensor failure and plant variation due to unknown environment changes and the hard-to-estimate system degradation. Also, the back-calculation based anti-windup ESC scheme can also handle the problem comes from actuator saturation.

Chapter 5. Maximum Power Point Tracking for Photovoltaic System Using Adaptive Extremum Seeking Control

In order to maximize the PV power generation efficiency, it is crucial to locate the MPP in real time under realistic illumination conditions. The current-voltage (I - V) characteristics of PV device are nonlinear and the MPP may vary with the intrinsic and environmental conditions. The MPPT control is designed to seek the MPP regardless of the device and ambient changes. In this chapter, the AESC technique is applied to the MPPT problem for single-string photovoltaic system.

The PV cell model from [176] and a simple DC-DC converter are utilized to build up the simulation model. For the AESC controller design, the state-space dynamic equations are set up to represent the system structure with the nonlinear time-varying $I(V)$ relation with the control input being the duty ratio of the pulse-width modulator (PWM) of the DC-DC buck converter. A Gaussian kernel based RBFNN is adopted to approximate the unknown $I(V)$ characteristics. A projection algorithm based parameter learning law is applied to guarantee the convergence of the RBFNN parameters to fit the unknown nonlinear relationship between states, and a Lyapunov based inverse optimal design technique is used to ensure the convergence to the optimum [43].

The remainder of this chapter is structured as follows. Section 5.1 presents the PV simulation model including the DC-DC buck converter. Section 5.2 describes the control-oriented approximated analytical modeling of PV system dynamics, and then presents the AESC design and the parameter estimation algorithm following the design procedure

provided in [43]. Simulation results are given in Section 5.3 with performance comparison to those of the dither ESC.

5.1. Photovoltaic System Model

There are two kinds of PV models used in this study for different purposes. First, a detailed physics based model is built as the virtual plant for simulation. Then a state-space model of PV-buck system is obtained based on an approximate PV model, which is intended for AESC controller design. The detailed physics based model is presented in the remainder of this section, while the state-space model will be presented in Section 5.2.

For detailed PV modeling, the equivalent circuit of PV system in Fig. 5.1 [176] is adopted. Its current-voltage relation can be modeled as [176, 208]:

$$I = I_{PV} - I_0 \left[\exp \left(\frac{V + R_s I}{V_t a_{if}} \right) - 1 \right] - \frac{V + R_s I}{R_p} \quad (5.1)$$

where V and I are the output voltage and current, respectively. I_{PV} is the light generated current that is proportional to the irradiance and I_0 is the reverse saturation (or leakage) current of the diode. $V_t = N_s k T / q$ is the thermal voltage of the array with N_s cells connected in series. q is the electron charge with the value of $1.60217646 \times 10^{-19}$ C, $k = 1.3806503 \times 10^{-23}$ J/K is the Boltzmann constant, a_{if} is the ideality factor, and N_p is the number of parallel connections of cells. R_s and R_p are the equivalent series and shunt resistances of the array, respectively.

I_{PV} is also to be influenced by the temperature [176]:

$$I_{PV} = (I_{PV,n} + K_I \Delta T) \frac{G}{G_n} \quad (5.2)$$

where $I_{PV,n}$ is the light generated current at the nominal condition (25°C and 1000W/m²), and $\Delta T = T - T_n$. T and T_n are the actual and nominal temperatures, respectively. G and G_n are the actual and nominal irradiance rate on the device surface, respectively. K_I is the short-circuit temperature coefficient. The diode saturation current I_0 is given by [176]

$$I_0 = I_{0,n} \left(\frac{T_n}{T} \right)^3 \exp \left[\frac{qE_g}{ak} \left(\frac{1}{T_n} - \frac{1}{T} \right) \right] \quad (5.3)$$

where E_g is the bandgap energy of the semiconductor, and $I_{0,n}$ is the nominal saturation current.

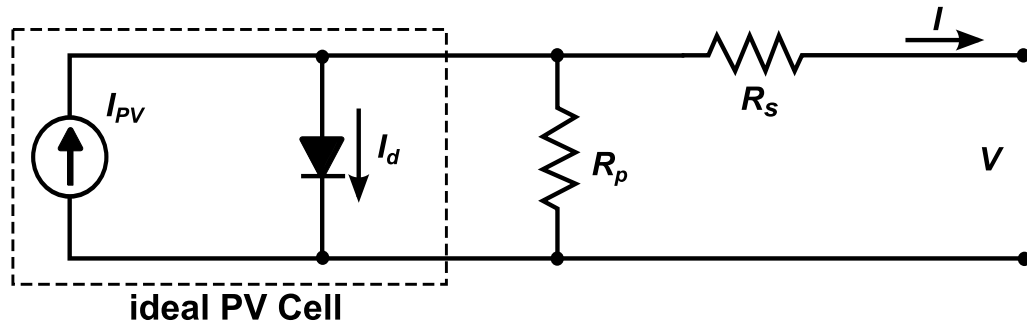


Figure 5.1: PV cell equivalent circuit

The simulation study in this paper adopts a PV array with 15×2 modules, and each module has 54 cells in series [41]. The I - V and P - V characteristics at 25 °C under different irradiance rates are shown in Fig. 1.6. The generated current is shown to increase with the irradiance level. Similarly, the I - V and P - V characteristics under nominal irradiance rate 1000W/m² at different temperatures are shown in Fig. 1.7. The

power output decreases with the device temperature. Notice that the MPP voltage varies for all the cases in Figures 1.6 and 1.7, while temperature change leads to more pronounced changes of the MPP voltage. This suggests that MPPT can yield more benefit under temperature change.

The PV output can be connected to DC load (e.g. battery or DC motor) or AC load (e.g. grid or AC motor). For either case, DC-DC converter is normally needed for the conversion between different voltage levels. As this study aims to evaluate an MPPT control algorithm, a simple scenario of DC resistive load is adopted, as shown in Fig. 5.2. The duty ratio D of the pulse-width modulator (PWM) is used to adjust the input voltage of the DC-DC converter (also the output of the PV array) to achieve MPPT. The DC-DC converter, such as buck, boost and buck-boost types, is chosen in a case-dependent fashion. In this study, a buck converter is used in order to step down the voltage, also shown in Fig. 5.2. The analysis in Section 5.2 can be easily applied to the cases of using other types of DC-DC converters. In this circuit, the inductance is set as $L = 5 \text{ mH}$, the capacitor as $C = 1 \text{ mF}$, and the resistive load as $R = 10 \Omega$.

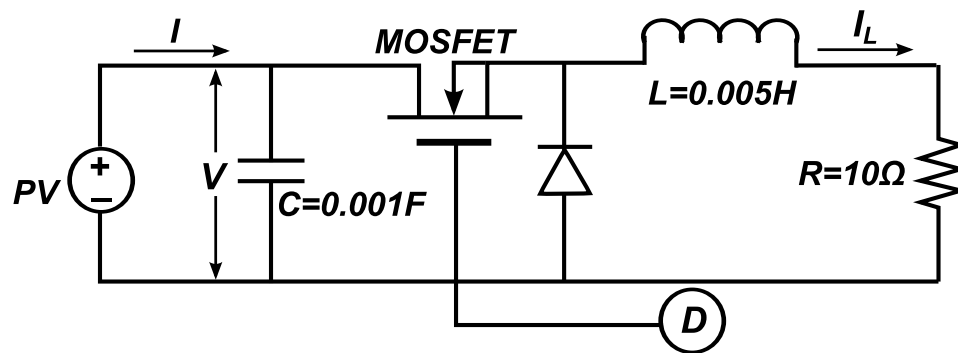


Figure 5.2: PV array with front-end buck converter

5.2. AESC Based MPPT Design for PV Systems

5.2.1. Analytical Modeling of PV Dynamics

For control oriented modeling of PV system, Fig. 5.2 can be described by two sets of differential equations based on ON/OFF position of the MOSFET switch [167]. The state equations with switch *on* (State 1) is given as:

$$\frac{dV}{dt} = \frac{i(V)}{C} - \frac{i_L}{C} \quad (5.4)$$

$$\frac{di_L}{dt} = \frac{V}{L} - \frac{i_L}{R} \quad (5.5)$$

where $i(V)$ represents the nonlinear mapping between the output current and the terminal voltage of the PV array, i_L is the inductor current. If the switch is turned *off* (State 0), the state equations become:

$$\frac{dV}{dt} = \frac{i(V)}{C} \quad (5.6)$$

$$\frac{di_L}{dt} = -\frac{i_L R}{L} \quad (5.7)$$

To obtain a unified system dynamics, Eqs. (5.4) to (5.7) are combined into a pair of state equations via a typical averaging method for PWM based switching circuits [209]:

$$\frac{dV}{dt} = \frac{i(V)}{C} - \frac{i_L}{C} D \quad (5.8)$$

$$\frac{di_L}{dt} = -\frac{i_L R}{L} + \frac{V}{L} D \quad (5.9)$$

where duty ratio D is defined as the portion of State 1 within a period of PWM operation. To ensure a better approximation of the nonlinear relation $i(V)$ in the

parameter updating process, the ranges of the PV output voltage (V) and the inductor current (i_L) are normalized (divided by 100 Volt and 10 Amp, respectively, for the simulation case) into the following state and output equations:

$$\frac{dx}{dt} = -\frac{R}{L}x + \frac{k_1}{L}su \quad (5.10)$$

$$\frac{ds}{dt} = \frac{k_2}{k_1 C} \mu(s) - \frac{1}{k_1 C} xu \quad (5.11)$$

$$y = k_1 k_2 \mu(s) s \quad (5.12)$$

where $x = i_L \in [0, +\infty)$ is the inductance current, $s = V / k_1 \in [0, V_M / k_1]$ is a scaled PV terminal voltage with $k_1 = 100$, V_M is the maximum voltage of the PV system. $\mu = i(V) / k_2 \in [0, I_M / k_2]$ with $k_2 = 10$, I_M is the maximum current, $y(=P) = iV$ is the power output of the PV array, and $u = D \in [0, 1]$ is the control input to be designed for MPPT control. The objective of AESC is to search for the maximum power output y .

5.2.2. Design of AESC Based PV MPPT

The steady-state PV power output can be expressed by

$$y_e = k_1 k_2 \mu(s_e) s_e \quad (5.13)$$

where subscript e stands for equilibrium or steady-state value. The unknown nonlinearity $\mu(s)$ can be approximated with certain kernel functions. In this dissertation study, the RBFNN is adopted [43, 88]. The RBFNN can uniformly approximate the continuous nonlinearity $\mu(s)$ on a compact set [88], i.e.

$$\mu[s(t)] = W^{*T} S[s(t)] + \mu_l(t) \quad (5.14)$$

with $\mu_l(t)$ as the approximation error. The basis function vector is given by

$$S[s(t)] = [s_1[s(t)], s_2[s(t)], \dots, s_l[s(t)]]^T \quad (5.15)$$

The ideal weight W^* is obtained by

$$W^* := \arg \min_{W \in \Omega_w} \left\{ \sup |W^T S(s) - \mu(s)| \right\} \quad (5.16)$$

where $\Omega_w = \{W \mid \|W\| \leq w_m\}$. w_m is a positive constant representing the upper bound of the weights, which is to be chosen at the design stage. Substituting Eq. (5.14) into Eq. (5.13) yields

$$y_e = k_1 k_2 (W^{*T} S(s_e) + \mu_l(t)) s_e \quad (5.17)$$

In (5.13), $\mu(s)$ represents the value of $i(V)/k_2$, which is bounded and in the range of $[0, I_M/k_2]$. The term of $W^{*T} S(s)$ is bounded by construction. So we can have the assumption that the radial basis function neural network approximation error is bounded, i.e. $|\mu_l(t)| \leq \bar{\mu}_l$ over a compact set with constant $\bar{\mu}_l > 0$.

Taking the first- and second-order derivatives of Eq. (5.17) yields

$$\frac{\partial y_e}{\partial s_e} = k_1 k_2 W^{*T} [dS(s_e) s_e + S(s_e)] + k_1 k_2 \mu_l(t) \quad (5.18)$$

$$\frac{\partial^2 y_e}{\partial s_e^2} = k_1 k_2 W^{*T} [d^2 S(s_e) s_e + 2dS(s_e)] \quad (5.19)$$

where $dS = \partial S / \partial s$ and $d^2 S = \partial^2 S / \partial s^2$. The basis function vector $S(s)$ is given by

$$S(s) = [b_1(s) \quad b_2(s) \quad \dots \quad b_l(s)] \quad (5.20)$$

and Gaussian kernels are adopted, i.e.

$$b_i(s) = \exp \left[\frac{-(s - \varphi_i)^T (s - \varphi_i)}{\sigma_i^2} \right], \quad i = 1, 2, \dots, l \quad (5.21)$$

where φ_i and σ_i are the center and the width of the Gaussian function, respectively. The derivatives of the basis function in (5.21) are

$$\frac{\partial S_i}{\partial s} = -2 \frac{(s - \varphi_i)}{\sigma_i^2} \exp \left[-\frac{(s - \varphi_i)^2}{\sigma_i^2} \right] \quad (5.22)$$

$$\frac{\partial^2 S_i}{\partial s^2} = \left(-2 \frac{1}{\sigma^2} + 4 \frac{(s - \varphi_i)^2}{\sigma^4} \right) \exp \left[-\frac{(s - \varphi_i)^2}{\sigma_i^2} \right] \quad (5.23)$$

The objective of the PV MPPT problem is to design a controller and parameter estimation law such that the maximum steady-state power output y^* can be found, and the ideal weight W^* can be obtained to achieve the ideal approximation. The AESC design in this study mainly follows the procedure given in [43].

With the substitution of Eq. (5.14), Eqs. (5.10) and (5.11) become

$$\dot{x} = -\frac{R}{L}x + \frac{k_1}{L}su \quad (5.24)$$

$$\dot{s} = \frac{k_2}{k_1 C} \left[W^{*T} S(s) + \mu_l(t) \right] - \frac{1}{k_1 C} xu \quad (5.25)$$

Let \hat{W} denotes the estimate of the true weights W^* . Let \hat{s} and \hat{x} denote the predictions of s and x , respectively. The dynamics of these predicted states can be derived as

$$\dot{\hat{x}} = -\frac{R}{L}\hat{x} + \frac{k_1}{L}su + k_x e_x + c_1(t)^T \hat{W} \quad (5.26)$$

$$\dot{\hat{s}} = \frac{k_2}{k_1 C} \hat{W}^T S - \frac{1}{k_1 C} xu + k_s e_s + c_2(t)^T \hat{W} \quad (5.27)$$

where k_x , k_s , $c_1(t)$ and $c_2(t)$ are parameters and design variables to be designed.

Subtracting Eq. (5.26) and (5.27) from Eq. (5.24) and (5.25) yields the dynamics for the state estimation errors $e_x = x - \hat{x}$ and $e_s = s - \hat{s}$ as

$$\dot{e}_x = -k_x e_x - c_1(t)^T \dot{\hat{W}} \quad (5.28)$$

$$\dot{e}_s = \frac{k_2}{k_1 C} \tilde{W}^T S + \frac{k_2}{k_1 C} \mu_l(t) - k_s e_s - c_2(t)^T \dot{\hat{W}} \quad (5.29)$$

with $\tilde{W} = W^* - \hat{W}$. In Eq. (5.18), the gradient tracking error is defined as the difference between the estimated gradient and 0 (the gradient corresponding to the optimum):

$$z = k_1 k_2 \hat{W}^T [dS(s)s + S(s)] \quad (5.30)$$

To drive the parameter and state estimations towards their respective desired values, a dither signal $d(t)$ is added, i.e.

$$z_s = \hat{W}^T [dS(s)s + S(s)] - d(t) \quad (5.31)$$

for which $k_1 \cdot k_2 > 0$ are removed for simplicity. The tracking error dynamics can be given as

$$\begin{aligned} \dot{z}_s &= \frac{d}{dt} \left\{ \hat{W}^T [dS(s)s + S(s)] - d(t) \right\} \\ &= \dot{\hat{W}}^T [dS(s)s + S(s)] + \hat{W}^T [d^2 S(s) \dot{s} + 2dS(s) \dot{s}] - \dot{d}(t) \end{aligned} \quad (5.32)$$

Let $\Gamma_1 = dS(s)s + S(s)$ and $\Gamma_2 = d^2 S(s)s + 2dS(s)$, we have

$$\begin{aligned} \dot{z}_s &= \dot{\hat{W}}^T \Gamma_1 + \hat{W}^T \Gamma_2 \dot{s} - \dot{d}(t) \\ &= \dot{\hat{W}}^T \Gamma_1 + \hat{W}^T \Gamma_2 \left[\frac{k_2}{k_1 C} \tilde{W}^T S - \frac{1}{k_1 C} xu + \frac{k_2}{k_1 C} \tilde{W}^T S + \frac{k_2}{k_1 C} \mu_l \right] - \dot{d}(t) \end{aligned} \quad (5.33)$$

By defining

$$\eta_1 = e_x - c_1(t)^T \tilde{W} \quad (5.34)$$

$$\eta_2 = e_s - c_2(t)^T \tilde{W} \quad (5.35)$$

$$\eta_3 = z_s - c_3(t)^T \tilde{W} \quad (5.36)$$

the following Lyapunov function candidate can be constructed,

$$V = \frac{1}{2} \eta^T \eta = \frac{1}{2} \eta_1^2 + \frac{1}{2} \eta_2^2 + \frac{1}{2} \eta_3^2 \quad (5.37)$$

Take the time derivative of V yields

$$\begin{aligned} \dot{V} &= \eta_1 \dot{\eta}_1 + \eta_2 \dot{\eta}_2 + \eta_3 \dot{\eta}_3 \\ &= \eta_1 \left[-k_x \eta_1 - k_x c_1(t)^T \tilde{W} - \dot{c}_1(t)^T \tilde{W} \right] \\ &\quad + \eta_2 \left[\frac{k_2}{k_1 C} \tilde{W}^T S + \frac{k_2}{k_1 C} \mu_l - k_s \eta_2 - k_s c_2(t)^T \tilde{W} - \dot{c}_2(t)^T \tilde{W} \right] \\ &\quad + \eta_3 \left\{ \dot{\tilde{W}}^T \Gamma_1 + \frac{\hat{W}^T \Gamma_2}{k_1 C} \left[k_2 \hat{W}^T S(s) - xu + k_2 \tilde{W}^T S + k_2 \mu_l \right] \right. \\ &\quad \left. - \dot{d}(t) - \dot{c}_3(t)^T \tilde{W} + c_3(t)^T \dot{\tilde{W}} \right\} \end{aligned} \quad (5.38)$$

By setting the dither signal as

$$\dot{d}(t) = c_3(t)^T \dot{\tilde{W}} + \dot{\tilde{W}}^T \Gamma_1 - k_d d(t) + \hat{W}^T \Gamma_2 a(t) \quad (5.39)$$

with $k_d > 0$ and external signal $a_e(t)$ to be assigned. Then the control law is

$$u = \frac{k_1 C}{x} \left[\frac{k_2}{k_1 C} \hat{W}^T S(s) - a_e(t) + (k_d / \hat{W}^T \Gamma_2) d(t) + (k_z / \hat{W}^T \Gamma_2) z_s \right] \quad (5.40)$$

In order to secure the convergence of the system, $a(t)$ need to be designed to provide persistent excitation. Equation (5.38) can then be reduced into

$$\begin{aligned}
\dot{V} = & \eta_1 \left[-k_x \eta_1 - k_x c_1(t)^T \tilde{W} - \dot{c}_1(t)^T \tilde{W} \right] \\
& + \eta_2 \left[\frac{k_2}{k_1 C} \tilde{W}^T S + \frac{k_2}{k_1 C} \mu_l - k_s \eta_2 - k_s c_2(t)^T \tilde{W} - \dot{c}_2(t)^T \tilde{W} \right] \\
& + \eta_3 \left[-k_z \eta_3 - k_z c_3(t)^T \tilde{W} + \hat{W}^T \Gamma_2 \left(\frac{k_2}{k_1 C} \tilde{W}^T S + \frac{k_2}{k_1 C} \mu_l \right) - \dot{c}_3(t)^T \tilde{W} \right]
\end{aligned} \tag{5.41}$$

To eliminate the terms with \tilde{W} , let

$$\dot{c}_1^T = -k_x c_1^T \tag{5.42}$$

$$\dot{c}_2^T = -k_s c_2^T + \frac{k_2}{k_1 C} S \tag{5.43}$$

$$\dot{c}_3^T = -k_z c_3^T + \frac{k_2}{k_1 C} \hat{W}^T \Gamma_2 S^T \tag{5.44}$$

Substituting Eqs. (5.42), (5.43) and (5.44) into (5.41) yields

$$\begin{aligned}
\dot{V} = & -k_x \eta_1^2 - k_s \eta_2^2 + \frac{k_2}{k_1 C} \eta_2 \mu_l - k_z \eta_3^2 + \frac{k_2}{k_1 C} \eta_3 \hat{W}^T \Gamma_2 \mu_l \\
\leq & -k_x \eta_1^2 - k_s \eta_2^2 + \frac{k_2}{2k_1 k_3 C} \mu_l^2 + \frac{k_2 k_3}{2k_1 C} \eta_2^2 - k_z \eta_3^2 \\
& + \frac{k_2}{2k_1 C k_4} \mu_l^2 + \frac{k_4 k_2}{2k_1 C} \left(\hat{W}^T \Gamma_2 \right)^2 \eta_3^2
\end{aligned} \tag{5.45}$$

where k_3 and k_4 are positive constants. To cancel the positive terms in (5.45), k_x , k_s and k_z can be designed as

$$k_x = k_{x0} \tag{5.46}$$

$$k_s = k_{s0} + \frac{k_2 k_3}{2k_1 C} \tag{5.47}$$

$$k_z = k_{z0} + \frac{k_4 k_2}{2k_1 C} \left(\hat{W}^T \Gamma_2 \right)^2 \tag{5.48}$$

where k_{x0} , k_{s0} and k_{z0} are positive constants. Finally, Eq. (5.45) becomes

$$\dot{V} \leq -\frac{k_{m1}}{2} \eta^T \eta + \frac{k_2}{2k_1 C k} \mu_l(t)^2 = -k_{m1} V + \frac{k_2}{2k_1 C k_{m2}} \mu_l(t)^2 \quad (5.49)$$

where $k_{m1} = 2 \min \{k_{x0}, k_{s0}, k_{z0}\}$ and $k_{m2} = 0.5 \min \{k_3, k_4\}$. Reference [43] derived an explicit bound for $\|\eta\|$ as

$$\|\eta\| \leq \alpha_1 e^{\lambda_1(t-t_0)} + \sqrt{\frac{k_2}{2k_1 k_{m2} C}} \sup_{t_0 \leq \tau \leq t} |\mu_l(\tau)| \quad (5.50)$$

with $\alpha_1 = \sqrt{V(t_0)}$ and $\lambda_1 = 1/(2k_{m1})$. Equation (5.50) assures the convergence of η to a small neighborhood of the origin. To show the convergence of the error signals e_x , e_s and z_s , we still need to ensure the convergence of the parameter estimation errors \tilde{W} and also $c_1(t)$, $c_2(t)$, $c_3(t)$ are bounded.

The boundedness and the convergence of the parameter estimates \hat{W} can be ensured by setting an appropriate parameter update law and assigning the proper external signal $a(t)$ to provide the persistent excitation [43]. The parameter update law is designed as

$$\dot{\hat{W}} = \text{Proj}[\Upsilon(t)e, \hat{W}] \quad (5.51)$$

where

$$\text{Proj}[\Upsilon(t)e, \hat{W}] = \begin{cases} \gamma_w \Upsilon(t)^T e & \begin{cases} q(\hat{W}) \leq w_m \text{ or} \\ q(\hat{W}) \geq w_m \text{ and } \gamma \hat{W}^T \Upsilon(t)^T e \leq 0 \end{cases} \\ \gamma_w \left[I - \gamma^2 q(\hat{W}) \frac{\hat{W} \hat{W}^T}{\hat{W}^T \hat{W}} \right] \Upsilon(t)^T e & \text{otherwise} \end{cases} \quad (5.52)$$

with γ_w being a positive gain. Vector $\Upsilon(t)$ is defined as

$$\Upsilon(t) = [c_1(t) \quad c_2(t) \quad c_3(t)] \quad (5.53)$$

The function $q(\hat{W})$ is given by

$$q(\hat{W}) = [M(\hat{W}) - w_m^2] / \epsilon^2 + w_m \epsilon \quad (5.54)$$

where w_m and ϵ are positive constants. The idea of barrier function is used in defining the convex function $M(\hat{W})$:

$$M(\hat{W}) = \hat{W}^T \hat{W} + \ln \left(\left\| \text{diag} [I \hat{W} - I(a_c - \delta_c)] \right\|^2 \right) + \ln \left(\left\| \text{diag} [I(b_c - \delta_c) - I \hat{W}] \right\|^2 \right) \quad (5.55)$$

with $a_c > 0, b_c > 0, \delta_c > 0$. The γ in Eq. (5.52) is defined via the gradient $\text{grad}[q(\hat{W})]$:

$$\begin{aligned} \gamma \hat{W}^T &= \text{grad} [q(\hat{W})] \\ &= \hat{W}^T + \frac{1}{\left\| \text{diag} [I \hat{W} - I(a_c - \delta_c)] \right\|} \hat{W}^T + \frac{1}{\left\| \text{diag} [I(b_c - \delta_c) - I \hat{W}] \right\|} \hat{W}^T \end{aligned} \quad (5.56)$$

The upper bound of the parameter estimates is guaranteed by the properties of the projection algorithm and the construction of $q(\hat{W})$ as $\|\hat{W}\| \leq \sqrt{b_c N_k}$ [43, 210], where N_k is the number of kernels used in the RBF neural network.

To evaluate the boundedness of $c_1(t)$, $c_2(t)$ and $c_3(t)$, we can combine Eq. (5.42)-Eq. (5.44) and Eq. (5.53) into

$$\dot{\Upsilon}(t) = -K(t) \Upsilon(t) + B(t) \quad (5.57)$$

with

$$K(t) = \begin{bmatrix} k_x & 0 & 0 \\ 0 & k_s & 0 \\ 0 & 0 & k_z \end{bmatrix} \quad (5.58)$$

$$B(t) = \begin{bmatrix} 0 & \frac{k_2}{k_1 C} S & \frac{k_2}{k_1 C} \hat{W}^T \Gamma_2 S^T \end{bmatrix}^T \quad (5.59)$$

As k_x , k_s and k_z are positive as shown in (5.46)-(5.48), so the resultant dynamics

$$\dot{\Upsilon}(t) = -K(t) \Upsilon(t) \quad (5.60)$$

is globally exponentially stable.

Based on [43], to show $\Upsilon(t)$ is bounded, one needs to show the elements of $B(t)$ are bounded functions of time with

$$\|B(t)\|^2 = \frac{k_2^2}{k_1^2 C^2} S^T S + \frac{k_2^2}{k_1^2 C^2} (\hat{W}^T \Gamma_2)^2 S^T S \quad (5.61)$$

For the operation of a practical PV system, the scaled terminal voltage s is finite and thus bounded. From Eqs. (5.20) and (5.21), $\|S\| \leq \sqrt{N_k}$ can be easily satisfied, and further

from Eqs. (5.22) and (5.23), we have $\|dS\| \leq 2\sqrt{\frac{N_k V_M}{k_1 \sigma_m^2}}$ and $\|d^2 S\| \leq 2\sqrt{\frac{N_k}{\sigma_m^2}} + 4\sqrt{N_k} \frac{V_M}{k_1 \sigma_m^2}$.

So the bound of Γ_2 can be given by

$$\|\Gamma_2\| \leq \frac{V_M}{k_1} \|d^2 S\| + 2\|dS\| \leq \frac{2V_M}{k_1} \sqrt{\frac{N_k}{\sigma_m^2}} + \frac{4V_M^2}{k_1^2 \sigma_m^2} \sqrt{N_k} + 4\sqrt{\frac{N_k V_M}{k_1 \sigma_m^2}} \quad (5.62)$$

So the bound of the norm of $B(t)$ can be given by

$$\|B(t)\| \leq \frac{k_2}{k_1 C} \sqrt{N_k} + \frac{k_2}{k_1 C} w_m \cdot \left[2\sqrt{\frac{N_k V_M}{k_1 \sigma_m^2}} + 4\sqrt{\frac{N_k V_M^2}{k_1^2 \sigma_m^2}} + 4N_k \sqrt{\frac{V_M}{k_1 \sigma_m^2}} \right] \quad (5.63)$$

which leads to the boundedness of $\Upsilon(t)$.

Furthermore, the external signal $a(t)$ needs to be designed to satisfy the following

assumption: $\exists T > 0$ and $k_N > 0$, s.t. $\int_t^{t+T} \Upsilon(\tau)^T \Upsilon(\tau) d\tau \geq k_N I_N$, where $\Upsilon(t)$ is the

solution of (5.57) and I_N is the N -dimensional identity matrix. The convergence of the parameter estimation error \tilde{W} , the state errors e_x and e_s , and the tracking error z_s to a small neighborhood of the origin can then be guaranteed. The detailed derivation and proof can be find in [43].

5.3. Simulation Study

The simulation study is carried out for the PV system with buck converter described in Section 5.1, and the AESC controller designed in Section 5.2.2. The simulation platform is Simulink® 7.3 SimPower-Systems™ with Matlab® R2009a. The initial condition of the system state variables and their estimated values were set to

$$i_L(0) = 0.1A, V(0) = 0.1V, \hat{x}(0) = 0.1, \hat{s}(0) = 0.1$$

The design parameters in the adaptive controller (5.40) and the parameter update law (5.51) are chosen as:

$$\gamma_w = 100, k_d = 0.1, k_{z0} = 1, k_{x0} = 1000, k_{s0} = 1, k_3 = 1, k_4 = 0.1$$

A 5-term RBFNN is selected, with the centers and width as

$$\varphi_i = 0.6 + 4.8(i-1)/4 \text{ and } \sigma_i = 0.6, \quad i = 1, 2, 3, 4, 5$$

to cover the rang of $[0, 6]$. The initial conditions for the parameter update weights are set as

$$\hat{W}_i(0) = 0.1 \quad i = 1, 2, \dots, 5$$

The external signal $a_e(t)$ is designed as

$$a_e(t) = 10^{-4} \cdot \sum_{i=1}^{10} \omega_i [A_{1i} \sin(\omega_i t) + A_{2i} \cos(\omega_i t)]$$

A_{1i} and A_{2i} are randomly chosen from a unit normal distribution. The frequencies are chosen as

$$\omega_i = 10^3 \cdot [1 + (i-1)10/9] \quad i = 1, 2, \dots, 10$$

$c_1(t)$, $c_2(t)$, $c_3(t)$ are initialized as zero vectors, while for the dither signal $d(t)$, $d(0) = 0$.

To evaluate the performance of the AESC MPPT controller, a dither ESC controller shown in Chapter 6 has also been simulated for the same simulation examples. The performances of AESC and dither ESC MPPT with nominal conditions are compared in Fig. 5.3, with the same initial conditions as $i_L(0) = 22.1$ A and $V(0) = 300$ V. The controllers are set with the sampling period of 1×10^{-4} second. The theoretical maximum power is 5884W at $T = 25^\circ\text{C}$ and $G = 1000\text{W/m}^2$. The steady-state MPPT result given by dither ESC is 5874W and 5838W by the AESC, which differ trivially. The AESC leads to small steady-state error (about 0.78%) due to the approximation error of nonlinear relation $i(V)$ in the parameter updating process, compares to 0.17% for the dither ESC. The AESC demonstrates a much quicker transient time, with the 1% settling time of 0.035s compared to 0.4s for the dither ESC.

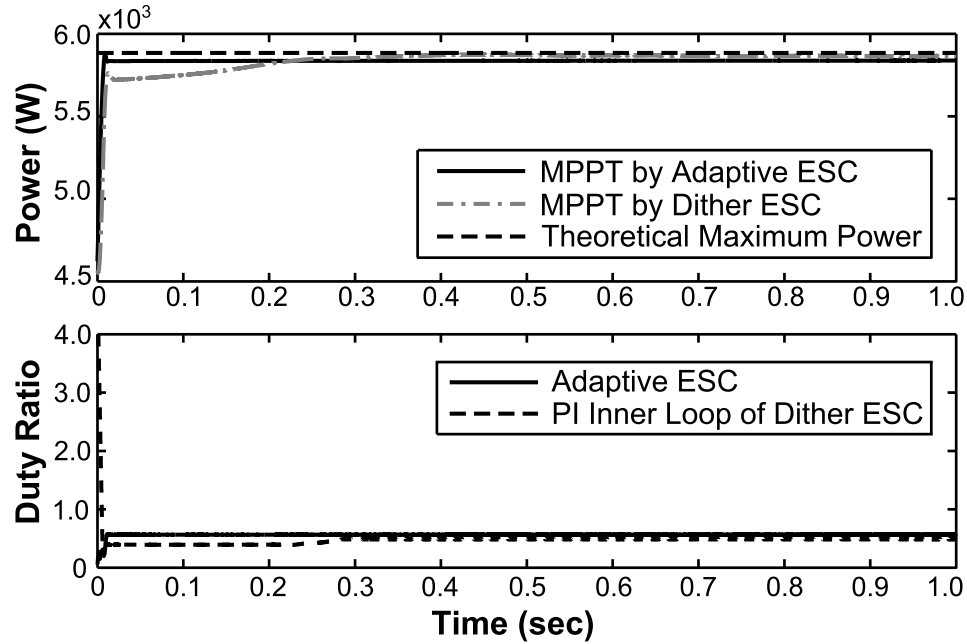


Figure 5.3: Comparison of PV MPPT results with AESC and dither ESC

Figure 5.4 shows the case of AESC MPPT with a step change of temperature from 25°C ($0\sim 0.1\text{s}$) down to 17°C ($0.1\sim 0.2\text{s}$). The steady-state power outputs of the PV array are 5838W and 6061W , respectively, with the theoretical optima of 5884W and 6082W , respectively, plotted as the dotted line. The bottom plot shows the profile for the corresponding control input u (duty ratio). Figure 5.5 shows the case of dither ESC MPPT with a step change of temperature from 25°C ($0\sim 1.5\text{s}$) down to 17°C ($1.5\sim 3\text{s}$). The bottom plot shows the performance of the PV power output as 5874W and 6048W , respectively, with the theoretical optima (dotted line) of 5884W and 6082W , respectively. The setting time for this change differs dramatically: 2.5 ms for the AESC and 220 ms for the dither ESC.

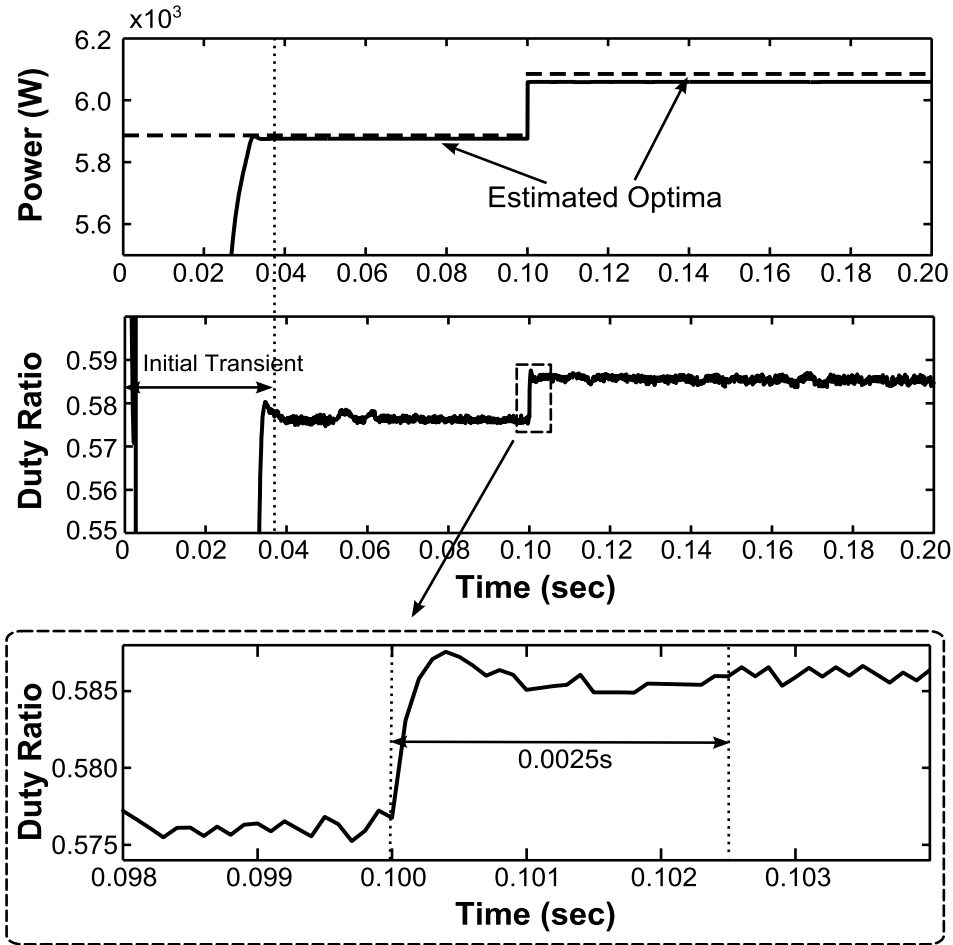


Figure 5.4: AESC MPPT with a step change of temperature from 25°C to 17°C

Figure 5.6 shows the case of AESC MPPT with a step change of irradiance rate from 1000W/m^2 (0~0.1s) to 500 W/m^2 (0.1~0.2s). The PV power outputs are 5838W and 2501W, respectively, with the theoretical optima (the dotted lines) of 5884W and 2576W, respectively. The bottom plot shows the corresponding control input u . Figure 5.7 shows the case of dither ESC MPPT with a step change of irradiance rate similar to Fig. 5.6, from 1000W/m^2 (0~1.5s) to 500 W/m^2 (1.5~3s). The PV power outputs are 5874W and 2527W, respectively, with the theoretical optima (the dot lines) being 5884W and 2576W, respectively. The settling time was 4 ms for the AESC versus 320 ms for the dither ESC.

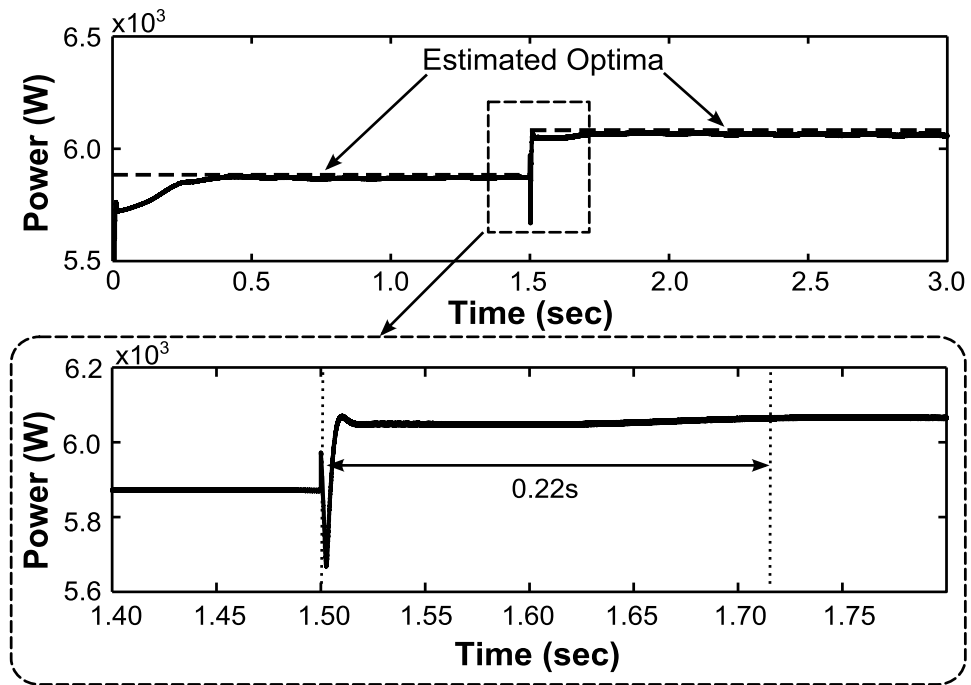


Figure 5.5: Dither ESC MPPT with a step change of temperature 25°C to 17°C

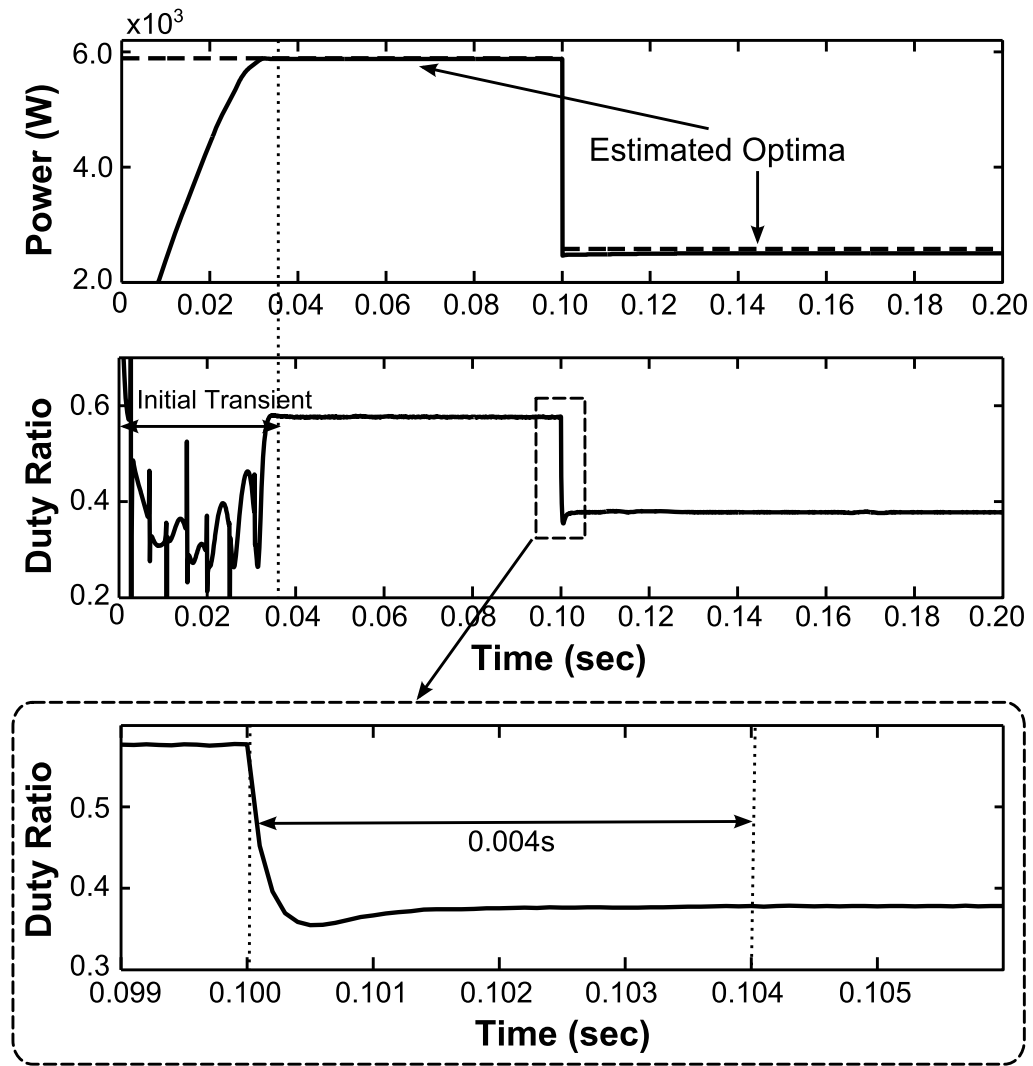


Figure 5.6: AESC MPPT with a step change of irradiance rate from 1000 to 500W/m^2

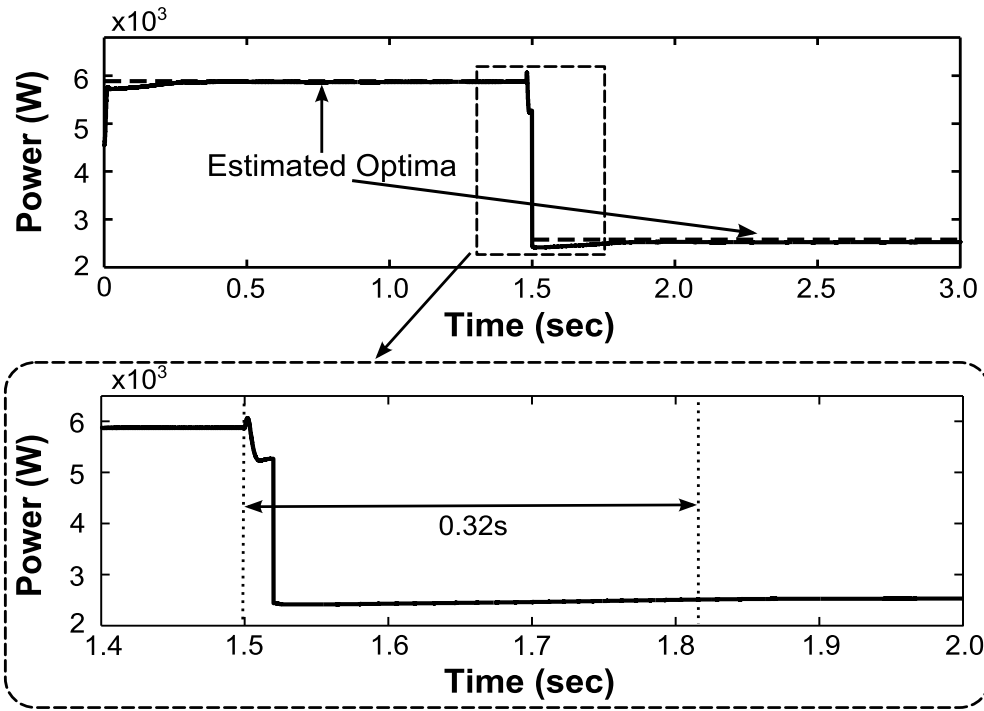


Figure 5.7: Dither ESC MPPT with a step change of irradiance rate from 1000 to 500W/m²

Figure 5.8 shows the case of AESC MPPT with a simultaneous step change of both temperature (from 25 °C to 17°C) and irradiance (from 1000 W/m² to 800 W/m²) at 0.1s. The steady-state power outputs are 5838 W and 4692 W, respectively, with the theoretical optima (the dot lines) of 5884W and 4695W, respectively. The bottom plot shows the corresponding control input u . Figure 5.9 shows the case of dither ESC based MPPT with a similar simultaneous step change of both temperature (from 25 °C to 17°C) and irradiance (from 1000 W/m² to 800 W/m²) at 1.5s. The PV power outputs are 5874W and 4679W, respectively, with the theoretical optima (the dot lines) being 5884W and 4695W, respectively. The settling time was 3.3 ms for the AESC versus 420 ms for the dither ESC.

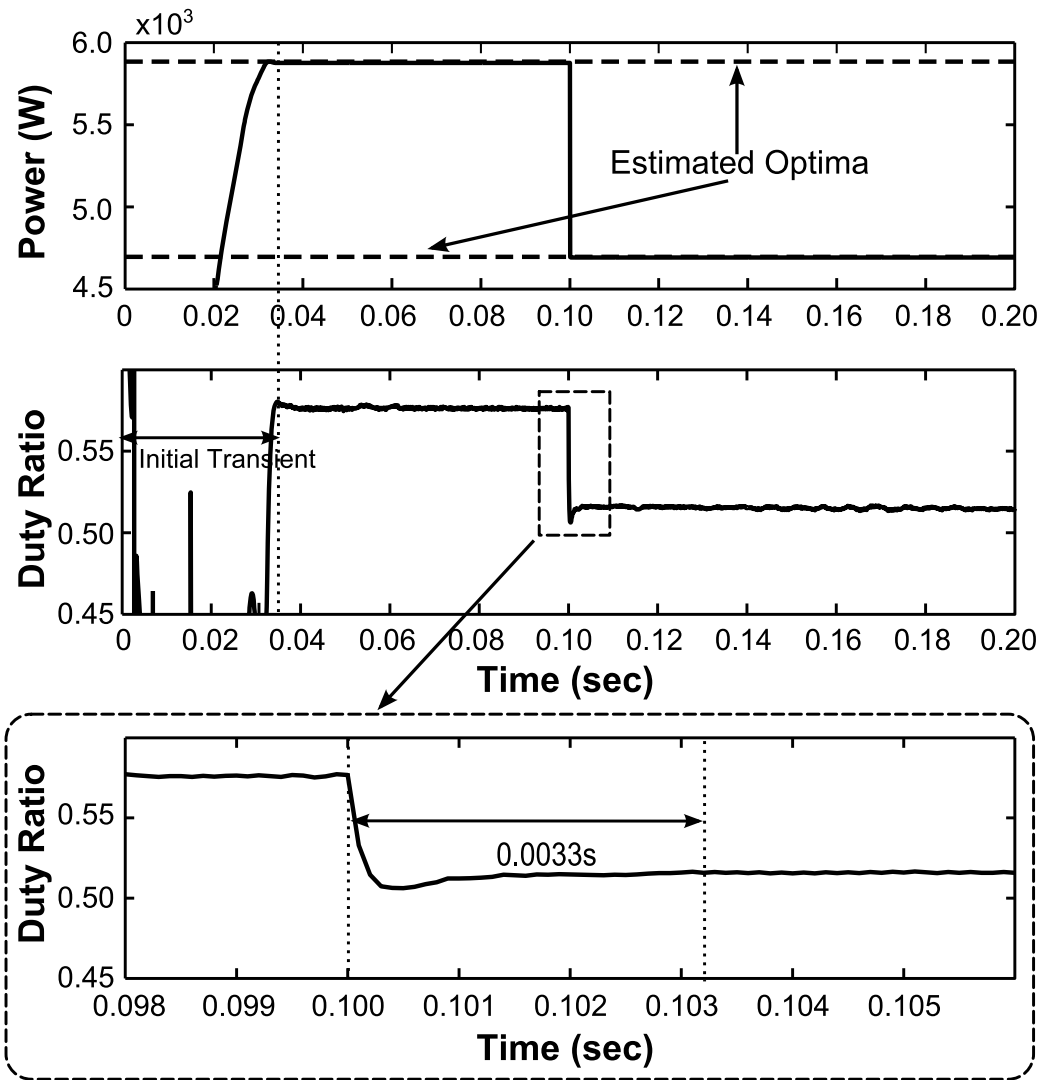


Fig. 5.8. AESC MPPT with a simultaneous step change of both temperature (25°C to 17°C) and irradiance rate (1000 to 800 W/m^2)

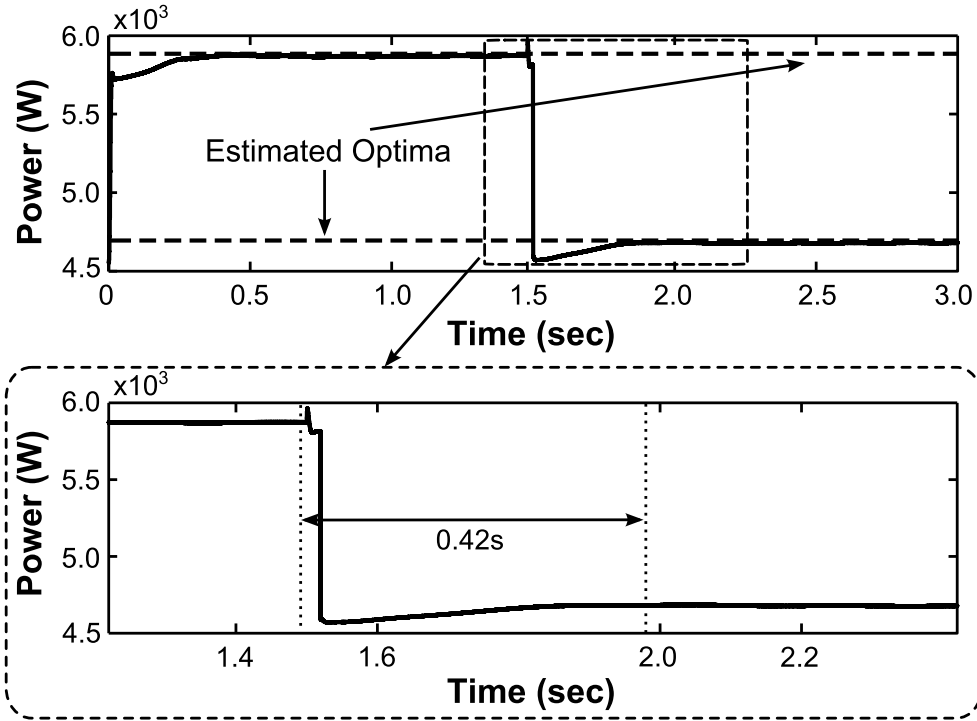


Fig. 5.9. Dither ESC MPPT with a simultaneous step change of both temperature (25°C to 17°C) and irradiance Rate (1000 to 800 W/m^2)

For all the above cases, it reveals that the AESC can achieve much fast transient with very small degradation in terms of steady-state convergence accuracy. The dither-based ESC only observes the power output change and does not gain the knowledge of the system structure information, the tuning parameters of the controller must be selected carefully to safely secure the system stability when encounter different intrinsic or environmental conditions, which means the controller cannot always stay with the best speed option. On the other hand, design of AESC requires the basic knowledge of the system, and RBF NN is used to approximate the major system nonlinearity. Lyapunov theory is used to secure the stability of the controlled system with observed system states feedback. However it is still a very plain explanation, a mathematical explanation and proof of the convergence speed is still desired.

The AESC MPPT framework performance is then evaluated by some more extremal scenarios in order to evaluate the transient performance achievable. Three different scenarios are studied. First, simulation is performed with a step change of irradiance rate from 1000 W/m^2 ($0 \sim 0.1\text{s}$) to 300 W/m^2 ($0.1 \sim 0.2\text{s}$). The upper subplot of Fig 5.10 shows the PV power output trajectory searched by AESC. The steady-state power outputs of the PV array are 5838 W and 1322 W , respectively, with the theoretical optima of 5884 W and 1329 W , respectively. Notice that the PV array power output with former control input (duty ratio) is 755.6 W . A 566.4 W difference is gained by AESC MPPT method with the 1% settling time of about 0.024 sec . The control input duty ratio signal is shown in the lower subplot of Fig. 5.10. Observable variation of the steady-state output is due to the fluctuation in $a(t)$ which sustains the persistence excitation condition for parameter estimation.

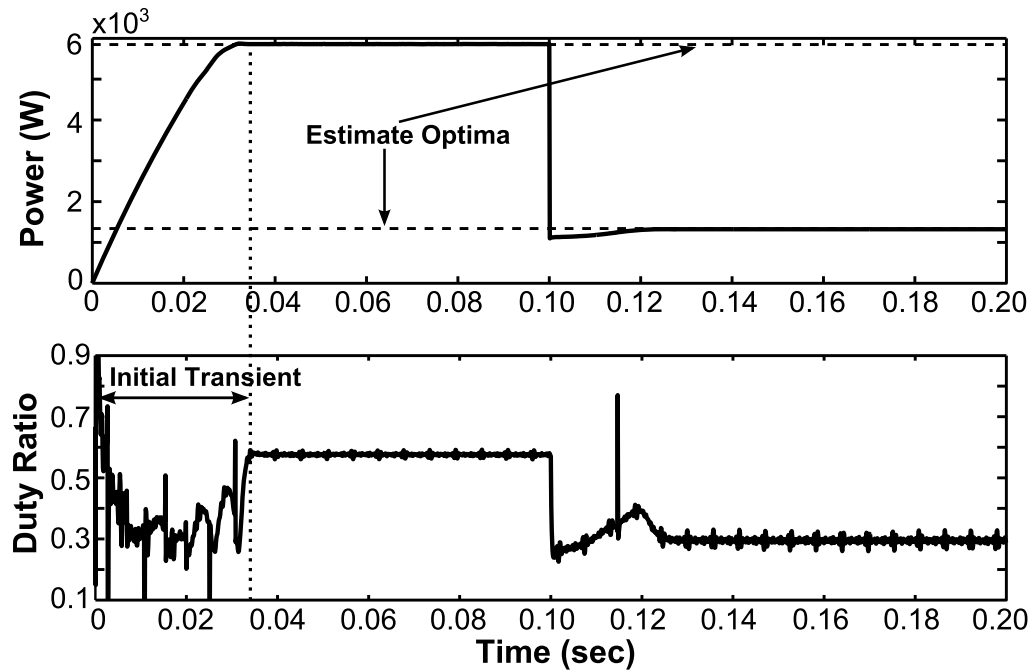


Figure 5.10: AESC MPPT with a step change of irradiance rate from 1000 to 300 W/m^2

Then for a more realistic scenario, a ramp change of temperature from 298K (0~0.1s) down to 290K (0.2~0.3s) with a 0.1sec ramp period (0.1~0.2s) is tested. The amplitude of the external signal $a(t)$ is reduced due to the smaller change of temperature comparing to the irradiance change. The upper subplot of Fig 5.11 shows the PV power output by the AESC MPPT. The steady-state power outputs of the PV array are 5859 W and 6049W, respectively, with the theoretical optima of 5884 W and 6052 W, respectively. The zoomed control input duty ratio signal is shown in the lower subplot of Fig. 5.11.

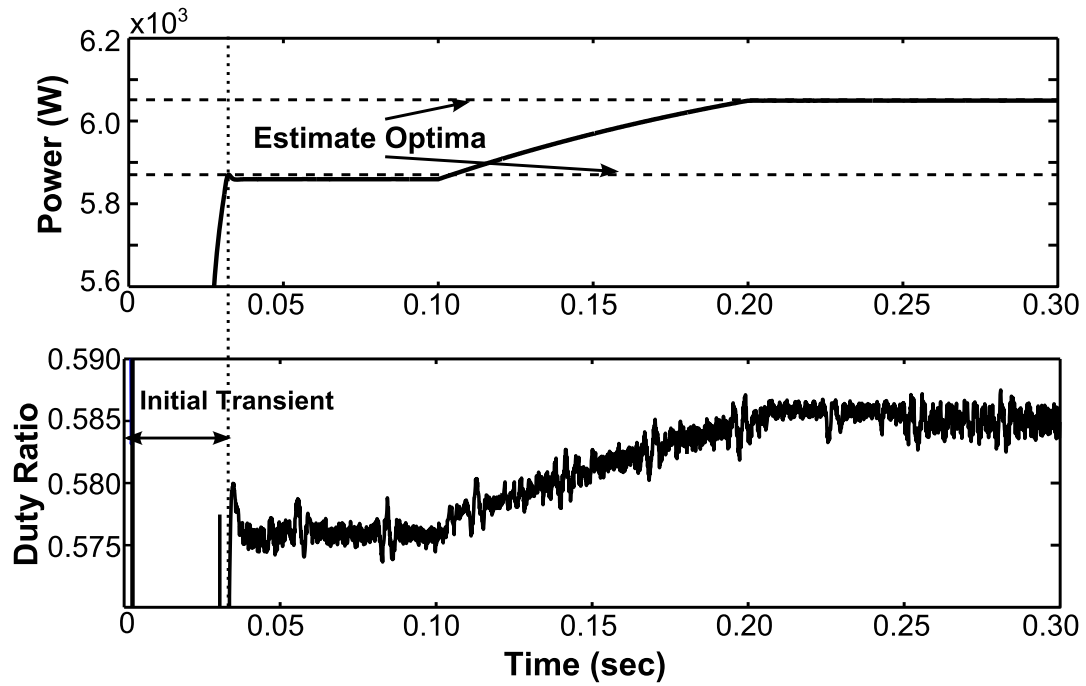


Figure 5.11: AESC MPPT with a ramp change of temperature from 25°C to 17°C

Finally, the effectiveness of the AESC controller is tested with a combined environmental change of irradiance rate and temperature as shown in the upper subplot of Fig. 5.12. The middle subplot of Figure 5.12 shows the AESC searched PV power output performance. The steady-state power outputs of the PV array are 5838W, 1365W and 5841W, respectively, with theoretical optima of 5884W, 1366W and 5884W,

respectively. The control input duty ratio signal is shown in the lower subplot of Fig. 5.12.

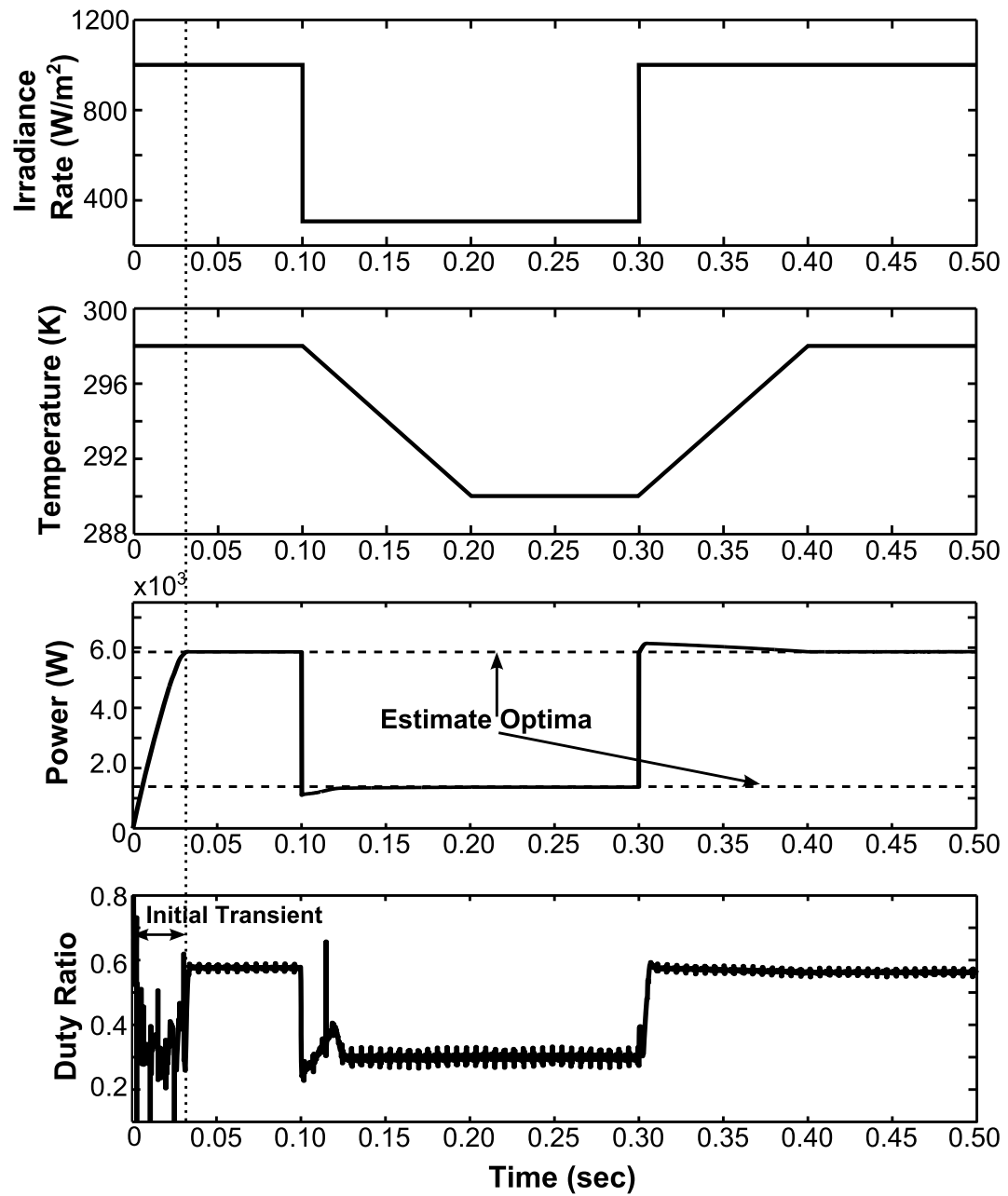


Figure 5.12: AESC MPPT under a combined change of irradiance rate and temperature

For all the above cases, the AESC also achieve very fast transient with good steady-state convergence accuracy. In summary, the above simulation results under various condition changes show significant improvement in transient performance using the AESC over the dither ESC, with only slight increase of steady-state error.

Chapter 6. Detection of Internal Resistance Change for Photovoltaic Arrays Using Extremum Seeking Control MPPT Integrated Signals

A serially connected group of PV modules forms a PV string. The PV strings can be grouped into a PV array with parallel and/or serial connections. MPPT and fault diagnosis are two important aspects for reducing the COE for PV array system. In this study, the dither based ESC is applied to achieve the MPPT control and simultaneously to detect the change of internal resistance for fault detection purpose. There are two kinds of modeling described in this Section, one is the simulation model used as a virtual plant, with more involved physics of photovoltaic generation. The other model is a simplified model for the transfer function analysis to illustrate the impact of internal resistance on the transient behavior of the dithered PV responses. Under square dither perturbations, the steady-state output of PV output signals consist of a number of small-amplitude step responses. The transient characteristics of such step responses are affected by the PV internal resistance. The internal resistance, especially the shunt resistance, is an important indicator for the degradation of the PV device. A small-signal transfer function analysis is performed for the PV buck system, which validates such impact.

A simulation study is first conducted for single-string PV systems, and the simulation results show that ESC can achieve satisfactory MPPT under a square-wave dither input. Typical transient characteristics, such as integrated absolute error (IAE), show a strong correlation with the internal resistance. Applicability of this scheme to multi-string PV is

then demonstrated with a multi-input ESC based on the total power feedback, with the internal resistance of individual module detectable from one output signal. A serially connected multi-string PV system is considered in this chapter.

The simulation model of PV system adopted in this study will be described in Section 6.1. Section 6.2 presents the dither ESC based PV MPPT, with both the single-input ESC MPPT for the single-string PV system and the multi-input ESC MPPT for multi-string PV system. The investigation of ESC integrated detection of change of internal shunt resistance is presented in Section 6.3, and the summary will be given in Section 6.4.

6.1. Simulation Model of Photovoltaic System

This chapter involves two different models of the PV system with buck converter. This section describes the simulation model with more involved physics of photovoltaic generation, which is used as a virtual plant. Section 6.3 presents the other model, which is a simplified one for the transfer function analysis to illustrate the impact of internal resistance on the transient behavior of the dithered PV responses.

The PV module model used for the simulation study follows the one by Villalva *et al.* [176] which is same as described in Section 5.1. In this study, constant terminal voltage is assumed, as shown in Fig. 6.1. The input voltage of the DC-DC converter is controlled by adjusting the duty ratio D of the pulse-width modulator (PWM) with a proportional-integral (PI) control. A simple buck converter is used for a voltage step-down scenario, with inductance $L = 0.1$ mH, capacitor $C = 5$ mF, and the terminal voltage $V_o = 5$ V.

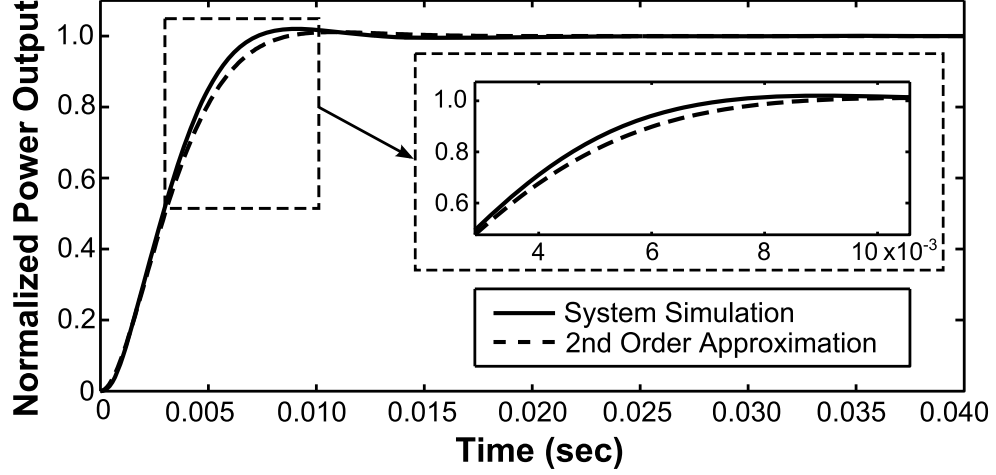


Figure 6.3: Step responses of PV full simulation model and the 2nd–order estimate

A normalized step response of the power output is shown in Fig. 6.3, with which the input dynamics is approximated as a 2nd–order system:

$$\hat{F}_I(s) = \frac{508^2}{s^2 + 833.12s + 508^2} \quad (6.1)$$

As the cutoff frequency ω_c of the input dynamics is 430 rad/sec, the dither frequency ω_d is then selected as 115.2 rad/sec. The high pass filter $F_{HP}(s)$ and low pass filter $F_{LP}(s)$ are chosen as

$$F_{HP}(s) = \frac{s^2}{s^2 + 80.156s + 69.1^2} \quad (6.2)$$

$$F_{LP}(s) = \frac{34.6^2}{s^2 + 41.52s + 34.6^2} \quad (6.3)$$

The dither amplitude is selected as 0.05 V. The dither phase angle is selected as 0.72 radian.

To evaluate the performance of the dither ESC controller, a single-string PV module is tested under nominal condition (i.e. 25°C and 1000W/m²). The simulation starts at a

fixed voltage reference of 10 V, and the ESC controller is turned on at $t = 0.1$ sec. Figure 6.4 shows the power-voltage curve of the PV system, the simulation starts at point A, with voltage fixed at 10 V and the estimated corresponding power is 81.43 W. The estimated maximum achievable power output as 209.1 W and the corresponding optimal voltage as 27.15V (point B). The potential improvement of the power output is 127.67 W, 156.8% comparing to the initial point. The ESC search results are shown in Fig. 6.5. The average steady-state voltage is 27.11 V, and the average power output is 208.9 W. The 1% settling time is about 0.21 sec. Compared to the optimum in the P - V characteristic in Fig. 6.4, the steady-state errors are about 0.15% and 0.096% for the input voltage of the DC-DC converter and the PV power output, respectively.

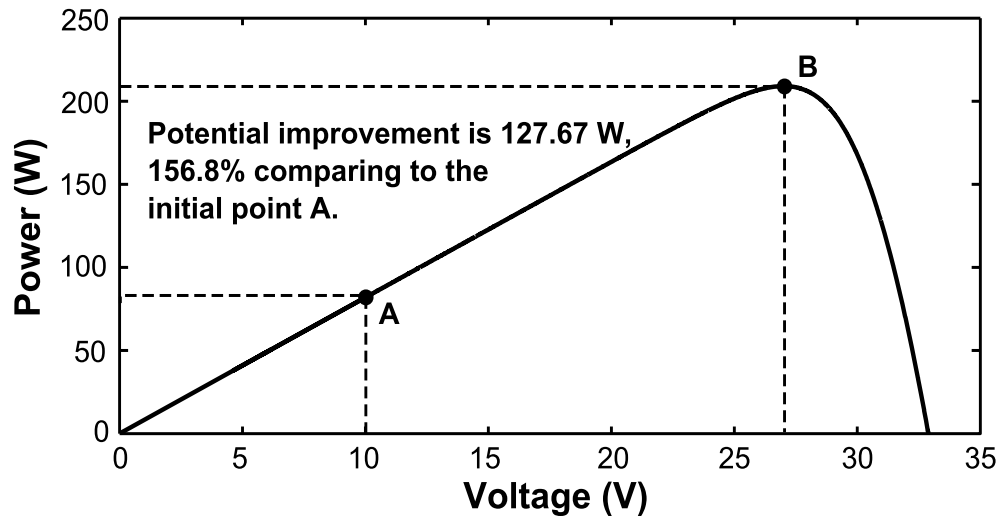


Figure 6.4: P - V characteristic of single PV module under nominal conditions

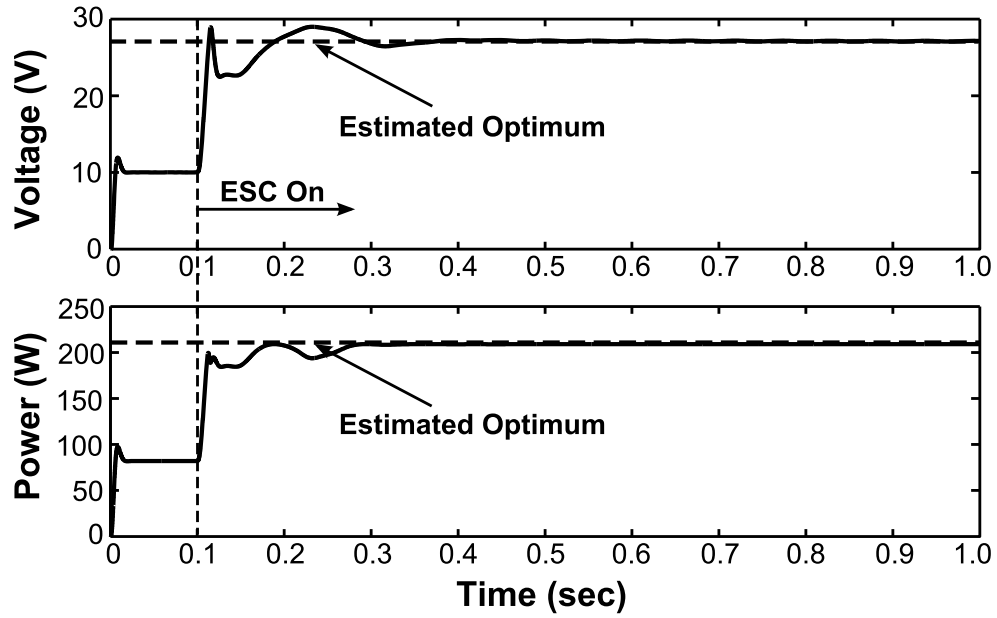


Figure 6.5: ESC simulation results for single-string PV under nominal conditions

6.2.2. Multi-Input ESC MPPT for Multi-String PV System

Multi-string configuration has been considered as a more cost effective topology for a grid connected PV systems [211-214]. The PV strings can be connected in series and/or parallel to meet the voltage/current requirements. Serial connection leads to larger voltage while parallel connection leads to larger current. As illustrated in Fig. 6.6, n PV strings are connected in series, with each string equipped with a DC/DC converter. All the DC/DC converters are connected to outside device via a common DC link. The major advantage of this multi-string structure lies in the fact that the mismatch issue for serial connection and the partial shading problem can be significantly relieved [215, 216].

In this study, instead of developing individual MPPT controllers for each string, the multi-input dither ESC is considered for the MPPT of the multi-string PV array, where the feedback (i.e. the performance index) used is the total power of the PV array. This can significantly reduce the number of system output measurements.

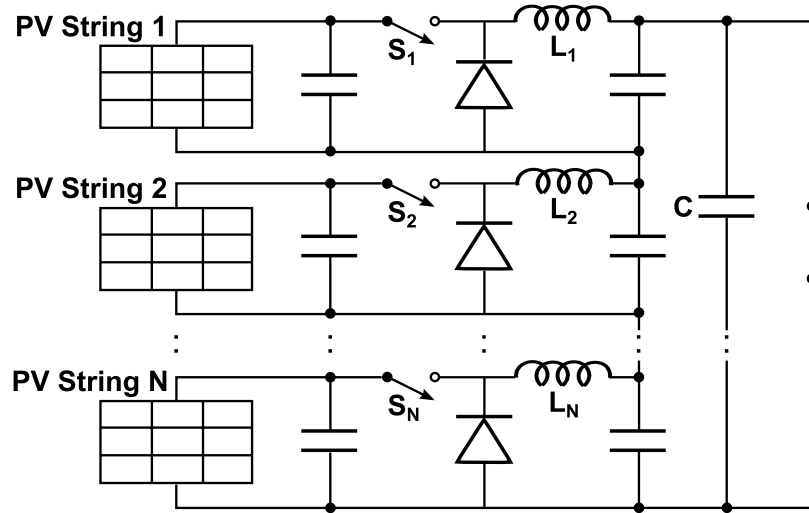


Figure 6.6: Schematic illustration for series connected multi-string structure

The PV string is represented by a group of series connected PV modules, and a PV array consists of N strings in series is considered as shown in Fig. 6.6. Each string is assumed to be equipped with its own DC/DC converter, and all the DC/DC converters are connected to a common DC bus with series configuration.

The buck converter is considered for the simulation example, with S_1 through S_N being the switches for each converter. The terminal voltage at the DC bus is the sum of all the string's voltages. The current flowing through the load is the overall output current of the converters. As a simple treatment, a resistive load $R_o = 10 \Omega$ is used.

The ESC control strategy is investigated for the maximum power point tracking purpose of the multi-string PV system, to find its maximum achievable power output at given temperature and irradiation.

The multi-input ESC scheme as shown in Fig. 6.7 is constructed as multi-loop (N channels), each input channel for each PV string. The dither frequencies are distinct from different loops. The control inputs are the voltage references for individual strings. The

input voltage for each channel is regulated by respective inner PI controller. With series connection, the outputs of buck-converters are connected to the terminal DC bus. With converter losses ignored, the total power can be approximated as the sum of the converter power outputs. The overall power at the DC bus is used as the feedback signal. A single high-pass filter is utilized to filter out the DC component of the dithered cost function output signal and keep the harmonics part. The first harmonic signals which represent the $\frac{dl}{d\hat{u}}$ gradient are then converted into DC terms by multiplying N different demodulation signals. Different low-pass filters are designed separately to remove the high frequency term of the signals, and keep the DC terms. The online optimal searching is then achieved by using the integrators to eliminate the extracted gradient signals.

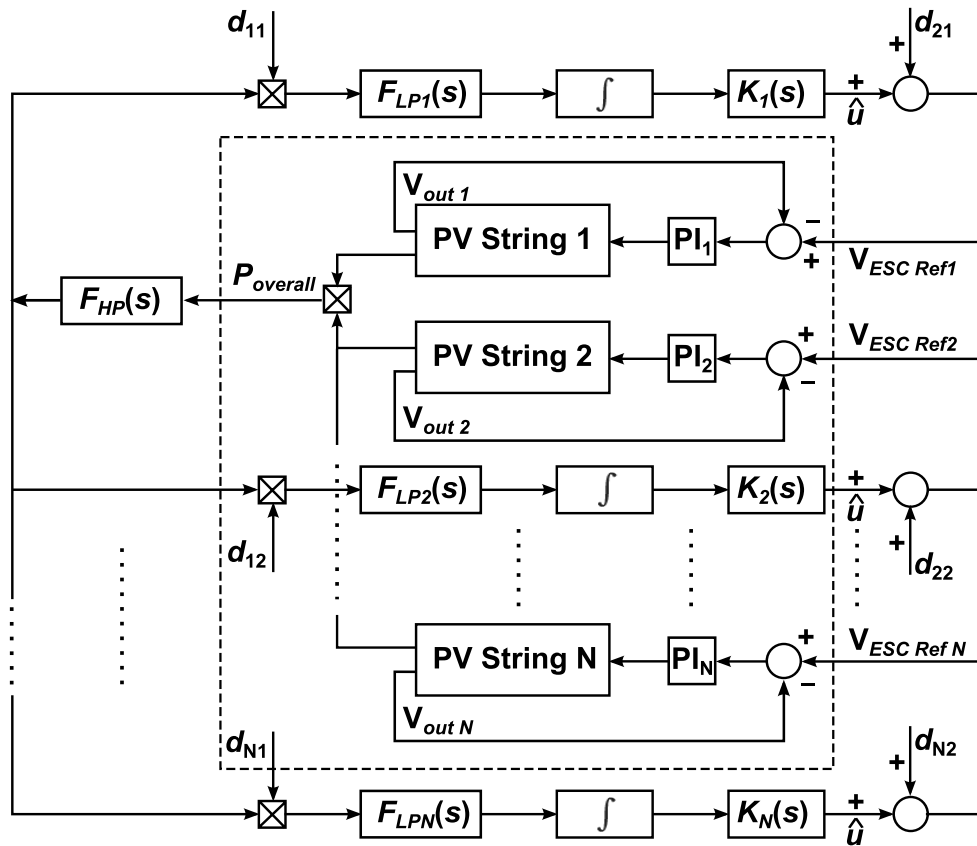


Figure 6.7: Multi-input ESC scheme for multi-string PV system

For simplicity and the idea-proof purpose, a two-string PV array is then considered for the simulation study. The PV array consists of two serially connected PV strings; each string has four serially connected PV cells. Simulations are conducted with Matlab® R2009a Simulink® 7.3 and SimPowerSystems.

To introduce more string-to-string difference, String 1 is set with 25°C and 1000 W/m², while String 2 is set with 25°C and 500 W/m². The P - V curves are shown in Fig. 6.8. For String 1, the maximum power and the corresponding voltage are estimated 761.6 W and 110.1 V (shown as point C), respectively. For String 2, the maximum estimated achievable power and the corresponding voltage are 334.1 W and 104.1 V (shown as point D), respectively. Therefore, the maximum total power is 1095.7 W by adding up the two string power outputs. Accordingly, the power map can be shown as the 3D surface in Fig 6.9.

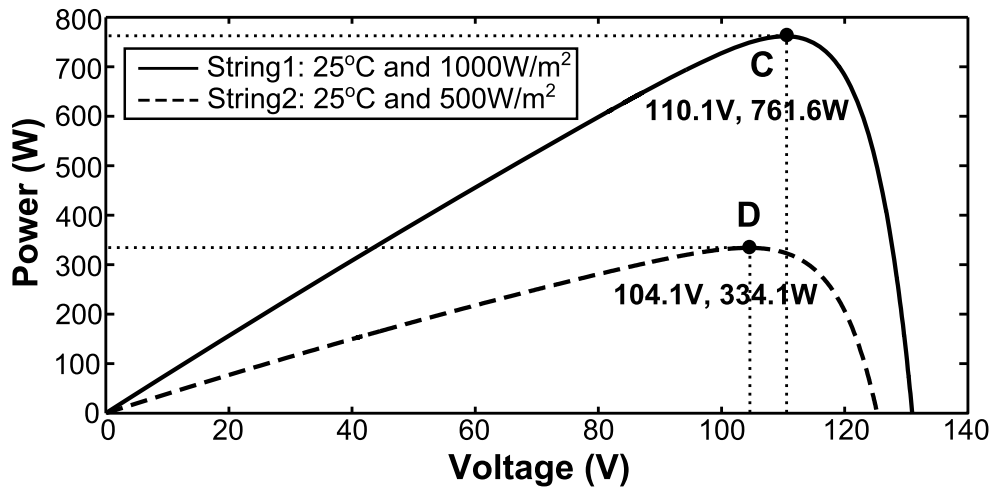


Figure 6.8: P - V curves for two-string PV array: String 1 with 25°C and 1000 W/m²,
String 2 with 25°C and 500 W/m²

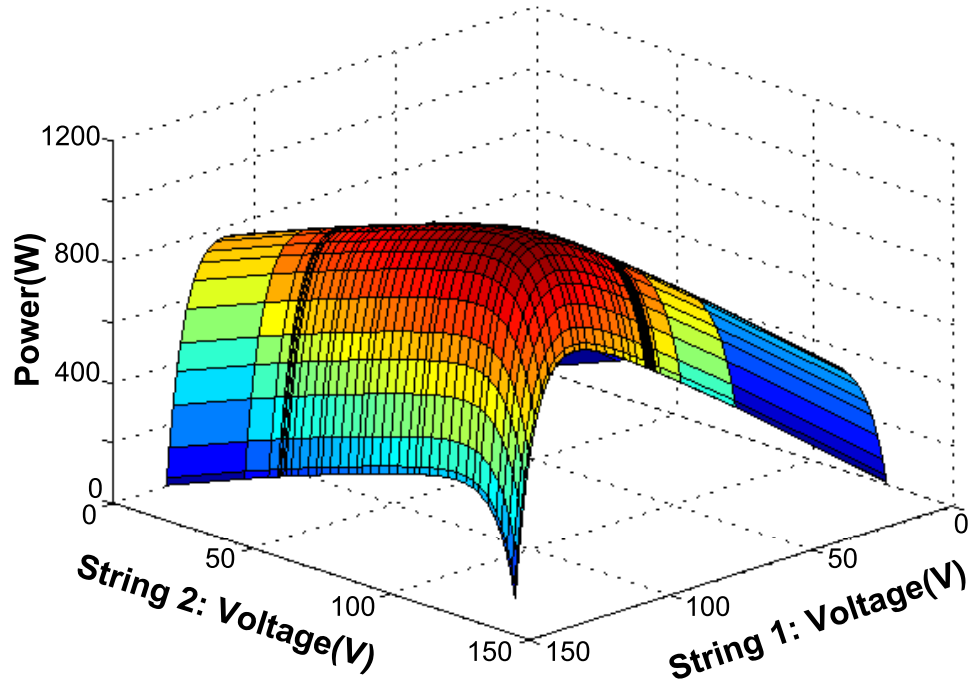


Figure 6.9: 3-D power map for the two-string PV system in Fig. 6.8

The ESC design mainly follows the dither based ESC design guidelines presented in Section 4.2. As stated above, the objective of the multi-input ESC strategy is to maximize the total power output from the DC bus. Due to the relation between the maximum power output and the corresponding voltage, and the quick response from the PV cell (without the buck converter), so the dynamics of the corresponding voltage is considered instead.

From the corresponding voltages step responses, the input dynamics is estimated as

$$\hat{F}_l(s) = \frac{92500}{s^2 + 570s + 92500} \quad (6.4)$$

for which the cut-off frequency is about 212 rad/sec. The dither frequencies of the two input channels are selected as 31.4 rad/sec and 25.1 rad/sec, respectively. The high-pass filter is selected as

$$F_{HP}(s) = \frac{s^2}{s^2 + 21.8544s + 18.84^2} \quad (6.5)$$

The low-pass filters are selected as

$$F_{LP1}(s) = \frac{9.42^2}{s^2 + 11.304s + 9.42^2} \quad (6.6)$$

$$F_{LP2}(s) = \frac{7.85^2}{s^2 + 9.42s + 7.85^2} \quad (6.7)$$

To compensate for the phase shift due to the input dynamics and the high-pass filter $F_{HP}(s)$, the dither phase angles are selected as $\alpha_1 = 0.609$ radian and $\alpha_2 = 0.713$ radian respectively. A 90° phase difference is also reinforced between the two channels.

During the first second of simulation, the PV operates in open loop with reference voltage set at 90 volts. Then the ESC with sinusoidal dither is turned on. Figure 6.10 shows the front-end (converter input) voltage trajectories. The ESC searching process demonstrates a 1% settling time of 0.35 second. The voltages searched by the ESC are 109.6 V and 103.5 V, with steady-state errors about 0.45% and 0.58%, for Channels 1 and 2, respectively.

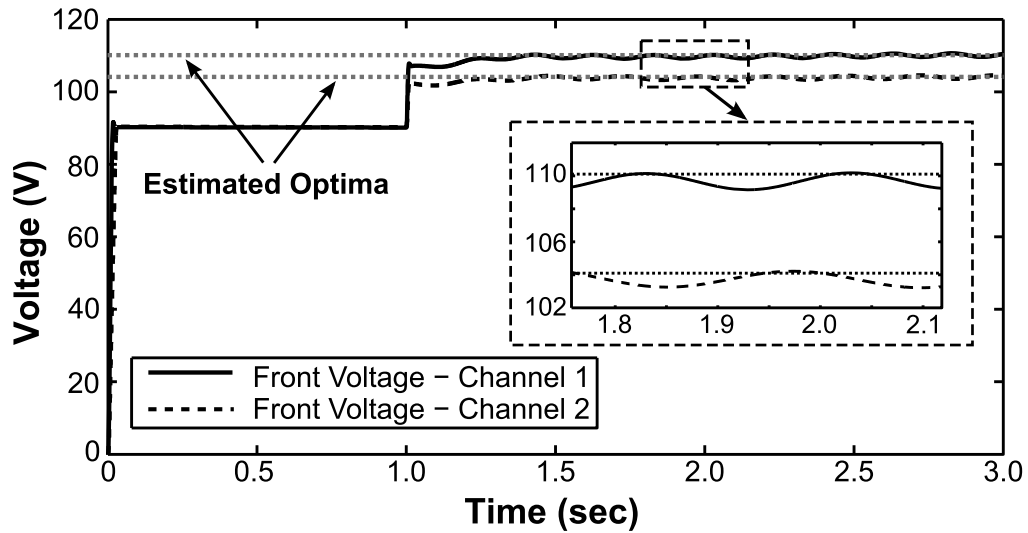


Figure 6.10: Voltage profiles for two-input ESC MPPT with sinusoidal dither: String 1

with 25°C and 1000 W/m^2 , String 2 with 25°C and 500 W/m^2

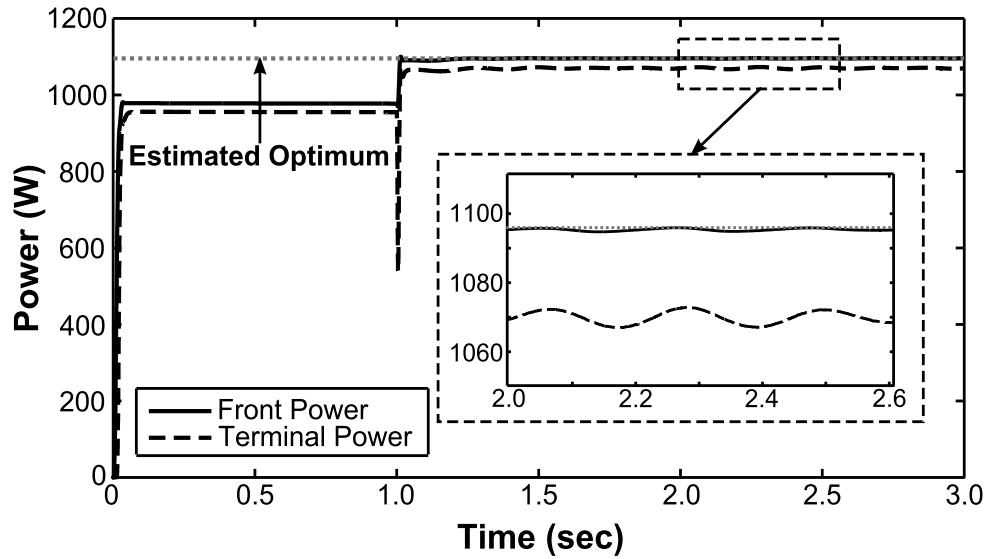


Figure 6.11: Power profiles for two-input ESC MPPT with sinusoidal dither: String 1 with 25°C and 1000 W/m², String 2 with 25°C and 500 W/m²

The ESC searched power profiles are shown in Fig. 6.11. The ESC searched maximum total converter front-end power is 1095.2 W, which is very close to the estimated power output of the MPP (1095.7 W), with the steady-state error only about 0.05%. The DC-bus terminal power is about 26 W lower than the front power due to the power loss within the circuit.

6.3. ESC Integrated Detection of Change of Internal Shunt Resistance

In this section, the relation between the change of the internal shunt resistance and the transient characteristics in the steady-state ESC signals under square-wave dither perturbation will be investigated. First, in order to evaluate the impact of the internal shunt resistance on the transient characteristics in small-amplitude step responses (e.g. the steady-state dithered output), a small-signal transfer function analysis is conducted based on linear model in Fig. 6.12, derived from the generic PV circuit model by [177].

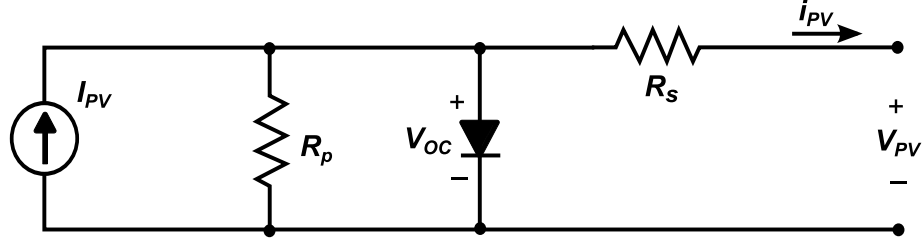


Figure 6.12: PV array linear circuit model current source ($v_{PV} < V_{mp}$)

Applying the typical averaging method to the PV-buck system in Fig. 6.1, yields the following state-space model [209]:

$$L \frac{di}{dt} = v d_D - V_o \quad (6.8)$$

$$C \frac{dv}{dt} = \frac{V_{eq} - v}{R_{eq}} - i d_D \quad (6.9)$$

where d_D is the duty ratio, $V_{eq} = I_{pv} R_p$ and $R_{eq} = R_p + R_s$ are the Thévenin equivalent voltage and resistance, respectively. The capital-letter variables represent the steady-state values, while variables with symbol “ \sim ” represent the small-magnitude perturbations. The key variables in Eqs. (6.8) and (6.9) are [177, 209]:

$$v = V + \tilde{v}, i = I + \tilde{i}, d_D = D + \tilde{d} \quad (6.10)$$

Substituting (6.10) into (6.8) and (6.9) and neglecting products $\tilde{v}\tilde{d}$ and $\tilde{i}\tilde{d}$ of higher-order terms of small amplitude, we have

$$L \frac{d\tilde{i}}{dt} = VD + \tilde{v}D + V\tilde{d} - V_o \quad (6.11)$$

$$C \frac{d\tilde{v}}{dt} = -\frac{\tilde{v}}{R_{eq}} - I\tilde{d} - \tilde{i}D - ID + \frac{V_{eq} - V}{R_{eq}} \quad (6.12)$$

Performing the Laplace transform on (6.11) and (6.12) yields

$$sL\tilde{i}(s) = D\tilde{v}(s) + V\tilde{d}(s) \quad (6.13)$$

$$sC\tilde{v}(s) = -\frac{1}{R_{eq}}\tilde{v}(s) - I\tilde{d}(s) - D\tilde{i}(s) \quad (6.14)$$

The small-signal transfer function from the duty-ratio change to the voltage can thus be obtained as

$$G_{vd}(s) = \frac{\tilde{v}(s)}{\tilde{d}(s)} = -\frac{s\frac{I}{C} - \frac{DV}{LC}}{s^2 + s\frac{1}{CR_{eq}} + \frac{D^2}{LC}} \quad (6.15)$$

Assume that all other parameters in Eq. (6.15) constant. $R_{eq} = R_p + R_s$ appears in the damping term of the denominator in the transfer function (6.15), which will affect the transient characteristics of the step responses. Since in general, $R_p \gg R_s$, the change of the shunt resistance will thus have stronger impact on the transient characteristics, which can potentially be used for detecting the change of the shunt resistance associated with the PV degradation. Since the change of damping related parameters can be better reflected from the step responses, square-wave dither is adopted for the proposed ESC integrated detection of change in shunt resistance. The ESC design in Section 6.2 can be applied with duty ratio d as the control input.

As shown in Fig. 6.13, the ESC search results in the average steady-state voltage of 27.08 V and the PV power output of 207.3 W, respectively, with 1% settling time of about 0.44 sec. Compared to the estimated optimum in the P - V characteristic shown in Fig. 6.4, the steady-state errors are about 0.26% and 0.86% for the input voltage of the DC-DC converter and the PV power output, respectively.

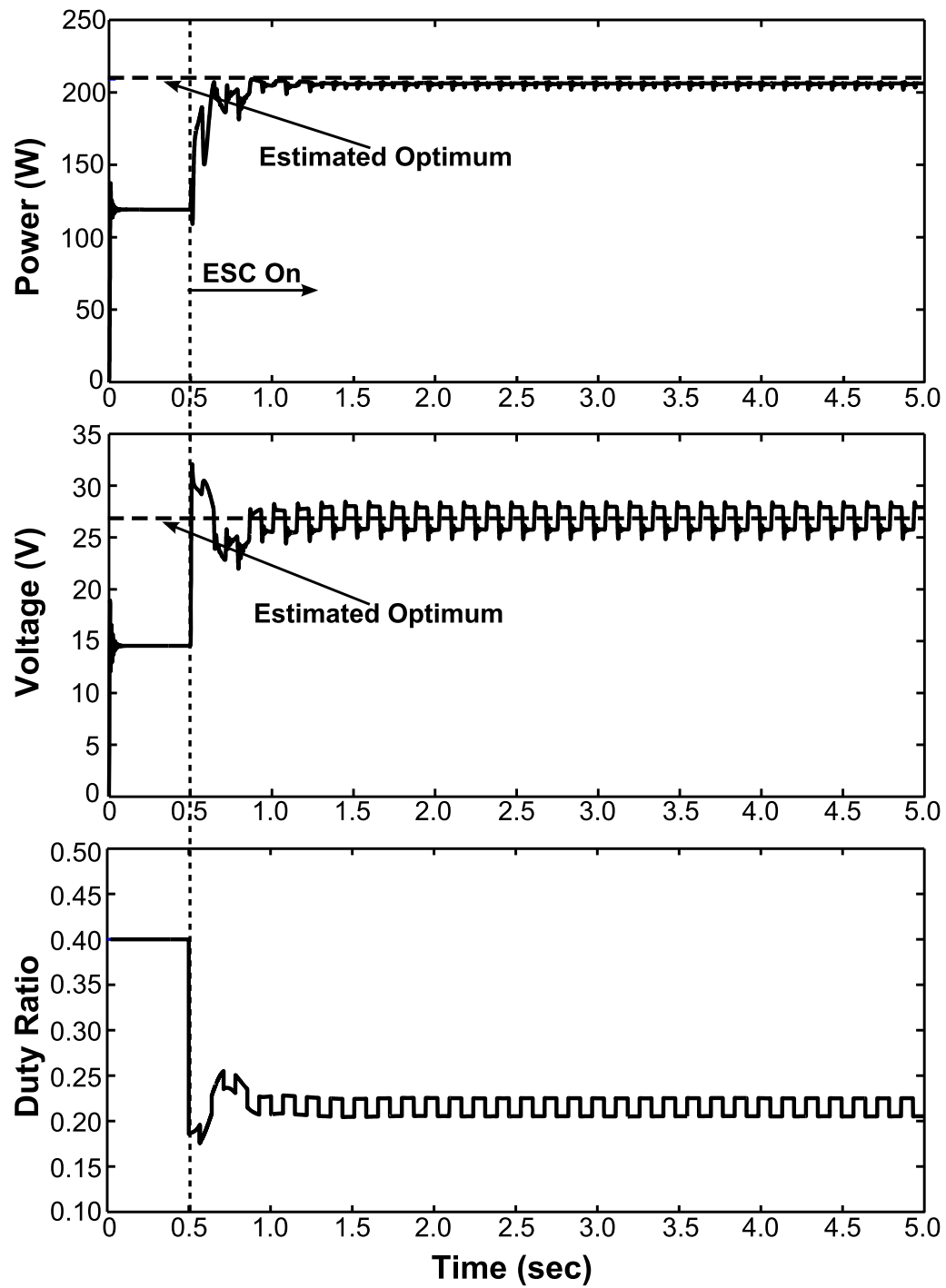


Figure 6.13: ESC simulation results for single PV module under nominal conditions with duty ratio as control input: upper subplot: power; middle subplot: voltage; lower subplot:

duty ratio

Figure 6.14 compares the voltage profiles for several different shunt resistances, with a zoomed view for about ½ cycle of a square-wave dithered output. It reveals that at the rising edge of the voltage transient signal, the PV module with lower shunt resistance value experiences a longer settling time. Among all typical transient characteristics, the integral performance indices have shown better separation as the shunt internal resistance changes (e.g. ISE, IAE, ITSE and ITAE). Table I summarizes the four integral performance indices which are calculated with the first half period (starting from the rising edge) of the ESC voltage signal (about 0.06 sec) after reaching the steady state, with the respective steady-state values removed.

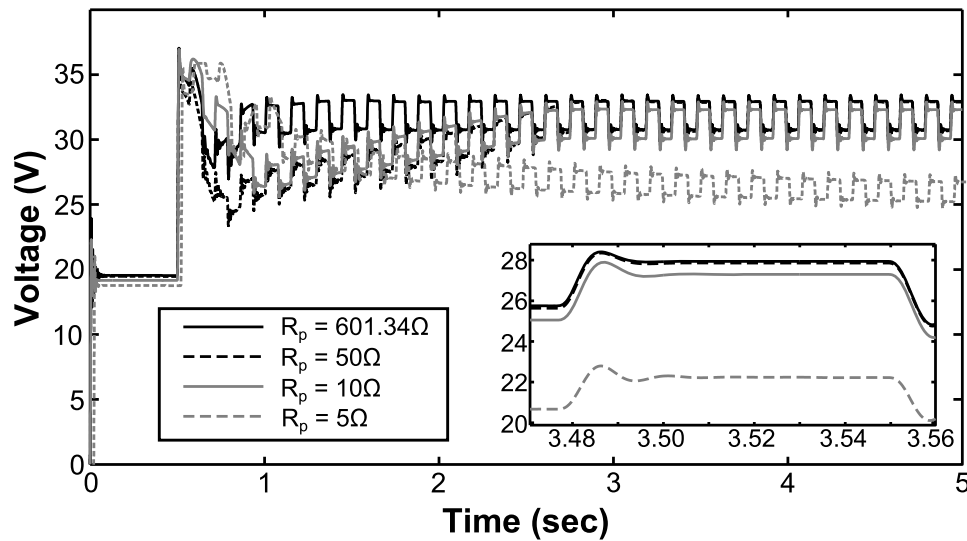


Figure 6.14: Comparison of ESC searched voltage with different shunt resistances

The integral performance indices are computed by

$$ISE_i = \int_{t_1}^{t_2} \left(\frac{V_i(\tau) - V_{is}}{h_i} \right)^2 d\tau \quad (6.16)$$

$$IAE_i = \int_{t_1}^{t_2} \left| \frac{V_i(\tau) - V_{is}}{h_i} \right| d\tau \quad (6.17)$$

$$ITSE_i = \int_{t_1}^{t_2} (\tau - t_1) \cdot \left(\frac{V_i(\tau) - V_{is}}{h_i} \right) d\tau \quad (6.18)$$

$$ITAE_i = \int_{t_1}^{t_2} (\tau - t_1) \cdot \left| \frac{V_i(\tau) - V_{is}}{h_i} \right| d\tau \quad (6.19)$$

where $[t_1, t_2]$ is the selected dither period, V_i is the voltage signal, and V_{is} is the mean value of the steady-state voltage signal. h_i is the amplitude of the square-wave dithered voltage signal, i.e. half of the difference between the steady-state values of the rising edge and falling edge of the square-wave dithered signal, which is included to reduce the influence of voltage amplitude change, e.g. due to power loss or irradiance change.

TABLE 6.1

ESTIMATED MAXIMUM ACHIEVABLE POWER AND INTEGRAL PERFORMANCE INDICES OF SQUARE-WAVE DITHER OUTPUT UNDER DIFFERENT SHUNT RESISTANCE R_p

R_p (Ω)	P_{max} (W)	ISE _i	IAE _i	ITSE _i	ITAE _i
601.34	209.14	6.037	19.471	0.0106	0.0567
100	203.33	6.118	19.484	0.0109	0.0573
50	196.10	6.189	20.506	0.0114	0.0678
20	175.53	6.668	21.747	0.0125	0.0776
10	139.95	9.670	28.313	0.0206	0.1254
8	123.90	12.470	34.166	0.0295	0.1778
6	97.04	20.729	61.817	0.0845	0.9479
5	80.63	34.437	113.211	0.4558	2.8137
4	65.05	89.402	224.285	2.2765	6.4818

As shown in Table 6.1, the maximum achievable power of the PV module decreases when R_p decreases, but have notable change only when R_p reduces down to 20 Ω or lower. Meanwhile, the integral performance indices values increase significantly while

the internal shunt resistance decreases below $20\ \Omega$, and especially when R_p is lower than $6\ \Omega$. Therefore, the integral performance indices evaluated at the rising edge of the voltage transient signal can be a promising detection probe for avoiding the severe degradation in PV power generation due to the significant change in internal shunt resistance.

Meanwhile, it is noteworthy that shunt resistance R_p also changes with temperature and irradiation level which are not degradation factors. Banerjee and Anderson [217] showed the temperature dependence of the shunt resistance above a threshold temperature by experimental analysis, and also investigated the irradiation induced impact on shunt resistance. Bouattour *et al.* [44] investigated the dependence of the shunt resistance on the illumination intensity. These studies showed that the change of shunt resistance is limited due to these degradation irrelevant environment factors. According to [188], the PV device degradation may cause far more significant reduction of R_p value, which can reduce as low as $0.2\ \Omega$ with significant decrease of the PV output power. For the PV module in Section 6.2.1, the estimated P - V and I - V curves under different R_p values are shown in Fig. 1.8 and Fig. 1.9.

The power curve does not change too much when $R_p \in [50, 601.34]\ \Omega$, but will show significant change when $R_p < 10\ \Omega$, e.g. the maximum achievable power is reduced by over 60% when R_p drops to $5\ \Omega$. The simulation results show significant change in transient characteristics for R_p value below $20\ \Omega$. In this range, the change of internal resistance is little affected by the degradation irrelevant environmental factors such as temperature and irradiation. Therefore, under the square-wave dither, degradation related

change of internal resistance can be detected when the ESC steady-state transient characteristics demonstrate significant changes.

For the multi-string case, the ESC integrated detection of internal shunt resistance change is simulated with two strings in parallel connection, under the nominal environment conditions as aforementioned, i.e. 25°C and 1000 W/m². Each string contains only one single module, and the respective duty ratio signals are control inputs. The internal shunt resistance of Channel 1 is of the nominal value 601.34 Ω , while that of Channel 2 is valued from the nominal 601.34 Ω , 10 Ω , 8 Ω , 6 Ω and 5 Ω . Figure 6.15 shows the simulation results for the case of Channel 2 internal resistance being 8 Ω . The multi-string ESC searched powers are 208.9 W and 122.8 W, respectively, as shown in the upper subplot, which are very close to the estimated optima (209.14 W and 123.9 W as shown in Table 6.1). The corresponding voltage profiles are shown in lower subplot.

Similar to the previous simulation of single-string case, the integral error indices are calculated as shown in Table 6.2. Please note that the dither frequencies of Channel 1 and Channel 2 are different as required by the multi-input ESC design. So the integral error index of the nominal value (601.34 Ω) in Channel 1 has a slightly difference compared to the nominal value (601.34 Ω) in Channel 2. The changes of the internal shunt resistance R_p in Channel 2 do not affect much on the transient performance in Channel 1. The results of Channel 2 with different internal shunt resistance R_p show clearly monotonic increase of integral error indices.

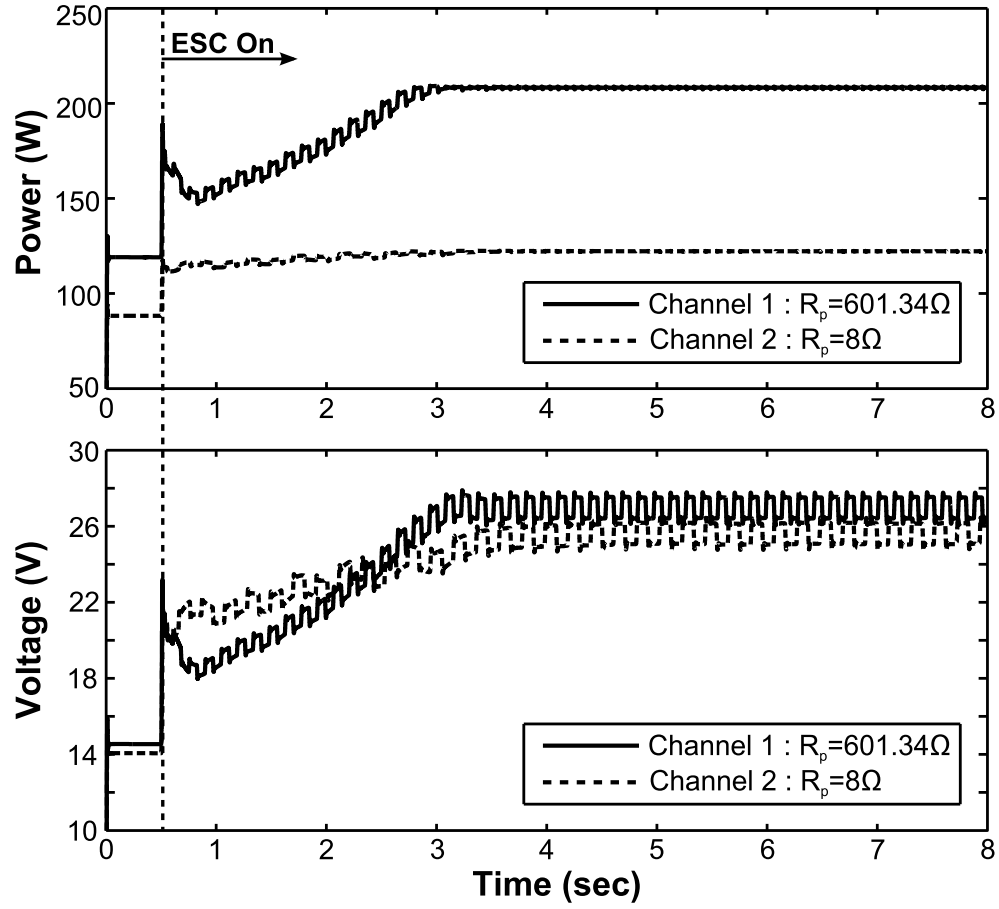


Figure 6.15: ESC simulation for two-string PV array of different internal resistance

TABLE 6.2

INTEGRAL PERFORMANCE INDICES OF SQUARE-WAVE DITHER OUTPUT UNDER DIFFERENT R_p WITH MULTI-STRING FRAMEWORK

Channel 1:

R_p (Ω)	ISE_i	IAE_i	$ITSE_i$	$ITAE_i$
(601.34, 601.34)	5.765	24.013	0.0144	0.146
(601.34, 10)	6.388	25.446	0.0163	0.155
(601.34, 8)	6.400	25.495	0.0163	0.157

(601.34 , 6)	6.407	25.689	0.0163	0.168
(601.34 , 5)	6.463	26.119	0.0163	0.184

Channel 2:

$R_p (\Omega)$	ISE _i	IAE _i	ITSE _i	ITAE _i
(601.34, 601.34)	6.627	29.514	0.0182	0.347
(601.34, 10)	10.726	44.291	0.0424	0.720
(601.34, 8)	13.315	57.537	0.0845	1.231
(601.34, 6)	25.007	127.714	0.7874	4.293
(601.34, 5)	44.601	164.995	1.2771	5.476

6.4. Summary

The proposed dither ESC integrated detection of the change in internal resistance is investigated from both analysis and control implementation standpoints. The small-signal transfer function analysis justified the impact of the internal resistance on the transient characteristics of step responses. The simulation study consists of two parts: single-string case and multi-string case. For both cases, the monotonic relationship between integral error indices and the shunt internal resistance is clearly demonstrated, which strongly validates the proposed scheme. For the multi-string case, the integral error indices results showed that the coupling effect is rather weak, which indicates that the detection performance would be quite consistent even under multi-string operation. The proposed ESC integrated detection scheme achieves online monitoring of the internal resistance of

individual PV string with relatively simple computation, and does not require the use of any additional sensor. For PV health monitoring, consistent prognostic features can thus be developed based the integral error indices of the steady-state signals of the dither ESC outputs.

Chapter 7. Conclusion and Future Work

In this chapter, this dissertation research will be summarized. An overview of the achievements in this dissertation research is given, along with a conclusion of the contributions. Finally, some possible future work is suggested that may be followed by further research.

7.1. Summary of Research Work and Contribution

As described in Chapter 1, development of net-zero energy buildings is anchored on two pillars: enhancing the generation and reducing the consumption. This dissertation study can be deemed as three control related case studies that endorse such understanding: 1) minimize the power consumption of the chilled-water plant that consists of a screw chiller and cooling tower; 2) maximize the power generation of PV system; 3) control integrated monitoring of internal resistance of PV system which would facilitates prognostic health monitoring and in turn avoid the power loss and reduce the O&M cost.

All the three pieces of work are imprinted with the same background: extremum seeking control. The unanimous choice of self-optimizing control is not coincidence, but reflecting the realistic challenge in controls of net-zero energy buildings. Building HVAC systems are inherently complex, nonlinear and time-varying dynamic processes mingled with the ambient conditions and occupancy variations. However, HVAC practice expects as low as possible investment for control design and implementation. HVAC controllers are desired to be simple, easy to tune, and easy to maintain. In parallel, the on-site (or building integrated) renewable generation for the net-zero energy buildings shares some

similarities. For photovoltaic systems, although the electrical systems are model-wise more tractable than the thermofluid systems in HVAC, the intrinsic and environmental conditions change dramatically. Finally, control and monitoring of both HVAC and renewable generation systems are desired to rely on fewer measurements and if possible, more reliable and more cost-effective measurements. The research approaches adopted in this dissertation study have reflected these considerations.

In this dissertation study, the following aspects of research have been covered for both self-optimizing control of chiller water system and PV system MPPT and fault detection. For dynamic modeling and optimization control of chilled water system, the major milestones accomplished are

- Development of Modelica based dynamic simulation models for a chilled-water system, with major efforts paid to a counter flow cooling tower and a screw chiller.
- Implementation and simulation of dither ESC based self-optimizing control scheme for chilled water system operation.

For the PV MPPT and fault detection, the major accomplishments are:

- Investigation and implementation of MPPT control of PV system using the adaptive ESC.
- Investigation and implementation of the dither ESC based single- and multi-string PV MPPT with integrated degradation detection.

The major contributions of this dissertation research are summarized as follows.

- 1) Modeling of Chiller-Tower Cycle Plant. In this dissertation study, the Modelica based chilled water system components are developed including the mechanical draft counter flow wet cooling tower and the screw compressor. The dynamic

model of cooling tower is developed by utilizing the finite-volume method and one dimensional heat and mass transfer analysis with the assumptions follow [104]. The steady-state performance of the proposed cooling tower model is evaluated with the experimental data from [195]. The transient behavior is evaluated via benchmarking against the case studies in [107] and investigation through tower cell performances with the changes of tower inlet conditions. A static screw compressor model is developed with assumed polytropic compression process due to its relatively small thermal inertia. The entire chiller-tower cycle test plant including two liquid cycles as shown in Fig. 1.5: one is the chiller-tower water cycle, and the other is the chiller refrigerant cycle. The model of chiller-tower cycle can benefit not only the ESC design in this dissertation study, but would facilitate many other tasks, e.g. modeling and control of plants with multiple chillers and cooling towers, fault detection and diagnosis. The cooling towers are also widely used in power and chemical industry. The evaporative cooling process is also adopted in the home evaporation air coolers. The Modelica based model developed in this study can be easily extended to such applications.

- 2) Self-optimizing Operation of Chilled Water System using Dither ESC: Dither ESC is implemented to achieve the self-optimizing operation on the chilled water model developed with Dymola and TIL library. As the cooling tower inlet water mass flow rate assumed to be constant, the variable part of the total power consumption (tower fan + chilled compressor) of the chilled water system is taken as the feedback to the ESC controller. The cooling tower fan speed is set as the control input. The effectiveness of the ESC controller is evaluated through

simulation study with different condition changes. The anti-windup ESC scheme [156] is applied to avoid the potential integral windup problem may be caused by the operation limitation of the cooling tower fan (actuator saturation). The inner loop evaporator superheat and chiller leaving temperature controls are also achieved by regulating the valve flow area and the compressor slide-valve opening.

- 3) MPPT Control for PV System Using Adaptive ESC: The adaptive ESC [43] is applied to the PV MPPT problem using Simulink. A single PV array [176] is treated as a whole to evaluate the control scheme. The state-space model of PV-buck system is derived with averaging analysis for AESC design. The $I(V)$ nonlinearity is treated as an unknown term and it is estimated by the RBFNN based adaptive update law. The duty ratio of the PWM of the DC-DC buck converter is used as the control input. The convergence of the controlled system is ensured by Lyapunov based inverse optimal design technique [43].
- 4) Dither ESC Based MPPT for Integrated Detection of PV Internal Resistance Change. The key consideration behind this work is that the internal resistance of PV module affects the transient characteristics of step changes, while the dither ESC MPPT with square-wave dither has its steady-state signals being effectively trains of small-amplitude step responses. The small-signal transfer function analysis is performed to demonstrate such impact. The idea is demonstrated with both single- and multi-string PV systems using single- and multi-input dither ESC. For multi-string PV systems, the total power signal of the PV system at the DC bus is used as the feedback, and the PV output voltages of individual PV

modules are used as the control input. The simulation results reveal the qualitative relationship between the internal shunt resistance and the integral error indices. An encouraging observation is that the coupling between different channels seems weak, which implies the possibility of consistent monitoring using the proposed idea for multi-string scenarios.

7.2. Recommended Future Work

This dissertation study has developed the Modelica based dynamic modeling of the mechanical draft counter flow cooling tower and the chiller-tower cycle test plant. A major missing work is that no field test data are available to sustain the proposed models. Experimental validation of the proposed detailed physical based models would be a great benefit in the future. The effectiveness of the Dither ESC based self-optimizing operation of the chilled water system is only evaluated through simulation. The experimental studies on a realistic chilled water system would be desirable in the future with possibly improved parameter tuning and control design.

In this study, the chiller-tower cycle treats the air handling unit (AHU) part only as a variable load. As the AHU model has already been developed by [153], it is desirable to involve the AHU part into the chilled water system plant. Multiple-loop optimization control could be investigated on the entire chilled water system by involving economizer control, cooling tower fan control and cooling tower inlet water mass flow rate control (water pump control). With the proven effectiveness and the advantage of model-free feature, ESC is still recommended in the future work.

As in [79, 85], the adaptive ESC has been discussed with state constrained system, it could be interesting to investigate the state constraint within PV system, i.e. the current or voltage limitation on the PV array output. And also, in the proposed AESC control scheme on PV MPPT, the duty ratio of the converter PWM is selected as the control input, which is definitely limited in the range of $[0, 1]$. The input constraint problem of adaptive ESC is also interesting to consider.

For the MPPT and the ESC integrated detection, it would be beneficial to perform experimental studies to validate and improve the proposed strategies.

References

- [1] U. S. Department of Energy, *Building Energy Data Book*, Technical Report, 2010.
Available: <http://buildingsdatabook.eren.doe.gov>
- [2] J. E. Seem and Y. Li, *Control of Cooling Towers for Chilled Fluid Systems*, US Patent 12/777097, 2010.
- [3] J. E. Braun and G. T. Diderrich, "Near-Optimal Control of Cooling Towers for Chilled Water Systems," *ASHRAE Transactions*, vol. 96, no. 2, pp. 806-816, 1990.
- [4] Energy Information Administration, *Emissions of Greenhouse Gases in the United States*, U.S. Department of Energy DOE/EIA-0573(2007), 2007.
- [5] Environmental Protection Agency, *Green Building History in the U.S.*, 2010.
Available: <http://www.epa.gov/greenbuilding/pubs/about.htm>
- [6] U. S. Department of Energy, *Building Technologies Program*, Sep. 2011.
Available:
http://www1.eere.energy.gov/buildings/commercial/commercial_bookmark.html
- [7] T. T. Chow, G. Q. Zhang, Z. Lin and C. L. Song, "Global Optimization of Absorption Chiller System by Genetic Algorithm, Energy and Buildings," *Energy and Buildings*, vol. 34, no. 1, pp. 103-109, 2001.
- [8] K. F. Fong, V. I. Hanby and T. T. Chow, "HVAC System Optimization for Energy Management by Evolutionary Programming," *Energy and Buildings*, vol. 38, no. 3, pp. 220-231, 2006.
- [9] ASHRAE, *ASHRAE Handbook -- HVAC Systems and Equipment (SI)*, 2008.
- [10] Z. Ma, S. Wang, X. Xu and F. Xiao, "A Supervisory Control Strategy for Building Cooling Water Systems for Practical and Real Time Applications," *Energy Conversion & Management*, vol. 49, no. 8, pp. 2324-2336, 2008.

- [11] A. Kaya and A. Sommer, "Energy Management of Chillers by Multilevel Control and Optimization," *Journal of Dynamic Systems, Measurement, and Control*, vol. 107, no. 4, pp. 270-277, 1985.
- [12] REN21, *Renewables 2011 Global Status Report*, 2011.
Available:
http://www.ren21.net/Portals/97/documents/GSR/REN21_GSR2011.pdf
- [13] C. Martin, *Global Solar Energy May Reach 980 Gigawatts by 2020*, 2010.
Available: http://www.seia.org/cs/news_detail?pressrelease.id=1132
- [14] F. W. Yu and K. T. Chan, "Economic Benefits of Optimal Control for Water-Cooled Chiller Systems Serving Hotels in a Subtropical Climate," *Energy and Buildings*, vol. 42, no. 2, pp. 203-209, 2010.
- [15] C.-W. Liu and Y.-K. Chuah, "A Study on an Optimal Approach Temperature Control Strategy of Condensing Water Temperature for Energy Saving," *International Journal of Refrigeration*, vol. 34, no. 3, pp. 816-823, 2011.
- [16] T. James, A. Goodrich, M. Woodhouse, R. Margolis and S. Ong, *Building-Integrated Photovoltaics (BIPV) in the Residential Sector: An Analysis of Installed Rooftop System Prices*, Technical Report, NREL/TP-6A20-53103, Nov. 2011.
- [17] H. P. Desai and H. K. Patel, "Maximum Power Point Algorithm in PV Generation: An Overview," in *7th International Conference on Power Electronics and Drive Systems*, pp. 624-630, Bangkok, Thailand, Nov. 2007.
- [18] J. A. der Cueto, "Method for Analyzing Series Resistance and Diode Quality Factors from Field Data. Part II: Applications to Crystalline Silicon," *Solar Energy Materials & Solar Cells*, vol. 59, no. 4, pp. 393-405, 1999.
- [19] Carrier, "Optimizing Chiller Plant Efficiency: Factors to Consider," *HVAC Analysis*, vol. 3, no. 1, pp. 1-5, 2011.
- [20] Y. Yao and J. Chen, "Global Optimization of a Central Air Conditioning System Using Decomposition Coordination Method," *Energy and Buildings*, vol. 42, no. 5, pp. 570-583, 2010.

- [21] Y. Yao, Z. W. Lian, Z. J. Hou and X. J. Zhou, "Optimal Operation of a Large Cooling System Based on Empirical Model," *Applied Thermal Engineering*, vol. 24, no. 16, pp. 2303-2321, 2004.
- [22] V. Tyagi, H. Sane and S. Darbha, "An Extremum Seeking Algorithm for Determining the Set Point Temperature for Condensed Water in a Cooling Tower," in *Proceedings of the 2006 American Control Conference*, pp. 1127-1131, Minneapolis, MN, Jun. 2006.
- [23] H. S. Sane, C. Haugetetter and S. A. Bortoff, "Building HVAC Control Systems - Role of Controls and Optimization," in *Proceedings of the 2006 American Control Conference*, pp. 1121-1126, Minneapolis, MN, Jun. 2006.
- [24] S. K. Wang, *Handbook of Air Conditioning and Refrigeration*, 2nd. ed., New York, NY: McGraw-Hill, 2000.
- [25] ASHARE, *ASHRAE Handbook -- HVAC Applications (A)*, 2007.
- [26] Modelica Association, *Modelica and Modelica Association*, 2012.
Available: <http://www.modelica.org>
- [27] Dassault Systèmes, *Dymola: Multi-Engineering Modeling and Simulation*, 2012.
Available: <http://www.3ds.com/products/catia/portfolio/dymola>
- [28] MathWorks, *Simulink: Simulation and Model-Based Design*, 2012.
Available: <http://www.mathworks.com/products/simulink/>
- [29] TLK-Thermo GmbH, *Engineering Services and Software for Thermal Systems*, 2012.
Available: <http://www.tlk-thermo.com/index.php>
- [30] W. Zhang, C. Zhang and G. Ding, "Transient Modeling of an Air-Cooled Chiller with Economized Compressor. Part I: Model Development and Validation," *Applied Thermal Engineering*, vol. 29, no. 11-12, pp. 2396-2402, 2009.
- [31] P. Li, *Dynamic Modeling and Self-Optimizing Control of Building HVAC Systems*, Department of Mechanical Engineering, University of Wisconsin - Milwaukee, Milwaukee, WI, Ph.D. Dissertation, 2011.

- [32] C. Hua, J. Lin and C. Shen, "Implementation of a DSP-Controlled Photovoltaic System with Peak Power Tracking," *IEEE Transactions on Industrial Electronics*, vol. 45, no. 1, pp. 99-107, 1998.
- [33] K. H. Hussein, I. Muta, T. Hoshino and M. Osakada, "Maximum Photovoltaic Power Tracking: An Algorithm for Rapidly Changing Atmospheric Conditions," in *IEE Proceedings: Generation, Transmission and Distribution*, vol. 142, no. 1, pp. 59-64, 1995.
- [34] E. Koutroulis, K. Kalaitzakis and N. C. Voulgaris, "Development of a Microcontroller-Based, Photovoltaic Maximum Power Point Tracking Control System," *IEEE Transactions on Power Electronic*, vol. 16, no. 1, pp. 46-54, 2001.
- [35] H. E.-S. A. Ibrahim, F. F. Houssiny, H. M. Zein El-Din and M. A. El-Shibini, "Microcomputer Controlled Buck Regulator for Maximum Power Point Tracker for DC Pumping System Operates from Photovoltaic System," in *IEEE International Conference on Fuzzy Systems*, vol. 1, pp. 406 - 411, Seoul, South Korea, 1999.
- [36] M. Arutchelvi and S. Arul Daniel, "Voltage Control of an Autonomous Hybrid Generation Scheme Based on PV Array and Wind-Driven Induction Generators," *Electric Power Components and Systems*, vol. 34, no. 7, pp. 759-773, 2006.
- [37] C.-Y. Won, D.-H. Kim, S.-C. Kim, W.-S. Kim and H.-S. Kim, "New Maximum Power Point Tracker of Photovoltaic Arrays Using Fuzzy Controller," *PESC Record - IEEE Annual Power Electronics Specialists Conference*, vol. 1, pp. 396-403, 1994.
- [38] R. Leyva, C. Alonso, I. Queinnec, A. Cid-Pastor, D. Lagrange and L. Martinez-Salamero, "MPPT of Photovoltaic Systems Using Extremum-Seeking Control," *IEEE Transaction Aerospace and Electronic Systems*, vol. 42, no. 1, pp. 249-258, 2006.
- [39] S. L. Brunton, C. W. Rowley, S. R. Kulkarni and C. Clarkson, "Maximum Power Point Tracking for Photovoltaic Optimization Using Extremum Seeking," in *Proceedings for 34th IEEE Photovoltaic Specialists Conference (PVSC 2009)*, pp. 000013-000016, Philadelphia, PA, Jun. 2009.
- [40] P. Lei, Y. Li and J. E. Seem, "Modeling and Global MPPT Control for Photovoltaic Array with Variable Shading," *IEEE Transactions on Sustainable Energy*, vol. 2, no. 3, pp. 348-358, 2011.

- [41] P. Lei, Y. Li, Q. Chen and J. E. Seem, "Extremum Seeking Control Based Integration of MPPT and Degradation Detection for Photovoltaic Arrays," in *Proceedings of the 2010 American Control Conference*, pp. 3536-3541, Baltimore, MD, Jun. 2010.
- [42] S. J. Moura and Y. A. Chang, "Asymptotic Convergence through Lyapunov-Based Switching in Extremum Seeking with Application to Photovoltaic Systems," in *Proceedings of the 2010 American Control Conference*, pp. 3542-3548, Baltimore, MD, Jun. 2010.
- [43] M. Guay, D. Dochain and M. Perrier, "Adaptive Extremum Seeking Control of Continuous Stirred Tank Bioreactors with Unknown Growth Kinetics," *Automatica*, vol. 40, no. 5, pp. 881-888, 2004.
- [44] M. A. Bouattour, A. A. Tarabsheh, I. Radev and M. B. Schubert, "Shunt Detection in Amorphous Silicon Modules by Current/Voltage Measurements," in *the 25th European Photovoltaic Solar Energy Conference & Exhibition / 5th World Conference on Photovoltaic Energy Conversion*, pp. 2924-2927, Valencia, Spain, Sep. 2010.
- [45] California Energy Commission and the California Public Utilities Commission, *List of Eligible SB1 Guidelines Compliant Photovoltaic Modules*, 2012.
Available: http://www.gosolarcalifornia.ca.gov/equipment/pv_modules.php
- [46] U. S. Department of Energy, *Energy Efficiency & Renewable Energy - Energy Basics: Photovoltaic Cell Materials*, 2011.
Available:
http://www.eere.energy.gov/basics/renewable_energy/pv_cell_materials.html
- [47] S. Bowden and C. Honsberg, *Lifetime of PV Modules - Degradation and Failure Modes*, 2012.
Available: <http://pvcdrom.pveducation.org/MODULE/Failure.htm>
- [48] E. E. van Dyk, E. L. Meyer, F. J. Vorster and A. W. R. Leitch, "Long-Term Monitoring of Photovoltaic Devices," *Renewable Energy*, vol. 25, no. 2, pp. 183-197, 2002.
- [49] D. Sera and R. Teodorescu, "Robust Series Resistance Estimation for Diagnostics of Photovoltaic Modules," in *Proceedings of the 35th Annual Conference of IEEE Industrial Electronics Society*, pp. 800-805, Porto, Portugal, Nov. 2009.

- [50] F. J. Pern, I. L. Eisgruber and R. H. Micheels, "Spectroscopic, Scanning Laser OBIC and *I-V/QE* Characterizations of Browned EVA Solar Cells," in *Proceedings of the 25th IEEE PV Specialists Conference*, pp.1255-1258, Washington, D.C., May 1996.
- [51] E. L. Meyer, *Investigation of Properties and Energy Rating of Photovoltaic Modules*, University of Nelson Mandela Metropolitan, Port Elizabeth, South Africa, M.Sc. Thesis, 1999.
- [52] C. R. Osterwald and T. J. McMahon, "History of Accelerated and Qualification Testing Terrestrial Photovoltaic Modules: A Literature Review," *Progress in Photovoltaics: Research and Applications*, vol. 17, no. 1, pp. 11-33, 2009.
- [53] T. J. McMahon, T. S. Basso and S. R. Rummel, "Cell Shunt Resistance and Photovoltaic Module Performance," in *Proceedings of 25th IEEE Photovoltaic Specialist Conference*, pp. 1291-1294, Washington, D.C., May 1996.
- [54] C. Zhang and R. Ordóñez, *Extremum-Seeking Control and Applications: A Numerical Optimization-Based Approach*, New York, NY: Springer-Verlag, LLC, 2012.
- [55] M. Leblanc, "Sur l'électrification des Chemins de fer au Moyen de Courants Alternatifs de Frequence Elevee," in *Revue Generale de l'Electricite*, France, 1922.
- [56] C. S. Drapper and Y. T. Li, *Principles of Optimalizing Control Systems and an Application to the Internal Combustion Engine*, ASME, 1951.
- [57] A. L. Frey, W. B. Deem and R. J. Altpeter, "Stability and Optimal Gain in Extremum-Seeking Adaptive Control of a Gas Furnace," in *Proceedings of the Third IFAC World Congress*, vol. 48A, London, British, 1966.
- [58] O. L. R. Jacobs and G. C. Shering, "Design of a Single-Input Sinusoidal-Perturbation Extremum-Control System," in *Proceedings of IEE*, vol. 115, no. 1, pp. 212-217, Jan. 1968.
- [59] V. V. Kazakevich, "Extremum Control of Objects with Inertia and of Unstable Objects," *Soviet Physics Doklady*, vol. 5, pp. 658-661, 1960.

- [60] I. S. Morosanov, "Method of Extremum Control," *Automation Remote Control*, vol. 18, pp. 1077-1092, 1957.
- [61] A. A. Pervozvanskii, "Continuous Extremum Control System in the Presence of Random Noise," *Automation Remote Control*, vol. 21, pp. 673-677, 1960.
- [62] P. F. Blackman, "Extremum-Seeking Regulators," in *An Exposition of Adaptive Control*, J. H. Westcott (Ed), Macmillan, New York, NY, 1962.
- [63] S. M. Meerkov, "Asymptotic Methods for Investigating Stability of Continuous Systems of Automatic Optimization Subjected to Disturbance Action," *Avtomatika i Telemekhanika*, vol. 12, pp. 14-24, 1968.
- [64] J. Sternby, "Extremum Control Systems: An Area for Adaptive Control?," in *Proceedings of the Joint American Control Conference*, San Francisco, CA, 1980.
- [65] J. Sternby, "Adaptive Control of Extremum Systems," *Methods and Applications in Adaptive Control*, Lecture Notes in Control and Information Sciences, vol. 24, pp. 151-160, 1980.
- [66] K. J. Åström and B. Wittenmark, *Adaptive Control*, New Jersey: Prentice Hall, 1995.
- [67] M. Krstić and H.-H. Wang, "Stability of Extremum Seeking Feedback for General Nonlinear Dynamic Systems," *Automatica*, vol. 36, no. 4, pp. 595-601, 2000.
- [68] J. Y. Choi, M. Krstić, K. B. Ariyur and J. S. Lee, "Extremum Seeking Control for Discrete-Time Systems," *IEEE Transactions on Automatic Control*, vol. 47, no. 2, pp. 318-323, 2002.
- [69] M. Krstić, "Performance Improvement and Limitations in Extremum Seeking Control," *Systems and Control Letters*, vol. 39, no. 5, pp. 313-326, 2000.
- [70] M. Krstić and H. Deng, *Stabilization of Nonlinear Uncertain Systems*, Springer, 1998.
- [71] Y. Tan, D. Nešić, I. Mareels and A. Astolfi, "On Global Extremum Seeking in the Presence of Local Extrema," *Automatica*, vol. 45, no. 1, pp. 245-251, 2009.

- [72] Y. Tan, D. Nešić and I. Mareels, "On the Choice of Dither in Extremum Seeking Systems: A Case Study," *Automatica*, vol. 44, no. 5, pp. 1446-1450, 2008.
- [73] Y. Tan, D. Nešić and I. Mareels, "On Non-Local Stability Properties of Extremum Seeking Control," *Automatica*, vol. 42, no. 6, pp. 889-903, 2006.
- [74] D. Nešić, "Extremum Seeking Control: Convergence Analysis," *European Journal of Control*, vol. 15, no. 3-4, pp. 331-347, 2009.
- [75] M. A. Rotea, "Analysis of Multivariable Extremum Seeking Algorithms," in *Proceedings of American Control Conference*, vol. 1, pp. 433-437, Chicago, IL, 2000.
- [76] G. C. Walsh, "On the Application of Multi-Parameter Extremum Seeking Control," in *Proceedings of American Control Conference*, vol. 1, no. 6, pp. 433-437, Chicago, IL, 2000.
- [77] K. B. Ariyur and M. Krstić, "Analysis and Design of Multivariable Extremum Seeking," in *Proceedings of the American Control Conference*, vol. 4, pp. 2903-2908, Nov. 2002.
- [78] K. B. Ariyur and M. Krstić, *Real-Time Optimization by Extremum-Seeking Control*. New York: John Wiley & Sons, Inc., NY, 2003.
- [79] D. DeHaan and M. Guay, "Extremum-Seeking Control of State-Constrained Nonlinear Systems," *Automatica*, vol. 41, no. 9, pp. 1567-1574, 2005.
- [80] M. Guay, D. Dochain and M. Perrier, "Adaptive Extremum-Seeking Control of Nonisothermal Continuous Stirred Tank Reactors," *Chemical Engineering Science*, vol. 60, no. 13, pp. 3671-3681, 2005.
- [81] M. Guay and T. Zhang, "Adaptive Extremum Seeking Control of Nonlinear Dynamic Systems with Parametric Uncertainties," *Automatica*, vol. 39, no. 7, pp. 1283-1293, 2003.
- [82] N. Hudon, M. Guay, M. Perrier and D. Dochain, "Adaptive Extremum-Seeking Control of Convection-Reaction Distributed Reactor with Limited Actuation," *Computers and Chemical Engineering*, vol. 32, no. 12, pp. 2994-3001, 2008.

- [83] V. Adetola and M. Guay, "Parameter Convergence in Adaptive Extremum-Seeking Control," *Automatica*, vol. 43, no. 1, pp. 105-110, 2007.
- [84] R. van der Steen, "Adaptive Extremum-Seeking Control Applied to Bioreactors," Traineeship Report, Eindhoven, April, 2004.
- [85] N. Hudon, M. Guay, M. Perrier and D. Dochain, "Adaptive Extremum Seeking Control of a Tubular Reactor with Limited Actuation," in *Proceedings of American Control Conference*, vol. 7, pp. 4563-4568, Portland, OR, June 2005.
- [86] P. Cougnon, D. Dochain, M. Guay and M. Perrier, "On-Line Optimization of Fedbatch Bioreactors by Adaptive Extremum Seeking Control," *Journal of Process Control*, vol. 21, no. 10, pp. 1526-1532, 2011.
- [87] X. Li, Y. Li and J. E. Seem, "Maximum Power Point Tracking for Photovoltaic System Using Adaptive Extremum Seeking Control," to appear in *IEEE Transactions of Control Systems Technology*, DOI:10.1109/TCST.2012.2223819, 2012.
- [88] R. M. Sanner and J. E. Siotine, "Gaussian Networks for Direct Adaptive Control," *IEEE Transactions of Neural Networks*, vol. 3, no.6, pp. 837-863, 1992.
- [89] W. H. Walker, W. K. Lewis and W. H. McAdams, *Principles of Chemical Engineering*. New York: McGraw-Hill, NY, 1923.
- [90] F. Merkel, "Verdunstungskühlung," in *the VDI Forschungsarbeiten*, Berlin, No. 275, 1925.
- [91] M. Lucas, P.J. Martínez and A. Viedma, "Experimental Study on the Thermal Performance of a Mechanical Cooling Tower with Different Drift Eliminators," *Energy Conversion and Management*, vol. 50, no. 3, pp. 490-497, 2009.
- [92] B. A. Qureshi and S. M. Zubair, "A Complete Model of Wet Cooling Towers with Fouling in Fills," *Applied Thermal Engineering*, vol. 26, no. 16, pp. 1982-1989, 2006.
- [93] E. Elsarrag, "Experimental Study and Predictions of an Induced Draft Ceramic Tile Packing Cooling Tower," *Energy Conversion and Management*, vol. 47, no. 15-16, pp. 2034-2043, 2006.

- [94] J.-U.-R. Khan, M. Yaqub and S. M. Zubair, "Performance Characteristics of Counter Flow Wet Cooling Towers," *Energy Conversion and Management*, vol. 44, no. 13, pp. 2073-2091, 2003.
- [95] M. P. Maiya, "Analysis of Modified Counter-Flow Cooling Towers," *Heat Recovery Systems & CHP*, vol. 15, no. 3, pp. 293-303, 1995.
- [96] N. Ninic, A. Vehauc, "The Effect of the Choice of the Enthalpy Zero Point on Cooling Tower Design and Packing Data Processing," *Wärme - und Stoffübertragung*, vol. 27, no. 5, pp. 305-310, 1992.
- [97] J. W. Sutherland, "Analysis of Mechanical-Draught Counterflow Air/Water Cooling Towers," *ASME Transactions*, vol. 105, no. 3, pp. 576-583, 1983.
- [98] H. B. Nottage, "Merkel's Cooling Diagram as a Performance Correlation for Air-Water Evaporative Cooling Systems," *ASHVE Transactions*, vol. 47, pp. 429-448, 1941.
- [99] G. Yadigaroglu and E. L. Pastor, "An Investigation of the Accuracy of the Merkel Equation for Evaporative Cooling Tower Calculations," in *AIAA/ASME Thermophysics and Heat Transfer Conference*, ASME 74-HT-59, Boston, MA, 1974.
- [100] D. R. Baker and H. A. Shryock, "A Comprehensive Approach to the Analysis of Cooling Tower Performance," *ASME Journal of Heat Transfer*, vol. 83, pp. 339-350, 1961.
- [101] H. J. Lowe and D. G. Christie, "Heat Transfer and Pressure Drop Data on Cooling Tower Packings, and Mode Studies of the Resistance of Natural-Draught Towers to Airflow," in *ASME Heat Transfer Proceedings*, pp. 933-950, New York, NY, 1961.
- [102] J. L. Threlkeld, *Thermal Environmental Engineering*. New Jersey: Prentice-Hall Inc., 1970.
- [103] H. Jaber and R. L. Webb, "Design of Cooling Towers by Effectiveness-NTU Method," *ASME Journal Heat Transfer*, vol. 111, no. 4, pp. 837-843, 1989.

- [104] J. E. Braun, *Methodologies for the Design and Control of Central Cooling Plants*, University of Wisconsin - Madison, Madison, WI, Ph. D. Dissertation, 1988.
- [105] J. E. Braun, S. A. Klein and J. W. Mitchell, "Effectiveness Models for Cooling Towers and Cooling Coils," *ASHRAE Transactions*, vol. 95, no. 2, pp. 164-174, 1989.
- [106] M. A. Bernier, "Cooling Tower Performance: Theory and Experiments," *ASHRAE Transactions*, vol. 100, no. 2, pp. 114-121, 1994.
- [107] M. A. Bernier, "Thermal Performance of Cooling Towers," *ASHRAE Journal*, vol. 37, no. 4, pp. 56-61, 1995.
- [108] W. F. Stoecker, *Procedures for Simulating the Performance of Components and Systems for Energy Calculations*, New York, NY: ASHRAE, 1967.
- [109] M. S. Söylemez, "Theoretical and Experimental Analyses of Cooling Towers," *ASHRAE Transactions*, vol. 105, pp. 330-337, 1999.
- [110] J. C. Kloppers and D. G. Kroger, "Loss Coefficient Correlation for Wet-Cooling Tower Fills," *Applied Thermal Engineering*, vol. 23, no. 17, pp. 2201-2211, 2003.
- [111] M. Poppe and H. Rogener, "Berechnung Von Rückkühlwerken," *VDI-Wärmeatlas*, pp. Mi 1-Mi 15, 1991.
- [112] J. C. Kloppers and D. G. Kroger, "Cooling Tower Performance Evaluation: Merkel, Poppe and e-NTU Methods of Analysis," *ASME Journal of Engineering for Gas Turbines and Power*, vol. 127, no. 1, pp. 1-7, 2005.
- [113] J.-u.-R. Khan and S. M. Zubair, "An Improved Design and Rating Analyses of Counter Flow Wet Cooling Towers," *ASME Journal of Heat Transfer*, vol. 123, no. 4, p. 770-778, 2001.
- [114] S. P. Fisenko, A. A. Brin, A. I. Petruchik, "Evaporative Cooling of Water in a Mechanical Draft Cooling Tower," *International Journal of Heat and Mass Transfer*, vol. 47, no. 1, pp. 165-177, 2004.

- [115] M. Wetter, *Modelica Library for Building Energy and Control Systems*, 2009.
Available: <https://gaia.lbl.gov/bir>
- [116] N. Milosavljevic and P. Heikkila, "A Comprehensive Approach to Cooling Tower Design," *Applied Thermal Engineering*, vol. 21, no. 9, pp. 899-915, 2001.
- [117] L. Kairouani, M. Hassairi, Z. Tarek, "Performance of Cooling Tower in South of Tunisia," *Building and Environment*, vol. 39, no. 3, pp. 351-355, 2004.
- [118] P. Naphon, "Study on the Heat Transfer Characteristics of an Evaporative Cooling Tower," *International Communications in Heat and Mass Transfer*, vol. 32, no. 8, pp. 1066-1074, 2005.
- [119] G.-Y. Jin, W.-J. Cai, L. Lu, E. L. Lee and A. Chiang, "A Simplified Modeling of Mechanical Cooling Tower for Control and Optimization of HVAC Systems," *Energy Conversion and Management*, vol. 48, no. 2, pp. 355-365, 2006.
- [120] A. Ataei, M. H. Panjeshahi and M. Gharaie, "Performace Evaluation of Counter-flow Wet Cooling Towers Using Exergetic Analysis," *Transactions of the CSME*, vol. 32, no. 3-4, pp. 499-512, 2008.
- [121] X. Li, Y. Li and J. E. Seem, "Dynamic Modeling of Mechanical Draft Counter-Flow Wet Cooling Tower with Modelica," in *Proceedings of 2010 ASME Dynamic Systems and Control Conference*, vol. 2, pp. 687-694, Cambridge, MA, Sep. 2010.
- [122] X. Li, Y. Li, J. E. Seem and P. Li, "Dynamic Modeling and Self-Optimizing Operation of Chilled Water Systems Using Extremum Seeking Control," *Energy and Buildings*, Dec. 2012.
Available: <http://dx.doi.org/10.1016/j.enbuild.2012.12.010>
- [123] F. Bosnjakovic, *Technische Thermodynamik*. Dresden: Verlag von Theodor Steinkopff, 1965.
- [124] S. Bendapudi, J. E. Braun and E. A. Groll, "A Comparison of Moving-Boundary and Finite-Volume Formulations for Transients in Centrifugal Chillers," *International Journal of Refrigeration*, vol. 31, no. 8, pp. 1437-1452, 2008.

- [125] R. Cohen, "Advances in Compressor Technology," *International Journal of Refrigeration*, vol. 13, no. 4, pp. 274-277, 1990.
- [126] A. Futakawa, "Improvements in Compressors with Special Emphasis on Interesting Developments in Japan," presented at *the International Compressor Engineering Conference*, pp. 339-351, Purdue University, West Lafayette, IN, 1984.
- [127] J. Sauls, "Development of a Comprehensive Thermodynamic Modeling System for Refrigerant Screw Compressors," presented at *the International Compressor Engineering Conference*, pp. 151-156, Purdue University, West Lafayette, IN, 1996.
- [128] Z. Xing, *Screw Compressor : Theoretical Design and Application*, Mechanical Industry Publishing Company of China, 2000.
- [129] A. Kovacevic, N. Stosic and I. K. Smith, "The CFD Analysis of a Screw Compressor Suction Flow," presented at *the International Compressor Engineering Conference*, pp. 909-916, Purdue University, West Lafayette, IN, 2000.
- [130] P. C. Hanlon, *Compressor Handbook*, McGraw-Hill, 2001.
- [131] S. Jonsson, "Performance Simulations of Twin-Screw Compressors with Economizer," *International Journal of Refrigeration*, vol. 14, no. 6, pp. 345-350, 1991.
- [132] H. Wu, X. Peng, Z. Xing and P. Shu, "Experimental Study on P - V Indicator Diagrams of Twin-Screw Refrigeration Compressor with Economizer," *Applied Thermal Engineering*, vol. 24, no. 10, pp. 1491-1500, 2004.
- [133] N. Stosic, I. Smith and A. Kovacevic, *Screw Compressors: Mathematical Modeling and Performance Calculation*, New York, NY: Springer, 2005.
- [134] W. S. Lee, R. H. Ma, S. L. Chen, W. F. Wu and H. W. Hsia, "Numerical Simulation and Performance Analysis of Twin Screw Air Compressors," *International Journal of Rotating Machinery*, vol. 7, no. 1, pp. 65-78, 2001.

- [135] N. Sessaiah, R. K. Sahoo and S. K. Sarangi, "Theoretical and Experimental Studies on Oil Injected Twin Screw Air Compressor When Compressing Different Light and Heavy Gases," *Journal of Applied Thermal Engineering*, vol. 30, no. 4, pp. 327-339, 2010.
- [136] N. Sessaiah, S. K. Ghosh, R. K. Sahoo and S. K. Sarangi, "Mathematical Modeling of the Working Cycle of Oil Injected Rotary Twin Screw Compressor," *Applied Thermal Engineering*, vol. 27, no. 1, pp. 145-155, 2007.
- [137] S. V. Krichel and O. Sawodny, "Dynamic Modeling of Compressors Illustrated by an Oil-Flooded Twin Helical Screw Compressor," *Mechatronics*, vol. 21, no. 1, pp. 77-84, 2011.
- [138] J. Liu, Q. Li, F. Wang and L. Zhou, "A New Model of Screw Compressor for Refrigeration System Simulation," *International Journal of Refrigeration*, vol. 35, no. 4, pp. 861-870, 2012.
- [139] L. Fu, G. Ding, Z. Su and G. Zhao, "Steady-State Simulation of Screw Liquid Chillers," *Applied Thermal Engineering*, vol. 22, no. 15, pp. 1731-1748, 2002.
- [140] L. Fu, G. Ding and C. Zhang, "Dynamic Simulation of Air-to-Water Dual-Mode Heat Pump with Screw Compressor," *Applied Thermal Engineering*, vol. 23, no. 12, pp. 1629-1645, 2003.
- [141] W. Zhang, C. Zhang and G. Ding, "Transient Modeling of an Air-Cooled Chiller with Economized Compressor. Part II: Application to Control Design," *Applied Thermal Engineering*, vol. 29, no. 11-12, pp. 2403-2407, 2009.
- [142] L. Lu, W. Cai, Y. C. Soh, L. Xie and S. Li, "HVAC System Optimization - Condenser Water Loop," *Energy Conversion & Management*, vol. 45, no. 4, pp. 613-630, 2004.
- [143] J. Sun and A. Reddy, "Optimal Control of Building HVAC&R Systems Using Complete Simulation-Based Sequential Quadratic Programming (CSB-SQP)," *Building Environment*, vol. 40, no. 5, pp. 657-669, 2005.
- [144] E. F. Sowell and P. Haves, "Efficient Solution Strategies for Building Energy System Simulation," *Energy and Buildings*, vol. 33, no. 4, pp. 309-317, 2001.

- [145] S. B. Austin, "Chilled Water System Optimization," *ASHRAE Journal*, vol. 35, no. 7, pp. 50-56, 1993.
- [146] P. Haves, T. Salsbury, D. Claridge and M. Liu, "Use of Whole Building Simulation On-Line Performance Assessment: Modeling and Implementation issues," presented at *the Seventh International IBPSA Conference*, Rio de Janeiro, Brazil, 2001.
- [147] P. Jacobs and H. Henderson, *State of the Art Review: Whole Building, Building Envelope, and HVAC Component and System Simulation and Design Tools*, Technical Report, DOEOR22674/ARTI-21CR/605-30010-30020-01, 2002.
- [148] Y. Ma, F. Borrelli, B. Hancey, B. Coffey, S. Benga and P. Haves, "Model Predictive Control for the Operation of Building Cooling Systems," *IEEE Transactions on Control Systems Technology*, vol. 20, no. 3, pp. 796-803, 2011.
- [149] K. W. Roth, P. Llana, D. Westphalen and J. Brodrick, "Automated Whole Building Diagnostics," *ASHRAE Journal*, vol. 47, no. 5, pp. 82-84, 2005.
- [150] S. V. Shelton and C. T. Joyce, "Cooling Tower Optimization for Centrifugal Chillers," *ASHRAE Journal*, vol. 33, no. 6, pp. 28-36, 1991.
- [151] S. W. Wang and J. Burnett, "Online Adaptive Control for Optimizing Variable Speed Pumps of Indirect Water-Cooled Chilling Systems," *Applied Thermal Engineering*, vol. 21, no. 11, pp. 1083-1103, 2001.
- [152] H.-H. Wang, S. Yeung and M. Krstić "Experimental Application of Extremum Seeking on an Axial-Flow Compressor," *IEEE Transaction on Control System Technology*, vol. 8, no. 2, pp. 300-309, 2000.
- [153] P. Li, Y. Li and J. E. Seem, "Efficient Operation of Air-Side Economizer Using Extremum Seeking Control," *ASME Transactions - Journal of Dynamics Systems, Measurement and Control*, vol. 132, no. 3, pp. 031009 (10 pages), 2010.
- [154] D. J. Burns and C. Laughman, "Extremum Seeking Control for Energy Optimization of Vapor Compression Systems," presented at *the International Refrigeration and Air Conditioning Conference*, Purdue Univeristy, West Lafayette, IN, July 2012.

- [155] M. P. Cassidy and J. F. Stack, "Applying Adjustable Speed AC Drives to Cooling Tower Fans," in *Annual Petroleum and Chemical Industry Conference*, pp. 87-90, Dallas, TX, Sep. 1988.
- [156] Y. Li and J. E. Seem, *Extremum Seeking Control with Actuator Saturation Control*, US Patent 20100106331, 2010.
- [157] N. Femia, G. Petrone, G. Spagnuolo and M. Vitelli, "Optimization of Perturb and Observe Maximum Power Point Tracking Method," *IEEE Transaction Electronics*, vol. 20, no. 4, pp. 963-973, 2005.
- [158] Y. C. Kuo, T. J. Liang and J. F. Chen, "Novel Maximum-Power-Point Tracking Controller for Photovoltaic Energy Conversion System," *IEEE Transactions on Industrial Electronics*, vol. 48, no. 3, pp. 594-601, 2001.
- [159] M. Veerachary, T. Senjyu and K. Uezato, "Maximum Power Point Tracking Control of IDB Converter Supplied PV System," in *IEE Proceedings: Electric Power Applications*, vol. 148, no. 6, pp. 494-502, 2001.
- [160] G. J. Yu, Y. S. Jung, J. Y. Choi and G. S. Kim, "A Novel Two-Mode MPPT Control Algorithm Based on Comparative Study of Existing Algorithms," *Solar Energy*, vol. 76, no. 4, pp. 455-463, June 2004.
- [161] W. Xiao and W. G. Dunford, "A Modified Adaptive Hill Climbing MPPT Method for Photovoltaic Power Systems," in *Proceedings of 35th Annual IEEE Power Electronics. Specialists Conference*, vol. 3, pp. 1957-1963, 2004.
- [162] T. Hiyama, S. Kouzuma and T. Imakubo, "Identification of Optimal Operating Point of PV Modules Using Neural Network for Real Time Maximum Power Tracking Control," *IEEE Transactions on Energy Conversion*, vol. 10, no. 2, pp. 360-367, 1995.
- [163] M. G. Simoes, N. N. Franceschetti and M. Friedhofer, "A Fuzzy Logic Based Photovoltaic Peak Power Tracking Control," in *IEEE International Symposium on Industrial Electronics*, vol. 1, pp. 300-305, Pretoria, South Africa, July 1998.
- [164] B. M. Wilamowski and X. Li, "Fuzzy System Based Maximum Power Point Tracking for PV System," in *Proceedings of IEEE 2002 28th Annual Conference of the Industrial Electronics Society*, vol. 4, pp. 3280-3284, Nov. 2002.

- [165] T. Noguchi, S. Togashi and R. Nakamoto, "Short-Current Pulse-Based Maximum Power Point Tracking Method for Multiple Photovoltaic and Converter Module System," *IEEE Transactions on Industrial Electronics*, vol. 49, no. 1, pp. 217-223, 2002.
- [166] T. Yoshida, K. Ohniwa and O. Miyashita, "Simple Control of Photovoltaic Generator Systems with High-Speed Maximum Power Point Tracking Operation," *European Power Electronics and Drives Journal*, vol. 17, no. 1, pp. 38-42, 2007.
- [167] C.-C. Chu and C.-L. Chen, "Robust Maximum Power Point Tracking Method for Photovoltaic Cells: A Sliding Mode Control Approach," *Solar Energy*, vol. 83, no. 8, pp. 1370-1378, 2009.
- [168] J. Creaby, Y. Li and J. E. Seem, "Maximizing Wind Power Capture Using Multi-Variable Extremum Seeking Control," *Wind Engineering*, vol. 33, no. 4, pp. 361-387, 2009.
- [169] A. Favache, D. Dochain, M. Perrier and M. Guay, "Extremum-Seeking Control of Retention for a Microparticulate System," *Canadian Journal of Chemical Engineering*, vol. 86, no. 5, pp. 815-827, 2008.
- [170] R. Leyva, C. Olalla, H. Zazo, C. Cabal, A. Cid-Pastor, I. Queinnec and C. Alonso, "MPPT Based on Sinusoidal Extremum-Seeking Control in PV Generation," *International Journal of Photoenergy*, vol. 2012, pp. 1-7, 2011.
- [171] H. Zazo, R. Leyva and E. del Castillo, "Analysis of Newton-Like Extremum Seeking Control in Photovoltaic Panels," presented at *the International Conference on Renewable Energies and Power Quality*, Santiago de Compostela, Spain, Mar. 2012.
- [172] C. Zhang, Z. Zhang, M. Chen and Z. Qian, "An Improved Variable Step-Size Maximum Power Point Tracking (MPPT) Based on Extremum Seeking Control (ESC) in Grid-Connected Photovoltaic Micro-Converter System," presented at *the 2012 IEEE International Symposium on Industrial Electronics*, pp. 1765-1770, Hangzhou, China, May 2012.
- [173] H. Malek, S. Dadras, Y. Chen, R. Burt and J. Cook, "Maximum Power Point Tracking Techniques for Efficient Photovoltaic Microsatellite Power Supply System," presented at *the 26th Annual AIAA/USU Conference on Small Satellite*, Utah State University, Logan, UT, 2012.

- [174] A. Ghaffari, M. Krstić and D. Nėstić, "Multivariable Newton Based Extremum Seeking," *Automatica*, vol. 48, no. 8, pp. 1759-1767, 2012.
- [175] A. Ghaffari, S. Seshagiri and M. Krstić, "Power Optimization for Photovoltaic Micro-Converters Using Multivariable Gradient-Based Extremum-Seeking," presented at *the American Control Conference*, pp. 3383-3388, Montreal, QC, June 2012.
- [176] M. G. Villalva, J. R. Gazoli and E. R. Filho, "Comprehensive Approach to Modeling and Simulation of Photovoltaic Arrays," *IEEE Transactions on Power Electronics*, vol. 24, no. 5, pp. 1198-1208, 2009.
- [177] M. G. Villalva and E. R. Filho, "Dynamic Analysis of the Input-Controlled Buck Converter Fed by a Photovoltaic Array," *Sba Controle Automação Sociedade Brasileira de Automatica*, vol. 19, no. 4, pp. 463-474, 2008.
- [178] H. S. Rauschenbach, *Solar Cell Array Design Handbook*, New York: Van Nostrand Reinhold, 1980.
- [179] NREL, *Reliability Concerns and Associated with PV Technologies*, 2010. Available:
http://www.nrel.gov/pv/performance_reliability/pdfs/failure_references.pdf
- [180] T. Ishii, T. Takashima and K. Otani, "Long-Term Performance Degradation of Various Kinds of Photovoltaic Modules under Moderate Climatic Conditions," *Progress in Photovoltaics: Research and Applications*, vol. 19, no 2, pp. 170-179, 2011.
- [181] C. R. Osterwald, A. Anderberg, S. Rummel and L. Ottoson, "Degradation Analysis of Weathered Crystalline-Silicon PV Modules," in *the 29th IEEE PV Specialists Conference*, NREL/CP-520-31455, New Orleans, LA, May 2002.
- [182] J. A. Mazer, *Solar Cells: An Introduction to Crystalline Photovoltaic Technology*, Boston: Kluwer Academic Publishers, 1997.
- [183] D. L. Staebler and C. R. Wronski, "Reversible Conductivity Charges in Discharge-Produced Amorphous Si," *Applied Physics Letters*, vol. 31, no. 4, pp. 292-294, 1977.

- [184] E. L. Meyer and E. E. v. Dyk, "Monitoring I_{sc} , V_{oc} and Performance Parameters of Photovoltaic Modules," presented at *the 17th European Photovoltaic Solar Energy Conference*, pp. 524-527, 2001.
- [185] E. E. v. Dyk, B. J. Scott, E. L. Meyer and A. W. R. Leitch, "Temperature Dependence of Performance of Crystalline Silicon Photovoltaic Modules," *South African Journal of Science*, vol. 96, no. 2, pp. 198-200, 2000.
- [186] F. J. Pern, A. W. Czanderna, K. A. Emery and R. G. Dhere, "Weather Degradation of EVA Encapsulant and the Effect of Its Yellowing on Solar Cell Efficiency," presented at the *22nd IEEE PV Specialists Conference*, pp. 557-560, 1991.
- [187] H. Lukamp, *Reliability Study of Grid Connected PV Systems*, Technical Report, IEA-PVPS, Report IEA-PVPS Task7 IEA T7-08, 2002.
- [188] E. L. Meyer and E. E. v. Dyk, "The Effect of Reduced Shunt Resistance and Shading on Photovoltaic Module Performance," presented at *the 31th Photovoltaic Specialists Conference*, pp. 1331-1334, 2005.
- [189] E. Q. B. Macabebe and E. E. v. Dyk, "Extraction of Device Parameters from Dark Current-Voltage Characteristics of PV Devices," *Physica Status Solidi (c)*, vol. 5, no. 2, pp. 616-619, 2008.
- [190] M. Banavar, A. Spanias and T. Takehara, *Synthesis Lectures on Power Electronics: Signal Processing for Solar Array Monitoring, Fault Detection, and Optimization*, Morgan & Claypool Publishers, 2012.
- [191] Z. Zhang, J. Shi, J. Zhang, X. Wu and M. Li, "Study on Fault Detection for Photovoltaic Array Using Infrared Image," *Advanced Materials Research*, vol. 512-515, pp. 280-284, 2012.
- [192] Sandia National Laboratories, *PV Arc-Fault Detection and Mitigation Program*, 2012.
Available: http://energy.sandia.gov/?page_id=9108
- [193] P. Lei, *Maximum Power Point Tracking of Photovoltaic Systems via Extremum Seeking Control*, University of Wisconsin - Milwaukee, Milwaukee, WI, M. Sc. Thesis, 2012.

- [194] P. Li, Y. Li and J. E. Seem, "Consistent Initialization of System of Differential-Algebraic Equations for Dynamic Simulation of Centrifugal Chillers," *Journal of Building Performance Simulation*, vol. 5, no. 2, pp. 115-139, 2012.
- [195] W. M. Simpson and T. K. Sherwood, "Performance of Small Mechanical Draft Cooling Towers," *Refrigerating Engineering*, vol. 52, no. 6, pp. 535-543, 574-576, 1946.
- [196] C. C. Richter, *Proposal of New Object-Oriented Model Libraries for Thermodynamic Systems*, TU Braunschweig, Germany, Ph. D. Dissertation, 2008.
- [197] ASHRAE, *ASHRAE Equipment Guide*, Atlanta, GA: American Society of Heating, Refrigerating and AirConditioning Engineers Inc., 1983.
- [198] D. G. Kröger, *Air-Cooled Heat Exchangers and Cooling Towers - Thermal Flow Performance Evaluation and Design*, Penn Well Corporation, 2004.
- [199] J. L. Grange, "Calculating the Evaporated Water Flow in a Wet Cooling Tower," presented at *the 9th IAHR Cooling Tower and Spraying Pond Symposium*, von Karman Institute, Brussels, Belgium, 1994.
- [200] C. Bourillot, *TEFERI, Numerical Model for Calculating the Performance of an Evaporative Cooling Tower*, Report CS-3212-SR., Electric Power Research Institute, CA, Aug. 1983.
- [201] J. C. Kloppers and D. G. Kröger, "The Lewis Factor and Its Influence on the Performance Prediction of Wet Cooling Towers," *International Journal of Thermal Science*, vol. 44, no. 9, pp. 879-884, 2005.
- [202] R. D. Clark, *Building Systems and Equipment Simulation Program Hvacsim+ User Manual*, National Bureau of Standards and Technology, Washington D.C., 1985.
- [203] K. J. Åström and T. Hägglund, *PID Controllers: Theory, Design, and Tuning*. Research Triangle Park, NC: Instrument Society of America, 1995.
- [204] C. Bohn and D. P. Atherton, "An Analysis Package Comparing PID Anti-Windup Strategies," *IEEE Control System Magazine*, vol. 15, no. 2, pp. 34-40, 1995.

- [205] P. March and M. Turner, "Anti-Windup Compensator Designs for Nonsalient Permanent-Magnet Synchronous Motor Speed Regulators," *IEEE Transactions on Industry Applications*, vol. 45, no. 5, pp. 1598-1609, 2009.
- [206] K. Ohishi, E. Hayasaka, T. Nagano, M. Harakawa and T. Kanmachi, "High-Performance Speed Servo System Considering Voltage Saturation of a Vector-Controlled Induction Motor," *IEEE Transactions on Industrial Electronics*, vol. 53, no. 3, pp. 795-802, 2006.
- [207] Y. Peng, D. Vrancic and R. Hanus, "Anti-Windup, Bumpless, and Conditioned Transfer Techniques for PID Controllers," *IEEE Control Systems Magazine*, vol. 16, no. 4, pp. 48-57, 1996.
- [208] M. A. S. Masoum, H. Dehbonei and E. F. Fuchs, "Theoretical and Experimental Analysis of Photovoltaic Systems with Voltage and Current Based Maximum Power Point Tracking," *IEEE Transactions on Energy Conversion*, vol. 17, no. 4, pp. 514-522, 2002.
- [209] R. W. Erickson and D. Maksimovic, *Fundamentals of Power Electronics*, Kluwer Academic Publishers, 2001.
- [210] J.-B. Pomet and L. Praly, "Adaptive Nonlinear Regulation: Estimation from the Lyapunov Function," *IEEE Transactions of Automatic Control*, vol. 37, no. 6, pp. 729-740, 1992.
- [211] J. Gao, D. Feng and H. Peng, "Study on the Multi-String Photovoltaic Control System," *Computer Science for Environmental Engineering and Ecoinformatics*, vol. 158, no. 1, pp. 12-18, 2011.
- [212] S. Kouro, K. Asfaw, R. Goldman, R. Snow, B. Wu and J. Rodriguez, "NPC Multilevel Multistring Topology for Large Scale Grid Connected Photovoltaic Systems," presented at the *2010 2nd IEEE International Symposium on Power Electronics for Distributed Generation System (PEDG)*, pp. 400-405, Hefei, China, 2010.

- [213] C. S. Edrington, S. Balathandayuthapani and J. Cao, "Analysis and Control of a Multi-String Photovoltaic System Interfaced with a Utility Grid," presented at *the 2010 IEEE Power and Energy Society General Meeting*, pp. 1-6, Minneapolis, MN, 2010.

- [214] Florida Solar Energy Center, *Type of PV Systems*, 2007.
Available:
http://www.fsec.ucf.edu/en/consumer/solar_electricity/basics/types_of_pv.htm

- [215] M. Meinhardt, G. Cramer, B. Burger and P. Zacharias, "Multi-String Converter with Reduced Specific Costs and Enhanced Functionality," *Solar Energy*, vol. 69, supplement 6, pp. 217-227, 2001.

- [216] J.-M. Kwon, B.-H. Kwon and K.-H. Nam, "Grid-Connected Photovoltaic Multi-String PCS with PV Current Variation Reduction Control," *IEEE Transaction on Industrial Electronics*, vol. 56, no. 11, pp. 4381-4388, 2009.

- [217] S. Banerjee and W. A. Anderson, "Electron Irradiation Effects on the Shunt Resistance of Silicon Solar Cells," *Solar Cells*, vol. 20, no. 4, pp. 315-321, 1987.

- [218] General Electric Company, *Heat Transfer and Fluid Flow Data Book*. New York, NY: General Electric Co., Corporate Research Division, 1982.

- [219] J. A. Goff, *Saturation Pressure of Water on the New Kelvin Scale, Humidity and Moisture Measurement and Control in Science and Industry*. New York, NY: A. Wexler and W. H. Wildhack, Reinhold Publishing Co., 1965.

- [220] V. M. Faires and C. M. Simmang, *Thermodynamics*, 6th ed., Macmillan Publishing Co. Inc., 1978.

- [221] A. Johannsen, "Plotting Psychrometric Charts by Computer," *The South African Mechanical Engineer*, vol. 32, pp. 154-162, 1982.

- [222] S. Bendapudi, *Development and Evaluation of Modeling Approaches for Transients in Centrifugal Chillers*, Purdue University, West Lafayette, IN, Ph.D. Dissertation, 2004.

- [223] N. C. Lemke, "Untersuchung zweistufiger Flüssigkeitskühler mit dem Kältemittel CO₂," *Forschungsberichte des Deutschen Kälte- und Klimatechnischen Vereins Nr. 73, DKV*, Stuttgart, 2005.
- [224] P. Li, J. E. Seem and Y. Li, "A New Explicit Equation for Accurate Friction Factor Calculation of Smooth Pipes," *International Journal of Refrigeration*, vol. 34, no. 6, pp. 1535-1541, 2011.
- [225] F. P. Incropera, D. P. DeWitt, T. L. Bergman and A. S. Lavine, *Fundamentals of Heat and Mass Transfer*, 6th ed, John Wiley & Sons, 2006.
- [226] V. Gnielinski, "New Equations for Heat and Mass Transfer in Turbulent Pipe and Channel Flow," *International Chemical Engineering*, vol. 16, pp. 359-368, 1976.
- [227] P. J. Marto, "Heat Transfer in Condensation," in *Boilers Evaporators & Condensers*, S. Kakac, Ed., Wiley-Interscience, 1991, pp. 525-570.
- [228] V. K. Dhir and J. H. Lienhard, "Laminar Film Condensation on Plane and Axisymmetric Bodies in Non-Uniform Gravity," *International Journal of Heat Transfer*, vol. 93, no. 1, pp. 97-100, 1971.
- [229] W. Nusselt, "The Condensation of Steam on Cooled Surfaces," *Zeitschrift des Vereines Deutscher Ingenieure*, vol. 60, pp. 541-546, 1916.
- [230] M. Belghazi, A. Bontemps, J. C. Signe and C. Marvillet, "Condensation Heat Transfer of a Pure Fluid and Binary Mixture Outside a Bundle of Smooth Horizontal Tubes. Comparison of Experimental Results and a Classical Model," *International Journal of Refrigeration*, vol. 24, no. 8, pp. 841-855, 2001.
- [231] M. M. Chen, "An Analytical Study of Laminar Film Condensation: Part 2 - Single and Multiple Horizontal Tubes," *Transaction of ASME, Journal of Heat Transfer*, vol. 83, no. 1, pp. 55-60, 1961.
- [232] D. Q. Kern, "Mathematical Development of Loading in Horizontal Condensers," *AIChE Journal*, vol. 4, no. 2, pp. 157-160, 1958.
- [233] M. Belghazi, A. Bontemps and C. Marvillet, "Experimental Study and Modelling of Heat Transfer during Condensation of Pure Fluid and Binary Mixture on a

Bundle of Horizontal Finned Tubes," *International Journal of Refrigeration*, vol. 26, no. 2, pp. 214-223, 2003.

- [234] W. M. Rohsenow and M. Cambridge, "Heat Transfer and Temperature Distribution in Laminar-Film Condensation," *Transactions of the ASME*, vol. 78, pp. 1645-1648, 1956.
- [235] W. Tegethoff, *Communication with TLK-Thermo*, 2010.
- [236] S. K. Wang, *Handbook of Air Conditioning and Refrigeration*, 1st ed., New York, NY: McGraw-Hill, 1993.
- [237] R. C. Arora, *Refrigeration and Air Conditioning*, Prentice-Hall of India Pvt. Ltd, 2010.
- [238] E. Parr, *Industrial Control Handbook*, 3rd ed., New York, NY: Industrial Press, Inc., 1999.

Appendix A. Calculation of Merkel's Number

The calculation of the Merkel's number follows the method described in Kröger [198]. The specific heat of the dry air c_{pa} from 220K to 380K under the standard atmospheric pressure (101325Pa) is determined by [218]:

$$c_{pa} = 1.0454 \times 10^3 - 3.1618 \times 10^{-1} T + 7.0838 \times 10^{-4} T^2 - 2.705 \times 10^{-7} T^3 \quad (J \cdot kg^{-1} K^{-1}) \quad (A.1)$$

where T is the local temperature of dry air.

The specific heat of the saturated water vapor c_{pv} from 273.15K to 380K is determined by [219]:

$$c_{pv} = 1.3605 \times 10^3 + 2.31334 T - 2.46784 \times 10^{-10} T^5 + 5.91332 \times 10^{-13} T^6 \quad (J / kg) \quad (A.2)$$

The specific heat of saturated water liquid c_{pwm} from 273.15K to 380K is [220]:

$$c_{pwm} = 8.156 \times 10^3 - 2.8063 \times 10 T + 5.1128 \times 10^{-2} T^2 - 2.1758 \times 10^{-13} T^6 \quad (J / kg \cdot K) \quad (A.3)$$

The vapor pressure of the saturated water vapor p_v from 273.15K to 380K is determined by [219]:

$$p_v = 10^z \quad (N / m^2) \quad (A.4)$$

where

$$\begin{aligned} z = & 10.8(1 - 273.15 / T) + 5.028 \log_{10}(273.15 / T) + 1.505 \times 10^{-4} \left[1 - 10^{-8.297\{(T/273.15)-1\}} \right] \\ & + 4.2873 \times 10^{-4} \left[10^{4.76955(1-273.16/T)} - 1 \right] + 2.78612 \end{aligned} \quad (A.5)$$

The humidity ratio of moist air ω is determined by [221]:

$$\omega = \left(\frac{2501.6 - 2.3263(T_{wb} - 273.15)}{2501.6 + 1.8577(T - 273.15) - 4.184(T_{wb} - 273.15)} \right) \left(\frac{0.62509 p_{vwb}}{p_{abs} - 1.005 p_{vwb}} \right) - \left(\frac{1.00416(T - T_{wb})}{2501.6 + 1.8577(T - 273.15) - 4.184(T_{wb} - 273.15)} \right) \quad (kg / kg \text{ dry air}) \quad (A.6)$$

where T_{wb} is the local wet bulb temperature. p_{vwb} is the vapor pressure using wet-bulb temperature, and p_{abs} is the local station pressure.

The humidity ratio for the saturated air ω_s is determined by [221]:

$$\omega_s = \left(\frac{0.62509 p_{vwb}}{p_{abs} - 1.005 p_{vwb}} \right) \quad (A.7)$$

The latent heat of vaporization for the saturated water liquid h_{fgw} from 273.15K to 380K is determined with [218]

$$h_{fgw} = 3.4831814 \times 10^6 - 5.8627703 \times 10^3 T + 12.139568 T^2 - 1.40290431 \times 10^{-2} T^3 \quad (J / kg) \quad (A.8)$$

The enthalpy of the air-vapor mixture per unit mass of dry air h_{ma} is determined by [198]:

$$h_{ma} = c_{pa}(T - 273.15) + \omega [h_{fgwo} + c_{pv}(T - 273.15)] \quad (J / kg \text{ dry air}) \quad (A.9)$$

where h_{fgwo} is the latent heat of vaporization for the saturated water liquid evaluate at outlet water temperature.

The formula for obtaining the Merkel's number Me_M is [198]

$$Me_M = \int_{T_{wo}}^{T_{wi}} \frac{c_{pw} dT_w}{(h_{masw} - h_{ma})} \approx \frac{c_{pwm}(T_{wi} - T_{wo})}{2} \cdot \left[\frac{1}{h_{maswo} - h_{mai}} - \frac{1}{h_{maswi} - h_{mao}} \right] \quad (A.10)$$

where h_{masw} is the enthalpy of the air-vapor mixture per unit mass of dry air at the local

water temperature. h_{maswo} and h_{maswi} are the enthalpy of the air-vapor mixture per unit mass of dry air estimated at the outlet and the inlet water temperatures, respectively. T_{wi} and T_{wo} are the inlet and outlet water temperatures, respectively. h_{mai} and h_{mao} are the enthalpy of the air-vapor mixture per unit mass of dry air estimated at the inlet and outlet air temperatures, respectively. The specific heats can be evaluated at $(T + 273.15)/2$ and the latent heat h_{fgwo} is evaluated at 273.15K.

Appendix B. Parameters for Steady-State Evaluation of Cooling Tower Model

The steady-state evaluation of the mechanical-draft counter-flow wet cooling tower model uses the experimental data from [195], the simulation model layout for the cooling tower body (evaporative cooling process) is shown in Fig. 3.5. The geometric parameters of cooling tower used in the steady-state evaluation are listed in Table B.1.

TABLE B.1
GEOMETRIC PARAMETERS USED IN STEADY-STATE EVALUATION OF COOLING TOWER
MODEL

	Description	Values
Moist air tube	Inner Diameter	1.0494 m
	Length	0.9033 m
	Cell number	7
Liquid tube	Inner Diameter	1.0494 m
	Length	0.9033 m
	Cell number	7
NTU fitting parameter in Eq. (3.21)	c	1.684
	n	-0.391

The initialization conditions for the water and the moist air are given in Table B.2.

TABLE B.2
INITIAL CONDITIONS FOR WATER AND MOIST AIR

	Description	Values
Moist air	Initialization method	Constant temperature
	Initial value for temperature	303.15 K
Water	Initialization method	Constant temperature
	Initial value for liquid temperature	300 K

The parameters of collection basin model used in the simulation are: sump volume is 0.1 m^3 and inlet water temperature is 295.15 K.

Appendix C. Modeling Details for Chiller-Cycle Components

The chiller cycle modeling described in Chapter 3 mainly adopted the work in [31]. The dynamic modeling of condenser, evaporator and expansion devices from [31] are included here for reference.

C.1. Condenser and Evaporator

C.1.1. Finite Volume Method Based Modeling

The modeling of condenser and evaporator requires quality heat exchanger models since they can capture the major transients in the chiller system. There are mainly two methods for heat exchangers modeling: 1) the finite volume (FV) method and 2) the moving boundary (MB) method [124]. The FV method is based on discretizing the heat exchanger into a number of fixed control volumes and integrating the balance equations over each volume. The MB method is based on dividing the heat exchanger into variable-length control volumes that correspond to each phase region. The number of control volumes and the length of each control volume depend on the actual system operation. For shell-and-tube heat exchanger modeling in centrifugal chiller systems, the comparison between the FV and MB methods has been extensively studied by Bendapudi *et al.* [124]. For simulation of both individual components and the whole chiller system, the FV method was found to be more robust for scenarios of start-up and transient load change. The MB method was also found to be less accurate for charge prediction. Although the FV method amounted to about 20% increase in computation time, the trade-

off is worthwhile considering the improvement in the modeling accuracy. Therefore, the FV method was adopted in this study.

- **Shell- and Tube-Side Geometry**

According to Bendapudi [222], assumptions of concentric, tube-in-tube and counter-flow can be applied to the shell-and-tube heat exchanger modeling in chillers. For both condenser and evaporator, the water flows at the tube-side and the refrigerant flows at the shell-side. The shell-side heat transfer area is computed from the outer surface area of the water tubes and a surface enhancement factor. In this study, the condenser and evaporator were modeled based on the *TubeAndTube* heat exchanger model in TIL. Figure C.1 shows the Dymola layout of the condenser model developed in the TIL library.

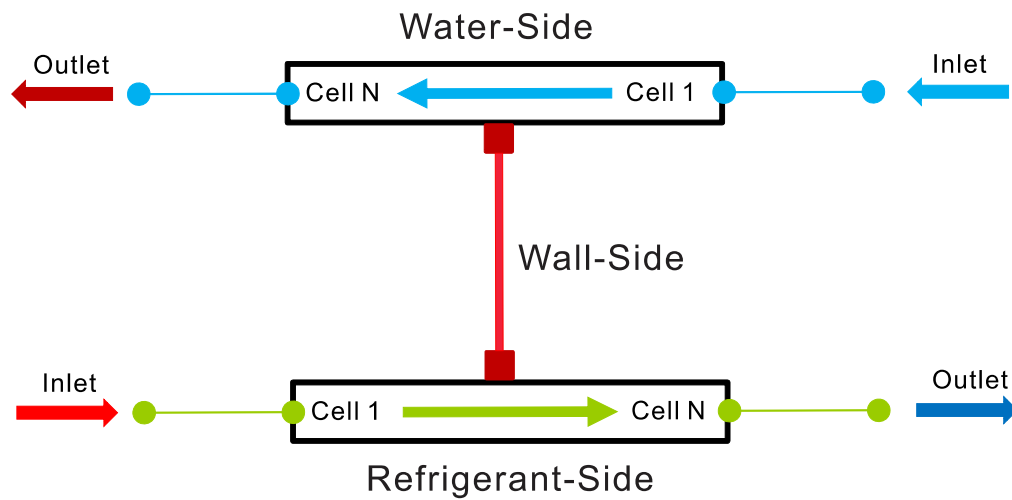


Figure C.1: Modelica model layout of the condenser model (reproduced and modified with permission from TIL's *TubeAndTube* heat exchanger model)

To adapt the above model to the flooded type shell-and-tube heat exchangers, some modifications are needed. The difference in geometric dimensions between a shell-and-tube heat exchanger and a tube-by-tube heat exchanger mainly lies at the shell side. As

the refrigerant flows at the shell side, the face flow area A_f and the volume of the refrigerant V_{tot} can be computed as [222]:

$$A_f = \frac{1}{4} \pi (D_s^2 - N d_o^2) \quad (C.1)$$

$$V_{tot} = A_f L_{tot} \quad (C.2)$$

where D_s is the shell diameter, N is the total number of tubes, d_o is the tube outer diameter, and L_{tot} is the total tube length.

The Reynolds number Re_r in each refrigerant cell is determined based on the average velocity v_{mean} :

$$Re_r = \frac{v_{mean} d_o}{\nu} \quad (C.3)$$

where

$$v_{mean} = \frac{\dot{m}_{mean}}{\rho_r A_f} \quad (C.4)$$

$$\dot{m}_{mean} = (\dot{m}_{r,in} + \dot{m}_{r,out}) / 2 \quad (C.5)$$

ν is the kinetic viscosity, ρ_r is the mean density in each refrigerant cell, \dot{m}_{mean} , $\dot{m}_{r,in}$ and $\dot{m}_{r,out}$ are the mean, inlet and outlet mass flow rates of each refrigerant cell, respectively.

- **Mass and Energy Balance Equations**

With the FV method, both the refrigerant and water sides are discretized into a fixed number of control volumes (called “cells” in TIL). For the refrigerant side, a single-cell

model named as *RefrigerantCell*¹ is modified from TIL.Cells; while for the water side, the same model of *LiquidCell* is adopted from TIL.Cells. Both the mass and energy balance equations are formulated in these two single-cell models, respectively. An integer parameter “nCells” (number of cells) can be used to duplicate multiple instances of the *RefrigerantCell* and *LiquidCell* and construct a finite volume based heat exchanger model.

In the *RefrigerantCell*, the mass balance equation is given as [196]:

$$V_r \frac{d\rho_r}{dt} = \dot{m}_{r,in} + \dot{m}_{r,out} \quad (C.6)$$

where V_r is the Volume in each refrigerant cell.

The energy balance is derived by applying the first law of thermodynamics for an open control volume [196]:

$$\frac{dh_r}{dt} = \frac{1}{M_r} \left(\dot{m}_{r,in} (h_{r,in} - h_r) + \dot{m}_{r,out} (h_{r,out} - h_r) + \dot{Q}_r + V_r \frac{dp}{dt} \right) \quad (C.7)$$

where h_r , $h_{r,in}$ and $h_{r,out}$ are the mean, inlet and outlet specific enthalpies in each refrigerant cell, respectively. M_r is the mass in each refrigerant cell. \dot{Q}_r is the rate of heat transfer to each refrigerant cell.

To avoid automatic differentiation in Dymola, the time derivative of density ($d\rho_r / dt$) is manually transformed in terms of the state variables [196]:

$$\frac{d\rho_r}{dt} = \left(\frac{\partial \rho_r}{\partial h_r} \right)_p \frac{dh_r}{dt} + \left(\frac{\partial \rho_r}{\partial p} \right)_{h_r} \frac{dp}{dt} \quad (C.8)$$

¹ The modified *RefrigerantCell* model includes phase-dependent heat transfer calculations for condenser and evaporator.

Note that a Modelica tool such as Dymola includes algorithms to symbolically transform differential equations in terms of their states. In the *Modelica.Media* Library, to transform differential equations into desired state variables, one needs to set the flag “preferredMediumStates = true” when declaring the medium model BaseProperties. Such option is also available in TILMedia by setting the flag “stateSelectPreferForInputs = true” when declaring thermodynamic variables.

It is important to note that dp/dt ² is assumed invariant for each pressure level³. This is a key assumption originally proposed by Lemke [223] with experimental validation and later implemented into TIL by Richter [196]. A recent work by Li *et al.* [224] justified the assumption on the refrigerant based vapor compression cycle. As illustrated in Fig. C.2, the assumption can be expressed as [223]:

$$\frac{dp_{in}}{dt} = \frac{dp_{out}}{dt} \quad (C.9)$$

where p_{in} and p_{out} are the inlet and outlet pressures, respectively.

According to Richter [20], the key benefit of this assumption is that dp/dt would become known quantities instead of unknowns in Eqs. (C.8) and (C.9), which would improve the numerical efficiency and robustness of refrigerant cycle simulations.

² The subscript “r” is not placed on dp/dt because dp/dt is only defined at the refrigerant side and neglected at the water side.

³ By neglecting pressure drops, chillers have two pressure levels: 1) condenser-side pressure, and 2) evaporator-side pressure.

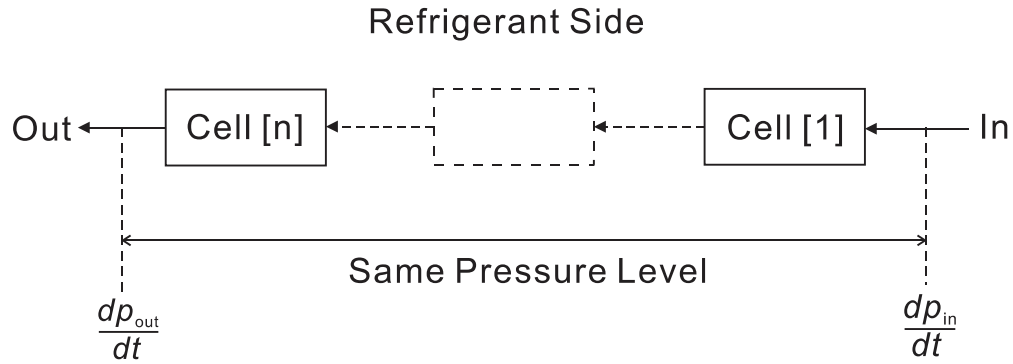


Figure C.2: Illustrative diagram for the dp/dt assumption

However, there is a limitation in Lemke's experimental validation. The experiments were conducted on a gas cooler from a transcritical refrigeration system, where the refrigerant is in the supercritical state only. Thus, it is not appropriate to draw a quick conclusion that this assumption can also be applied to typical vapor compression refrigeration systems such as chillers in this study, which would undergo phase transitions rather than the supercritical state only. This concern is addressed in this study with experimental investigation on a vapor compression chiller.

In *LiquidCell*, the state variable includes temperature only. Thus, the calculation of time derivative of pressure (dp/dt) is neglected. Similar to *RefrigerantCell*, the mass and energy balance equations are manually transformed to the state variable.

- **Water and Refrigerant Sides' Heat Transfer**

The convective heat transfer coefficients are implemented in the basic cell models of both *RefrigerantCell* and *LiquidCell*. Figure C.3 shows the schematic for the water and refrigerant sides' heat transfer in the basic cell models.

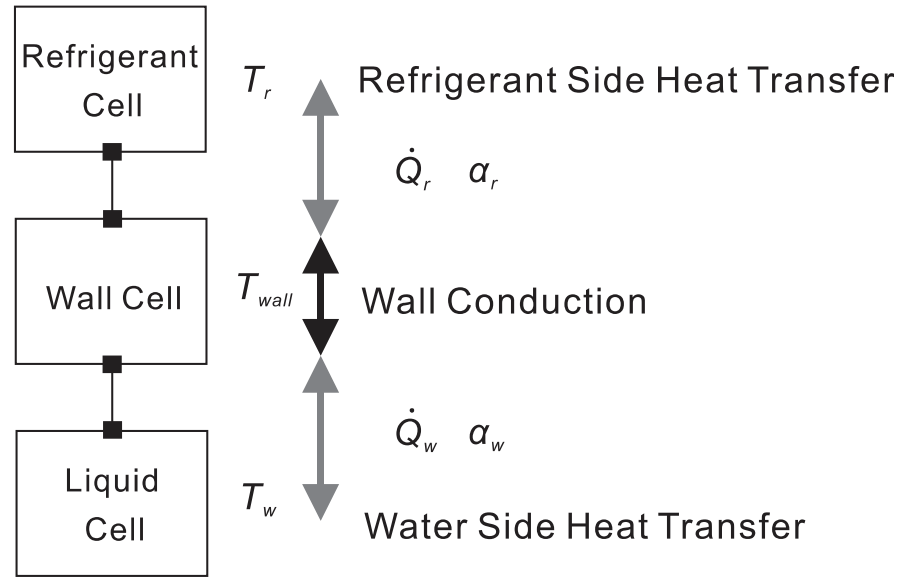


Figure C.3: Illustration of water and refrigerant sides' heat transfer in basic cell models

In Fig C.3, the convective heat transfer rates on the water and refrigerant sides can be determined from Newton's law of cooling [196]:

$$\dot{Q}_w = \alpha_w A_w (T_{wall} - T_w) \quad (C.10)$$

$$\dot{Q}_r = \alpha_r A_r (T_{wall} - T_r) \quad (C.11)$$

where \dot{Q}_w is the rate of heat transfer to each liquid cell. α_w and α_r are the water side and refrigerant side local convective heat transfer coefficients, respectively. A_w and A_r are the heat transfer area in each liquid and refrigerant cells, respectively. T_{wall} , T_w and T_r are the mean temperature in each wall cell, liquid cell and refrigerant cell, respectively.

Neglecting axial conduction, the energy storage at the wall cell can be modeled as [225]:

$$M_{wall} c_{p,wall} \frac{dT_{wall}}{dt} = \dot{Q}_r + \dot{Q}_w \quad (C.12)$$

where M_{wall} is the mass in each wall cell. $c_{p,wall}$ is the specific heat capacity of wall material.

- **Water Side Heat Transfer**

For the water side, the flow region is turbulent mainly due to high water flow rates. Thus, the Gnielinski correlation [226] can be applied:

$$Nu_w = \frac{(C_f / 2)(Re_w - 1000) Pr_w}{1 + 12.7(C_f / 2)^{1/2} (Pr_w^{2/3} - 1)} \quad (C.13)$$

where Nu_w is the water side Nusselt number. C_f is the fanning friction factor in smooth pipes. Re_w is the water side Reynolds number. Pr_w is the water side Prandtl number.

The Fanning friction factor developed by in [224] is applied:

$$C_f = \frac{-0.0015702}{\ln(Re)} + \frac{0.3942031}{\ln(Re)^2} + \frac{2.5341533}{\ln(Re)^3} \quad (C.14)$$

Finally, the water side connective heat transfer coefficient can be determined as [225]:

$$\alpha_w = \frac{Nu_w k_w}{d_i} \quad (C.15)$$

where k_w is thermal conductivity of water. d_i is the tube inner diameter.

- **Refrigerant Side Heat Transfer**

Compared to the water side, the heat transfer at the refrigerant side is more complex due to the two-phase flow situation. For condenser, suitable convective heat transfer correlation is needed for describing condensation process in the two-phase region; while for evaporator, a suitable correlation is needed for the boiling process in the two-phase region. In addition, smooth transitions between the single-phase and two-phase heat transfer correlations are necessary for implementation.

For condensation in the two-phase region, extensive study has been reported for condensation inside tubes. Also, there have been good models for condensation over a

single tube. However, the condensation over tube bundles is much more complicated. The presence of neighboring tubes brings forth additional complexities. As described in [227], “In the idealized case, the condensation from a given tube is assumed to drain by gravity to the lower tubes in a continuous and laminar sheet. In reality, depending on the spacing-to-diameter ratio of the tubes and whether they are arranged in a staggered or inline configuration, the condensate from one tube may not fall on the tube directly below it, but instead may flow sideways. In addition, experimental study has shown that condensate does not drain from a horizontal tube in a continuous sheet but in discrete droplets along the tube axis. When these droplets strike the lower tube, considerable splashing can occur, causing ripples and turbulence in the condensate film. Perhaps most important of all, large vapor velocities can create significant shear forces on the condensate, stripping it away, independent of gravity.”

For laminar film condensation on a horizontal tube, Dhir and Lienhard [228] proposed a correlation based on Nusselt’s analysis [229]. It is also widely used to correlate the heat transfer for the condenser model with tube bundle on the shell side. This model does not consider the condensation inundation effect, heat transfer coefficient increase in a tube bundle, or the surface enhancement effect. Belghazi *et al.* [230] conducted a study on condensation on the exterior of a bank of smooth tubes for pure fluid and for zeotropic binary mixture HFC23/HFC134a. For the test of pure HFC134a, the experimental data on the first tube deviate from the Nusselt theory [229] by –5%. The effect of heat flux to the condensation inundation was considered by modifying Chen’s correlation [231] based on the exponent in Kern’s correlation [232]. However, the method proposed in this paper cannot predict the increase of heat transfer coefficient in

the tube bundle since it is difficult to determine the pattern of condensate falling from the upper rows. Later, Belghazi *et al.* [233] studied the film condensation of downward vapor flowing on staggered bundles of horizontal finned tubes, using HFC134a and the binary zeotropic mixture HFC23/HFC134 as the refrigerants. Experimental study was conducted based on five commercial tubes with dissimilar fin pitches. Experimental results indicated that the condensation curve method underestimated the heat transfer coefficient for the first row. A modified condensation curve method was then proposed by adding the effect of Lewis number. This method has good agreement (within $\pm 10\%$) with the experimental data in terms of the total heat flux prediction. This method also improved the prediction of heat transfer coefficient for the first row, but still it cannot accurately predict the heat transfer coefficient all other rows because it is difficult to calculate the increase of heat transfer coefficient due to the upper rows.

For the condenser side, Dhir and Lienhard's correlation [228] is adopted with a surface enhancement factor to account for the effect of surface enhancement and the increase of heat transfer coefficient in tube bundles due to particular patterns of the condensate. For the evaporator side, the boiling heat transfer correlation is adopted from Bendapudi's work [222] based on an empirical correlation from the manufacturer.

The geometries of the condenser and evaporator in this work follow the models from Bendapudi *et al.*'s experimental study [124]. The heat transfer coefficients in their model were determined with some empirical correlations from the manufacturers, and the surface enhancement factors were determined with experimental data. This study adopts the empirical heat transfer models and the surface enhancement factors from Bendapudi *et al.*'s work [124] for the idea-proof purpose.

In general, refrigerant flow in the evaporator undergoes transitions between two-phase and superheat regions, as illustrated in Fig. C.4. For detailed flow patterns of forced convection boiling in a tube, refer to [225]. In Fig. C.4, the boiling heat transfer coefficient α_{boil} is given by [222]:

$$\alpha_{boil} = e_1 + \frac{\dot{Q}_{boil}''}{e_2} \quad (C.16)$$

where \dot{Q}_{boil}'' is boiling heat flux in kW/m². e_1 and e_2 are the manufacture's coefficients for heat transfer calculation in evaporator.

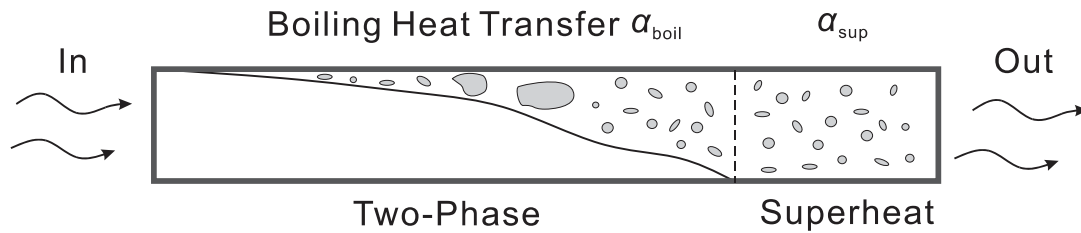


Figure C.4: Illustrative diagram of heat transfer regions in the evaporator

The superheat heat transfer coefficient α_{sup} is given by Bendapudi *et al.* [124]:

$$\alpha_{sup} = \frac{C_{sf,sup} \sqrt{\text{Re}_r} \text{Pr}_r k_r}{d_o} \quad (C.17)$$

where $C_{sf,sup}$ is the surface enhancement factors for superheat refrigerants. Pr_r is the refrigerant side Prandtl number. k_r is the thermal conductivity of refrigerant.

The schematic in Figure C.5 shows the heat transfer regions in the condenser. The heat transfer coefficient of condensation is given by [228]:

$$\alpha_{cond} = C_{sf,cond} \left[\frac{g \rho_l (\rho_l - \rho_v) k_l^3 h'_{fg}}{\mu_l (T_{sat} - T_t) d_o} \right]^{1/4} \quad (C.18)$$

where α_{cond} is the condensation heat transfer coefficient. $C_{sf,cond}$ is the surface enhancement factor for condensation heat transfer. ρ_l and ρ_v are the density of saturated refrigerant liquid and saturated refrigerant vapor, respectively. k_l is the thermal conductivity of saturated refrigerant liquid. μ_l is the dynamic viscosity of the saturated refrigerant liquid.

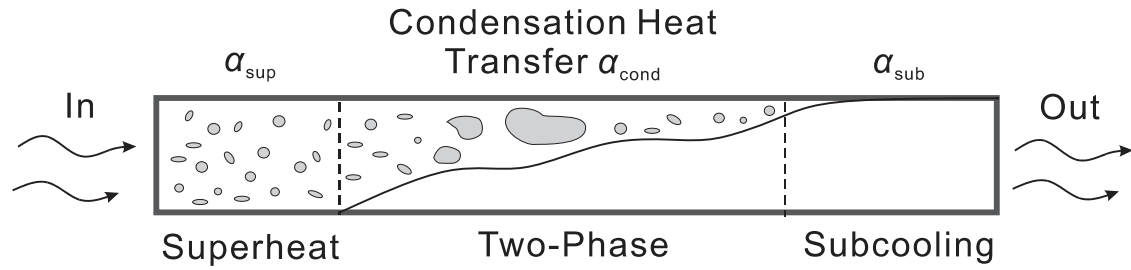


Figure C.5: Illustrative diagram of heat transfer regions in the condenser

Note that h_{fg} is the modified latent heat of vaporization [234]. The same correlation for superheat heat transfer described in Eq. (C.17) is adopted except for a different surface enhancement factor. The subcooling heat transfer coefficient is also given in Bendapudi *et al.* [124]:

$$\alpha_{sub} = \frac{C_{sf,sub} \sqrt{Re_r} Pr_r k_r}{d_o} \quad (C.19)$$

where α_{sub} is the sub-cooling heat transfer coefficient. $C_{sf,sub}$ is the surface enhancement factor for sub-cooling refrigerant.

For condenser, smooth transition of heat transfer coefficients among different phase regions is reinforced and implemented as follows. Implementation for the evaporator side is very similar.

equation

```

.....
if noEvent(properties.x < 0.5) then
// Handle transitions between two-phase and subcooling
alpha=CF_alpha_condenser*spliceFunction(alpha_twophase,alpha_subcool,properties.x -
0.02,0.0001) “CF_alpha_condenser is the overall surface enhancement factor of condenser”;
else
// Handle transitions between two-phase and superheat
alpha=CF_alpha_condenser*spliceFunction(alpha_superheat,alpha_twophase,properties.x -
0.98,0.0001);
end if;

```

Code Segment C.1: Implementation of heat transfer coefficients at the condenser side

C.1.2. Variable Refrigerant Level (VRL) Based Modeling

Recently, TLK-Thermo proposed a simplified method of heat exchanger modeling [235], i.e. the so-called variable refrigerant level (VRL) modeling approach. The basic idea of VRL modeling is to connect a large tank of refrigerant with a bank of water tubes via a heat port. The liquid level of the refrigerant, or equivalently the volume ratio of liquid refrigerant to the total volume of the tank, is varied depending on the magnitude of heat transfer between the water tubes and the refrigerant in the tank.

In particular, the large tank has two outlet fluid ports, i.e. the liquid port and the gas port. Same tasks are performed as for a phase separator, i.e., when the liquid port is connected, the outlet flow will be liquid refrigerant; when the gas port is connected, the outlet flow will be refrigerant vapor. The bank of water tubes can be realized by multiplying the heat transfer area of a single liquid tube by the number of tubes (i.e. the parameter “nParallelTubes”). Heat transfer from the water tubes to the refrigerant in the

tank is realized by the interface of a heat port placed on the liquid tube and the tank models.

The volume of the tank is fixed, but the volume ratio of refrigerant in the tank can be easily monitored. In this modeling approach, the heat transfer coefficient in the liquid tubes can be tuned to match the experimental results for the outlet refrigerant and liquids. Compared to detailed formulation such as the finite volume method, which requires extensive experimental data as well as detailed geometric information to calibrate, this approach has the advantage in model validation when there are not enough information and experimental data available to calibrate the model with details.

This approach is implemented with existing component models in TIL. For the modeling of shell-and-tube heat exchangers, the component model *IdealSeparator* can be adopted together with *LiquidTube* model to formulate dynamic models of condenser and evaporator. Figure C.6 shows the implementation of condenser model with variable refrigerant level in TIL. The construction of an evaporator model is very similar. In Fig. C.6, a “Pressure State Element” is placed at the refrigerant side to compute the time derivative of pressures (dp/dt). The “Ideal Separator” is referred to the aforementioned big tank with two outlet fluid ports. For the case of condenser, the liquid port is connected to the outlet refrigerant flow. The “Heat Port” between the “Liquid Tube” and the “Ideal Separator” is connected to transfer thermal energy. Upon clicking the “liquid Tube” model, it is convenient to set up the number of liquid tubes to be included into the condenser via the parameter “nParallelTubes”, and the corresponding heat transfer area can be automatically updated.

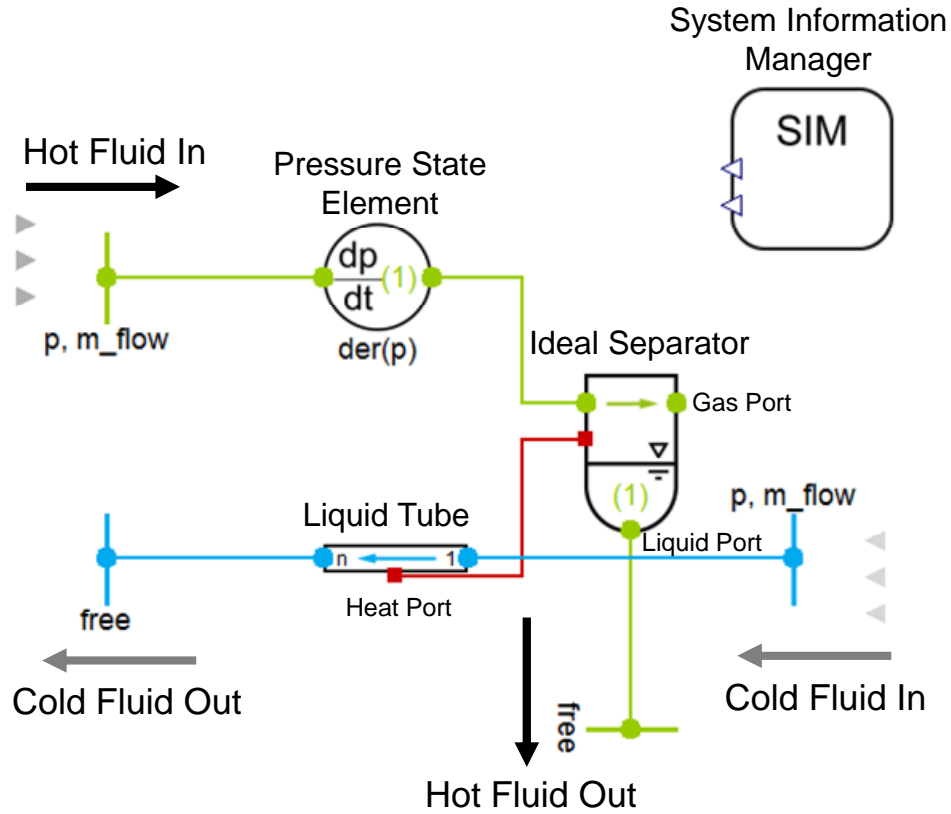


Figure C.6: Modelica model of a VRL-based condenser in TIL

C.2. Expansion Device

The expansion valve is a key component for the refrigeration cycle, which is typically used to control the superheat at the outlet of the evaporator by adjusting the valve opening. The key functionality of the expansion valve is to regulate the refrigerant pressure to a lower level while roughly maintaining the enthalpy of the refrigerant. In centrifugal chillers, orifice plates or float valves are often used to throttle the pressures and thus control the flow rates [236]. In the current model development, an orifice plate model is adopted from TIL by assuming a quadratic relation of the pressure difference across the valve and the corresponding mass flow rate. The flow rate through the

expansion valve can be adjusted by the effective flow area (A_{eff}). The *TIL.Chillers* package also adopts the thermal expansion valve developed by Bendapudi [222].

C.2.1. Orifice Plate

Assuming one-dimensional flow, for the control volume drawn in Fig. C.7, the mass balance of an orifice plate is given by

$$\dot{m}_{v,in} + \dot{m}_{v,out} = 0 \quad (C.20)$$

where $\dot{m}_{v,in}$ and $\dot{m}_{v,out}$ are the inlet and outlet refrigerant mass flow rates of expansion valve.

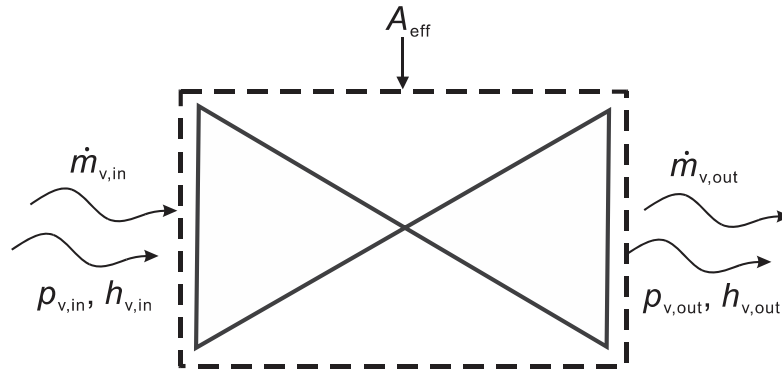


Figure C.7: Control volume of an orifice plate

Further assume that the throttle process is isenthalpic, i.e.

$$h_{v,in} = h_{v,out} \quad (C.21)$$

where $h_{v,in}$ and $h_{v,out}$ are the inlet and outlet specific enthalpies of expansion valve.

For compressible flow, the orifice flow is characterized by [237]:

$$\dot{m}_{v,in} = \varepsilon C_D \frac{A_{out}}{\sqrt{1 - (A_{out} / A_{in})^2}} \sqrt{x} \quad (C.22)$$

where A_{in} and A_{out} are the cross-sectional areas at the inlet and outlet of the orifice plate.

And $x = 2\rho_{v,in} (p_{v,in} - p_{v,out})$ with $\rho_{v,in}$ represents the inlet refrigerant density of the expansion valve, $p_{v,in}$ and $p_{v,out}$ are the pressures at the inlet and outlet of the expansion valve. In Eq. (C.22), the expansion factor ε characterizes the degree of compressibility. When $\varepsilon = 1$, Eq. (C.22) becomes the orifice flow equation for incompressible flow. As Parr states [238], the difficulty is to determine the discharge coefficient (C_D) and it is also very difficult to quantify the expansion factor ε since it is related to the specific heat ratio, the inlet and outlet cross-sectional areas, and the pressures. In TIL's *orifice valve* model, these terms are lumped into a single parameter called effective flow area (A_{eff}). The mass flow rate through the orifice valve is thus simplified to

$$\dot{m}_{v,in} = A_{eff} \sqrt{x} \quad (C.23)$$

In Eq. (C.23), it can be seen that $d\dot{m}_{v,in} / dx \rightarrow \infty$ as $x \rightarrow 0$, this would cause Newton-like solvers to stop due to the infinite derivative. In order to avoid such difficulty, an alternative implementation of the valve equation is considered. For simplicity in the analysis followed, let us define

$$x_0 = \left(\frac{\dot{m}_{smooth}}{A_{eff_smooth}} \right)^2 \quad (C.24)$$

where A_{eff_smooth} is effective flow area for the smoothing function used in the orifice plate.

\dot{m}_{smooth} is the valve mass flow rate for the smoothing function used in the orifice plate.

In TIL's implementation, the valve equation is approximated by a cubic polynomial

$$\dot{m}_{v,in} = A_{eff} \sqrt{x_0} \left[\frac{5x}{4x_0} - \frac{1}{4} \left(\frac{x}{x_0} \right)^3 \right] \quad (C.25)$$

within the interval $x \in [-x_0, x_0]$. As $x \rightarrow 0$, it follows $\dot{m}_{v,in} \rightarrow 0$, which gives the same

solution as Eq. (C.23). The cubic polynomial $\frac{5x}{4x_0} - \frac{1}{4}\left(\frac{x}{x_0}\right)^3$ has finite derivatives over the whole interval $x \in [-x_0, x_0]$ and the problem of division-by-infinite derivative is avoided.

C.2.2. Thermal Expansion Valve

Unlike the orifice plate, the opening of a thermal expansion valve (TXV⁴) is regulated by the pressure differential based on the temperature feedback at the evaporator outlet. As shown in Fig. C.8, the TXV operation is determined by the net effect of the following three pressures: 1) bulb pressure p_{bulb} , 2) evaporator pressure p_e , and 3) minimum opening pressure dp_{min} .

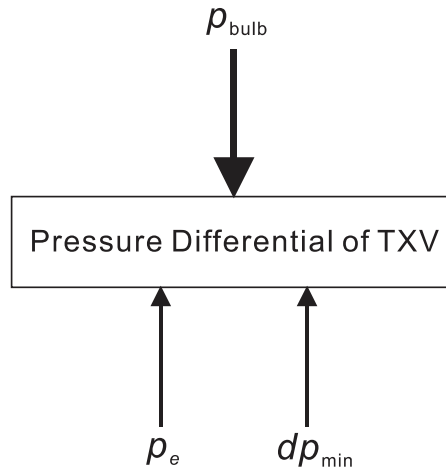


Figure C.8: Illustrative diagram of forces acting on a TXV

The *TIL.Chillers* package adopts the TXV model developed by Bendapudi [222]. The key model equations are summarized as follows. Like the orifice plate, The TXV model is also modeled as a static device under the assumption of isenthalpic process. The heat

⁴ Some literatures also abbreviate thermal expansion valve as TEV.

transfer between the sensing bulb and the evaporator outlet temperature is modeled based on the lumped capacitance method with a time constant C_b [222], i.e.

$$C_b \frac{dT_b}{dt} = (T_{e,out} - T_b) \quad (C.26)$$

where T_b and $T_{e,out}$ are the temperature at heat port b and refrigerant temperature at evaporator outlet, respectively.

The valve lift is computed with the net pressure shown in Fig. C.8. [222]:

$$y_{lift} = k_{spring} (p_{bulb} - p_e - dp_{min}) \quad (C.27)$$

with k_{spring} being the spring constant. y_{lift} is the valve lift. For more details, refer to Bendapudi [222].

In the model implementation, the valve lift is numerically bounded to avoid a negative lift, and the corresponding Modelica codes are given below.

equation

.....

dp_push = max(1e-5, (p_bulb - portB.p - dp_min)) "Lower bound";

// Upper bound

lift = min(maxlift, k_spring*(dp_push/1e3)) "Divide by 1e3 to convert to kPa";

Code Segment C.2: Numerical bounds for the thermal expansion valve model

Notice that

$$p_{bulb} = P_{sat}(T_{e,out}) \quad (C.28)$$

where $P_{sat}(\cdot)$ is a thermodynamic state function that computes the saturation pressure given the temperature. The valve flow area A_v is approximated as a quadratic equation based on the valve lift [222].

$$A_v = f_0 y_{\text{lift}} + f_1 y_{\text{lift}}^2 \quad (\text{C.29})$$

Finally, the mass flow rate across the valve is determined as [222]

$$\dot{m}_{v,\text{in}} = C_d A_v \sqrt{x} \quad (\text{C.30})$$

where a constant discharge coefficient C_d is adopted. Again, similar to the implementation for the orifice plate model, the same numerical treatment is applied to avoid infinite derivative at $x = 0$. The parameters of the TXV model are summarized in Appendix D.

Appendix D. Component Parameters Used in Chiller-Tower Cycle Simulation

Cycle Simulation

The Dymola layout for the chiller-tower cycle simulation is shown in Fig D.1.

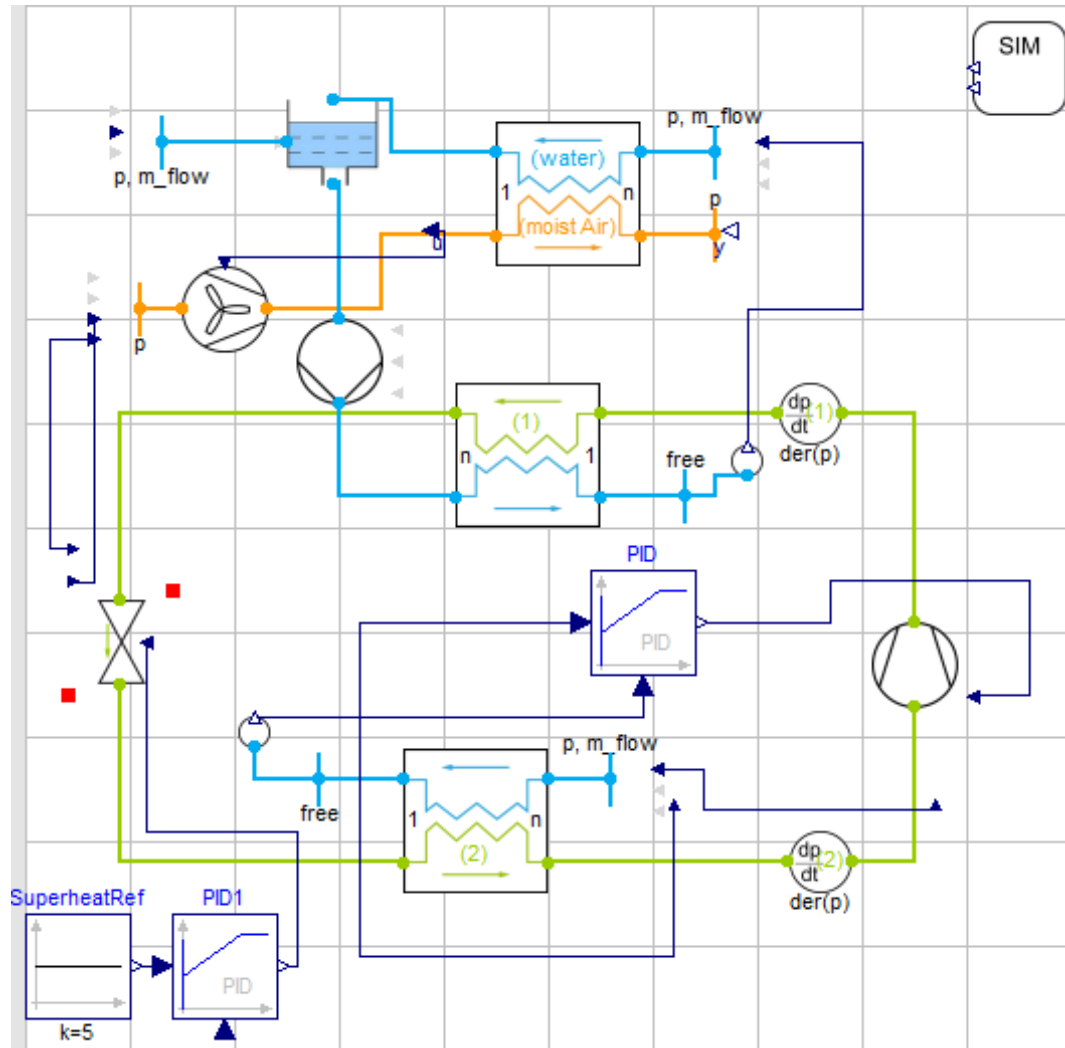


Figure D.1: Dymola layout of chiller-tower cycle

The specific component parameters used in the simulation are listed below:

TABLE D.1
GEOMETRIC PARAMETERS OF THE CONDENSER AND EVAPORATOR [222]

	Tube			Shell
	Inlet diameter	Outlet diameter	Length	Diameter
Evaporator	0.01606 m	0.01960 m	2.4384 m	0.39288 m
Condenser	0.01554 m	0.01905 m	2.4384 m	0.37760 m

TABLE D.2
PARAMETERS OF THE dp/dt COMPONENTS

	Parameter	Value
Initial value for pressure	Inlet of condenser	0.80 MPa
	Outlet of evaporator	0.40 MPa

TABLE D.3
PARAMETERS OF THE ORIFICE VALVE

Parameter	Value
Effective flow area	$0.675 \times 10^{-4} \text{ m}^2$
Valve smooth mass flow rate	0.0005 kg/s

TABLE D.4
PARAMETERS OF THE SCREW COMPRESSOR

Parameter	Value
Fixed compressor speed	50 Hz

Screw compressor displacement	0.0072 m ³
Adiabatic efficiency	0.8
Motor efficiency	0.85
Mechanical efficiency	0.95

TABLE D.5
PARAMETERS OF THE COOLING TOWER

	Description	Values
Moist air tube	Inner diameter	2.717 m
	Length	3.15 m
	Nominal mass flow rate	1 kg/s
	Nominal pressure drop	5Pa
	Cell number	8
Liquid tube	InnerDiameter	2.717 m
	Length	3.15 m
	Constant pressure drop	1000 Pa
	Cell number	8
NTU fitting parameter in Eq. (3.21)	c_{CT}	1.684
	n_{CT}	-0.391

TABLE D.6
PARAMETERS OF THE COOLING TOWER FAN

	Parameter	Value
Fan characteristic at	Pressure increase at $V_{flow} = 0$	500 Pa

nominal speed	Nominal fan speed	50 Hz
	Volume flow rate at $dp = 0$	2 m ³ /s
Fan efficiency settings	Fan efficiency	0.4
	Drive efficiency	1.0

Appendix E. Controller Parameters Used in DESC Based Chilled Water System Optimization Simulation

The Dymola layout for the simulation of dither ESC based optimization control of chilled water system is shown in Fig. E.1. The chilled-water system plant with inner loop controls of evaporator superheat control and chiller leaving water temperature control is shown in Appendix D.

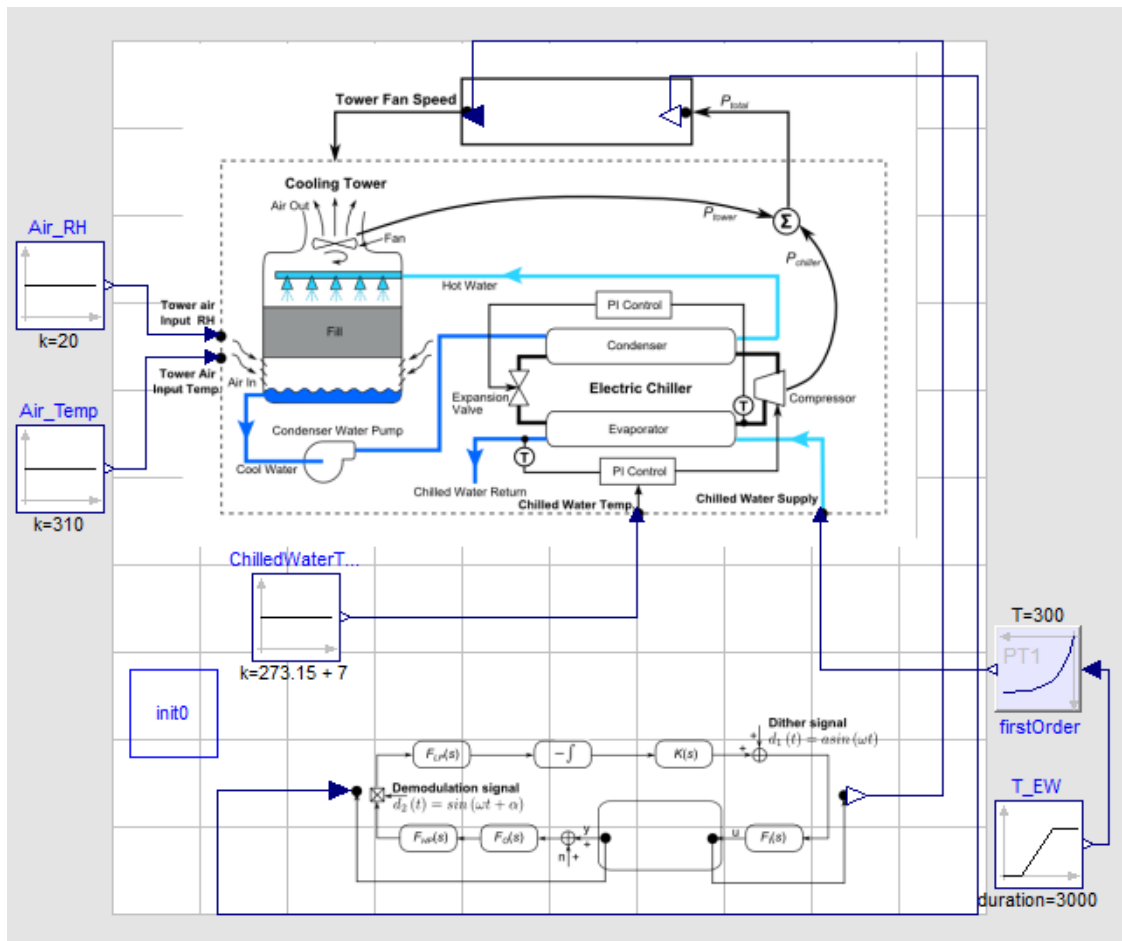


Figure E.1: Dymola layout for the simulation of dither ESC based optimization control of chilled-water system

The Dymola layout for ESC controller is shown in Fig. E.2. The Dymola layout for modified anti-windup ESC simulation is shown in Fig. E.3. and the Dymola layout for anti-windup ESC controller is shown in Fig. E.4.

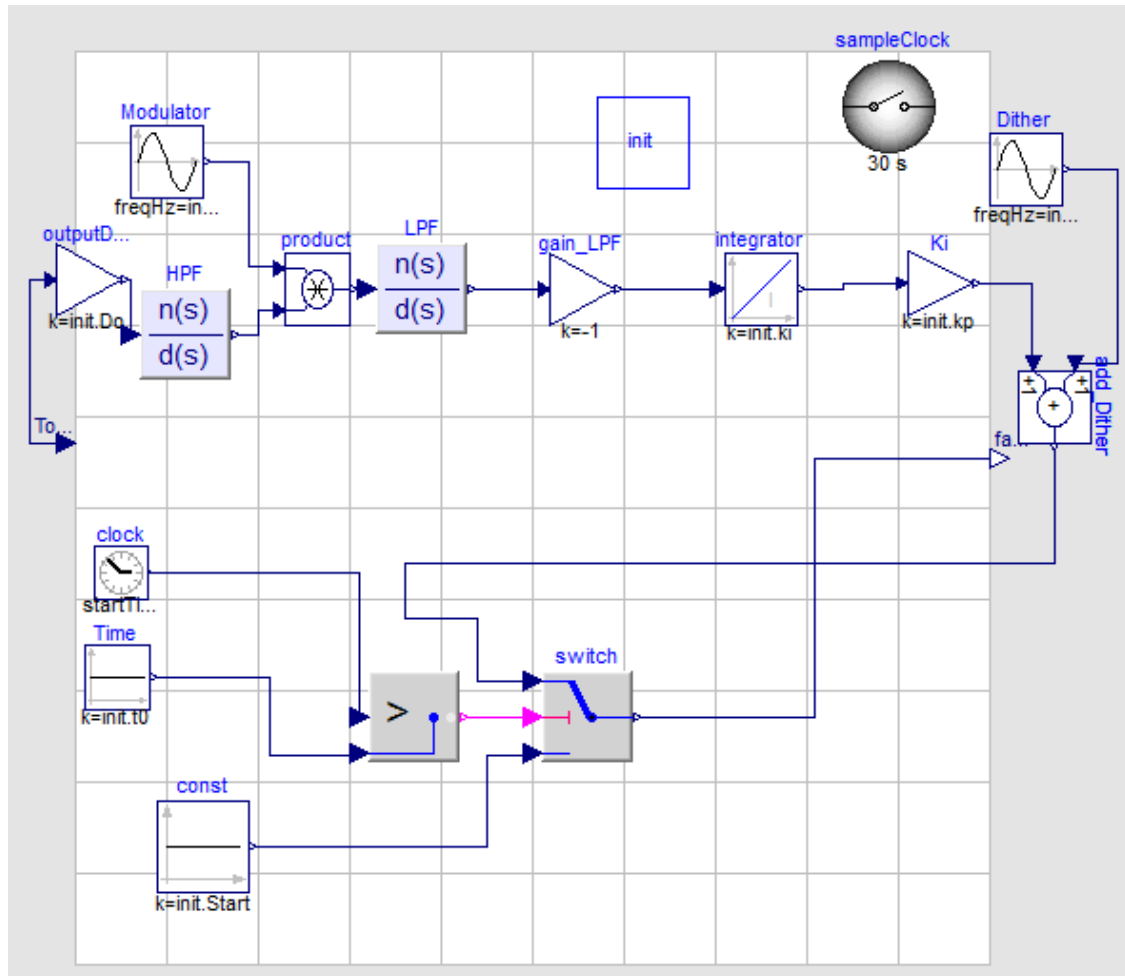


Figure E.2: Dymola layout of dither ESC controller

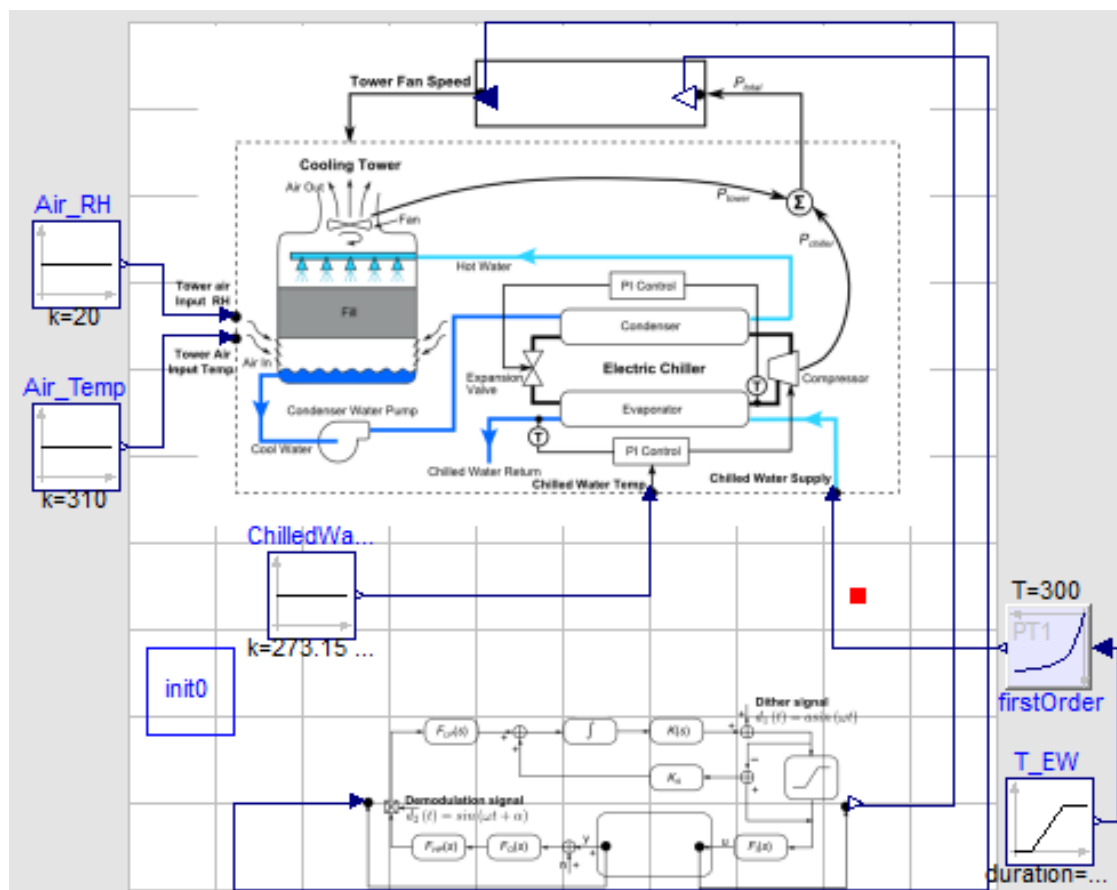


Figure E.3: Dymola layout for the simulation of anti-windup ESC based optimization control of chilled water system

The controller setting parameters are listed as:

PARAMETERS OF THE CONTROLLERS USED IN THE ESC BASED CHILLED WATER SYSTEM OPTIMIZATION

	Parameter	Value
Evaporator superheat control	Controller gain	−0.008
	Time constant of integrator block	1.0 s
Chiller leaving temperature control	Controller gain	−0.018
	Time constant of integrator block	0.66 s
Dither ESC Control	Sample time	30 s

	ESC controller gain	0.031
	Back-calculation gain	0.12

Appendix F. Simulink Models for Adaptive ESC MPPT

The Simulink layouts of the adaptive ESC based PV MPPT described in Chapter 5 are too complicated to be shown as a whole figure here. Instead, the components for AESC controller are shown in Figs. F.1 through F.4 separately.

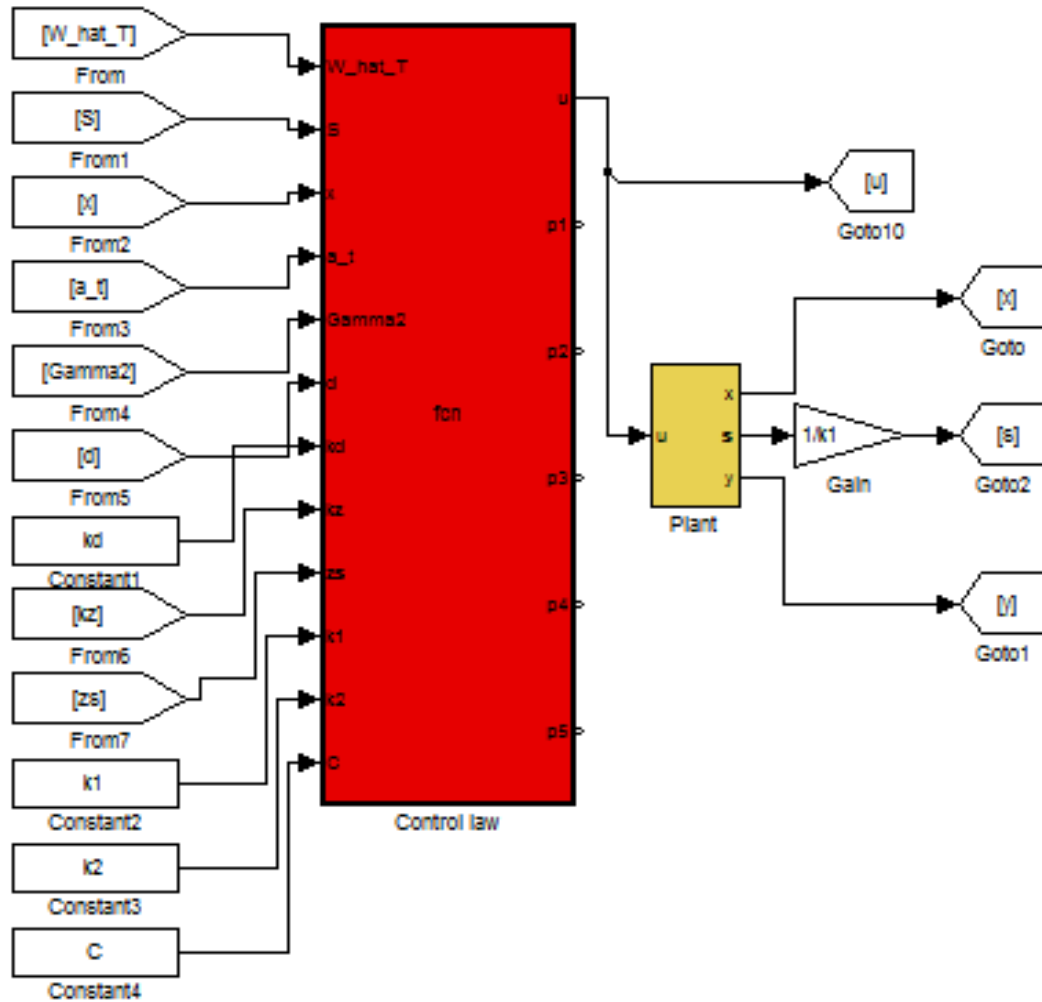


Figure F.1: Simulink layout of adaptive ESC based PV MPPT, control law and PV system plant

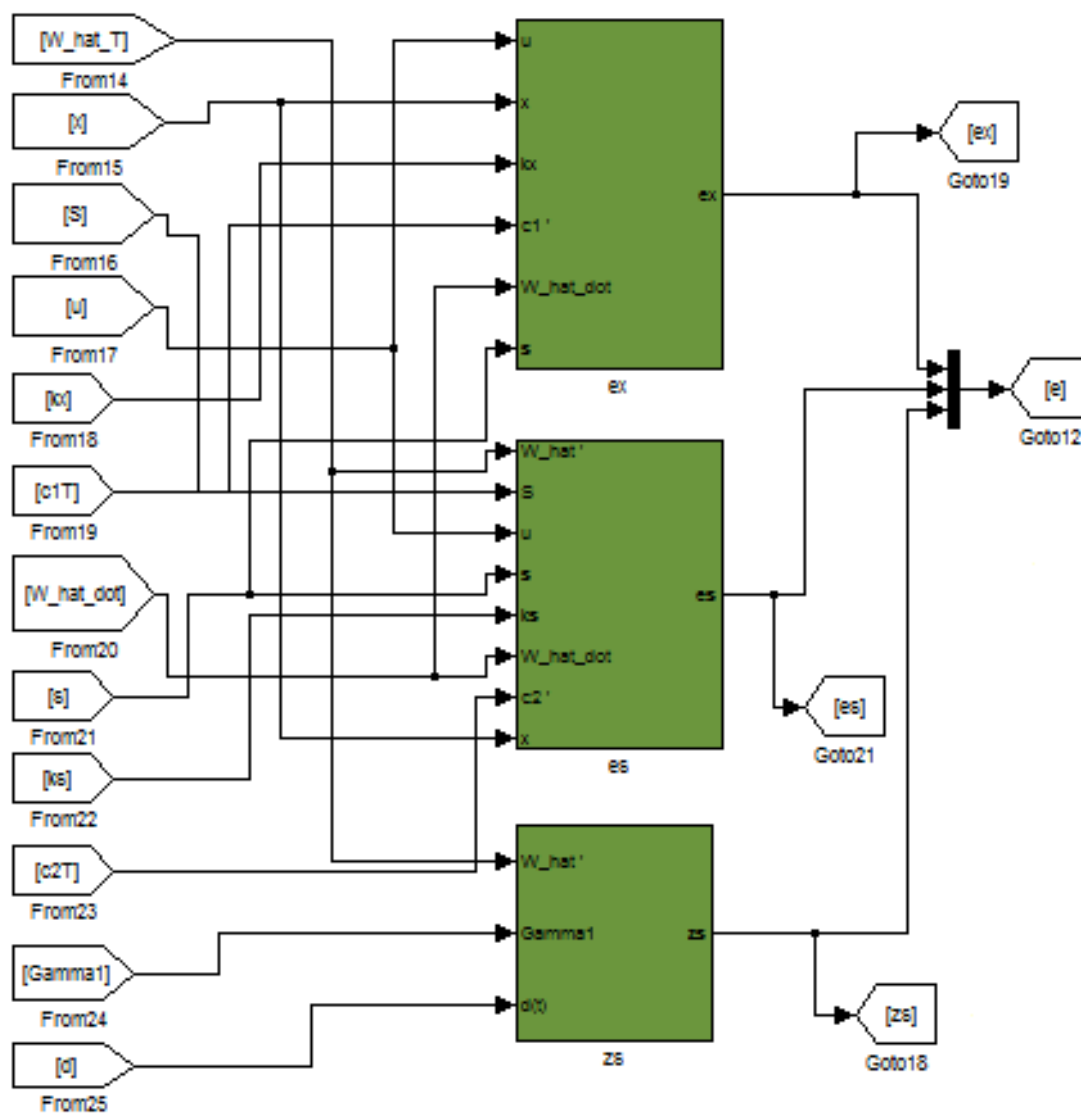


Figure F.2: Simulink layout of adaptive ESC based PV MPPT, state and tracking error estimates

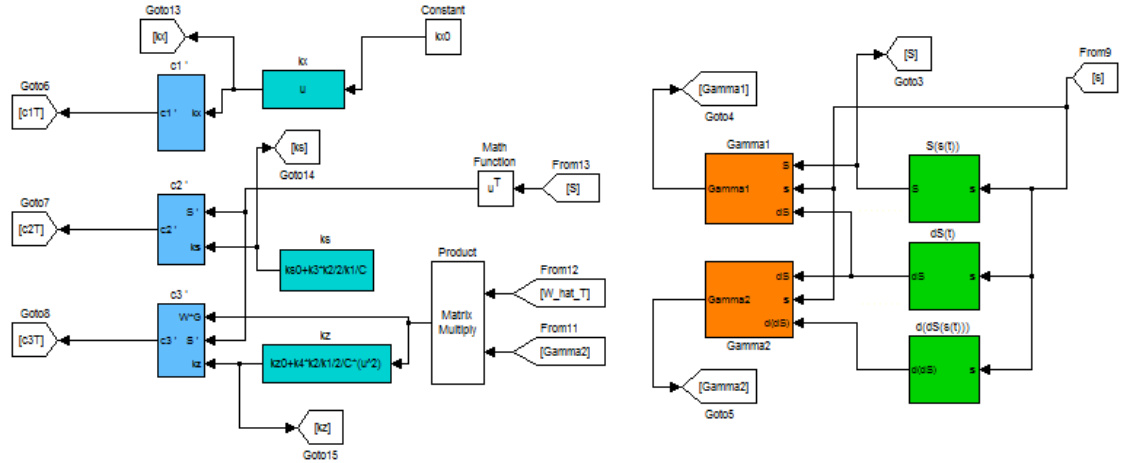


Figure F.3: Simulink layout of adaptive ESC based PV MPPT, design parameters

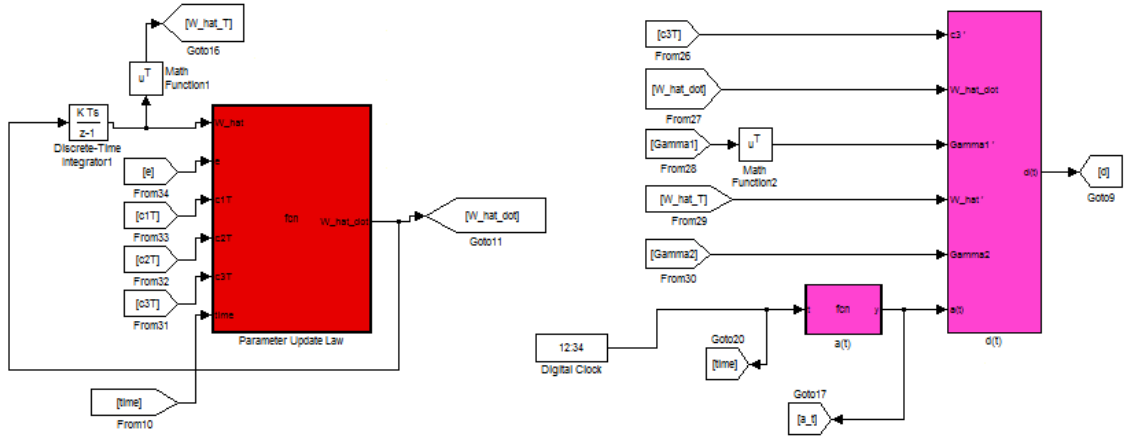


Figure F.4: Simulink layout of adaptive ESC based PV MPPT, parameter learning and dither signal

The detailed connection for “Plant” block in Fig. F.1, i.e. the yellow block, is shown in Fig. F.5.

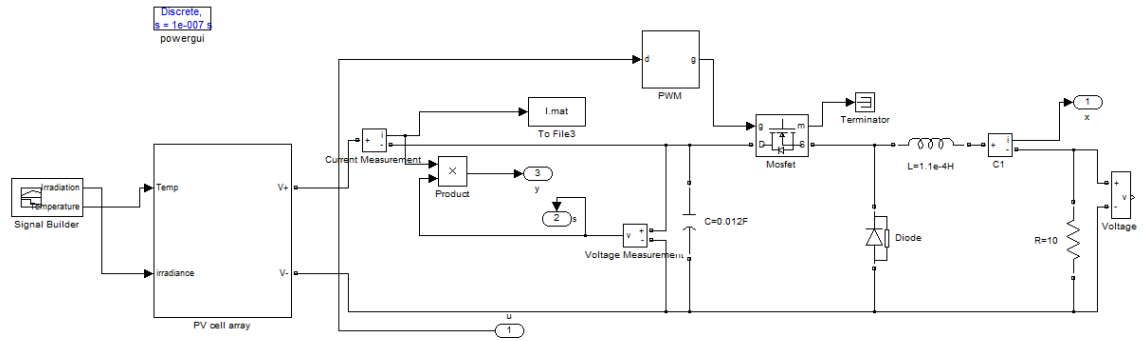


Figure F.5: Simulink layout of PV array plant

For, the detailed model structure, please refer to [176].

Appendix G. Simulink Schematics for ESC MPPT Integrated Detection of Internal Resistance Change

The Simulink schematics of the square-wave dither ESC based PV MPPT and internal resistance change detection on multi-string PV structure is shown in Fig. G.1.

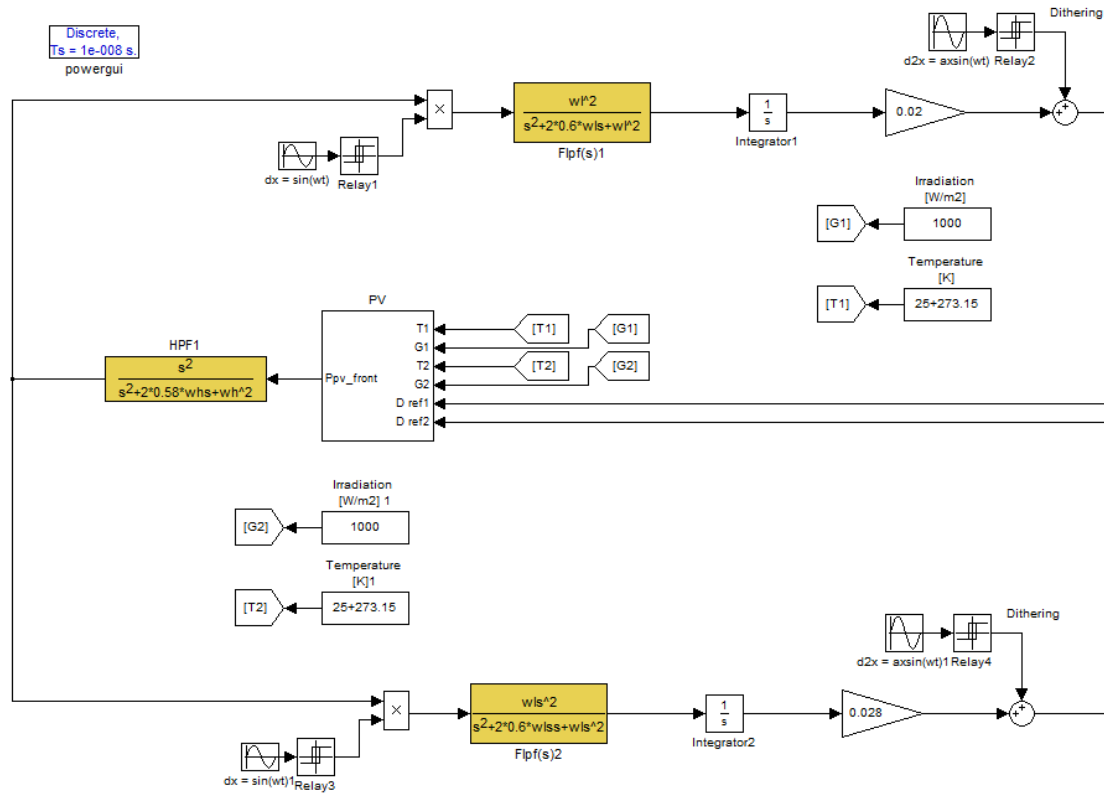


Figure G.1: Simulink layout of square-wave dither ESC on multi-string structure

The multi-string PV plant used in the simulation is shown in Fig. G.2.

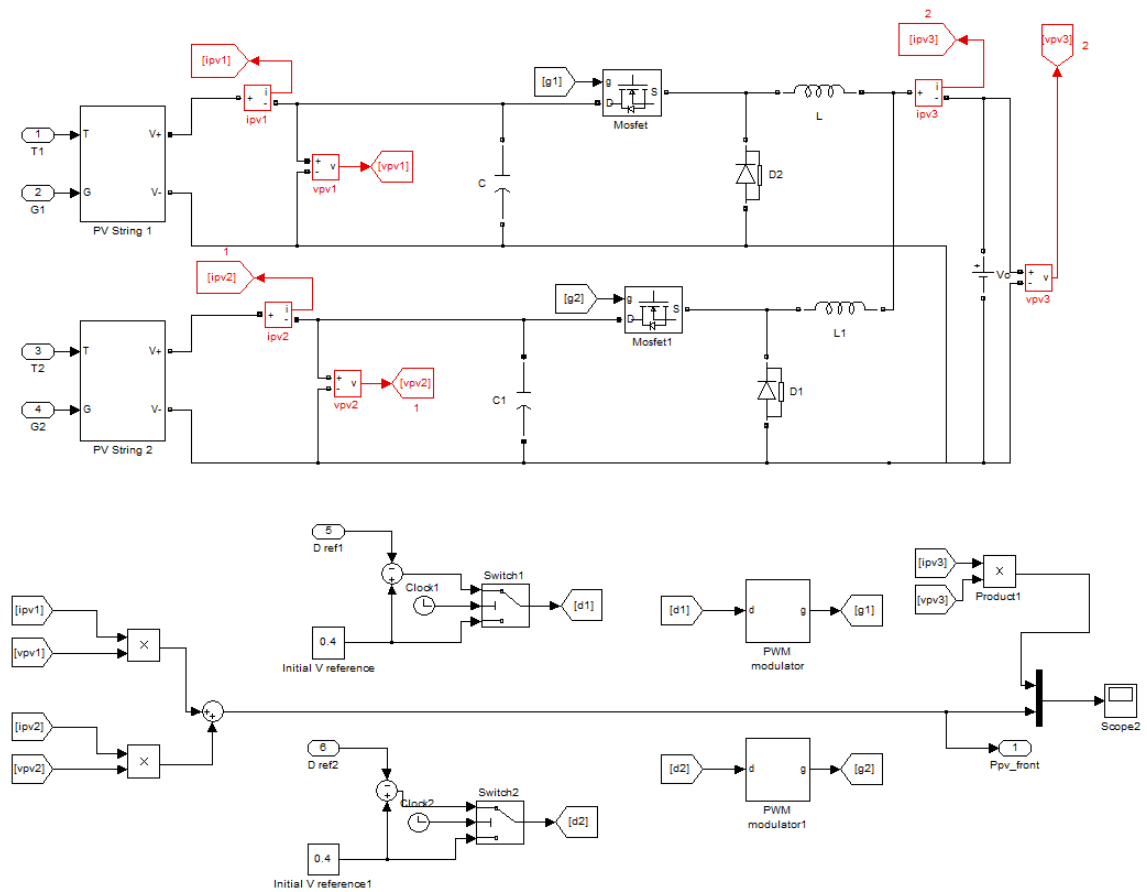


Figure G.2: Simulink layout of multi-string PV plant

CURRICULUM VITAE

Xiao Li

Place of birth: Qinhuangdao, Hebei Province, P. R. China

Education

B. Sc., Tsinghua University, Beijing, July 2006

Major: Automation

Dissertation Title: Investigation of Some Self-Optimizing Control Problems for Net-Zero Energy Buildings

Journal Publications:

- [1] **X. Li**, Y. Li, J. E. Seem and P. Lei, "Detection of Internal Resistance Change for Photovoltaic Arrays Using Extremum Seeking Control MPPT Signals," in review, submitted to IEEE Transactions of Control Systems Technology.
- [2] **X. Li**, Y. Li, J. E. Seem and P. Li, "Dynamic Modeling and Self-optimizing Operation of Chilled Water Systems Using Extremum Seeking Control," Energy and Buildings, Dec. 2012. Available: <http://dx.doi.org/10.1016/j.enbuild.2012.12.010>
- [3] **X. Li**, Y. Li and J. E. Seem, "Maximum Power Point Tracking for Photovoltaic System Using Adaptive Extremum Seeking Control," to appear in IEEE Transactions of Control Systems Technology, DOI:10.1109/TCST.2012.2223819, 2012.

Conference Proceedings:

- [1] **X. Li**, Y. Li, J. E. Seem and P. Li, "Extremum Seeking Control of Cooling Tower for Self-Optimizing Efficient Operation of Chilled Water Systems," in Proceedings of 2012 American Control Conference, pp. 3396-3401, Montreal, QC, Jun. 2012.
- [2] **X. Li**, Y. Li, J. E. Seem and P. Lei, "Maximum Power Point Tracking for Photovoltaic Systems Using Adaptive Extremum Seeking Control," in Proceedings of the 50th IEEE Conference on Decision and Control and European Control Conferences, pp. 1503-1508, Orlando, FL, Dec. 2011.
- [3] **X. Li**, Y. Li and J. E. Seem, "Dynamic Modeling of Mechanical Draft Counter-Flow Wet Cooling Tower with Modelica," in Proceedings of 2010 ASME Dynamic Systems and Control Conference, vol. 2, pp. 687-694, Cambridge, MA, Sep. 2010.